STUDY OF PHASE TRANSITIONS AND MAGNETO-CALORIC EFFECT IN Ni-Mn-X (X = Ga, Sn, In) FERROMAGNETIC SHAPE MEMORY ALLOYS

A thesis submitted

by

RAHUL DAS

to

Indian Institute of Technology Guwahati

in

partial fulfillment of the requirement for the award of the degree of
Doctor of Philosophy in Physics

Department of Physics
Indian Institute of Technology Guwahati
Guwahati – 781039, Assam, India

July 2013

Statement

The work contained in the thesis entitled "Study of phase transitions and magneto-caloric effect in Ni-Mn-X (X = Ga, Sn, In) ferromagnetic shape memory alloys" has been carried out by me under the supervision of Prof. A. Srinivasan and Dr. A. Perumal, at the Department of Physics, Indian Institute of Technology Guwahati. This work has not been submitted elsewhere for the award of any degree.

Rahul Das.

16th July 2013

(Rahul Das)

Roll No: 08612102

Department of Physics

Indian Institute of Technology Guwahati

Guwahati - 781039

Certificate

It is certified that the work contained in the thesis entitled "Study of phase transitions and magneto-caloric effect in Ni-Mn-X (X = Ga, Sn, In) ferromagnetic shape memory alloys" submitted by Rahul Das, a Ph. D. student of the Department of Physics, Indian Institute of Technology Guwahati for the award of degree of Doctor of Philosophy has been carried out under the supervision of myself and Dr. A. Perumal. This work has not been submitted elsewhere for the award of any degree.

16th July 2013

(Dr. A. Srinivasan)
Professor
Department of Physics
Indian Institute of Technology Guwahati
Guwahati – 781039

Certificate

It is certified that the work contained in the thesis entitled "Study of phase transitions and magneto-caloric effect in Ni-Mn-X (X = Ga, Sn, In) ferromagnetic shape memory alloys" submitted by Rahul Das, a Ph. D. student of the Department of Physics, Indian Institute of Technology Guwahati for the award of degree of Doctor of Philosophy has been carried out under the supervision of myself and Prof. A. Srinivasan. This work has not been submitted elsewhere for the award of any degree.

16th July 2013

(Dr. A. Perumal)
Associate Professor
Department of Physics
Indian Institute of Technology Guwahati
Guwahati – 781039

Dedicated

to

my parents

Acknowledgements

At the outset, I would like to express my deepest gratitude to my thesis supervisors Prof. A. Srinivasan and Dr. A. Perumal for giving me the opportunity to carry out my Ph.D. thesis work under their supervision. I am grateful to them for introducing me into the world of ferromagnetic shape memory alloys and for their keen interest in the progress of my thesis work. I am especially thankful to Srinivasan Sir for his constant encouragement, confidence and patience with me through all the years of my studentship.

I am grateful to my doctoral committee members, Prof. S. Ravi, Dr. D. Pal and Dr. S Kanagaraj for reviewing my research work regularly and for all their valuable suggestions for my doctoral research. I am thankful to the Head of the Department, Prof. S. Basu and all the faculty members of the Department of Physics for their support. I am indebted to Prof. S. B. Santra for his advice on critical behavior studies.

I am very much thankful to Dr. P. Saravanan, DMRL, Hyderabad for helping me to prepare the melt-spun ribbon samples. I am also thankful to Dr. Manoranjan Kar, IIT Patna for low temperature differential scanning calorimeter data.

I express my sincere thanks to Dr. Sidananda Sarma, Mr. Chandan Borgohain, Mr. Kula Senapati, Dr. Deba Kr. Sarma and Mr. Rituraj Saikia, the scientific officers of Department of Physics, CIF and Central workshop, for their support and cooperation during use of XRD VSM, PPMS, SEM, FESEM, workshop facilities in my Ph.D work. I am thankful to all my seniors, friends, lab-mates and research scholars of IITG for their support and cooperation. My special thanks go to Dr. Sidananda Sarma, Dr. M. P. C. Kalita, Dr. Rajendra Kr. Singh, Dr. Debabrata Mishra, Bhargab, Apurba, Akhilesh, Bhagaban, Arnab, Nisha, Shyni and Brahma.

I am deeply indebted to my parents, sisters, brother-in law and my love Mani for their support and encouragements. Finally, my sincere thanks are due to all those who have helped me in whatever manner during my Ph.D. work, some of whom I may have inadvertently forgotten to mention in this acknowledgement.

Rahul Das

PREFACE

Ferromagnetic shape memory alloys (FSMAs) are multifunctional smart materials. These are shape memory alloys with a ferromagnetic martensite phase. The shape memory effect in these alloys originate from the first-order diffusionless structural phase transition occurring between the high crystallographic symmetry austenite phase and a low symmetry martensite phase. The term shape memory indicates the ability of these alloys to ‘remember’ their original shape even after deformation and their capability to revert back to the original shape upon appropriate heat treatment. The coupling between crystal structure and magnetism has bestowed FSMAs with several novel properties. One such interesting property is related to the magneto-caloric effect (MCE).

MCE is an intrinsic property of a magnetic material due to which it heats up or cools down under the influence of an adiabatically applied magnetic field. Compared with the conventional gas-compression/expansion based refrigeration technology, MCE based magnetic refrigeration has several advantages such as energy efficiency, compactness and environment friendliness. Research interest in magnetic refrigerants was significantly enhanced with the discovery of giant magneto-caloric effect (GMCE) associated with the first-order structural transition in Gd based materials. Observation of large MCE in off-stoichiometric Ni–Mn–Ga Heusler alloy when the structural martensitic phase transitions accompanied with the magnetic phase transition, opened up the possibility of developing alternate magnetic refrigerant materials which are less expensive and non-toxic. Recently Ni-Mn-Sn and Ni-Mn-In FSMAs exhibit the large MCE with large magnetic entropy change (ΔS_M) and large adiabatic temperature change (ΔT_{ad}) near the martensitic transition temperature which highlights the potential of these alloys as magnetic refrigerants. Small variations in composition and partial substitution of a fourth element in ternary Ni–Mn–X (Ga, Sn, In) FSMAs have been found to have marked influence on their magnetic and structural (martensitic) transitions. Most of the investigations on these new MCE materials have concentrated on enhancing ΔS_M (or ΔT_{ad}) and hence were often performed under high magnetic fields of 5 Tesla or 8 Tesla and at sub-ambient temperatures. Practical applications demand magnetic refrigerants capable of stable and efficient operation at ambient conditions under low magnetic fields (say, < 2 Tesla) produced by cryogen-free magnets. To achieve these goals, magnetic refrigerant capacity (*RC*) and the width of the $\Delta S_M(T)$ curve of these magnetic refrigerants are the other important MCE parameters which need to be enhanced along with ΔS_M. By adopting different processing methods such as arc melting, melt spinning and ball milling, the shape and size of the FSMAs could be varied. It has been found in the present studies that these variations help in tailoring the MCE parameters of the FSMAs. This thesis work explores the influence of all these factors on the MCE achievable in Ni–Mn–X (Ga, Sn, In) FSMAs at fields ≤ 2 Tesla, so that the potential of these alloys for practical magnetic refrigerant application could be evaluated. The thesis consists of six chapters.

Chapter 1 presents a brief introduction to the content of the thesis. A review of literature relevant to the thesis work is also included in this chapter. Chapter 2 discusses the experimental techniques used in the present studies including the sample preparation methodologies adopted. The basic principle and the theory behind the experiments, the experimental set up and the measurement / methodology leading to the determination of the physical properties are also discussed here.

In Chapter 3, the composition dependence of structural and magnetic phase transformations with the associated changes in enthalpy (ΔE), Gibbs free energy (ΔG), and entropy (ΔS), and MCE of $Ni_{55}Mn_{21-x}Ga_{24+x}$ and its Co substituted variants are reported here. Room temperature X-ray diffraction patterns of all compositions except $Ni_{55}Mn_{18}Ga_{27}$ could be indexed to a non-modulated tetragonal (martensite) structure without ambiguity. However, $Ni_{55}Mn_{18}Ga_{27}$ alloy exhibited the $L2_1$ (austenite) structure. The unit cell volume of the tetragonal alloys increased and decreased with increasing Ga content and upon Co substitution, respectively. For some selected compositions, a direct transformation from paramagnetic high symmetric austenite phase to ferromagnetic low symmetric martensite phase (magneto-structural transition) was observed. Highest ΔS (ΔL, ΔG) of 24.1 $Jkg^{-1}K^{-1}$ (8.9 $kJkg^{-1}$, 482 Jkg^{-1}) accompanied by the highest ΔS_M of -17.7 $Jkg^{-1}K^{-1}$ for applied magnetic field change (ΔH) of 2 T was obtained for $Ni_{53.75}Mn_{20}Co_{1.25}Ga_{25}$ alloy at 373 K. The possibility of achieving large entropy change by Co substitution is discussed in this chapter.

Chapter 4 describes the MCE observed across the martensitic transition in $Ni_{50}Mn_{37-x}Fe_xSn_{13}$ and $Ni_{44}Mn_{43}(Co/Cu)_2Sn_{11}$ alloys. In the case of $Ni_{50}Mn_{37}Sn_{13}$, substitution of Fe leads to a decrease in the martensite start temperature (T_{Ms}) and an increase in the magnetization change (ΔM) as well as the thermal hysteresis around the martensitic transition. In the case of $Ni_{44}Mn_{43}(Co/Cu)_2Sn_{11}$ alloys, Curie temperature (T_C) shifts from 314 K to 327 K while ΔM measured under 0.1 T increases from 4.6 Am^2kg^{-1} to 7.4 Am^2kg^{-1} upon Co substitution. T_{Ms} (thermal hysteresis) changes for the Co substituted sample from 291 K to 191 K (from 25 K to 27 K). However, for the Cu substituted alloy, T_C, ΔM, T_{Ms} and the thermal hysteresis obtained are 298 K, 8.6 Am^2kg^{-1}, 270 K and 31 K, respectively. The martensitic transition of the parent ternary alloy ($Ni_{46}Mn_{43}Sn_{11}$) shifts to lower temperatures upon Co and Cu substitution. These studies demonstrate a means of tailoring both MCE and the temperature at which maximum MCE occurs in Ni-Mn-Sn alloys by Fe, Co and Cu substitution. $Ni_{44}Mn_{43}Cu_2Sn_{11}$ alloy exhibits maximum positive ΔS_M of 18.8 $Jkg^{-1}K^{-1}$ for ΔH of 1.8 T.

Chapter 5 discusses the effect of varying Ni/Mn ratio on the structural (martensitic) and magnetic phase transitions of parent Ni-Mn-In and Si substituted Ni-Mn-In alloys. In order to understand the influence of shape and particle size, $Ni_{51}Mn_{34}In_{14}Si_1$ alloy was prepared in ribbon and powder forms by melting spinning and ball milling, respectively. The highest ΔS_M (= 19.9 $Jkg^{-1}K^{-1}$) was observed for a ΔH of 1.2 T in bulk $Ni_{51}Mn_{34}In_{14}Si_1$ alloy. But this sample has a narrow operating temperature range [FWHM of $\Delta S_M(T)$ = 2.4 K] as well as comparatively small RC (= 35.9 Jkg^{-1}). Melt spinning at different wheel speeds and reduction of particle size by ball milling provided a means to vary the MCE parameters. The maximum RC of 40.4 Jkg^{-1}, maximum FWHM of ΔS_M(T) of 4.6 K and high ΔS_M of 11.2 $Jkg^{-1}K^{-1}$ were realized in annealed $Ni_{51}Mn_{34}In_{14}Si_1$ alloy powder with particle size ranging between 600 μm and 710 μm. Similarly, the best combination of MCE parameters (RC = 37.3 Jkg^{-1}, FWHM = 3.5 K and ΔS_M = 14.1 $Jkg^{-1}K^{-1}$) was obtained for melt spun (and annealed) ribbons prepared at a wheel speed of 16 ms^{-1}. The roles of solidification rate in melt spun ribbons and particle size effect in ball milled powders on tailoring the magnetic and magneto-caloric properties of Ni-Mn-In-Si FSMA are discussed. The nature of magnetic phase transition in the martensite and austenite phases in $Ni_{50}Mn_{35}In_{14}Si_1$ alloy has been studied by examining the critical behaviour near the phase transitions. Exchange bias originating from the competition of antiferromagnetism and ferromagnetism in this FSMA is also discussed in this chapter. These studies provide interesting insights on the nature of magnetism in this alloy.

Chapter 6 serves as a concluding chapter where in the scope for future work in this area is also pointed out in brief.

References and list of publications which have originated out of this thesis work are listed at the end of the thesis.

Contents

Chapter 1

INTRODUCTION

Choice of material has been a defining point in the development of mankind. Entire eras have been named after specific materials such as the primitive stone age, the early civilization time of bronze age, the industrialized iron age, the recent high technology silicon / polymer age and so on. The information age (1970 onwards) saw the development of microprocessors, microcontrollers and micro-electromechanical systems which resulted in faster and lighter computers and 'intelligent' machines. Metals, alloys, ceramics and plastics of yesteryears were 'engineered' into new and novel forms to meet the demands of the new era. In the present era materials capable of multiple functions at micrometer and nanometer dimensions are in great demand. Some such materials that exhibit one or more properties which can be dynamically changed in a controlled fashion by external stimuli are generally called as 'intelligent' or 'smart' materials [CULS96a, LEND02a, WANG12a]. Normally, smart materials use their reaction to the environmental stimulus to initiate or actuate an active change. 'Very smart' behaviour occurs when a material can sense more than one stimulus from the environment and react to them in a useful, reliable, reproducible and usually reversible manner [HUJS07a]. A number of smart materials have been demonstrated and many are still under development. Piezoelectric crystals which release a small electrical discharge when distorted, electro(magneto)-strictive materials which change their size when subjected to an external electric (magnetic) field, synthetic organic molecules such as azobenzene which undergo dimension change due to conformation change induced by a specific wavelength of light, half metallic ferromagnets which exhibit spin polarized current, multiferroics which respond to both electric and magnetic fields, shape memory materials (e.g., shape memory alloys and polymers) which respond to external changes in temperature and load by deforming and smartly recover their original shape under temperature/load cycling are some of the best examples of this class of materials. Since the process of loading/unloading or temperature cycling is inherently slow, the speed of shape change in shape memory alloys (SMAs) is limited. By applying an alternating magnetic field, faster shape or volume change or mechanical strain can be achieved in some magnetic alloys called magnetic shape memory alloys or ferromagnetic shape memory alloys (FSMAs) which have the potential to be the next generation 'very smart' actuator materials. In FSMAs, the magnetic and structural properties are strongly coupled with each other, which is rather rare in condensed matter systems. Such coupled phenomena in solids can lead to many interesting properties such as magneto-caloric effect (MCE), magnetic field induced strain (MFIS) and giant magneto-resistance (GMR) which have many technological applications. Since FSMAs are the materials of interest to this thesis work, their salient features are discussed below:

1.1. SHAPE MEMORY ALLOYS

Shape memory alloys (SMAs) are metallic alloys which can restore their pre-determined and original shape after deformation by loading-unloading or thermal cycling [DEZF13a]. SMAs have two solid state crystalline phases: a low temperature and low symmetry soft phase called 'martensite' and a high temperature high symmetry parent phase called 'austenite'. Diffusionless transition between these two phases results in fascinating behaviors such as recovery of large strains through the application or removal of heat or stress. The stress related effect is termed super-elasticity and ability of the deformed alloy to return to the original shape by heating is known as shape memory effect. These two unique phenomena make SMAs distinct from other metals and alloys. These unique properties of SMAs have been known since the 1930's [MACH03a, OTSU98a, OTSU99a].

In 1962, William J. Buehler and co-workers [BUEH63a] at the U.S. Naval Ordnance Laboratory discovered the thermally activated shape memory effect in a Ni-Ti alloy which is now popularly referred to as NITINOL. The austenite phase of NITINOL has the body centered cubic (BCC) crystal structure of $B2$-type with a lattice constant of ~3.015 Å. But the martensite phase of NITINOL has the monoclinic structure with distortions of $B19'$-type with the cell parameters a = 2.889 Å, b = 4.120 Å, and c = 4.622 Å and the monoclinic angle β = 96.8° [COMS96a]. The Young's modulus for austenite and martensite phases are 120 GPa and 50 GPa, respectively [THOM00a], i.e. austenite phase has more than twice the Young's modulus of the martensite phase. NITINOL could be plastically deformed up to ~ 8% in the martensite (monoclinic) phase which could be recovered from the deformation by heating it above the martensitic transition (or characteristic) temperature [THOM00a].

Apart from this, NITINOL can be easily obtained in different useful shape like wires, rods, tubes, ribbons, and thin sheets. Shortly after the discovery of NITINOL, a large number of studies demonstrated that the addition of a third element, such as Co or Fe to it, could significantly shift the martensitic transition temperature. The alloying technology which helped in a changing the desirable transition temperature led to a large number of commercial applications of SMAs [WUMI00a]. By early 1970's, SMAs such as Ti-Pd, Ti-Pt and Ti-Au exhibiting high temperature (approximately 370 K) martensitic transition were developed [DONK70a]. Recently, a wide variety of SMAs with specific characteristic temperature and associated properties have been developed [STRN95a, BOYD96a, LIUY03a, ALAM08a, ZHAN09a, TANA10a]. Even the characteristic temperature of NITINOL has been tailored to occur over a wide range (263 K to 350 K) by varying Ni/Ti ratio [DEZF13a]. Some important shape memory alloys and their characteristic temperature are listed in Table 1.1.

TABLE 1.1: Different types of shape memory alloys and their characteristic temperature

Alloy	**Characteristic temperature (K)**	**Reference**
$NiTi_{49.1}$	317.6	[STRN95a]
$NiTi_{49.5}$	326.0	[STRN95a]
$NiTi_{50}$	350.8	[STRN95a]
NiTi	315.9	[BOYD96a]
$NiTi_{45}$	263.0	[ALAM08a]
$NiTi_{44.1}$	273.0	[ALAM08a]
$NiTi_{40}Cu_{10}$	339.6	[STRN95a]
$NiTi_{41}Cu_{10}$	323.0	[STRN95a]
$NiTi_{41.5}Cu_{10}$	333.0	[STRN95a]
$NiTi_{25}Cu_{25}$	346.0	[LIUY03a]
CuAlBe	208.0	[ZHAN09a]
FeMnAlNi	< 223.0	[OMOR11a]
FeNiCuAlTaB	211.0	[TANA10a]

1.1.1. The Shape Memory Effect

The shape memory effect (SME) is observed in a SMA by the following process: the original shape of the SMA is defined as its shape in the austenite (high temperature) phase. If it is cooled below the martensite transition (or characteristic) temperature until it is completely transformed into its martensite (low symmetry) phase, it can be easily deformed from its original shape. If the deformed SMA is now heated through the martensitic transition temperature, it transforms to the high symmetry austenite phase and in that process 'remembers' its parent (original) shape and reverts back to it. Thus, the original shape recovery of the deformed SMA is related to the change in the crystal structure from the soft (low crystallographic symmetry) to hard (high crystallographic symmetry) phase at the characteristic temperature. To give the so-called 'original' shape which can be remembered by the SMA, the alloy is stressed or heat treated for a long time in the austenite (or parent) phase. The typical mechanism of the shape memory effect in two dimensions is represented by Figure 1.1.

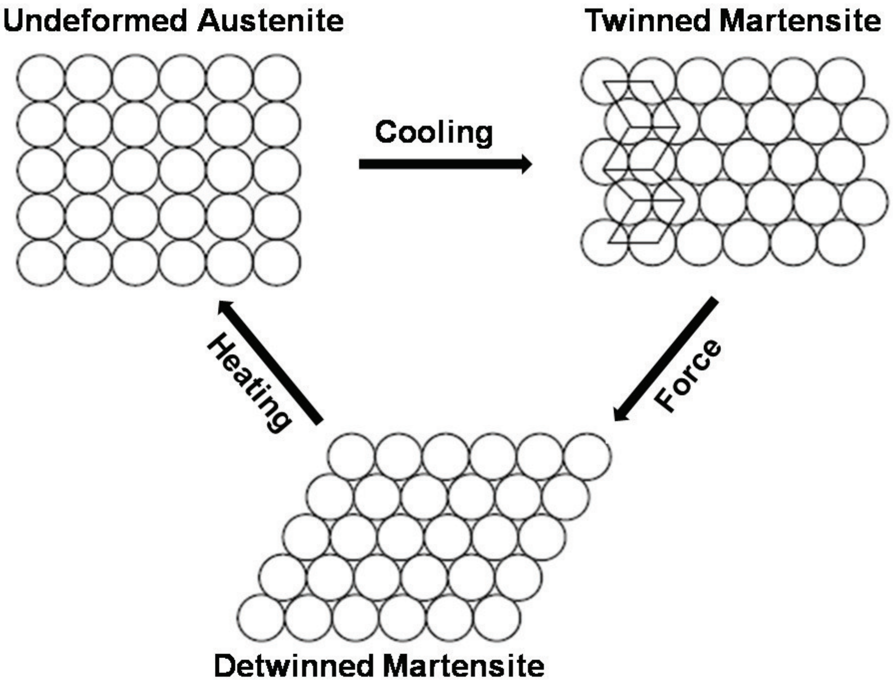

Figure 1.1: Two dimensional schematic representation of the mechanism of SEM in a SMA [LEND02a].

When the high symmetry (ordered cubic) structure is transformed to the low symmetry (complex twinned martensitic) structure, the twin boundaries can be effortlessly moved by an externally applied force to accommodate the applied stress. Thus, by minimizing any structural deformation at the microscopic level there is a new physical shape change on the macroscopic level, without any internal damage. Consequently, when the system is heated, the low symmetry complex structure transforms into the original cubic phase, reconstructing the original macroscopic shape [WAYM99a].

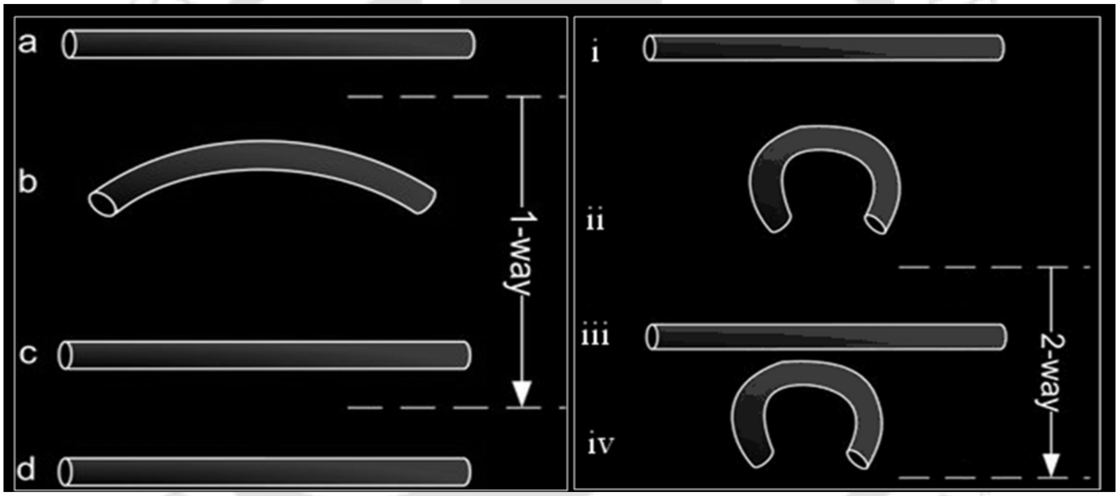

Figure 1.2: Schematic view of one-way and two-way shape memory effects. Starting from martensite (a/i), adding a deformation for training for the one-way or two-way effect (b/ii), heating the sample (c/iii) and cooling it again (d/iv).

However, SMAs can demonstrate two types of memory effects: the one-way memory effect and the two-way memory effect. Figure 1.2 depicts these two effects. When a SMA is in its low temperature, low symmetry state, it can be bent into a new shape (Figure 1.2b). It will retain that shape until it is heated above the crystallographic transition temperature. After being heated from a cooled deformed state; it recovers its original shape (Figure 1.2c), regardless of its shape in the low temperature state. When the temperature of the alloy is cooled again, it will remain in the high temperature original shape (Figure 1.2d), until a force is applied to deform it again i.e. cooling from high temperatures does not give a macroscopic shape change until a deformation is created in the low-temperature state. This demonstrates the one-way shape memory effect.

In the two-way SME, the material does not only remember the high temperature parent phase shape (*cf.* Figure 1.2iii) but also the low temperature martensite phase shape (*cf.* Figure 1.2iv) i.e., in this case, the material shows SME during both heating and cooling through the characteristic temperature. SMAs can show a two-way memory effect after a certain thermal training. By this, an SMA can 'learn' to behave in a certain way at a certain temperature. So, the trained alloy can show this effect without any external applied force. This type of effect is named as intrinsic two-way effect [PERK99a].

1.1.2. Pseudo-elastic effect

Pseudo-elasticity occurs when an SMA is completely composed of austenite phase. Alloys possessing this property exhibit almost rubber-like flexibility. Due to this effect, the crystallographic phase change (austenite to martensite) can be achieved by applying pure mechanical load or force at a constant temperature. However, since the paths of loading and unloading do not coincide, there is a hysteresis associated with energy dissipation.

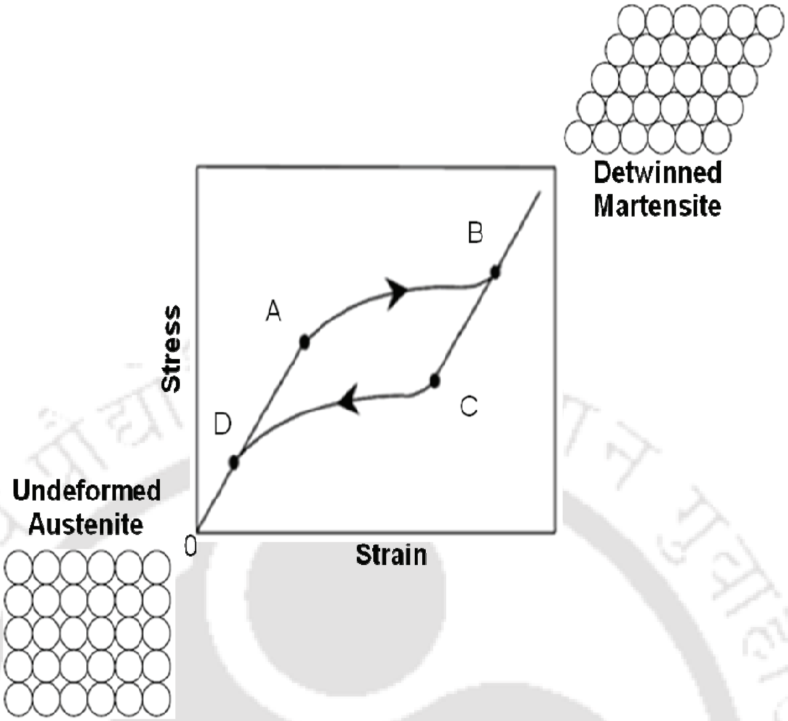

Figure 1.3: Stress-Strain diagram of a typical pseudo-elastic effect in an SMA [MACH03a].

Figure 1.3 depicts the Stress-Strain diagram corresponding to a typical pseudo-elastic SMA. An applied force by external load in austenite phase causes an elastic response until the critical value (point A) is reached. At this point the transformation to the martensitic phase begins, which subsequently ends at point B. At the point B, the crystal structure of the SMA is fully composed of detwinned martensite phase. For higher stress values, the alloy presents a linear response. During unloading, the alloy exhibits an elastic recovery from point B to C. Upon further unloading (i.e., from point C to D), one can note the reverse crystallographic martensitic transformation. From point D, the alloy presents an elastic discharge. After loading-unloading cycle, SMA has no residual strain [MACH03a]. Pseudo-elastic strain reported for a number of SMAs is listed in Table 1.2.

TABLE 1.2: Different types of shape memory alloys and their Pseudo-elastic strain.

Alloy	**Pseudo-elastic Strain (%)**	**Reference**
$NiTi_{49.1}$	3.6	[STRN95a]
$NiTi_{49.5}$	4.6	[STRN95a]
$NiTi_{50}$	2.2	[STRN95a]
NiTi	6.8	[BOYD96a]
$NiTi_{45}$	6.0	[ALAM08a]
$NiTi_{44.1}$	5.5	[ALAM08a]
$NiTi_{40}Cu_{10}$	3.4	[STRN95a]
$NiTi_{41}Cu_{10}$	3.1	[STRN95a]
$NiTi_{41.5}Cu_{10}$	2.8	[STRN95a]
$NiTi_{25}Cu_{25}$	2.5	[LIUY03a]
CuAlBe	2.4	[ZHAN09a]
FeMnAlNi	5.5	[OMOR11a]
FeNiCuAlTaB	13.5	[TANA10a]

1.1.3. Applications of shape memory alloys

SMAs are being used in a wide variety of fields including military, biomedical, safety, and robotics. SMAs can absorb and dissipate mechanical energy by undergoing a reversible hysteretic shape change during cyclic loading. The unique characteristics have made SMAs popular for a variety of application such as sensing and actuation, impact absorption and vibration damping. In 1993, Aiken and his coworkers proposed to increase the hysteresis damping in structures under earthquake using the SMAs as a passive energy dissipater [AIKE93a]. In F-14 fighter planes, the United States military has deployed NITINOL couplers since the late 1960s and there are no reported failures for nearly 50 years [LIAN90a]. Other two successful applications of SMA are as eyeglass frames and the antenna of mobile phones [ZIDE88a, WUMI00a]. So far, super-elastic SMA devices have made the most significant impact in both material consumption and commercial value. Many of the current applications of SMAs are in biomedical field. As an example, vascular stents developed by fine NITINOL wires can be woven into cylindrical shapes to reinforce blood vessels [WHIT97a]. The stent is pressed and inserted into the blood vessel through a cannula and above its transition temperature, the stent returns to its original cylindrical shape. Thus, it provides reinforcement to the walls of the blood vessel. Other biomedical applications of SMAs are vascular filters, medical guide-wires and guide-pins for surgery, etc [WANG91a]. SMAs, especially NITINOL, are being used in robotic actuators and micromanipulators to simulate human muscle motion [AVAD08a, BHAN12a]. Miscellaneous applications of SMAs include their use in smart clothing, household appliances and adaptive structures. The main advantages of SMA are its good mechanical properties, the controlled force it exerts upon activation and its excellent bio-compatibility. However, there are still some application limitations of SMAs that must be overcome before they can live up to their full potential. Since it generally takes a comparatively long time to cool down and heat up the SMA and hence for crystallographic transformation to occur, SMAs are best suited for low-frequency and quasi-static response control but not for high-frequency control. Faster response has been observed in some magnetic SMAs by applying an alternating magnetic field. Such alloys are known as ferromagnetic shape memory alloys (FSMAs).

1.2. FERROMAGNETIC SHAPE MEMORY ALLOYS

Ferromagnetic shape memory alloys (FSMAs) have created a great interest in the last two decades since they embody the properties of the conventional shape memory alloy (shape memory effect and pseudo-elasticity) as well some other useful properties like magneto-resistance and magneto-caloric effect, as a result of the coupling between structural and magnetic properties. Furthermore, compared to conventional SMAs, the ferromagnetic shape memory effect (FSME) demonstrated by FSMAs extends its operation of magnetic actuation to a much higher operating frequency.

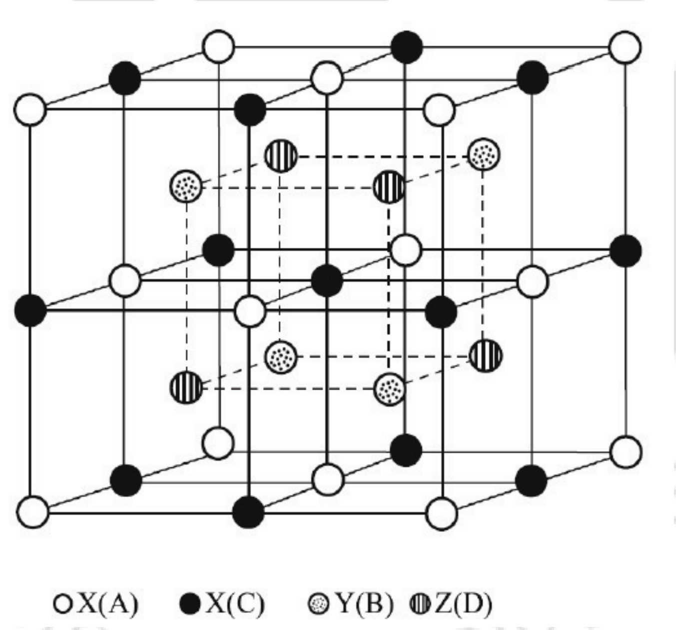

Figure 1.4: Atomic arrangement in a full Heusler (X_2YZ) alloy with $L2_1$ structure. Here, the four face centered cubic sub-lattices denoted as A, B, C and D are occupied by X, Y, X and Z atoms, respectively [LUOH13a].

Ni-Mn-Ga is the first reported ternary Heusler alloy based FSMA [WEBS84a, ULLA96a, ULLA97a]. Full Heusler compounds with the generic formula X_2YZ (where

X and Y are 3*d* elements and *Z* is a group IIIA–VA element) are named after a German mining engineer and chemist Friedrich Heusler, who studied such an alloy in 1903 [HEUS03a]. Normally in the austenite state, Heusler alloys crystallize in the ordered $L2_1$ structure (space group $Fm\bar{3}m$) which has four interpenetrating face centered cubic (*fcc*) sub-lattices [WEBS73a] A, B, C and D as shown in Figure 1.4. A and C sub-lattices have (0, 0, 0) and (1/2, 1/2, 1/2) Wyckoff coordinates which are occupied by X atoms. B and D sub-lattices have Wyckoff coordinates of (1/4, 1/4, 1/4) and (3/4, 3/4, 3/4), which are occupied by the Y and Z atoms, respectively. The magnetic property of the Heusler alloys is mainly due to the X and/or Y elements.

Some X_2MnZ Heusler alloys have been found to exhibit shape memory effect because of the crystallographically reversible thermoelastic martensitic transformation [GEJI99a, VASI99a, KAIN96a, OIKA01a, OIKA01b, WUTT01a, OIKA02a, OIKA02b]. In these metallic compounds, the magnetic moment is due to the Mn atoms. The exchange interaction between Mn atoms results in ferromagnetism which opens up the possibility of inducing shape (and dimensions) change and martensitic transformation by an externally applied magnetic field in addition to mechanical load and temperature (conventional SME). After the discovery of Ni_2MnGa FSMA, several off-stoichiometric Heusler alloys such as Co-Ni-Al [KAIN96a, OIKA01a, OIKA01b], Ni-Mn-Al [GEJI99a], Co-Ni-Ga [OIKA01b, WUTT01a], Fe-Ni-Ga [OIKA02a, OIKA02b] have also been found to display ferromagnetic shape memory behavior.

Magnetic field induced strain (MFIS) in single crystalline Ni-Mn-Ga alloys have reached a remarkable value of 10% [SOZI02a, PONS08a], and the response time is less than a millisecond. For this reason as well as its excellent thermal stability, Ni-Mn-Ga alloys are the most widely investigated FSMA in polycrystalline [ULLA01a], composite [FEUC03a, SCHE07a], fibers [SCHE08a] and textured [GAIT09a] form as alternatives to expensive single crystals. Recently, polycrystalline foams of Ni-Mn-Ga FSMAs have been found to exhibit large MFIS which is related to the pore size of the foam. When the grain size is larger than the pore size, MFIS of ~9% could be achieved [CHMI09a]. Since the new Heusler alloys such as Ni-Mn-Sn, Ni-Mn-In, Ni-Mn-Sb [SUTO04a, RAMA10a] with stoichiometric as well as off-stoichiometric compositions exhibit magnetic super-elasticity in the martensitic state, they have also become good candidates for actuator technology [KREN07a, KARA09a].

Depending on the composition of the FSMA, the temperatures of the ferromagnetic and the martensitic structural transitions can be finely tuned. The phenomenon of coupled magnetic and structural phase transition can result in many interesting properties including a large MCE around room temperature [BROW05a, PASQ05a, INGA07a].

1.2.1. Phase transitions

A phase of a system can be characterized by a state having uniform physical properties like density, atomic arrangements, magnetic order, crystal structure, chemical composition, etc [GORD68a, PORT92a]. A system can show different state forms which represent its different phases. Changes from one phase to the other are called phase transitions. A phase transition can be driven by different control variables—temperature, pressure, magnetic or electric field, etc. It is well known that during the transition from a high temperature phase to a low temperature phase, the free energies of both the phases are equal at the transition temperature (T_{tran}) [STAN71a]. But, the derivative of the free energy with respect to a control variable may differ. According to Ehrenfest, the order of any phase transition is defined by the lowest order of the derivative of the Gibbs free energy which exhibits discontinuity across the phase transition [HUAN63a, REIC80a, STAN71a].

If G_1 and G_2 are the free energies of the two phases, then for an n^{th} order phase transition,

$$\left.\frac{\partial^n G_1}{\partial T^n}\right|_{T=T_{tran}} \neq \left.\frac{\partial^n G_2}{\partial T^n}\right|_{T=T_{tran}} \tag{1.1}$$

But,

$$\left.\frac{\partial^{n-1} G_1}{\partial T^{n-1}}\right|_{T=T_{tran}} = \left.\frac{\partial^{n-1} G_2}{\partial T^{n-1}}\right|_{T=T_{tran}} \tag{1.2}$$

where n is an integer.

Some thermodynamic and magnetic variables that are derivatives of Gibbs free energy are given below:

$$\begin{gathered}
Entropy\ (S) = -\left(\frac{dG}{dT}\right)_P \\
Volume\ (V) = \left(\frac{dG}{dP}\right)_T \\
Magnetization\ (M) = -\left(\frac{dG}{dH}\right)_{T,P} \\
Heat\ capacity\ (C) = T\left(\frac{dS}{dT}\right) = -T\left(\frac{d^2G}{dT^2}\right) \\
Susceptibility\ (\chi) = \left(\frac{dM}{dH}\right) = -\left(\frac{d^2G}{dH^2}\right)
\end{gathered} \tag{1.3}$$

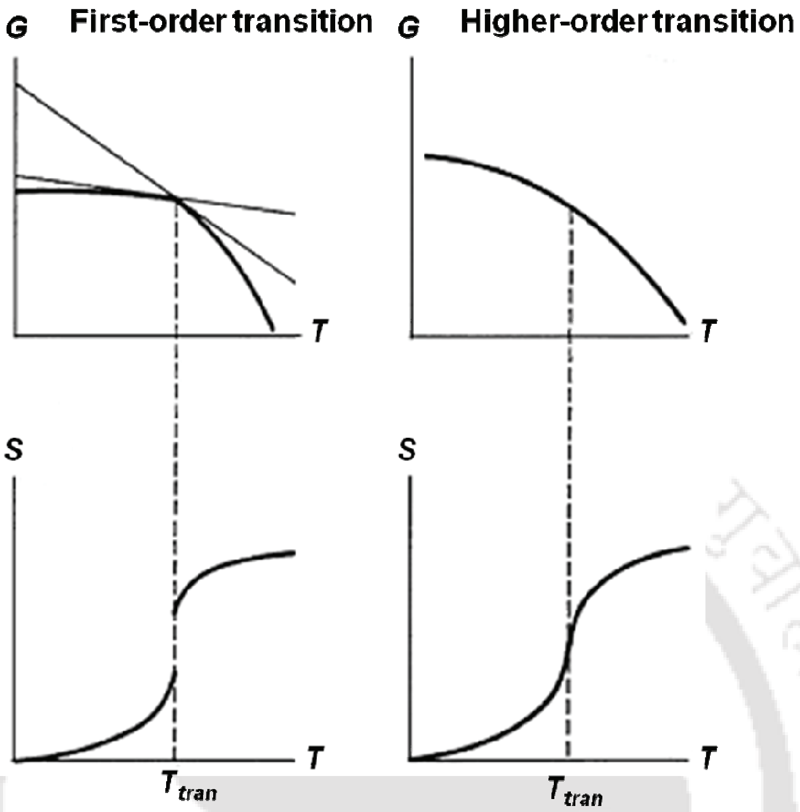

Figure 1.5: Ehrenfest's scheme for first and higher-order phase transitions [STAN71a].

As per Ehrenfest's scheme, discontinuity in volume, entropy, and magnetization across the phase transition signifies a first-order phase transition (shown in left side of Figure 1.5). On the other hand, continuity in volume, entropy, magnetization but discontinuity in second-order derivative of free energy (say, in heat capacity and susceptibility) across the phase transition qualifies these transitions as second-order (shown in right side of Figure 1.5). During the first-order phase transition, discontinuity in entropy leads to a latent heat (L) which defined as

$$L = T_{tran} \Delta S \tag{1.4}$$

where $\Delta S = \left[S_2 - S_1 \right]_{T_{tran}}$ i.e. the difference in entropy between the two phases at the transition temperature. In case of higher order phase transitions, there is no latent heat.

According to Landau theory of phase transitions, the concept of order parameter can be used to classify the phase transitions. Order parameter is an entity or observable, which by definition is zero in one phase and assumes finite values in the other [CHAI98a]. The finite change or discontinuity in the order parameter in the phase transition represents the first-order phase transition (Figure 1.6). On the other hand, if the order parameter shows a continuous variation at the phase transition, the transition is of higher-order.

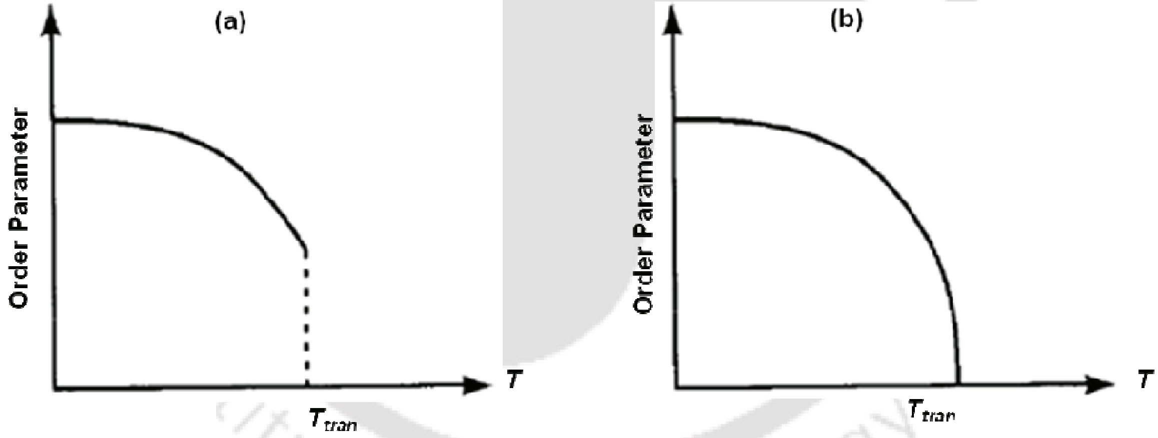

Figure 1.6: Order parameter as a function of temperature (T) for a (a) first-order phase transition, and (b) second-order phase transition [CHAI98a].

Generally FSMAs show two characteristic temperature induced phase transitions: a structural first-order phase transition at the martensitic transition temperature (T_M), and a magnetic second-order phase transition at the Curie temperature (T_C) of the austenitic and/or martensite phases, accompanied by a change in magnetization (ΔM) [SUTO04a, KREN05a, OIKA06a, BHOB07a, SHAR07a, PLAN09b, GAOB09a, JING09a, RAMA10a, KAZA11a]. In the next two sections, details of the martensitic and magnetic transitions are discussed.

1.2.1.1. Martensitic transition

The martensitic phase transition is a solid-state first-order structural phase transition which is displacive, diffusionless, cooperative and dominated by the strain-energy arising from shear-like displacements of atoms from a high symmetry phase to a lower symmetry phase [SARM09a]. The German metallurgist Adolf Martens was the pioneer in the study of the martensitic transitions on steels [KRAU05a]. The name "martensite" is named after him to describe the product phase of a martensitic transition. The parent phase (the gamma iron phase in steel) above the critical temperature was described as austenite, after Sir William Chandler Roberts-Austen. This type of transition has been observed in various materials other than steels such as nonferrous alloys, ceramics, minerals, polymers, etc [GARV75a, GUPT78a, KOOK93a, LOBO11a,]. As mentioned earlier, presence of the martensitic phase transition is the key behind the shape memory effect (conventional as well as magnetic) and super-elasticity of a material. Since the parent austenite phase has higher symmetry compared to the product martensite phase, the phase transition can result in more than one structural configuration of martensite phase called martensite variants [OTSU98a, OTSU02a, BHAT03a]. As an example, three martensite variants are possible when the transition occurs from cubic austenite phase to tetragonal martensite phase (Figure 1.7).

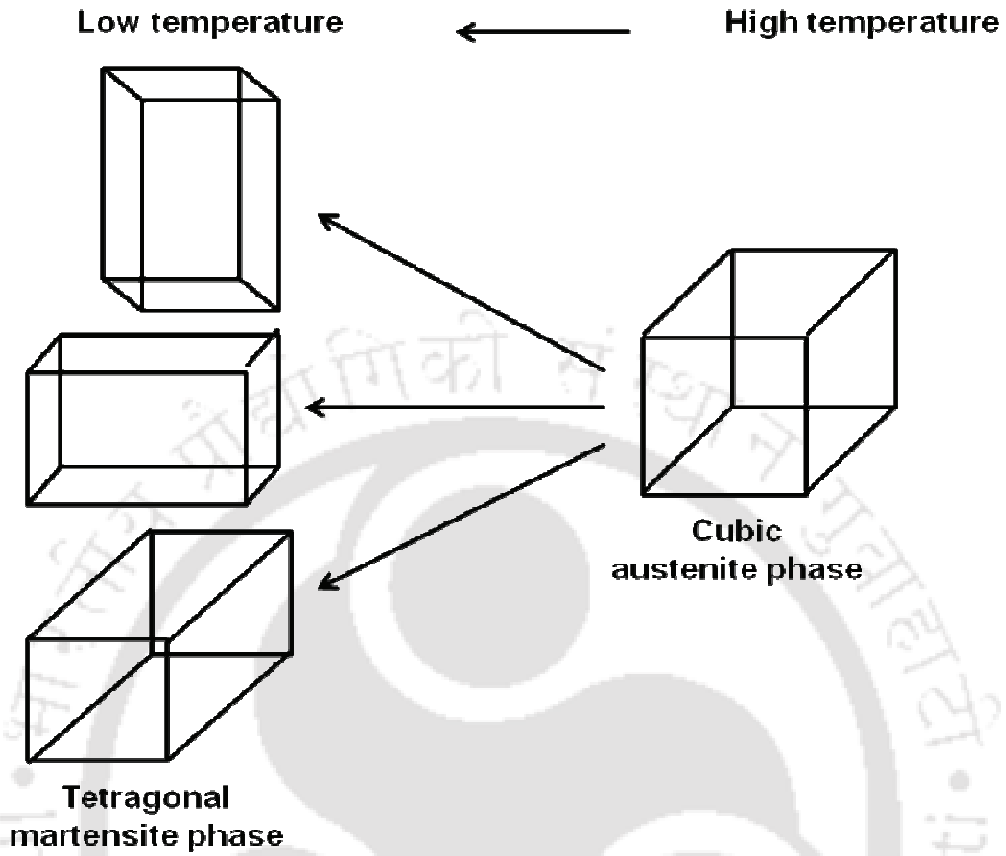

Figure 1.7: Different martensite variants in cubic → tetragonal martensitic phase transition.

The martensitic transition usually takes place over a temperature range and is characterized by a hysteresis behavior (a feature of first-order phase transition). The characteristic temperatures namely, martensite start (T_{Ms}) and martensite finish temperatures (T_{Mf}) during cooling process, and austenite start, (T_{As}) and austenite finish temperatures (T_{Af}) during heating process are indicated in Figure 1.8 [OTSU98a]. In the forward martensitic transition, the formation of martensite phase progresses between T_{Ms} and T_{Mf}, and in the reverse transition, austenite phase formation progresses between T_{As} and T_{Af}.

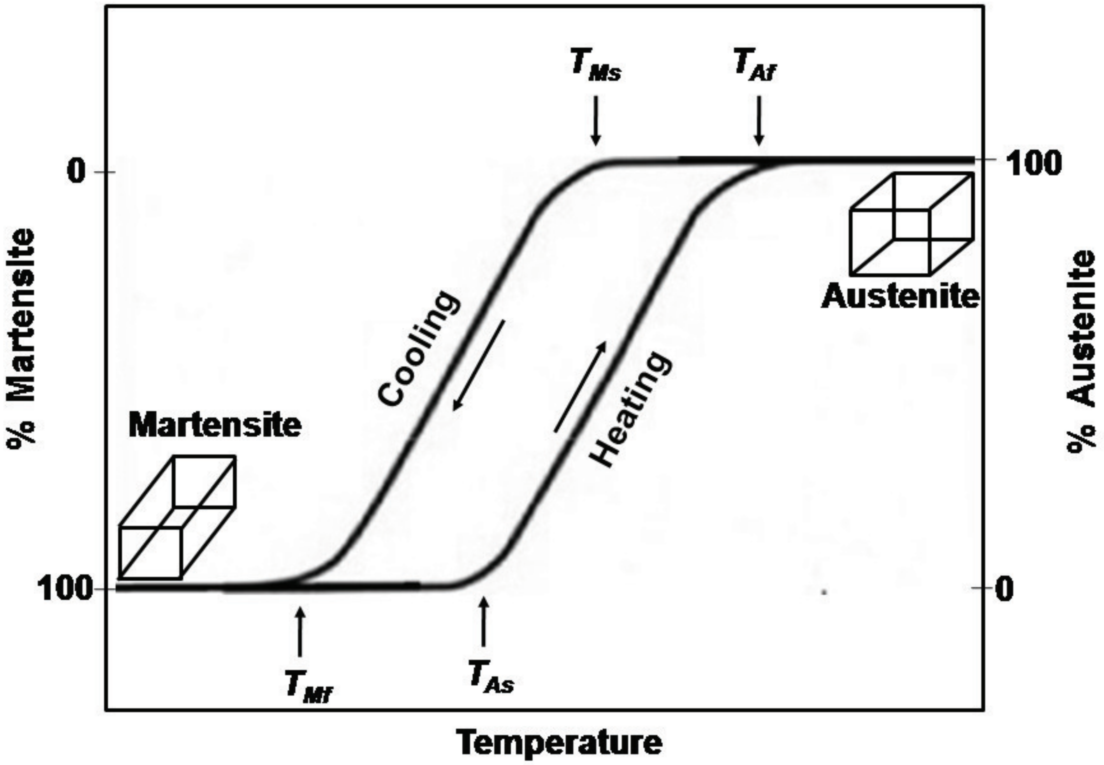

Figure 1.8: Temperature dependence of the phase fractions across the martensitic transition. Characteristic temperatures of the martensitic transition are indicated by vertical arrows.

For a reversible martensitic transition, the following conditions must be satisfied by a system [SARM09a]:

1) The driving force for the martensitic transition should be very less.

2) The interface between the austenite and the martensite phases has to be very mobile upon heating and cooling.

3) The martensitic transition should be structurally reversible, *i.e.*, the martensite should revert back to the austenite with its original orientation rather than re-nucleating into austenite in different orientations.

Martensitic transformations that satisfy the above conditions are called thermo-elastic martensitic transitions. Salient features of thermo-elastic martensitic transitions are given below [SARM09a]:

1) Martensitic transitions are usually first order solid state structural phase transitions which are displacive and diffusionless.
2) Their kinetics is dictated by the strain energy arising from shear displacement.
3) The displacement of atoms can be described as a homogeneous lattice deformation.
4) The atoms move in an organized manner relative to their surroundings and hence are known as 'military' transformations in contrast to diffusional 'civilian' transformations.

1.2.1.2. Magnetic transitions

Magnetization (M) is the order parameter for a ferromagnetic material and its value distinguishes the low temperature magnetic phase ($M \neq 0$) from the high temperature nonmagnetic one ($M = 0$). As can be seen from equation (1.3), M is defined as the first derivative of the Gibbs free energy with respect to magnetic field. Therefore, a discontinuity in M at the phase transition would signal the occurrence of a first-order of phase transition. On the other hand, if M is continuous at the phase transition, the transition should be of higher-order.

Magnetic phase transitions are found more commonly to be of second-order with continuous variation in the order parameter, M across the magnetic transition. In case of a continuous phase transition, it is typical that the order parameter, various response functions and correlation functions exhibit a non-analytic behavior as a function of thermodynamic variables in the vicinity of the critical point. Usually, this non-analytic behavior assumes power law dependence in deviations from the critical point values of variables such as temperature and magnetic field strength in the ferromagnetic ↔ paramagentic transition. The exponents related to such asymptotic relations are the critical exponents of the transition. The most common critical exponents, β, γ, and δ corresponding to the spontaneous magnetization (M_S), initial susceptibility (χ_0) and isothermal magnetization ($M_{T = T\square}$) are defined as follows:

$$\begin{aligned} &M_s(T) \propto |t|^{\beta} \qquad t<0 \\ &\chi_0(T) \propto |t|^{-\gamma} \qquad t>0 \\ &M(H, T=T_C) \propto H^{\frac{1}{\delta}} \qquad t=0 \end{aligned} \tag{1.5}$$

where $t = (T - T_C)/T_C$ is the reduced temperature. By comparing the values of exponents with various standard theoretical models such as mean-field ($\beta = 0.5$, $\gamma = 1$ and $\delta = 3$), 3D Heisenberg ($\beta = 0.365$, $\gamma = 1.386$ and $\delta = 4.8$) and 3D Ising ($\beta = 0.325$, $\gamma = 1.24$ and $\delta = 4.82$), the critical behaviour as well as the magnetic interaction in the materials can be explained [KAUL85a, GHOS98a, MOHA98a, KIMD02a]. For the magnetic phase transitions another important exponents corresponding to magnetic entropy change, ΔS_M defined as [OEST84a, FRAN06a, FRAN08a, FRAN11a]

$$\Delta S_M \propto H^n \tag{1.6}$$

Again a relationship between the exponent n and the critical exponents (β and δ) of amagnetic material has been expresed as [FRAN06a, FRAN08a].

$$n = 1 + \frac{1}{\delta}\left(1 - \frac{1}{\beta}\right) \tag{1.7}$$

The detail study on critical exponents associated with ferromagnetic ↔ paramagentic transition is needed to understand the nature of ΔS_M (H).

1.2.2. Ferromagnetic Shape Memory Effect

Ferromagnetic shape memory effect (FSME) occurs in the ferromagnetic martensite phase when an external magnetic field is applied. The martensite phase of FSMAs consists of multi-variant twin-related domains with a large magneto-crystalline anisotropy (K). Under an applied magnetic field, the magnetic moments of the martensite variants tend to align along the field direction. Due to large magneto-crystalline anisotropy, the energy cost of the magnetic moment rotation (from the easy axis towards the direction of the applied magnetic field) is larger than the energy required for twin boundary motion of the martensite variants. In such a situation, the applied magnetic field induces to a change in the shape of the material so that the twins can rearrange themselves or detwinning can occur.

The mechanism of magnetic field induced shape change is schematically illustrated in Figure 1.9. If the magnetic field is applied in the reverse direction, the twin boundaries can move back to their original positions and the alloy regains its original shape. Such magnetic field controlled shape memory effect in the ferromagnetic alloy is called as the FSME.

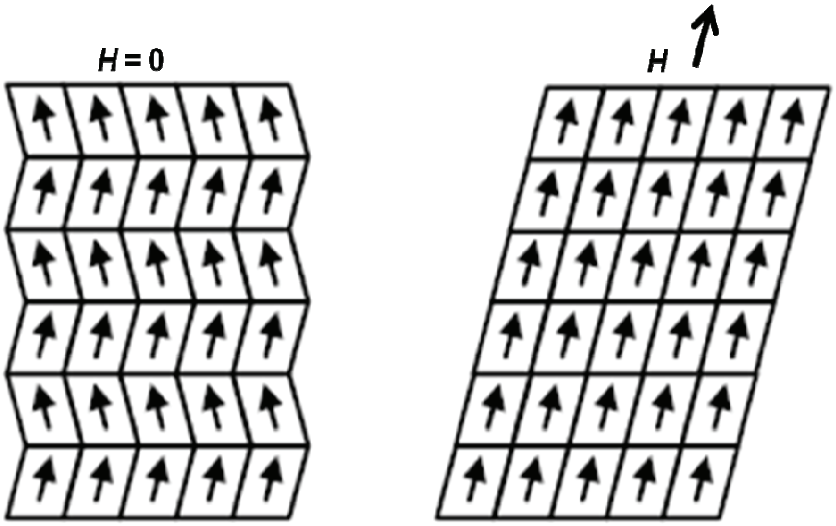

Figure 1.9: Magnetic field induced re-orientation of the martensitic variants.

Basically, the macroscopically observable field induced strains found in FSMAs are caused by the microstructural reorientation of martensitic twin variants. For each variant, there is a magnetic moment M which is pinned in the direction parallel to the magnetic easy axis due to the magneto-crystalline anisotropy. When a magnetic field H is applied, the direction of M changes from the easy axis to the direction of the applied magnetic field. For a large anisotropy, the angle between M and H may be reduced by the rotation of variant so that both the directions of M and the easy axis tend to orient along the direction of H. If magnetic moments of two neighboring variants are represented by two vectors M_1 and M_2, the Zeeman energy $[(M_2 - M_1) \cdot H]$ leads to a driving force on the variant boundaries [MORI09a]. So, the strain will be induced when the value of $K \geq (M_2 - M_1) \cdot H$. If $(M_2 - M_1) \cdot H >> \mathrm{K}$, the magnetic moments in the two variants align with the field direction and the Zeeman energy across the twin boundary almost vanishes and only limited strain can be achieved.

1.2.3. Effect of additive elements in ternary alloys

Addition of extra elements is a classical way to modify the properties of a given alloy [WANG01a, IMAN06a, PHAN07a, PONS08a, BARI11a, SURE11a]. So, addition of a fourth element can be an effective way to change the magnetic and structural properties of ternary full Heusler (X_2YZ) and off-stoichiometric Heusler alloys. The effect of different additional elements in Ni–Mn–Ga alloy has been studied in recent years [CHER01a, WUGH02a, LIUZ02a, CHER03a, KHOV03a, KOHO04a, CHER04a, KHAN05a, GLAV06a, WANG06a]. The martensitic transition temperature of Ni–Mn–Ga alloys is very sensitive to the presence of rare-earth elements. These rare-earth elements can also improve its mechanical strength. According to existing reports, substitution of Tb for Ga in $Ni_{50}Mn_{29}Ga_{21}$ alloy enhances T_{Ms}, whereas the addition of Sm in $Ni_{48}Mn_{33}Ga_{19}$ alloy decreases T_{Ms} [ZHAO04a, ZHAO04b]. Since Gd is ferromagnetic and has the highest Curie temperature among the rare-earth elements, addition of this rare earth element can affect the magnetic properties along with refinement of the grains and enhancement of strength of grain boundaries [GAOL06a, GAOL08a]. Magnetic properties and shape memory effect in Fe-doped $Ni_{52}Mn_{24}Ga_{24}$ alloy have been investigated by Wu *et al*. [WUGH02a]. On partially replacing Mn with Fe in $Ni_{52}Mn_{24}Ga_{24}$ having $L2_1$ crystal structure, the resulting alloy (i.e., $Ni_{52}Mn_{16}Fe_8Ga_{24}$) exhibits a large magnetic moment ($3.91\mu_B$ per formula unit) and a high T_C about 381 K without any structural change. By optimizing the magnetic and structural properties, improvement in MFIS, magneto-resistance, magnetic entropy, adiabatic temperature change (ΔT_{ad}) and refrigerant capacity (RC) have been achieved in FSMAs containing appropriate additive elements. Recently, a large MFIS of 8.5% under a field of

1 T has been reported in $Ni_{49}Fe_{18}Ga_{27}Co_6$ alloy for an externally applied stress of 8 MPa [MORI07a]. Apart from this, a very large MFIS (~12.8%) was observed at 293 K in $Ni_{46}Mn_{24}Ga_{22}Co_4Cu_4$ single variant sample [SOZI13a]. In many cases, the additional elements were carefully selected to modify the density of conduction electrons (e/a ratio) and the transition temperatures [ITOW07a]. The modification of interatomic distance or lattice parameters by incorporation of additional elements has also been studied [SHAR10b]. Addition of Co or Mn to Ni–Fe–Ga alloys (substituting for Ni or Fe) modifies the transition temperatures according to the changes produced in e/a ratio [MORI07a, PICO08a]. However, for the alloy in which Fe is substituted by Co, the shift of martensitic transition temperatures is higher than the others for the same change of e/a. These results suggest that the change in the size of the atoms which modify the lattice parameters also plays a role in controlling the transformation temperatures apart from the e/a ratio. In many report, both magnetic and martensitic transitions of Ni-Mn-Ga alloys were tuned with additive elements, which in turn might lead to large magnetic entropy change (ΔS_M) at a desired temperature. Substitution of Mn with Cu ($Ni_2Mn_{0.75}Cu_{0.25}Ga$ [KHAN07b]) and Co ($Ni_{2.15}Mn_{0.81}Co_{0.04}Ga$ [BAOB08a]) has yielded ΔS_M of -28 J/kg-K at 308 K and -14.2 J/kg-K at 345 K, respectively, for an applied magnetic field change, ΔH of 2 T. Substitution of Co with Mn ($Ni_{43}Mn_{43}Co_3Sn_{11}$) [GAOB09a] and Cu ($Ni_{50}Mn_{33}Cu_2Sn_{15}$) [GAOB09b]$^{.}$ has yielded ΔS_M of 33 $Jkg^{-1}K^{-1}$ at 188 K and 13.5 $Jkg^{-1}K^{-1}$ at ~206 K, respectively, for ΔH of 5 T. ΔT_{ad} of -1.5 K and -1.99 K have been achieved at martensitic transition for ΔH ~ 1.8 T in Ge and Al substituted $Ni_{50}Mn_{35}In_{15}$ alloy, respectively [KAZA11a]. Peak ΔS_M of 124 $Jkg^{-1}K^{-1}$ and RC of 158 Jkg^{-1} have been found in $Ni_{50}Mn_{35}In_{12}Si_3$ alloy at 239 K for ΔH of 5 T [PATH08a].

1.2.4. Applications of ferromagnetic shape memory alloys

Ferromagnetic shape memory alloys (FSMAs) have been recently used as actuators to produce large and fast mechanical motion and force. Some important areas where the magnetic actuators have potential application are manufacturing automation, microsurgical instruments, micro-sensors, micro-actuators such as micro-valves, and stepper motors etc [KOHL99a, GOLU04a].

Figure 1.10 shows a schematic diagram of a basic FSMA actuator. In general, the actuating material is aligned with its easy magnetization axis (*c*-axis of martensite phase) along the direction of pre-stress in zero-magnetic field. When a magnetic field is applied perpendicular to the easy axis, the twin variants are rotated such that c-axis aligns parallel to the field direction. This leads to a large elongation (Δl) perpendicular to the field.

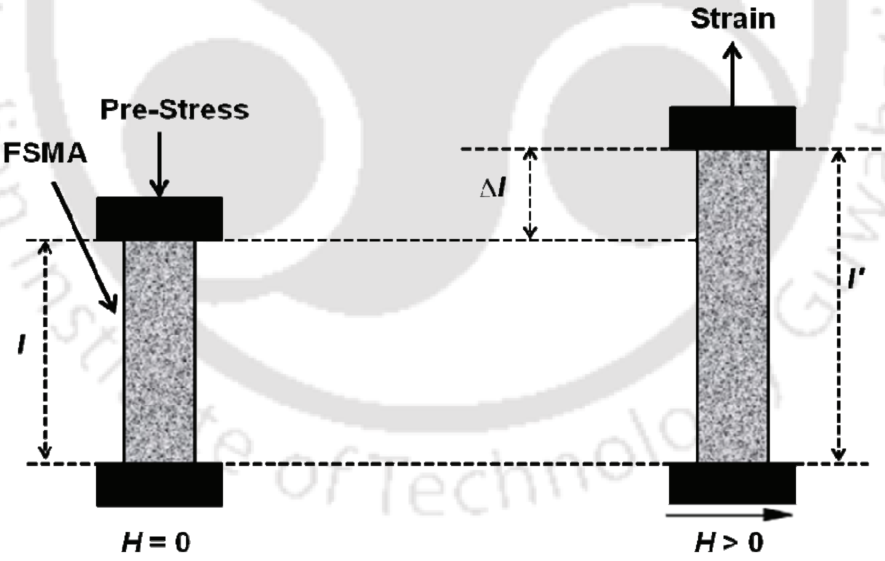

Figure 1.10: Schematic diagram of single crystal FSMA actuator [TANH08a].

Due to the possibility of achieving large MCE in FSMA when the structural and magnetic phase transitions occur at close temperature intervals, FSMAs are being considered for use as magnetic refrigerator materials. In the following section, MCE is discussed.

1.3. MAGNETO-CALORIC EFFECT

Magneto-caloric effect (MCE) refers to the thermal response of a material subjected to an external magnetic field which is due to the inter-dependence of thermal and magnetic properties of the material. This effect first observed by Emil Warburg in 1881 in pure Iron, which was found to warm up under an applied magnetic field [WARB81a]. In 1905, Langevin demonstrated the reversible temperature change caused by magnetizing a paramagnet [LANG05a]. But, it was only in the late 1920s that the origin of MCE was explained independently by Debye [DEBY26a] and Giauque [GIAU27a] who also suggested a new method of achieving low temperatures by adiabatic demagnetization. A few years later, Giauque and MacDougall experimentally demonstrated adiabatic demagnetization of a paramagnetic salt and also reached an ultra low temperature of 0.25 K using this process [GIAU33a].

Normally, MCE is an intrinsic property of a magnetic material and the strength of this effect can be characterized by the change in temperature arising from the application or removal of an external magnetic field. If a magnetic material is exposed to an external magnetic field under isothermal condition, the magnetic moments are aligned by the magnetic field and the entropy decreases (which is evident from Figure 1.11). But, under adiabatic condition, the total entropy is constant. In this case, the difference in magnetic entropy is transferred to lattice entropy via spin and lattice coupling. This transformation makes the atoms vibrate more rapidly. As a result, temperature of the material increases. On the other hand, the adiabatic removal of the external field causes the moments to re-randomize, thereby removing the entropy from the lattice or creating a cooling effect (as illustrated in Figure 1.11). Thus, the coupling of spin sub lattice with the magnetic field produces the MCE.

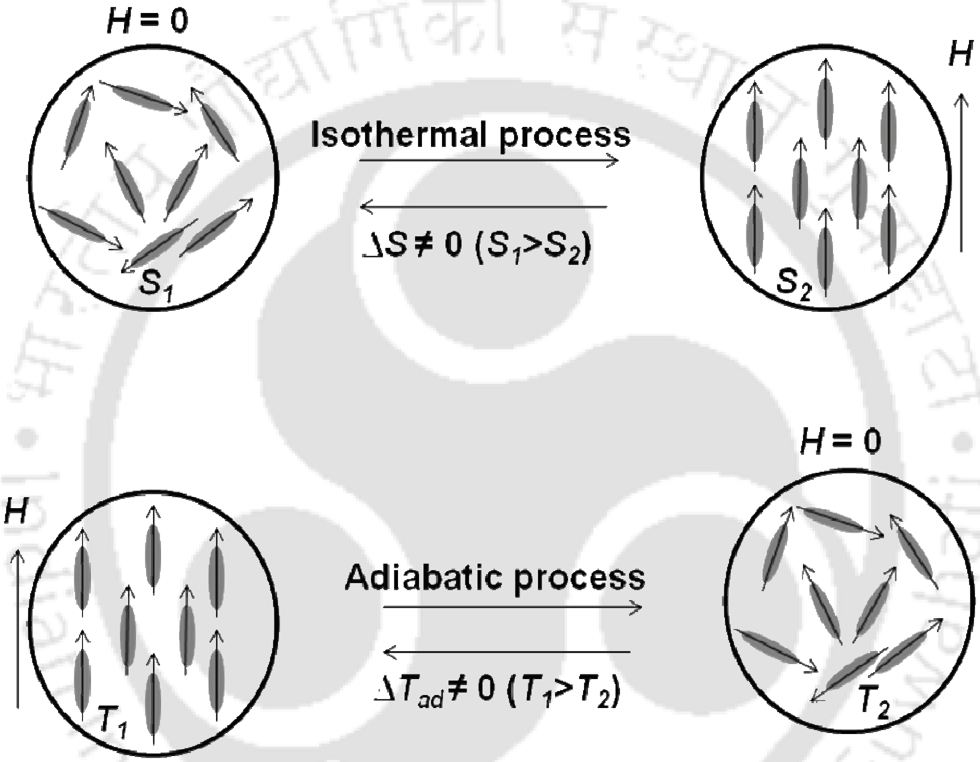

Figure 1.11: The basic mechanism of MCE when a magnetic field is applied to or removed from a magnetic system under different thermodynamic conditions [ROME13a].

The peak value of MCE can be obtained around temperatures where rapid changes in magnetization (*M*) with respect to temperature occur i.e. at the phase transition temperatures.

1.3.1. Magneto-caloric materials

There are several classes of materials which exhibit MCE. For a long period, the search for magneto-caloric compounds for applications was focused on rare-earth-based compounds because of the large MCE exhibited by them around room-temperature [GSCH94a, GSCH96a, BRUC08b]. The largest value of MCE was found in Gd, where the value of ΔS_M and ΔT_{ad} near the Curie temperature $T_C = 293$ K are about -9.8 Jkg^{-1}K^{-1} and 11.6 K, respectively for ΔH of 5 T [GSCH00b]. But its commercial usage is somehow limited because Gd is quite expensive (~\$4500 kg^{-1}).

In 1997, when Pecharsky and Gschneidner discovered the giant MCE in the $Gd_5Si_2Ge_2$ compound [PECH97a], the interest of MCE materials was reawakened. While undergoing a first-order phase transition near a magnetic phase transition, $Gd_5Si_2Ge_2$ exhibits large MCE which is about twice of that in Gd. More importantly, this alloy not only showed enhanced MCE but also opened the door to domestic applications such as home and automotive air conditioning [PECH05a]. Nonetheless, the T_C of $Gd_5Si_2Ge_2$ is about 276 K, which is much lower than that of Gd (293 K), making this alloy difficult for use in room-temperature applications [BRUC05a]. To overcome these difficulties, several other families of MCE materials have been (and are being) explored, especially materials without rare-earth elements, such as, Ni–Mn–Ga alloys [HUFS01a], Mn–As–Sb alloys [WADA01a], La–Fe–Co–S alloys [FUJI02a], Mn–Fe–P–As alloys [TEGU02a], La–Ca–Sr–Mn–O manganites [PHAN05a], Ni–Mn–Sn alloys [KREN05a], Ni–Mn–In [KREN07a] alloys, etc. According to theoretical analyses as well as the experimental results of existing magneto-caloric materials [PECH05a, BRUC05a, PHAN07a], the criteria for selecting materials for active MCE applications are following:

- Materials should exhibit large ΔS_M and ΔT_{ad} (i.e., large MCE).
- Materials should have large density of magnetic entropy but small lattice entropy.
- Thermal and magnetic hysteresis should be small (these are related to the reversibility and working efficiency of the MCE material).
- Materials with small specific heat and large thermal conductivity to ensure large temperature change and rapid heat exchange.
- Materials should also have high chemical stability, easily available with low cost and simple synthesis route.

1.3.2. Magneto-caloric parameters

Normally the strength of MCE is measured by the isothermal magnetic entropy change $(\Delta S_M)_T$ and adiabatic temperature change (ΔT_{ad}). In order to understand the relation between these two important MCE parameters, one can start with the general thermodynamic potentials (the internal energy U of the system, the enthalpy H, Helmholtz free energy F and Gibbs free energy G) which are related to the magnetic as well as thermodynamic variables as follows [SWAL62a, BAZA64a, VONO74a, TISH99b, TISH03a]:

$$U = U(S, V, M)$$
$$F = U - ST \tag{1.8}$$
$$\text{and } G = U - ST + PV - MH$$

where P, V, T, S, H and M are pressure, volume, absolute temperature, entropy, magnetic field and magnetization, respectively. Now, differential forms of U, F and G are

$$dU = TdS - PdV + HdM \tag{1.9}$$

$$dF = -SdT - PdV + HdM \tag{1.10}$$

$$dG = VdP - SdT - MdH \tag{1.11}$$

Using above equations, the variables *P, V, S, H* and *M* can be determined by the following equations of state:

$$P(T,H,V) = -\left(\frac{\partial F}{\partial V}\right)_{H,T} \tag{1.12}$$

$$V(T,H,P) = \left(\frac{\partial G}{\partial P}\right)_{H,T} \tag{1.13}$$

$$S(T,H,V) = -\left(\frac{\partial F}{\partial T}\right)_{H,V} \text{ or, } S(T,H,P) = -\left(\frac{\partial G}{\partial T}\right)_{H,P} \tag{1.14}$$

$$H(T,M,V) = \left(\frac{\partial F}{\partial M}\right)_{V,T} \tag{1.15}$$

$$M(T,H,P) = -\left(\frac{\partial G}{\partial H}\right)_{T,P} \tag{1.16}$$

From these equations of state, it is possible to derive the thermodynamic Maxwell relations

$$\left(\frac{\partial S}{\partial H}\right)_{T,P} = \left(\frac{\partial M}{\partial T}\right)_{H,P} \tag{1.17}$$

$$\left(\frac{\partial S}{\partial P}\right)_{T,H} = -\left(\frac{\partial V}{\partial T}\right)_{H,P} \tag{1.18}$$

$$\left(\frac{\partial S}{\partial M}\right)_{T,P} = -\left(\frac{\partial H}{\partial T}\right)_{M,P} \tag{1.19}$$

Considering *S* as a function of *T, P* and *H*, the total differential of *S* can be written as

$$dS = \left(\frac{\partial S}{\partial T}\right)_{H,P} dT + \left(\frac{\partial S}{\partial H}\right)_{T,P} dH + \left(\frac{\partial S}{\partial P}\right)_{T,H} dP \tag{1.20}$$

For an isothermal and isobaric process (for which $dT = 0$ and $dP = 0$),

$$dS = \left(\frac{\partial S}{\partial H}\right)_{T,P} dH \tag{1.21}$$

By integrating this equation, it is possible to obtain the finite isothermal entropy change for the change of magnetic field from H_i to H_f as

$$\Delta S_M(H,T) = S_M(H_i,T) - S_M(H_f,T) = \int_{H_i}^{H_f} \left(\frac{\partial S}{\partial H}\right)_T dH \tag{1.22}$$

Using the Maxwell relation, $\left(\frac{\partial S}{\partial H}\right)_T = \left(\frac{\partial M}{\partial T}\right)_H$

isothermal entropy change can also be expressed as

$$\Delta S_M = \int_{H_i}^{H_f} \left(\frac{\partial M}{\partial T}\right)_H dH \tag{1.23}$$

According to the second law of thermodynamics, the variation of *S* of a system is the infinitesimal transfer of heat (δ*Q*) to a closed system driving a reversible process, divided by the equilibrium temperature (*T*) of the system i.e.

$$dS = \left(\frac{\delta Q}{T}\right) \tag{1.24}$$

Again, at constant parameter, *x,* the heat capacity C_x of a system is defined as

$$C_x = \left(\frac{\delta Q}{dT}\right)_x \tag{1.25}$$

Since $\delta Q = TdS$, C_x can also be expressed as

$$C_x = T\left(\frac{\partial S}{\partial T}\right)_x \tag{1.26}$$

In terms of C_x, the total differential of S can be written as

$$TdS = C_{H,P}dT + T\left(\frac{\partial S}{\partial H}\right)_{T,P} dH + T\left(\frac{\partial S}{\partial P}\right)_{T,H} dP \tag{1.27}$$

For an adiabatic and isobaric process (i.e., $TdS = 0$ and $dP = 0$), the finite temperature change is obtained by the integration of the Maxwell relations as

$$\Delta T_{ad}(T,H) = -\int_{H_i}^{H_f} \frac{T}{C_H}\left(\frac{\partial M}{\partial T}\right)_H dH \tag{1.28}$$

Finally, it is possible to deduce that

$$\Delta T_{ad} \approx -\frac{T}{C_H}\Delta S_M \tag{1.29}$$

Usually, in common magnetic materials (ferromagnetic and paramagnetic), the magnetization in a constant magnetic field decreases with increasing temperature i.e. $(\partial M/\partial T)_H < 0$. In such a case, ΔT_{ad} is positive and the ΔS_M is negative for a positive magnetic field change ΔH and named as direct (or conventional) MCE, while the reversed condition is named as inverse MCE [TEGU02b, ZHAN04a, KREN05a, RANK09a]. Since ΔS_M is proportional to both $(\partial M/\partial T)_H$ and ΔH, the larger absolute value of $(\partial M/\partial T)_H$ and ΔH give the larger MCE.

1.3.3. Magneto-caloric effect in ferromagnetic shape memory alloys

FSMAs, which undergo a second-order magnetic as well as a first-order martensitic transition display excellent MCE properties. In the present section, the MCE of FSMAs around both the transitions is discussed.

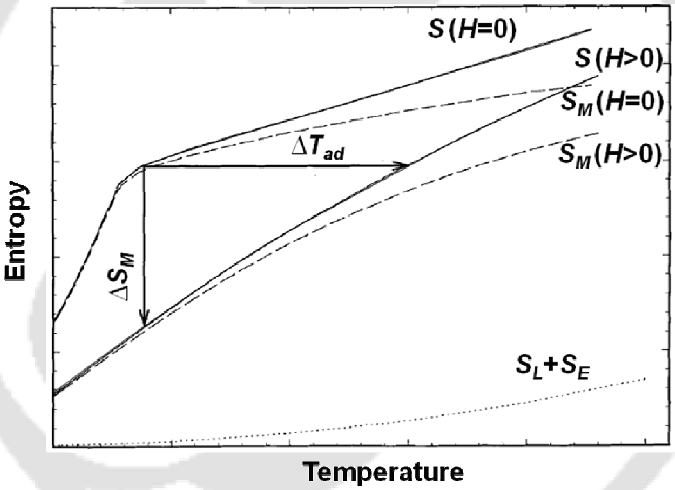

Figure 1.12: S-T diagram illustrating MCE near the T_C of a simple ferromagnetic material. The solid and dashed lines represent the total entropy and the magnetic entropy, respectively, in a magnetic field of $H = 0$ and $H > 0$. The dotted line represents the combined lattice and electronic (non magnetic) entropies [PECH99b].

In case of second-order magnetic phase transitions, M and S (the first derivative of the thermodynamic potential with respect to magnetic field and temperature, respectively) vary continuously, and there is no latent heat related to the transition. The

MCE in a simple ferromagnetic material near its T_C is shown in Figure 1.12. At constant pressure, the total S is a function of both T and H, and has three contributions, *viz*., magnetic (S_M), lattice (S_L) and electronic (S_E) [PECH99b]. With an increase in temperature of the material, all these contributions of S would increase. For isothermally applied magnetic field, entropy decreases and results in a magnetic entropy change ΔS_M. On the other hand, adiabatically removing the field causes adiabatic temperature change ΔT_{ad} (*cf*. Figure 1.12).

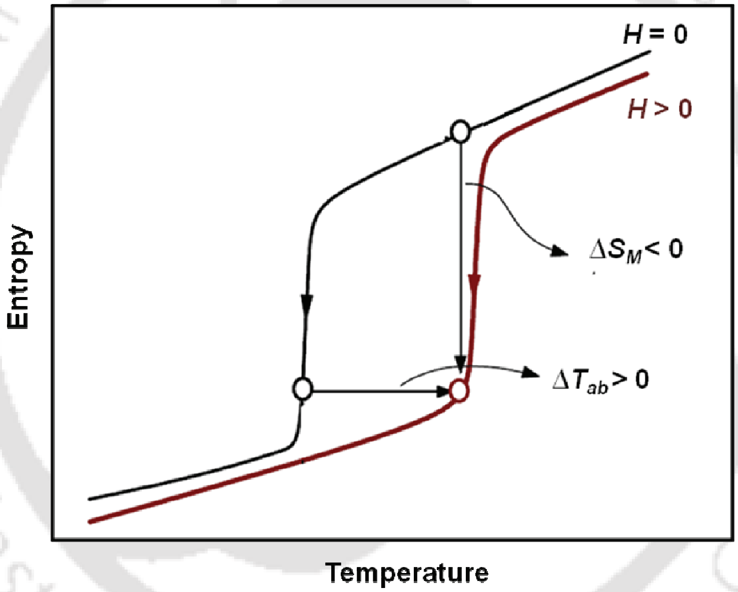

Figure 1.13: Temperature dependence of the total entropy in zero-field ($H = 0$) and in a magnetic field ($H > 0$) for MCE materials which exhibits the direct MCE around a first-order martensitic transition. [PECH06a]

At the first-order phase transition temperature, a jump in the entropy or magnetization means that the first derivative of the thermodynamic potential gives discontinuous functions because of the presence of latent heat [PECH01a, SPIC05a]. For a first-order transition, the S-T diagram under two different magnetic fields ($H = 0$ and $H > 0$) shown in Figure 1.13 from which the ΔS_M and the ΔT_{ad} can be graphically obtained from the vertical and horizontal distances between the two curves, respectively. Here, due to the application of magnetic field, the transition temperature shifts to higher values and gives rise to direct MCE (for which $\Delta S_M < 0$ and $\Delta T_{ad} > 0$). Among Ni-Mn-based FSMAs, the typical MCE material is the prototype FSMA Ni-Mn-Ga. Depending up on the composition of $Ni_{50}Mn_{50-x}Ga_x$ series of alloys, the second-order magnetic transition (of austenite phase) at $T_{A,C}$ varies between 315 and 380 K and the first-order martensitic transition at T_{Ms} varies between 175 and 220 K. A large value of direct MCE has been observed in the Ni-Mn-Ga when $T_{A,C}$ and T_{Ms} coincide [PARE03a].

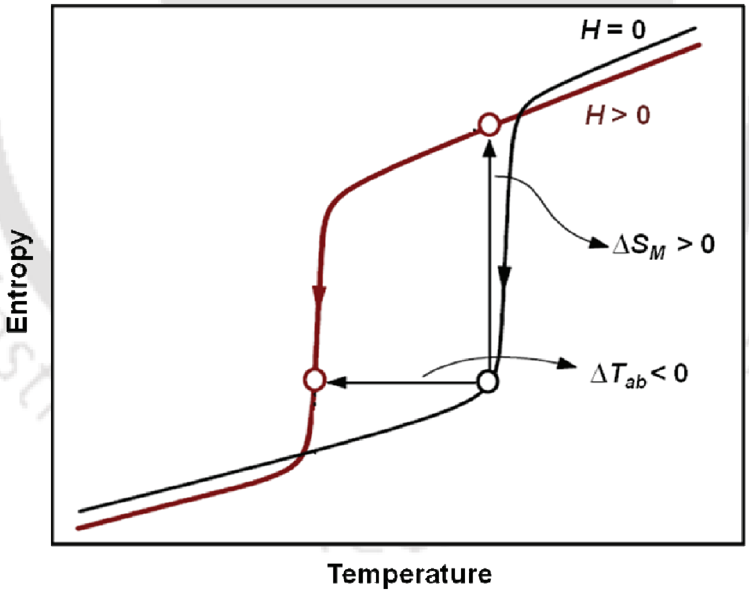

Figure 1.14: The temperature dependence of the total entropy in zero-field ($H = 0$) and in a magnetic field ($H > 0$) for MCE materials which exhibits the inverse MCE around a first-order martensitic transition [ROME13a].

Figure 1.14 schematically shows the *S*-*T* diagram for a MCE material under two different magnetic fields, $H = 0$ and $H > 0$. Here, application of magnetic field shifts the transition temperature to lower temperatures and gives rise to inverse MCE (i.e. $\Delta S_M > 0$ and $\Delta T_{ad} < 0$). Recently, other Ni-Mn based FSMAs such as Ni-Mn-Sn [KREN05a], Ni-Mn-In [HANZ06a, KREN07a, SHAR07b] and Ni-Mn-Sb [DUJZ07a, KHAN07a] have been found to exhibit large inverse MCE.

1.3.4. Magneto-caloric based magnetic refrigeration system

Nowadays, all of us rely too much on cooling technology for food safety, comfort, medical and industrial applications. As an example, 15 % of the total worldwide energy is consumed for refrigeration purposes [GSCH08a]. Until now, the most commonly used cooling devices are based on the gas-compression and expansion technology which use green-house gases such as chlorofluorocarbons (CFCs) and hydrochlorofluorocarbons (HCFCs) that are detrimental to our living environment. Recent development of new solid-sate cooling technology based upon MCE [WARB81a, TISH03a] has brought a green alternative to the conventional gas compression one [PECH05a, BRUC05a]. MCE based refrigeration has several advantages over the gas compression technology [PECH05a, PHAN07a] as listed below:

1. Magnetic refrigerator does not use greenhouse gases and is therefore an environment friendly cooling technology.
2. Magnetic refrigerator can reach higher cooling efficiency of up to 30–60% of a Carnot cycle, while the gas compression refrigeration has not crossed the 10% limit.

3. Magnetic refrigerators can be more compactly built even at a small scale, enabling the development of portable, battery-powered products.

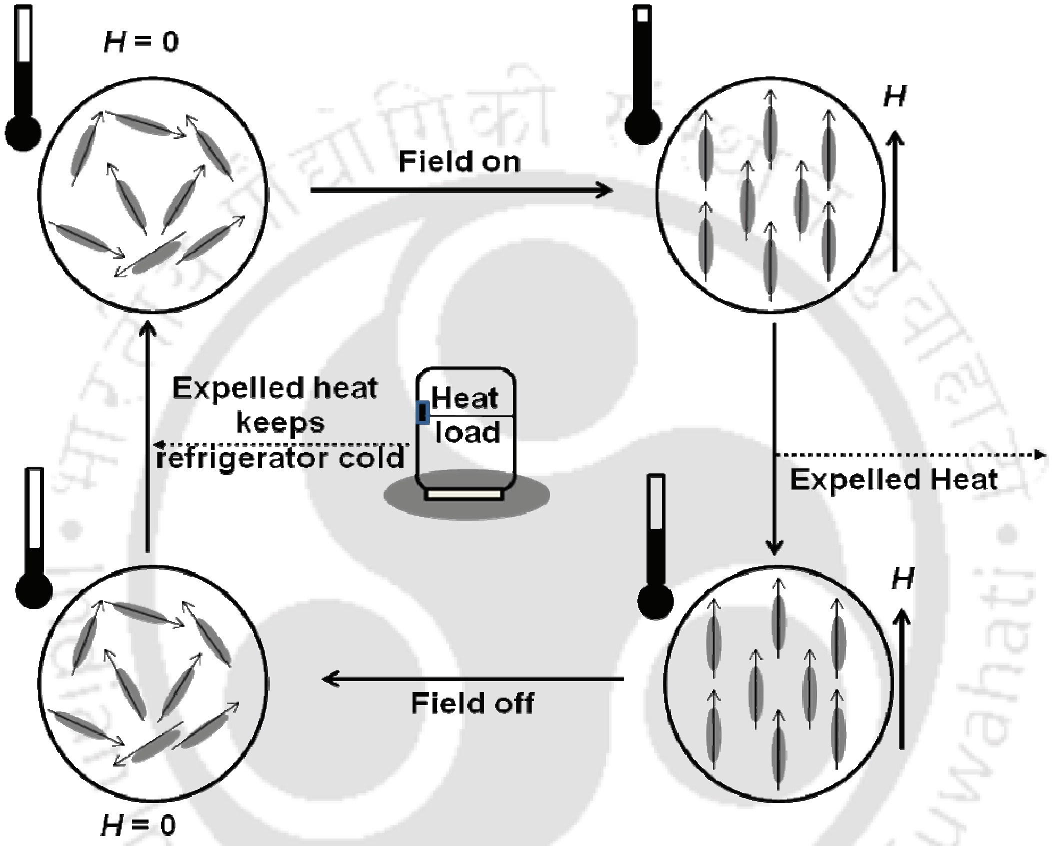

Figure 1.15: Schematic representation of a magneto-caloric material undergoing a magnetic refrigeration cycle [FRAN12a].

An example of refrigeration cycle for a MCE based refrigerator is shown in Figure 1.15. Initially, the material is in its ground state with randomly oriented spins. Due to the application of magnetic field, the spins are aligned resulting in heating of the material. This heat is removed from the magneto-caloric material to its surrounding by a heat-transfer medium. On removing the field, the spins are randomized. In doing so, the temperature of the material has been reduced to below the ambient temperature. At this condition, the material can accept heat from an external load. This would cool the external load and in processes would raise the temperature of the MCE material to ambient value. This is the working principle of a magnetic refrigerator cycle which is very similar to the adiabatic-isothermal vapor compression cycle used in conventional refrigeration technology.

The efficacy of a magneto-caloric material as a magnetic refrigerant is defined in terms of its refrigerant capacity (*RC*). It is a measure of the amount of heat that can be transferred between hot and cold reservoirs in an ideal refrigeration cycle. If there are two different magnetic refrigerants which differ only in their *RC* value, then the one with higher *RC* is expected to perform better because of its capability to transport larger amounts of heat in a real cycle [PECH01b]. *RC* can be estimated by integrating ΔS_M with respect to temperature over the full width at half maximum (FWHM) of $\Delta S_M (T)$ curve [PECH01b, SHAR07a, BING09a]. Mathematically, the procedure to obtaining *RC* is expressed as

$$RC = \int_{T_1}^{T_2} \Delta S_M (T, H)\, dT \tag{1.30}$$

The lower (T_1) and upper (T_2) limits of the FWHM represent the cold and hot temperatures, making them the analogues of the sink and source temperatures in the conventional refrigeration cycle.

For improving efficiency and affordability of MCE based refrigeration, current research endeavours aim at developing low cost magnetic materials exhibiting large MCE for low magnetic field change around room temperature.

1.4. EXCHANGE BIAS

Exchange bias (EB) is usually observed after field cooling in a material having interface between disparate magnetic phases such as ferromagnetic (FM) – antiferromagnetic (AFM) with T_C of the FM phase being higher than the Neel temperature, T_N of the AFM phase. When this type of a magnetic system is cooled down through its T_N, a unidirectional anisotropy is induced in the FM [MARC84a, MEIK57a, WOHL59a, BEAN60a, SCHM60a, LUBO62a, MEIK62a, JACO63a, KOUV63a, YELO71a]. EB is one of the phenomena associated with the exchange anisotropy created at the interface.

By considering an exchange interaction at the FM–AFM interface, unidirectional anisotropy and exchange bias can be qualitatively understood [MEIK62a, MEIK57a]. When the system is field cooled from an unmagnetized FM state to $T \geq T_N$, the FM spins are aligned by the field but the AFM spins remain as random orientation (Figure 1.16(a)). On further decreasing the temperature below T_N, the AFM spins next to the FM align ferromagnetically with those of the FM (due to the ferromagnetic interaction at the interface) and the other remaining spins in the AFM phase follow the AFM order so as to produce zero net magnetization (Figure 1.16(b)). If the field is now reversed at any temperature $T < T_N$, the FM spins start to rotate. On the other hand, if the AFM anisotropy is sufficiently strong, the AFM spins remain unchanged (Figure 1.16(c)) and this induces a microscopic torque on the rotated FM spins to keep them in their original position (Figure 1.16(c)). Thus, the FM spins get one single stable configuration, i.e. the anisotropy is unidirectional. To overcome the microscopic torque, an extra field is needed (Figure 1.16(d)). However, once the field is rotated back to its original direction, the FM spins will easily start to rotate since the torque and the field directions are the same (Figure 1.16(e)). Therefore, the material behaves as if there was an extra (internal) biasing field by which the FM hysteresis loop is shifted in the field axis, which is called the exchange bias [BEAN60a, MEIK57a, MEIK62a, JACO63a, YELO71a].

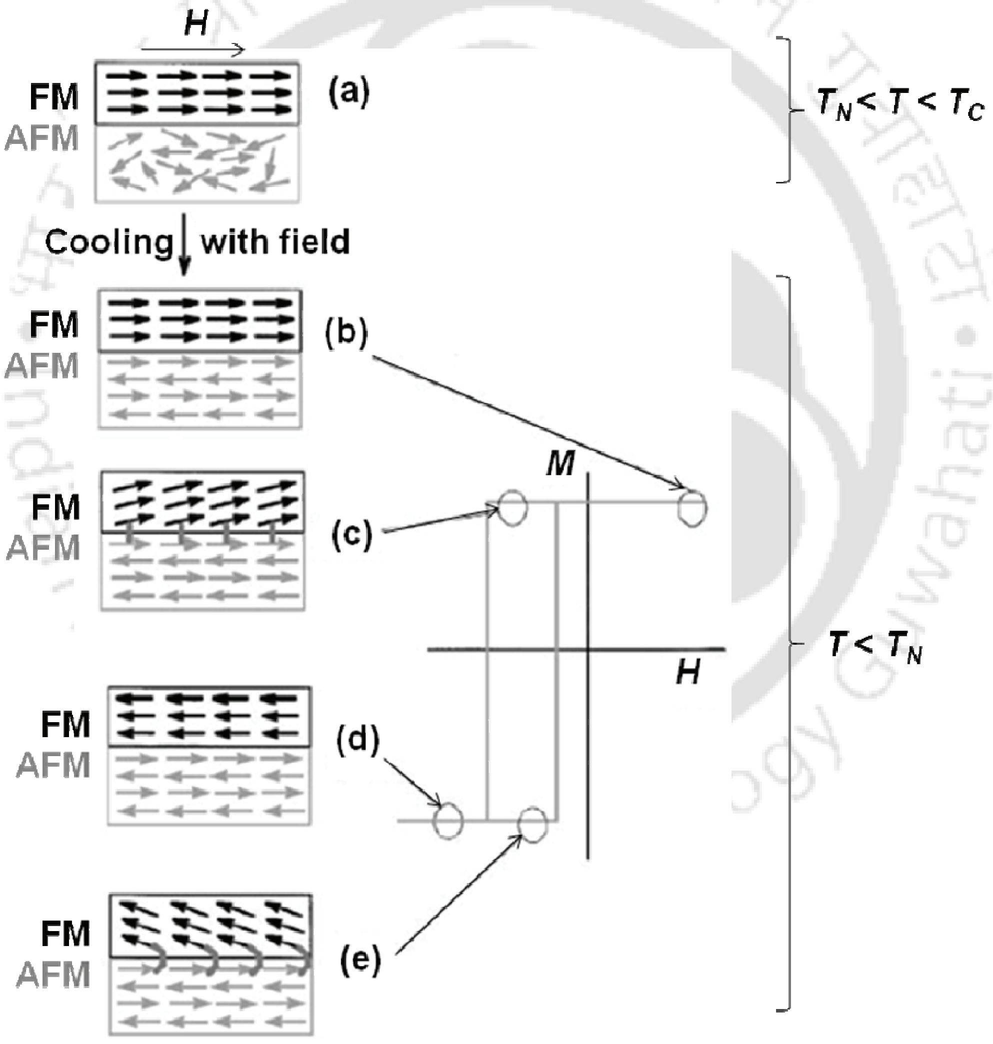

Figure 1.16: Illustration of the spin configurations at different stages of an exchange biased hysteresis loop [NOGU99a].

Although, these simple illustrations of spin configurations provide an intuitive picture, the roles of the many different parameters like anisotropy, roughness, and magnetic domain configurations have not yet been well understood.

1.4.1. Exchange bias materials

EB anisotropy was discovered in 1956 by Meiklejohn and Bean when Co/CoO core/shell nanoparticles were cooled in a static magnetic field [MEIK56a, MEIK57a]. Since then, EB effect has been observed in many different systems, such as Ni–NiO [SCHM60a, GEOG95a, YAOY95a, LOFF97a, LOFF97b, YAOY96a], Fe–FeO [MEIK58a], FeCo–FeCoO [DARN61a], Fe–Fe_3O_4 [LOFF97a, LOFF97b PAPA90a, HSUC94a], $Cu_{1-x}Mn_x$ [KOUV61a, IWAT70a], $Ag_{1-x}Mn_x$ [KOUV61a], $Ni_{1-x}Mn_x$ [KOUV59a, ABDU91a], $Au_{1-x}Fe_x$ [CAMP86a], $Fe_{1-x}Zr_x$ [MORI86a], thin film of some special compounds [KOOL96a, TANG84a, GLAV72a, HEIM94a, DAUG93a, GURN97a, LENS97a], etc. EB effect has also been reported in some FSMAs. $Cu_{44.7}Mn_{20.6}Al_{37.7}$ is the first off stoichiometric Heusler alloy in which the signature of EB anisotropy was reported [KOGA82a]. In 2007, Khan *et al.* reported the observation of EB effect in bulk polycrystalline $Ni_{50}Mn_{25+x}Sb_{25-x}$ FSMAs [KHAN07c]. While cooling the alloys in the presence of 50 kOe magnetic field to low temperatures, horizontal shifts in the hysteresis loops up to ~248 Oe were observed due to the coexistence of AFM and FM exchange interactions in the system. With increasing Mn concentration ranging x from 12 to 13.5 at.%, the EB field increased from 174 to 248 Oe.

EB effects have also been reported in Ni-Mn-Sn and Ni-Mn-In alloys [PATH09a, LIZJ07a, KHAN07d]. In $Ni_{50}Mn_{35}In_{15-y}Si_y$ alloys ($0 < y < 4$), the EB field increased with Si substitution and maximum EB field of ~ 170 Oe was observed for the alloy with y = 4 at 5 K when field cooled with 50 kOe field [PATH09b]. Until now, very few reports are available in the literature which focus on the EB effect in Ni-Mn based Heusler alloys.

1.4.2. Applications of exchange bias

Materials exhibiting EB effects have been proposed and utilized in several applications since their discovery [LUBO62a, KOOL96a, TANG84a, GLAV72a, HEIM94a, DAUG93a, GURN97a, LENS97a]. Until now, EB effects have been exploited in technological applications such as read head of magnetic recording media [TSAN97a, TONG99a, TSAN99a, GANG00a, LINT00a, LIUF00a, SONG00a, DOER01a, MACK01a, ARAK02a, MATS02a, TANA02a, ZHAN02a, ZHAN02b] and magneto-resistive random access memories (MRAM) [LIUY03, ZHEN03a, ZHEN04a]. It has also been proposed for stabilizing magnetization of superparamagnetic nanoparticles [WELL99a, THOM00a, SKUM03a, NOGU06a] and for improving coercivity and energy product of permanent magnets [SORT99a, SORT00a, SORT01a, SORT02a]. The enhanced coercivity of oxidized small particles provides the first potential technological application of EB [LUBO62a, GANG92a, PAPA90a]. However, the most popular systems for EB based industrial applications are thin film [KOOL96a, TANG84a, GLAV72a, HEIM94a, GURN97a, LENS97a]. The first proposed application of bilayers was as magnetic recording media. Recently, EB effect in thin film has caught the alteration of researches as part of a new class of spin-valve devices based on giant magneto-resistance (GMR) [KOOL96a, DIEN91a, HEIM94a, DAUG93a, GURN97a, LENS97a, DIEN94a]. In this type of device, two FM layers are separated by a non-magnetic layer with the moment of one of the FM layers being pinned by an AFM layer [DIEN91a, DIEN94a]. The pinned FM layer has a shifted loop. However, the other FM layer remains free and gives a conventional hysteresis loop [DIEN91a, DIEN94a]. Hence, if the magnetizations in the layers are parallel, the resistance is low. On the other hand, antiparallel magnetizations of the two FM layers result in high resistance [DIEN91a, DIEN94a].

The EB effect is usually observed in inhomogeneous materials and thin films. It is very rare in bulk systems. Therefore, both from scientific and technological application points of view, bulk materials exhibiting EB properties are of immerse interest.

1.5. MOTIVATION AND SCOPE OF THE PRESENT WORK

The above review shows the current interest and technological potential of FSMAs. It is also clear that Ni-Mn-X (X = Ga, Sn, In) FSMAs which exhibit rich physical phenomena have not yet been fully understood. Due to the martensitic transition, these materials display interesting multifunctional properties such as MFIS, magnetic super-elasticity, MCE, etc. These multifunctional properties result from the strong coupling between magnetic and structural properties in these materials. Actually, the possibility of achieving large MCE in Ni-Mn-X (X = Ga, Sn, In) FSMAs when the martensitic structural and magnetic phase transitions occur at close temperature intervals is a subject of both basic and applied interest [KHOV03b, ZHOU05a]. Since addition of non-magnetic as well as magnetic elements are known to influence the T_M and T_C of ternary FSMAs, selective elemental additives can improve the multifunctional properties of these alloys. In the present work, it would be shown that the main features of this magnetic and structural coupling are reflected in the unusual magneto-caloric properties displayed by these systems. Alloys with large ΔS_M (or ΔT_{ad}) have a huge potential in magnetic refrigeration. With regards to this potential use of Ni-Mn-X (X = Ga, Sn, In) FSMAs in technological applications, the magnitude of the ΔS_M (or ΔT_{ad}) found for a number of these materials is competitive when compared to other materials which are being investigated for room temperature refrigeration [BRUC08a].

Associated with the martensitic transition, these materials display interesting super-elasticity which is related to the possibility of realizing magnetic field induced large recoverable deformations in these materials. Therefore, these materials have the potential for magnetic field driven sensor and actuator applications with extremely fast response.

Taking a consolidated view of all these points, this thesis work focuses on understanding the influence of processing conditions, nature of the structural and magnetic phases, and additive elements on the MCE in Ni-Mn-X (X = Ga, Sn, In) FSMAs.

Chapter 2

EXPERIMENTAL TECHNIQUES AND PROCEDURES

In the course of the present investigations, several experimental techniques were used for the preparation and characterization of the samples. This chapter gives a brief description of these experimental techniques.

2.1. PREPARATION AND PROCESSING OF SAMPLES

Alloy samples have been prepared by three different routes, *viz*., arc melting of constituent elements, melt spinning of alloy ingot and ball milling of crushed pieces of alloy ingot. So, the final products were in the form of ingots, ribbons and powders. Subsequently, the as-prepared samples were annealed at different temperatures under high vacuum. The flow chart (Figure 2.1) schematically explains the procedures adopted. A brief description of the different techniques adopted in this work is given below:

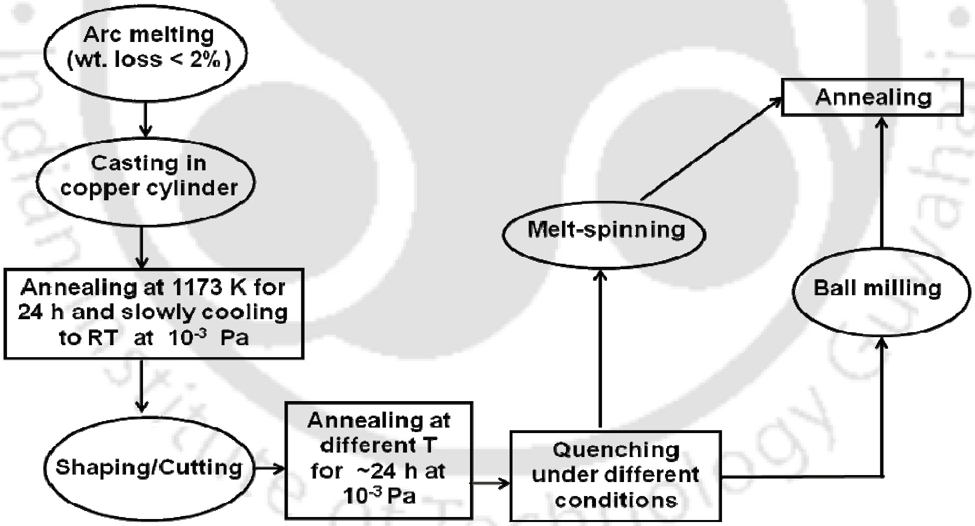

Figure 2.1: Flow chart describing the processing routes involved in the preparation of FSMAs in different forms.

2.1.1. Arc melting

In the present work, the alloy ingots were first prepared by arc melting the constituent elements. A commercial arc melting furnace (Make: Vacuum Techniques, India) was used for preparing the alloy ingots. Schematic diagram of an arc melting furnace is presented in Figure 2.2 [a high current (200 A) dc power supply used as electrical source is not shown here].

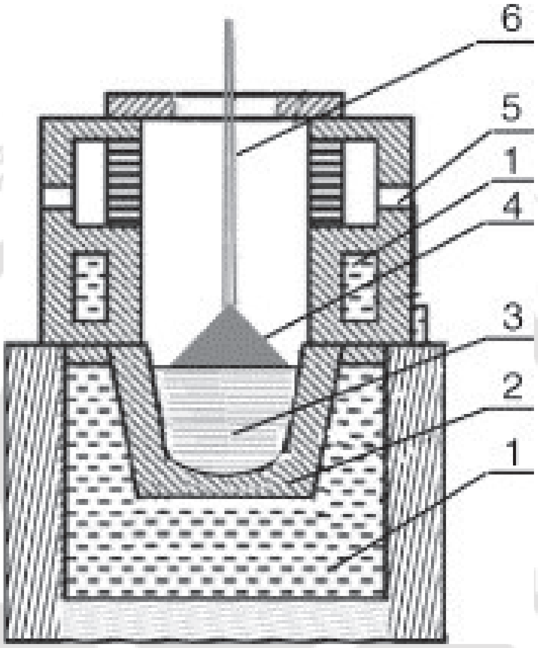

Figure 2.2: Schematic diagram of water-cooled copper-hearth electric arc melting furnace. Labels denote: (1) circulating water to cool the hearth, (2) copper hearth (cathode); (3) compacted metal blend, (4) electric arc struck between the electrodes (5) gas inlet valve (6) water cooled flexible electrode with tungsten tip (anode) [QINQ06a].

High purity (≥ 99.99%) elemental pieces as per the requirement of the target composition were weighed in a calibrated electronic balance of 0.01 mg resolution. Total charge weighing about 5 g was placed in the water-cooled copper hearth of the arc furnace and the chamber was pumped down to ~ 10^{-5} Torr (mm Hg). The chamber was then purged with high purity argon gas to remove traces of oxidizing atmospheric gases and finally filled with argon gas. DC arc was then struck between a high purity tungsten anode and the copper hearth cathode and the elemental pieces were melted in the heat generated by the arc carefully so as to ensure minimal loss of material due to the volatility. The cast ingot was then flipped around and re-melted several times to ensure complete melting and mixing of the constituent elements to yield a homogeneous alloy ingot. The ingot obtained after melting was molded (re-melted) in a dismountable copper cylinder kept on the water cooled hearth in order to obtain a 10 mm diameter cylindrical sample. As-cast ingots with weight loss > 2% were not consider for further processing. Since vitalization of low melting point elements such as Mn cannot be prevented, excess (up to 2 at.%) amount of such violate elements were added to achieve the desired net composition in the alloy ingot.

2.1.2. Melt spinning

Ribbon samples were prepared by melt spinning technique. Figure 2.3 shows the schematic diagram of a melt spinning apparatus. The arc melted alloy ingot is placed in a fused silica tube, which is situated inside a water-cooled RF-coil of an induction heater. When the induction coil is energized, the ingot kept inside the fused silica tube is melted. The molten alloy is ejected through the orifice at the bottom of the tube by pressurized argon gas on to a water-cooled copper wheel rotating at constant linear speed. The molten jet strikes the surface of the wheel and is immediately solidified in the form of a flat ribbon. The solidification (quenching) rate of the molten alloy can vary between 10^4 to ~10^7 K/sec depending on the processing conditions [HARG81a, CAHN83a, LUBO83a, ANAN84a, TKAT02a]. This results in the formation of long continuous ribbon samples with 1 – 5 mm width and 10 – 120 μm thickness. The several process parameters available, temperature of the molten alloy, orifice diameter, argon gas pressure, distance between the orifice and the wheel, angle of ejection of the melt and the linear wheel speed of the wheel are usually controlled to obtain ribbons with appropriate (amorphous or crystalline) structure, texture, grain size and thickness [NARA79a, LIEB81a, TKAT02a].

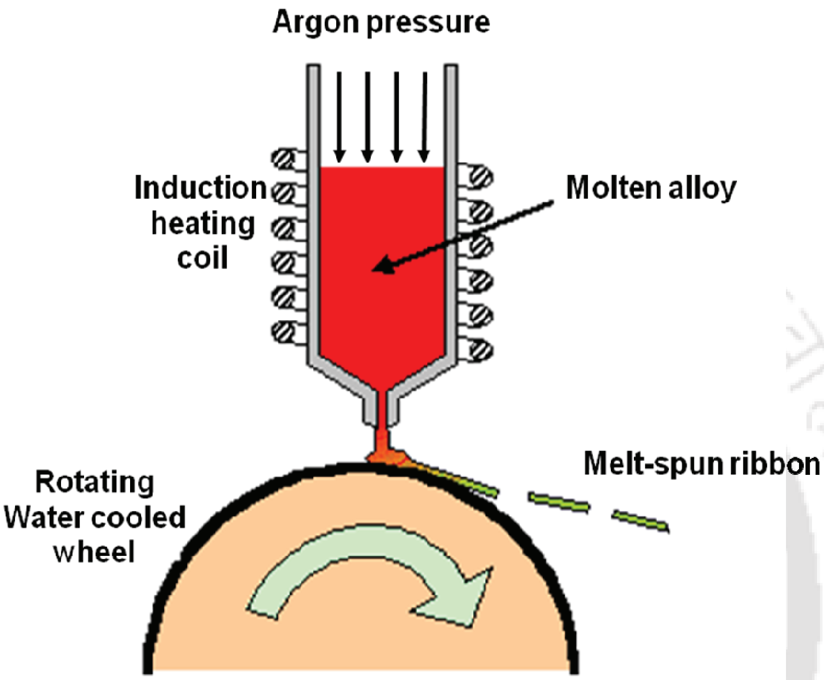

Figure 2.3: Schematic diagram of melt-spinning apparatus [MAGN13a].

2.1.3. Ball milling

Powder samples were prepared by mechanical milling in a planetary ball mill. In this process, the arc melted alloy ingot was crushed into small pieces of size < 3 mm and mechanically milled for several hours in a planetary ball mill (Make: Insmart Systems, India). A planetary ball mill comprises of a horizontal support disc on which vials are mounted. The vial rotates in a direction opposite to that of the disc, thereby, simulating a planetary motion. A photograph of the four-vial planetary mill used in the present studies is given in Figure 2.4.

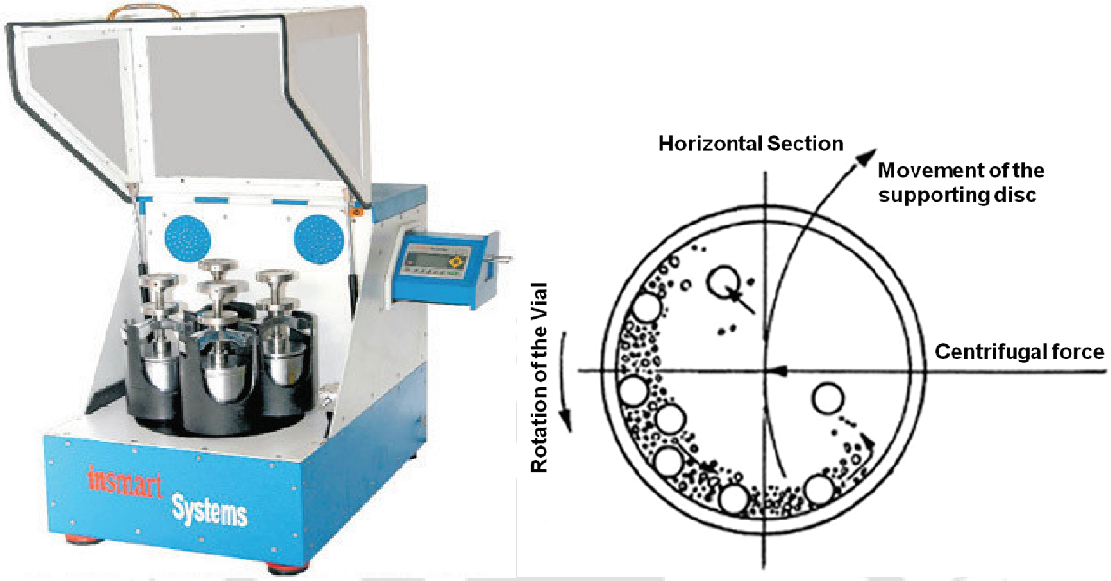

Figure 2.4: Photograph of the four-vial planetary mill used in the work and a schematic diagram of the horizontal section of a vial depicting the movement of the balls inside the vial due to its planet-like movement [ZHAN08a].

The planetary motion results in large centrifugal force acting on the balls kept inside the vial. This causes the balls to collide with themselves and with the wall of the vial with high impact. When an elemental powder mixture is placed in the vial along with the balls, the powders are subjected to repeated cold welding and fracture at the surfaces of the balls and the vial. This process initially results in particle size refinement. The size and shape of particles are controlled by the milling parameters such as powder to ball weight ratio, ball size (diameter), rotation speed, milling time, *etc*. [SURY01a, RAME12a]. If the milling is continued for longer periods, atomic mixing of the finely powdered elements would occur and result in alloy formation. Then, this process is referred to as mechanical alloying [SURY01a, FARA11a]. Nature of the milling vial and balls, powder-to-ball weight ratio, and rotation speed of the vial influence the alloying process along with the milling media

[SURY01a, RAME12a]. In the present investigations, particle size refinement of the alloy ingot pieces was the goal and hence milling time was limited to 7 h. Steel vials and steel ball were used and powder to ball ratio of 1:10 was maintained. The mill was programmed to halt for 10 minutes after every 15 minutes of operation to minimize heat generation in the vial. In spite of this care, accumulation of strain due to the mechanical grinding process cannot be entirely avoided. Annealing treatment had to be given to relieve the accumulated strains in the samples.

2.1.4. Processing of samples

As-prepared samples were processed under different conditions depending upon requirements. The different processing procedures adopted are briefly described below:

The as-cast ingots had to be homogenized and then annealed at appropriate temperature in order to obtain samples with consistent and reproducible properties. The metallic samples cannot be heat treated in air since they would oxidize. So, the as-prepared samples were taken separately in fused silica ampoules, which were pumped down to 10^{-5} Torr using an oil diffusion with rotary pump combination (Make: Vacuum Techniques, India) and then flame-sealed. The vacuum-sealed ampoules containing the samples were placed inside a raising hearth furnace (Make: OKAY, India, Model: 70T-4) and homogenized at ~ 1200 K. The well homogenized ingot was annealed at ~ 1200 K followed by quenching. Air and ice water were used as quenching media for preparing samples under different conditions.

Arc melted cylindrical ingots were cut into small pieces using a diamond saw (Make: Buehler, Model: Isomet 2000) and cleaned with acetone in an ultrasonic bath. For XRD measurement, a part of the annealed ingot was first crushed into fine powder and then heat treated again followed by quenching, so as to relieve stress accumulated while grinding the sample.

2.2. STRUCTURAL CHARACTERIZATION AND COMPOSITION ANALYSIS

2.2.1. Powder X-ray diffractometer

Two different powder X-ray diffractometers *viz*. Seifert XRD 3003 T/T (shown in Figure 2.5a) and Rigaku TTRAX III 18 kW were used in the thesis work, depending upon their availability. The X-ray diffraction (XRD) technique allows identification of various crystalline phases present in the alloys, degree of crystalline order, quantitative analysis of secondary phase present in a two-phase system, and provides other structural information such as the average size of the crystallites, residual strains present inside the crystallites, *etc*. A theta-theta (θ-θ) goniometer depicted in Figure 2.5b was used in the reflection (Bragg-Brentano) geometry [CULL01a] for collecting data.

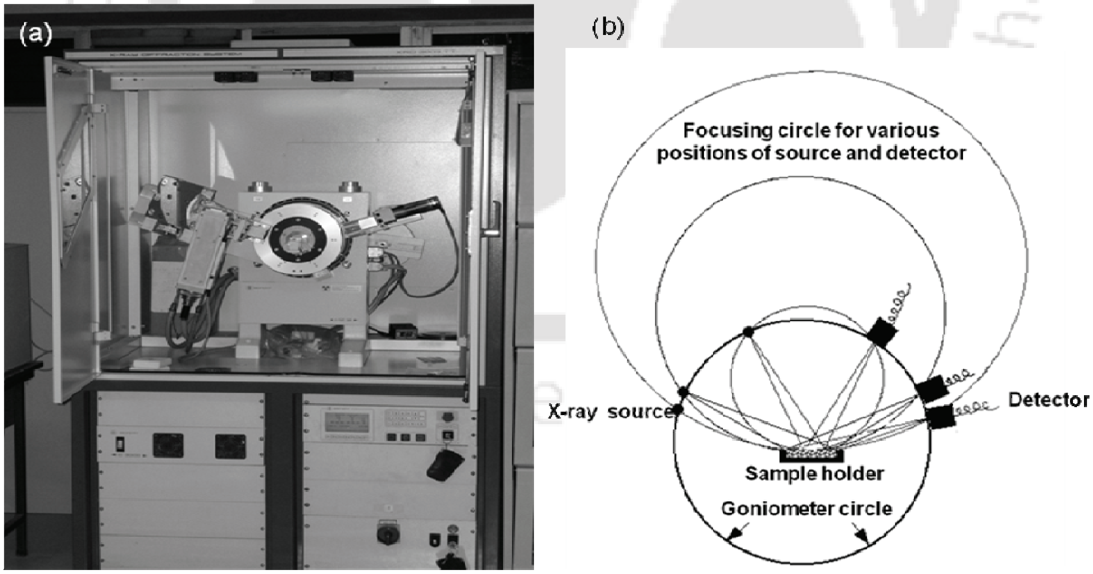

Figure 2.5: (a) Photograph of Seifert XRD 3003 T/T powder X-ray diffractometer, and (b) Bragg-Brentano diffraction geometry of a powder XRD.

A polymetamethylacrylate (PMMA) plate with a square depression of dimensions 25 mm × 25 mm × 0.5 mm coated with a thin layer of high vacuum grease was used as sample holder for XRD measurements. The sample in fine powder form was evenly spread over the square depression on the PMMA sample holder. The holder was mounted on the goniometer for recording the XRD patterns. A crystal has a periodic arrangement of atoms. Diffraction of X-rays occurs through constructive interference of X-rays scattered from atoms of a set of parallel planes in crystal lattice at a particular angular positions of the incident wave known as Bragg angles [CULL01a]. A schematic description of the diffraction phenomenon from a set of crystal planes is depicted in Figure 2.6.

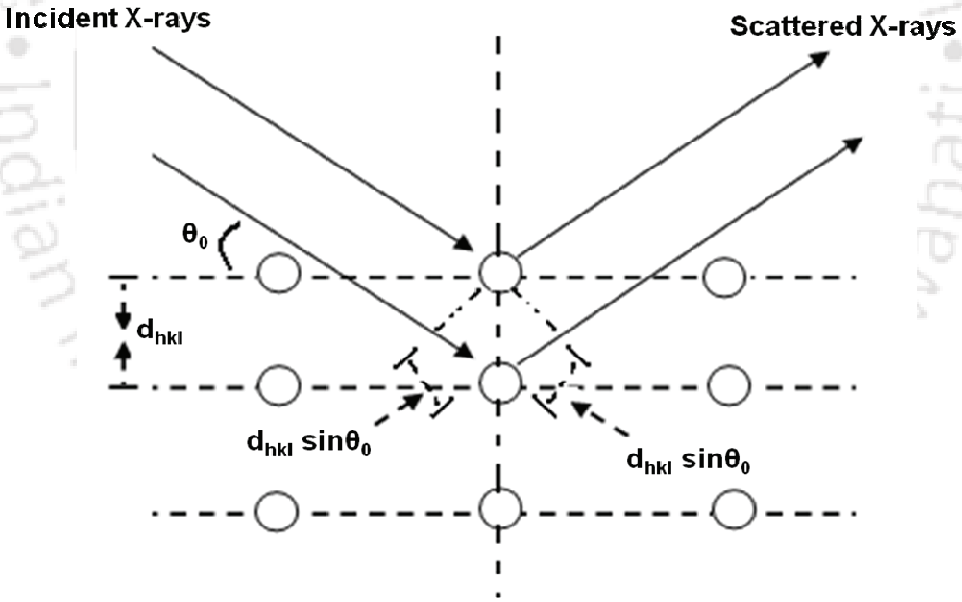

Figure 2.6: Schematic ray diagram of X-rays diffraction by a crystal.

The condition for obtaining constructive interference from a set of parallel plane is specified by the Bragg's law [CULL01a],

$$2d_{hkl} \sin\theta_0 = n\lambda \tag{2.1}$$

where d_{hkl} is the inter planer spacing of a set of planes with Miller indices ($h\ k\ l$), θ_o is the glancing angle, λ is the wavelength of the X-ray and n is the order of diffraction. A specific series of these angles at which constructive reflections are observed in a 2θ scan can be used to determine the Miller indices of crystal planes causing these reflections and the crystal structure can be identified from the systematic behaviour of these indices [CULL01a]. A standard polycrystalline silicon (Si) sample, was used for the calibration of the instrument. A typical (observed) XRD pattern of standard polycrystalline Si sample is shown in Figure 2.7.

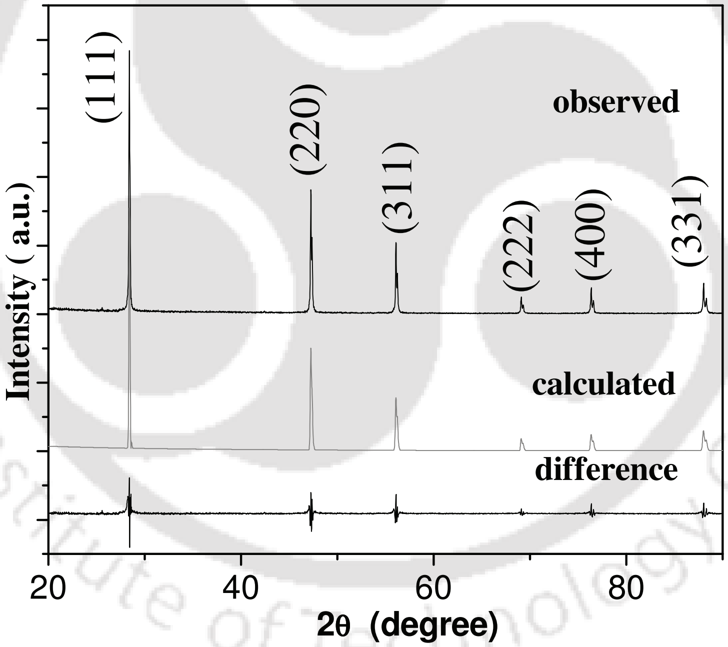

Figure 2.7: XRD pattern of Si sample (observed). Calculated and difference data correspond to least squares fitting performed on the observed data.

The Rietveld refinement technique has been employed to refine the crystal structures and extract crystallographic parameters from recorded powder XRD patterns. A public-domain software, Fullprof, was used for Rietveld analysis [RIET67a, RIET69a, LOUE98a] of

XRD patterns of the synthesized alloys. Two versions of source codes of Fullprof are available for users. The first corresponds to a program written in FORTRAN 77 which can be used in multiple platforms. The second version developed from the previous one, is coded in FORTRAN 95. Input files for this program should bear the extensions '*.pcr' and '*. dat'. The *.pcr file contains the title, type of analysis (X-ray, neutron or profile fitting), profile function used for fitting, number of phase present, wave length of the beam used for the collection of data along with the step size and 2θ range, number of iteration cycles, number of refined parameter and other crystallographic data. The *.dat file contains the intensity [counts per second (cps)] data which are recorded by the scintillation detector as a function of 2θ. Optional input files such as '*.bac' and '*.irf' can be used for specifying the background at each step of the scattering variable, and incorporating the instrumental resolution function, respectively. The two main output files are '*.out' and '*.sum' that contain all control variables and refined parameters. Another important output file is '*.prf' which contains observed and calculated profiles that are automatically used by a graphical interface program called *WinPLOTR*. This program generates three plots, viz., the calculated pattern from the input file *.pcr, the observed pattern from *.dat and their differences to graphically show the goodness of the fit. The control of the refined parameter is achieved by using a flag in the form of a code word. The sequences for refinement involves setting / optimizing the following parameters: (1) scale factor, (2) zero point of detector, first two background parameters and lattice constant(s), (3) overall Debye-Waller factor, (4) peak shape and asymmetry parameters, (5) atom occupancies, (6) individual isotropic thermal parameters, and (7) additional background parameters.

The quality of refinements are known based on the values of reliability factors such as R_p, R_{wp}, R_{exp}, R_{Bragg}, χ^2 and R_F that are defined as follows [ANIN01a]:

Profile factor, $$R_p = 100\frac{\sum_{i=1,n}\left|y_i - y_{c,i}\right|}{\sum_{i=1,n} y_i} \qquad (2.2)$$

Here, 'y_i' is the observed point (experimental), '$y_{c,i}$' is the calculated point and n represents the number of data points.

Weighted profile factor, $$R_{wp} = 100\left(\frac{\sum_{i=1,n}\omega_i\left|y_i - y_{c,i}\right|^2}{\sum_{i=1,n}\omega_i y_i^2}\right)^{1/2} \qquad (2.3)$$

Here, $\omega_i = \frac{1}{\sigma_i^2}$; σ_i^2 is the variance of the observation y_i.

Expected weight factor, $$R_{\exp} = 100\left(\frac{n-p}{\sum_i \omega_i y_i^2}\right)^{1/2} \qquad (2.4)$$

Here (n - p) is the number of degrees of freedom and 'p' is the number of refine parameters.

Reduced chi-square, $$\chi^2 = \left(\frac{R_{wp}}{R_{\exp}}\right)^2 \qquad (2.5)$$

Bragg factor, $$R_B = 100\left(\frac{\sum_h\left|I_{obs,h} - I_{cal,h}\right|}{\sum_h\left|I_{obs,h}\right|}\right)^{1/2} \qquad (2.6)$$

Here, 'h' levels the Bragg's reflections. $I_{obs,h}$ are the observed integrated intensities and $I_{cal,h}$ are the calculated intensities.

The crystallographic R_F factor, $$R_F = 100\left(\frac{\sum_h\left|F_{obs,h} - F_{cal,h}\right|}{\sum_h\left|F_{obs,h}\right|}\right) \qquad (2.7)$$

Here, $F_{obs,h}$ and $F_{cal,h}$ are the observed and calculated structural factors, respectively. The refinement procedure involves careful preparation of the input files and re-iteratively performing the refinement until a good graphical fit (difference plot with minimal undulation) along with least values of χ^2, R_B and R_F are obtained for the measured XRD pattern.

The values of χ^2, R_B and R_F obtained for standard Si sample using the above procedure are 1.86, 10.2 and 6.2, respectively. The percentage of residual strain can also be estimated using the refinable parameter U using the relation [FAJA10a],

$$Strain\ (\%) = \left(\frac{\pi}{1.8}\right)\sqrt{U - U_{ins}} \tag{2.8}$$

where U_{ins} is the instrumental parameter.

2.2.2. Scanning electron microscope

Scanning Electron Microscope (SEM, Leo 1430VP) with Energy Dispersive Spectroscopy (EDS) attachment (Oxford) has been used to study the surface morphology of the alloys and to determine the chemical composition of the alloys. SEM is a powerful microscope that uses electrons rather than light to form an image of objects such as fractured metal components, foreign particles, residues, polymers, electronic components, biological samples, and countless others. The shorter wavelength of electrons permits image magnifications of up to 100,000× as compared to about 2,000× for conventional light microscopy. A SEM also provides a greater depth of field than a light microscope, allowing complex, three-dimensional objects to remain sharp and in focus. This capability reveals details that cannot be resolved by light microscopy [SCAN12a].

A schematic representation and a photographic view of a SEM are shown in Figure 2.8a and 2.8b, respectively. Thermionically emitted electrons from a tungsten filament are accelerated towards an anode in a potential difference typically of the order of 10-20 keV and focused by condenser lenses on a spot volume of the specimen, resulting in the transfer of energy to the spot. These bombarding electrons, also referred to as primary electrons, dislodge electrons from the specimen itself. The dislodged electrons, also known as secondary electrons, are attracted and collected by a positively biased grid or detector, and then translated into a signal. To produce the SEM image, the electron beam is swept across the area being inspected, producing many such signals. These signals are then amplified, analyzed, and translated into images of the topography being inspected. Finally, the image is displayed on a screen.

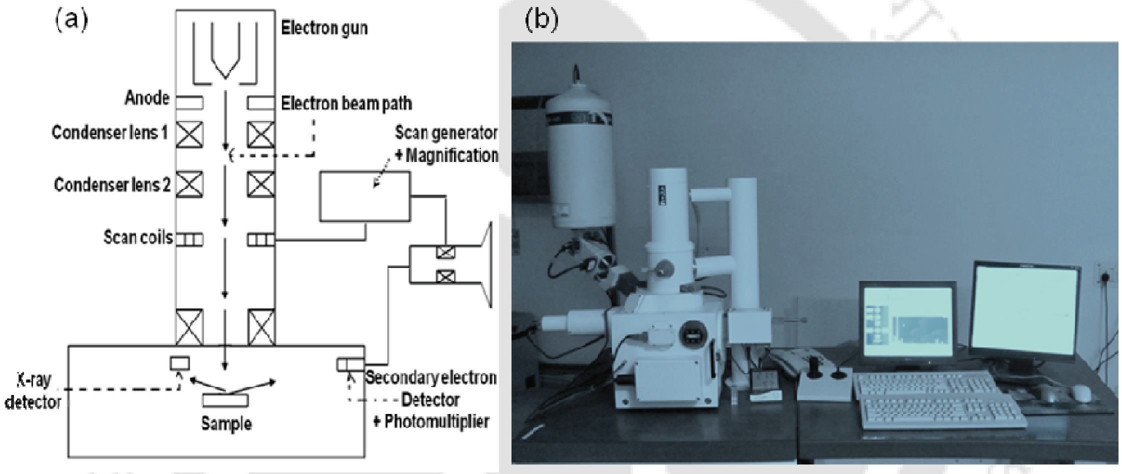

Figure 2.8: (a) Schematic view and (b) photograph of Leo 1430VP SEM equipped with EDS.

The energy of the primary electrons determines the quantity of secondary electrons collected during inspection. The emission of secondary electrons from the specimen increases as the energy of the primary electron beam increases, until a certain limit is reached. Beyond this limit, the collected secondary electrons diminish as the energy of the primary beam is increased, because the primary beam is already activating electrons deep below the surface of the specimen. Electrons coming from such depths usually recombine before reaching the surface for emission.

The most common imaging mode relies on detection of the lowest portion of the emitted energy distribution. Their very low energy means they originate from a subsurface depth of no larger than several angstroms. The signal is captured by a detector consisting of a scintillator-photomultiplier combination, and the output serves to modulate the intensity of cathode ray tube, which is rastered in synchronization with the raster-scanned primary beam. Resolutions as high as ~ 5 nm are possible with this microscope.

Apart from secondary electrons, the primary electron beam results in the emission of backscattered (or reflected) electrons from the specimen. Backscattered electrons possess more energy than secondary electrons and have a definite direction. As such, they cannot be collected by a secondary electron detector, unless the detector is directly in their path of travel. All emissions above 50 eV are considered to be backscattered electrons.

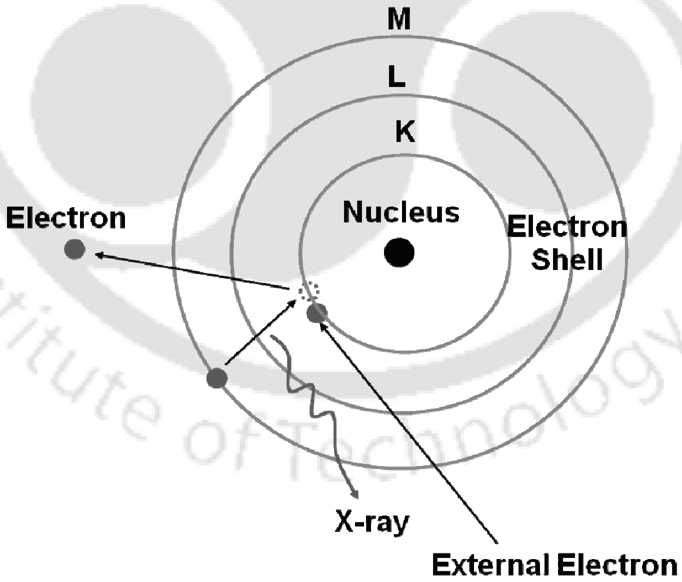

Figure 2.9: Principle of X-ray emission from an atom when a higher-energy electron from an outer shell fills the vacancy created due to excitation of an inner level electron by a high energy electron beam [LENG08a].

Backscattered electron imaging is useful in distinguishing one material from another, since the yield of the collected backscattered electrons increases monotonically with the specimen's atomic number Z ($\propto 0.05Z^{1/2}$). Backscatter imaging can distinguish elements with atomic number differences of at least 3, *i.e*. materials with atomic number differences of at least 3 would appear with good contrast on the image.

A SEM may be equipped with an EDS (*aka* EDX or EDAX) system to enable it to perform compositional analysis on specimen. EDS analysis is useful in identifying materials and contaminants, as well as estimating their relative concentrations on the surface of the specimen. During EDS analysis, the specimen is bombarded with an electron beam inside the SEM. The bombarding electrons collide with the electrons in the atoms of the specimen, knocking some of them off in the process. A position vacated by an ejected inner shell electron is eventually occupied by a higher-energy electron from an outer shell. To enable this, the transferring outer electron must give up some of its energy by emitting X-rays. This process is schematically shown in Figure 2.9. The amount of energy released by the transferring electron depends on which shell it is transferring from, as well as which shell it is transferring to. Furthermore, the atom of every element releases X-rays with unique amounts of energy during the transferring process. Thus, by measuring the amounts of energy present in the X-rays being released by a specimen during electron beam bombardment, the identity of the atom from which the X-ray was emitted can be established.

The output of an EDS measurement is an EDS spectrum (*cf*. Figure 2.10), which is just a plot of how frequently an X-ray is received for each energy level. An EDS spectrum normally displays peaks corresponding to the energy levels for which X-rays were received. Each of these peaks is unique to an atom, and therefore corresponds to a single element. The higher a peak in a spectrum, the more concentrated the element is in the specimen. Inset in Figure 2.10 shows the analyzed composition of the alloy.

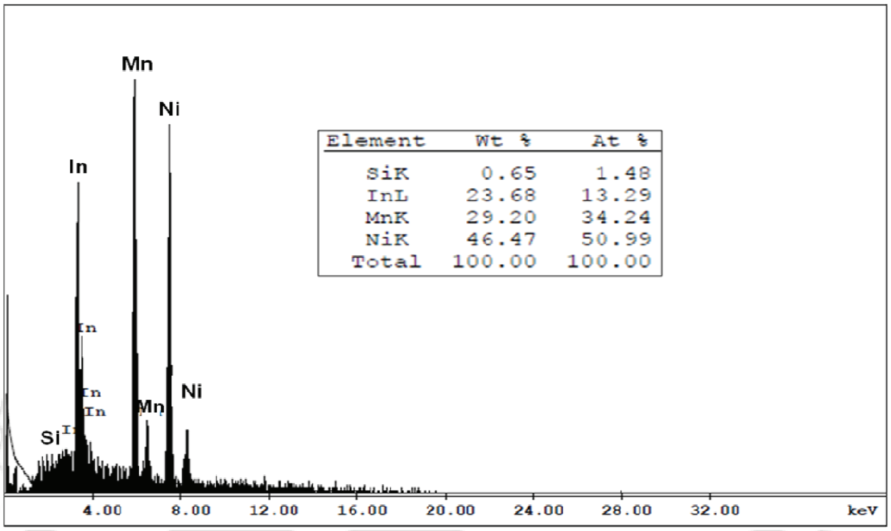

Element	Wt %	At %
SiK	0.65	1.48
InL	23.68	13.29
MnK	29.20	34.24
NiK	46.47	50.99
Total	100.00	100.00

Figure 2.10: A typical EDS spectrum of Ni-Mn-In-Si alloy. Inset shows the results of EDS analysis.

In the present work, the alloy specimen was placed on carbon coated tape and then gold coated to yield an electrically conducting surface for SEM observation.

2.3. MAGNETIC PROPERTY CHARACTERIZATION

2.3.1. Vibrating sample magnetometer

Vibrating Sample Magnetometer (VSM, Lakeshore Model 7410) has been used for performing magnetic measurements on the alloy samples. VSM [SVOB04a, HORS06a] measures the net dipole moment when the material is exposed to a magnetic field. The magnetic moment of the sample can be obtained either as a function of field (*M-H* curve) or as a function of temperature (*M-T* curve) using this instrument. Figure 2.11a and Figure 2.11b depict a schematic diagram and a snap shot of VSM, respectively.

The VSM operates on the principle of Faraday's law of induction, which tells us that a changing magnetic flux will produce an electric field [GRIFF95a]. When a sample is placed in a uniform magnetic field, a dipole moment proportional to the product of the sample’s susceptibility and the applied field is induced in the sample. If the sample is vibrated in a sinusoidal manner, an electrical signal can be induced in suitably located stationary pick-up coils (*cf*. Figure 2.11a). This signal has amplitude proportional to the magnetic moment of the sample, the vibrating amplitude and the vibration frequency. Through the use of lock-in-amplifier and feedback techniques, only that portion of the signal arising from the magnetic moment is picked up and is converted into direct read-out in *emu* units on a digital panel meter. The VSM consists of the following major parts: 1) water cooled electromagnet and power supply, 2) vibration exciter and sample holder (with angular position indicator), 3) sensing (pick-up) coils, 4) Hall probe, 5) amplifier, 6) control chassis, 7) lock-in amplifier and 8) computer interface.

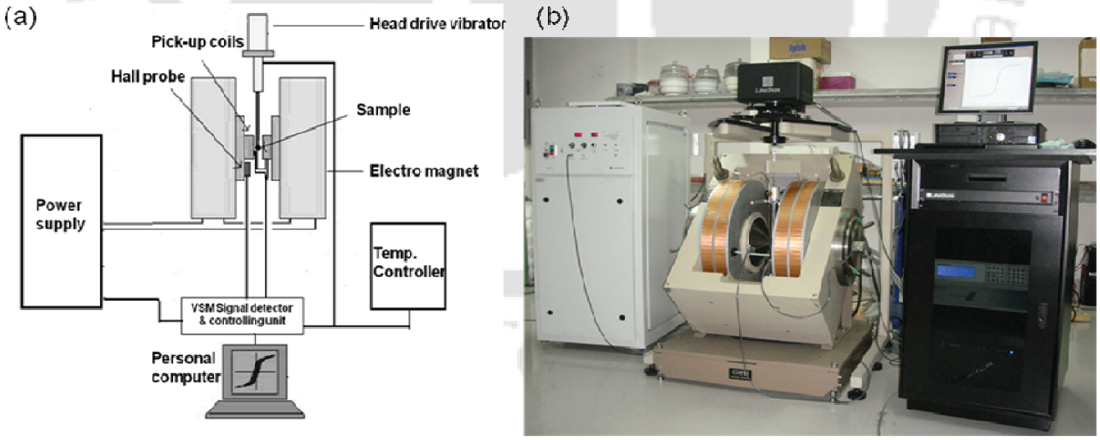

Figure 2.11: (a) Schematic diagram and (b) photograph of a Lakeshore VSM Model 7410.

The sample is fixed to the lower end of the sample holder after performing the calibration procedure using standard Ni sample. Subsequently, the measurement sequence is programmed using the software (IDEASVSM) provided with the instrument. The vibration exciter is then activated and the signal received from the probe and the pick-up coils is converted into the magnetic moment value of the sample. Magnetic field up to 3 T can be applied to the sample using this model of VSM. Normally, magnetic field is automatically increased in steps at a constant temperature (M - H measurements) by setting the program. These measurements provide M_{sat} value of the sample. Magnetization as a function of temperature at a constant applied field (M - T measurements) is recorded to obtain information of transition temperatures (T_C and T_M). A sharp decrease in magnetization is observed at the ferromagnetic to paramagnetic phase transition at T_C. T_C is generally determined from the minimum value of the first derivative of M - T data. The martensitic structural transition in FSMAs is accompanied by an abrupt change in magnetization measured at unsaturated fields. This is due to the change of magnetocryctalline anisotropy of the material during structural phase transitions.

The effective magnetic anisotropy constant K_{eff} of the ferromagnetic alloys can be calculated from the initial magnetization (M–H) curves using the law of approach to saturation [ANDR97a]. Generally, M as a function of applied field can be expressed as

$$M = M_{sat}\left(1 - \frac{a}{\sqrt{H}} - \frac{b}{H} - \frac{c}{H^2} - \cdots\right) + \chi_{hf} H + d\sqrt{H} \qquad (2.9)$$

where H is applied field, M_{sat} is a saturation magnetization, χ_{hf} is high field susceptibility and a, b, c, d are constant coefficients. The coefficients depend on the amount of structural defects and intrinsic fluctuations in the sample. According to Fähnle *et al.* [FAHN78a], the second term $\frac{a}{\sqrt{H}}$ can arise from point-like defects, intrinsic magneto-static fluctuations and randomly distributed magnetic anisotropy. c is related to the magneto-crystalline anisotropy. The constant d arises from the partial suppression of thermally excited spin waves in magnetic field. The paramagnetic term $\chi_{hf}H$ causes an increase in spontaneous magnetization at high external magnetic fields. The straight forward method for obtaining the coefficients would be to fit the experimental curve with this full expression. But, due to the large amount of coefficients involved, the fitting procedure gives ambiguous results. To overcome this, an alternate expression given below [JINZ98a] containing fewer coefficients is chosen as the fitting equation:

$$M(H) = M_{sat}\left(1 - \frac{c}{H^2}\right) \tag{2.10}$$

When applied field is increased to large values, domain wall movements become relatively unimportant and magnetization of the ferromagnetic sample is primarily controlled by domain rotation. With the assumption that atoms are oriented at random and strain distribution is homogeneous, the above equation is the best fit equation at high fields [WANG95a]. Deciding on the appropriate low field limit is a hurdle in this procedure. Graham *et al.* [GRAH93a] discussed this problem and has set the lower field limit for the case of as cast metallic glass at 1 T.

When paramagnetic contribution is comparable to the ferromagnetic contribution, the data obtained from M-H measurement cannot be fit with the above equation. So, data are first fit to the equation,

$$M = M_{sat}\left(1 - \frac{b}{H}\right) + \chi_{hf} H \tag{2.11}$$

and the paramagnetic contribution χ_{hf} obtained from the above fit is subtracted from the magnetization data [$M_{sat} \rightarrow (M - \chi_{hf}H)$] and the subtracted M_{sat} *vs* H data are then fitted to equation (2.10) to obtain the optimal c value. Once c value is correctly estimated, magneto crystalline anisotropy constant, K_{eff} can be calculated using the relation [JINZ98a],

$$K_{eff} = \mu_0 M_{sat} \left(\frac{15c}{4} \right)^{\frac{1}{2}} \tag{2.12}$$

VSM provides measured M_{sat} in units of emu/g (≅ $\mathrm{Am^2kg^{-1}}$) and so c estimated from the fitting procedure has the unit of $(\mathrm{Oe})^2$.

Magnetization tests have revealed that both the martensitic and the magnetic transitions in FSMAs are accompanied by an abrupt change in magnetization which results in a large MCE. The MCE parameter ΔS_M can be calculated from the isothermal *M versus H* curves. To evaluate ΔS_M, the integral in equation (1.23) can be approximately written as [PLAN09a, HUFS00a],

$$\Delta S_M [0 \rightarrow H; T(i)] = \frac{1}{\Delta T_i} \left[\int_0^H M(T_{i+1}) dH - \int_0^H M(T_i) dH \right] \tag{2.13}$$

where $T(i) = (T_{i+1} + T_i)/2$, and $\Delta T_i = T_{i+1} - T_i$ and the integrals are computed numerically using *M versus H* curves at discrete temperature intervals.

2.4. THERMAL CHARACTERIZATION

Certain valuable information about a material depends on the thermal response of the material. For a FSMA, the basic thermal properties are the endothermic and exothermic reactions during martensitic transition. To study the martensitic transitions, a differential scanning calorimeter (DSC) has been used. An important property of a FSMA is its heat capacity which was measured using a physical property measurement system (PPMS). In the following sections we briefly describe both these thermal instruments/ techniques.

2.4.1. Differential scanning calorimeter

Differential scanning calorimeter (DSC) is a thermo-analytic instrument [HATA98a] in which the difference in the amount of heat required to increase the temperature of a sample and a reference material is measured as a function of temperature. DSC curves are recorded either under a constant heating (or cooling) rate or under isothermal conditions (time scan at a constant temperature).

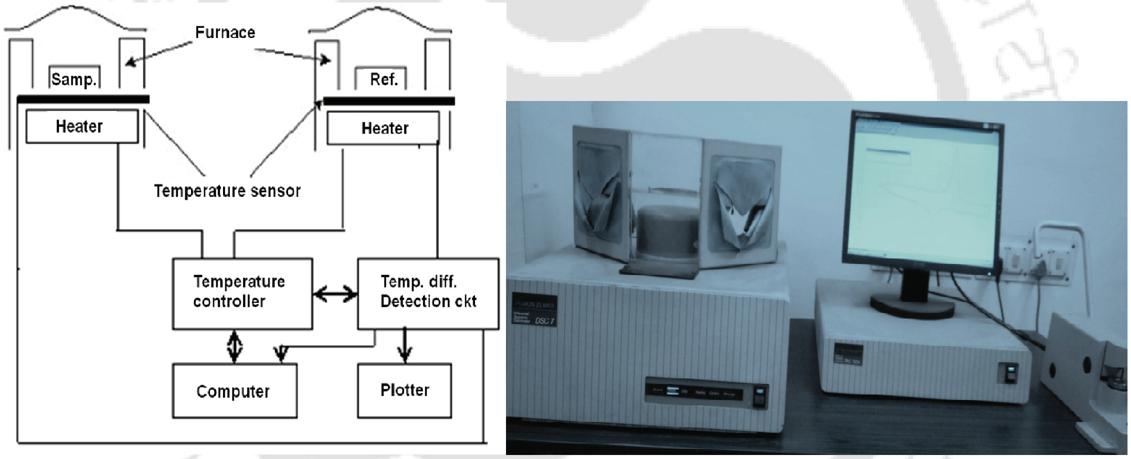

Figure 2.12: (a) Block diagram and (b) photograph of a power compensated DSC (PerkinElmer DSC 7).

A typical DSC consists of two isolated sealed pans, one containing the sample and the other a reference material (generally, Al_2O_3 or just the empty Al pan). The pans are covered with Al covers, which act as a radiation shield (Figure 2.12). The two pans are heated or cooled uniformly while the heat flow difference between the two is monitored. The basic principle underlying this technique is that, when the sample undergoes a physical transformation such as phase transition, more or less heat will need to flow to it in comparison with the reference in order to maintain both at the same temperature [HOHN03a]. More or less heat flowing to the same would depend on the process being endothermic or exothermic. In the power compensation type DSC, heat is supplied to either of the pans so that both are maintained at the same temperature. The heat flow (*dQ/dt*) is then estimated from this data. On the other hand, in a DSC based on heat-flux technique, the temperature difference (ΔT) between the two isolated pans is measured from which the heat flow is estimated. Hence, power compensation is the preferred technique for a sensitive DSC.

A commercial DSC (PerkinElmer, DSC7) based on the power compensation technique (shown in Figure 2.12b) was used in the current investigations. Weighed quantities of the sample pieces were crimped in Al sample pan and the thermal transformations occurring in the operating temperature range of was studied during the heating and cooling cycles under a constant heating/cooling rate.

DSC curves (*dQ/dt* versus *T* data) of 10 to 30 mg samples were recorded and analyzed using the Pyris^{TM} software. Temperature and enthalpy calibrations were performed using standard samples (In and Zn) prior to the measurements. High purity nitrogen gas was purged continuously throughout the runs. A typical DSC curve of a shape memory alloy is shown in Figure 2.13. The endothermic peak during heating and exothermic peak during cooling represents the reverse martensitic phase transformation and forward martensitic phase transformation, respectively. The point at which the endothermic peak starts during heating is called austenite start temperature (T_{As}) and the point at which endothermic peak finishes is called austenite finish temperature (T_{Af}). Similarly, the starting and finishing points of the exothermic peak during cooling are called martensite start (T_{Ms}) and martensite finish (T_{Mf}) temperatures, respectively.

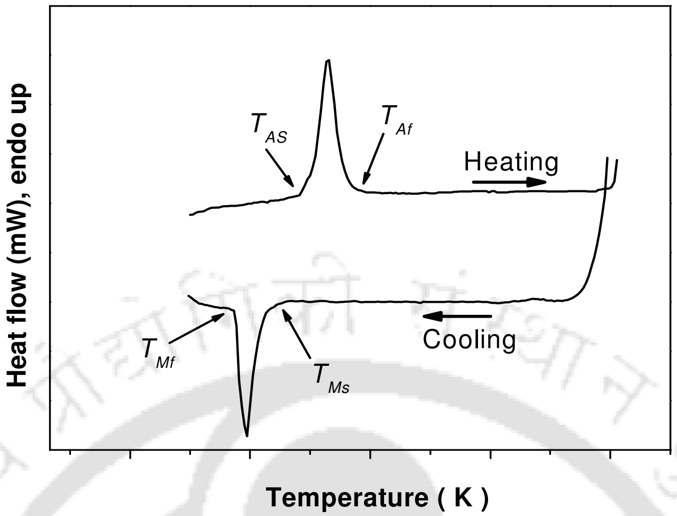

Figure 2.13: Typical DSC curve obtained for an FSMA sample in the current studies.

2.4.2. Physical property measurement system

A commercial physical property measurement system (PPMS, Quantum design model shown in Figure 2.14) was used to measure the heat capacity of the samples. PPMS performs a fully automated relaxation method [HEAT04a] for the measurement of heat capacity. The sample is mounted on a sample platform shown in Figure 2.15 using thermally conducting grease [HEAT04a]. In order to provide a known heating power to the platform and for measurement of the temperature of the platform, the sample platform has a heater and a temperature sensor. The sample platform is supported by thin wires which are connected to the puck and serves as calorimetric thermal bath. These wires also act as electrical connections for platform heater and temperature sensor. The puck also has a temperature sensor for measurement of the puck temperature. The whole arrangement is thermally shielded to prevent unwanted heating of the sample and the sample platform from the warmer surfaces of sample chamber. During experiment the sample chamber is held at a high vacuum.

Figure 2.14: Photographic view of PPMS, Quantum design model.

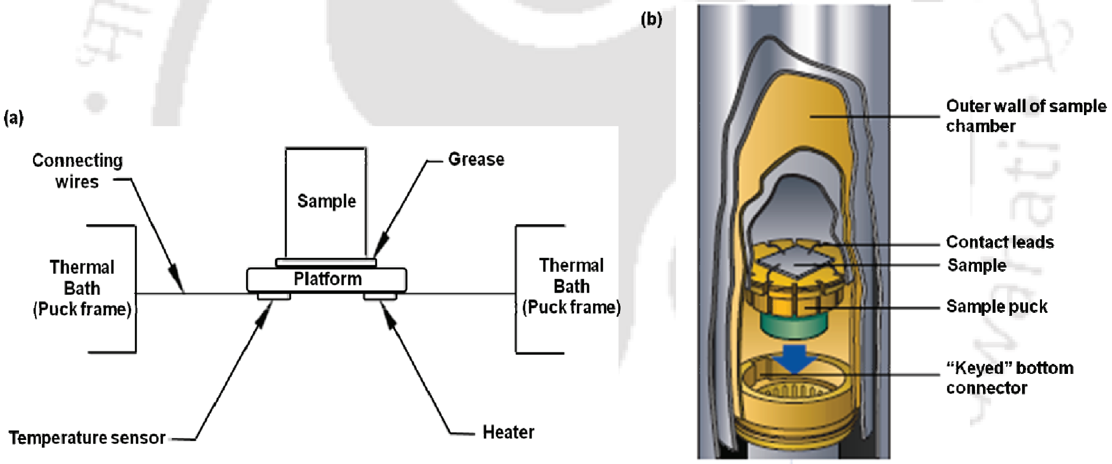

Figure 2.15: Schematic views of configuration of sample mounting for heat capacity measurement in PPMS.

For every measurement, the power is generated by the platform heater. The entire thermal response data of the sample platform is then fitted to two models to extract the heat capacity of the sample. One is a simple model in which a good thermal contact between the sample and the platform is considered, and both sample and platform are conducted to be at the same temperature. In the second model due to poor thermal contact between the sample and platform, there is a temperature difference between the two. The poor thermal contact model accounts for both the thermal relaxation of the sample platform to the bath temperature and the relaxation between the sample platform and the sample itself. This is also called the two-tau method. The following mathematical equations express the two models [HEAT04a].

In case of simple model:,

$$C_{total}\frac{dT}{dt}=-K_w\left(T-T_b\right)+P(t) \tag{2.14}$$

In case of two-tau model:

$$\begin{aligned} C_{platform}\frac{dT_p}{dt}&=P(t)-K_w\left[T_p(t)-T_b\right]+K_g\left[T_s(t)-T_p(t)\right]\\ C_{sample}\frac{dT_s}{dt}&=-K_g\left[T_s(t)-T_p(t)\right] \end{aligned} \tag{2.15}$$

where C_{total}, $C_{platform}$ and C_{sample} are the total (sample + platform) heat capacity, sample platform heat capacity and sample heat capacity, respectively. K_w and K_g are the thermal conductance of the supporting wires and grease, respectively. T_b, T_p, and T_s are the temperatures of bath (puck frame), platform, and sample respectively. $P(t)$ is the power applied by the heater.

In a typical measurement, the heat capacity of the addenda ($C_{addenda}$) is first measured using the simple model without any sample so that C_{total} = $C_{addenda}$. The experimental data recorded with the sample is fitted to the simple model as well the two-tau model using C_{total} = C_{sample} + $C_{addenda}$. Now, entropy at zero field ($S_{H=0}$) as a function of temperature can be evaluated from the heat capacity data at zero field ($C_{H=0}$) using the following relation [PECH01b, SHAR07a]:

$$S(T)_{H=0}=\int_0^T\frac{C(T)_{H=0}}{T}dT+S(T=0) \tag{2.16}$$

For solids, S (T = 0) is independent of H and can be assumed to be a constant or zero. Since ΔS_M for any field calculated from magnetization measurement is the difference of zero field entropy ($S_{H=0}$) and the entropy with field ($S_{H>0}$), the entropy at any field is given by

$$S(T)_{H>0} = S(T)_{H=0} + \Delta S_M(T)_{\Delta H>0} \tag{2.17}$$

If isentropic paths are followed from $S(T)_{H=0}$ to $S(T)_{H>0}$ curves the adiabatic temperature change (ΔT_{ad}) as a function of temperature can be obtained from the relation,

$$\Delta T_{ad}(T)_H = [T_H - T_{H=0}]_S \tag{2.18}$$

Since $\Delta T_{ad} \approx - T\Delta S_M/C_H$, where C_H is the specific heat at constant field, the shapes of $\Delta T_{ad}(T)$ curves take the inverted form of $\Delta S_M(T)$ curves. A negative value of ΔT_{ad} indicates inverse MCE and a positive ΔT_{ad} infers conventional (direct) MCE.

Chapter 3

INVESTIGATIONS ON Ni-Mn-Ga ALLOYS

Martensitic transformation in the prototype FSMA, Ni-Mn-Ga was first reported in 1984 [WEBS84a]. Shape memory effect was established in this alloy in 1990 [ZASI90a] and its magnetostrictive character was demonstrated in 1996 [ULLA96a, JAME96a]. In recent years, this Heusler alloy has received significant amount of attention due to its giant MFIS and large MCE. The magnetic phase transition in this alloy is interestingly coupled with the structural transition. Due to this, a direct transformation from paramagnetic austenite phase to ferromagnetic martensite phase (magneto-structural transition) occurs in this alloy, which is responsible for the realization of such a large MCE. In stoichiometric Heusler composition i.e., Ni_2MnGa, the magnetic (T_C = 376 K) and structural (T_M = 202 K) transitions are well separated. However, in an appropriate off-stoichiometric Heusler composition, both T_C and T_M can be made to merge into a combined magneto-structural transition. This is achieved by tailoring the structural and magnetic transition temperatures by changing the elemental composition (and thereby *e*/*a* ratio). The effect of excess Ni on the structural and magnetic properties of $Ni_{2+x}Mn_{1-x}Ga$ has been studied [VASI99a, WIRT97a] in the range of $0 \leq x \leq 0.2$, where a general tendency to increase T_M and to decrease T_C was observed with increasing Ni content before they merge as illustrated in Figure 3.1. The substitution of Ni in Mn sites in $Ni_{2+x}Mn_{1-x}$ Ga alloys results in the increase of *e*/*a* ratio and the dependence of T_M on *e*/*a* is more pronounced than that of T_C. So, the difference between T_M and T_C is narrowed down with increasing Ni content. As a result, the magneto-structural phase transition occurs in these alloys when *e*/*a* is between ~7.63 and ~7.65 [VASI99a, MARC04a, MOYA06a, PLAN09a]. In addition, it is also reported that magneto-structural phase transition occurs in $Ni_2Mn_{1-x}Co_xGa$ alloys when *e*/*a* ~7.65 [GOME06a]. Due to the magneto-structural transition, a remarkable entropy change, ΔS of 24 $Jkg^{-1}K^{-1}$ accompanied by high ΔS_M of 41 $Jkg^{-1}K^{-1}$ for a ΔH of 2T was exhibited by $Ni_{55}Mn_{20}Ga_{25}$ single crystals at ~313 K [PASQ05a].

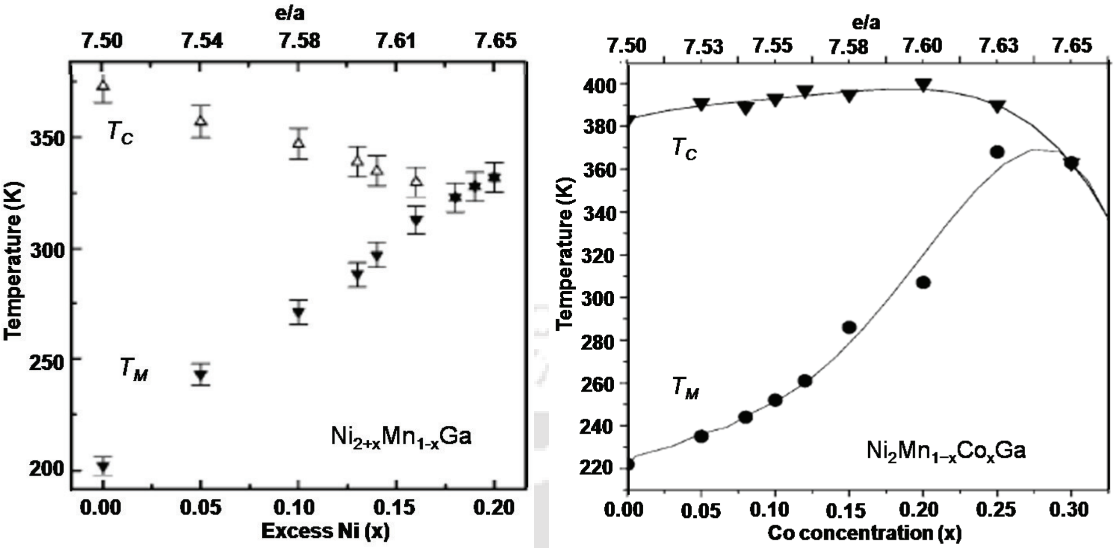

Figure 3.1: Composition dependencies of magnetic and structural phase transition temperatures of $Ni_{2+x}Mn_{1-x}Ga$ and $Ni_2Mn_{1-x}Co_xGa$ alloys [VASI99a, GOME06a, PLAN09a].

In this chapter, structural [T_{Ms}, changes in enthalpy (ΔE), entropy (ΔS) and free energy (ΔG)] and magnetic properties [M_{sat}, (K_{eff}), MCE and T_C] of $Ni_{55}Mn_{21-x}Ga_{24+x}$ and $Ni_{53.75}Mn_{21.25-x}Co_xGa_{25}$ alloys are presented.

3.1. Preparation

Since the martensitic and magnetic transition temperatures overlap for both Ni-Mn-Ga and Ni-Mn-Co-Ga systems when *e*/*a* = 7.65, alloy compositions were chosen such that *e*/*a* ratio was around this value. Polycrystalline $Ni_{55}Mn_{21-x}Ga_{24+x}$ (where x = 0, 1, 2 and 3) and $Ni_{53.75}Mn_{21.25-x}Co_xGa_{25}$ (where x= 1, 1.25, 1.5 and 2) alloy ingots were prepared by arc melting method followed by homogenization at 1173 K for 24 h and quenching in ice + water mixture as described in the previous chapter. The overall composition of the master alloys as determined by EDS analysis was found to be close to the nominal (starting) composition of the respective alloys (*cf.* Table 3.1 and Table 3.5).

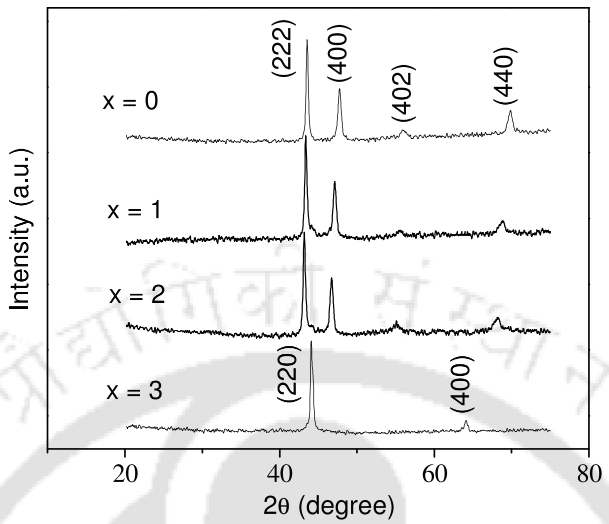

Figure 3.2: Room temperature XRD patterns of $Ni_{55}Mn_{21-x}Ga_{24+x}$ (x = 0, 1, 2 and 3) alloys.

3.2. Bulk $Ni_{55}Mn_{21-x}Ga_{24+x}$ (x = 0, 1, 2 and 3) alloys

3.2.1. Crystal structures

Room temperature powder XRD patterns of $Ni_{55}Mn_{21-x}Ga_{24+x}$ (where x = 0, 1, 2 and 3) alloys recorded using Cu-K_α radiation (λ = 0.15406 nm) are shown in Figure 3.2. Generally, Ni-Mn-Ga alloys are known to exhibit either orthorhombic or tetragonal structure in the martensitic phase [INGA07a]. The alloy with x ≤ 2 exhibited non-modulated (NM) tetragonal structure in martensitic phase and the sample with x = 3 exhibited the cubic $L2_1$ structure typical of the austenite phase.

Table 3.1 summarizes the lattice parameters estimated from the XRD patterns. Lattice parameters of the alloys with x = 0, 1, 2 and 3 are $a = b = 0.7612 \pm 0.0007$ nm; $c = 0.6527 \pm 0.0005$ nm, $a = b = 0.7708 \pm 0.0005$ nm; $c = 0.6473 \pm 0.0004$ nm, $a = b = 0.7771 \pm 0.0002$ nm; $c = 0.6468 \pm 0.0004$ nm, and $a = b = c = 0.5805 \pm 0.0001$ nm, respectively. With increased Ga substitution for Mn, the unit-cell volume slightly increased in the same (martensite) crystalline phase and finally transformed to a new (austenite) phase. The slight increase in unit cell volume within the same phase with Ga addition indicates that Ga atoms progressively substitute for Mn atoms.

TABLE 3.1: Measured composition, crystal phase, lattice parameters and unit-cell volume of $Ni_{55}Mn_{21-x}Ga_{24+x}$ (where x = 0, 1, 2 and 3) alloys.

Alloy ID	Measured Composition	*e/a*	Crystal phase	*a* (nm)	*b* (nm)	*c* (nm)	Unit-cell volume (nm^3)
x = 0	$Ni_{54.68}Mn_{20.90}Ga_{24.42}$	7.66	Martensite	0.7612	0.7612	0.6527	0.3782
x = 1	$Ni_{54.97}Mn_{20.15}Ga_{24.88}$	7.65	Martensite	0.7708	0.7708	0.6473	0.3846
x = 2	$Ni_{54.9}Mn_{18.91}Ga_{26.20}$	7.60	Martensite	0.7771	0.7771	0.6468	0.3906
x = 3	$Ni_{55.17}Mn_{18.13}Ga_{26.70}$	7.59	Austenite	0.5805	0.5805	0.5805	0.1956

3.2.2. Magnetic properties

Room temperature initial magnetization (*M-H*) curves of $Ni_{55}Mn_{21-x}Ga_{24+x}$ (x = 0, 1, 2 and 3) alloys recorded using the VSM are shown in Figure 3.3. It is observed that all are not saturated at room temperature for applied fields up to 2 T. The linear magnetic response of the alloy sample with x = 3 to applied field indicates that it is paramagnetic, whereas the alloys with x < 3 exhibit nonlinear magnetic response typical of ferromagnetic materials. Considering the structural data presented in Table 3.1, one can conclude that while the alloy with x = 3 is in paramagnetic austenite phase, the rest of the alloys with x < 3 are in ferromagnetic martensite state. It can be noticed that the magnetic response of the room temperature martensite alloys increases as x is increased. The room temperature saturation magnetization (M_{sat}) at 2 T increases from 35.77 Am^2kg^{-1} for the alloy with x = 0 to 51.86

Am^2kg^{-1} for the alloy with x = 2. The alloy with x = 2 represents a threshold martensite composition with the highest M_{sat} in this series of $Ni_{55}Mn_{21-x}Ga_{24+x}$ alloys.

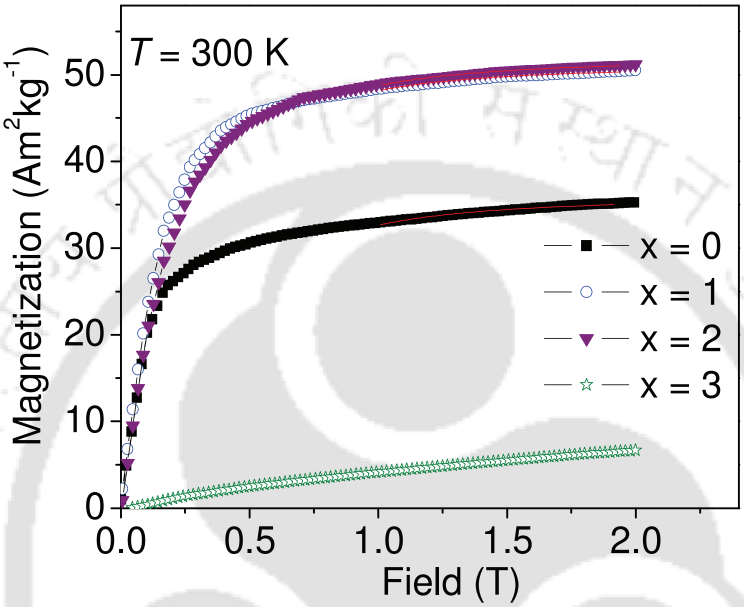

Figure 3.3: Initial magnetization curves of $Ni_{55}Mn_{21-x}Ga_{24+x}$ (x = 0, 1, 2 and 3) alloys at room temperature.

Field dependence of magnetization of a polycrystalline ferromagnetic material can be expressed in terms of the law of approach to saturation as

$$M(H) = M_{sat}\left(1 - \frac{c}{H^2}\right) \qquad (3.1)$$

where M_{sat} is the saturation magnetization and the term c/H^2 is attributed to the magneto-crystalline anisotropy. It is reported that the magnetic moments of Ni-Mn based ferromagnetic alloys originate from the localized moments of Mn atoms (about 4.0 μ_B per Mn ion, and ~ 0.3 μ_B per Ni atom) [WEBS84a]. This means that the increase in M_{sat} at 2 T from 35.77 Am^2kg^{-1} for x = 0 to 51.86 Am^2kg^{-1} for the alloy with x = 2 at room temperature in the martensite state of $Ni_{55}Mn_{21-x}Ga_{24+x}$ alloys is associated with magnetic moments of Mn atoms. The negative influence of Mn atoms on M_{sat} of $Ni_{50}Mn_{25+x}Ga_{25-x}$ alloys has also been observed by Jiang *et al.* [JIAN04a] who analyzed their data in the frame of a localized moment picture. The c/H^2 term in equation (3.1) gives the effective anisotropy constant (K_{eff}). For a tetragonal compound, K_{eff} is described by the relation [JINZ98a],

$$K_{eff} = \mu_0 M_{sat} \left(\frac{15c}{4} \right)^{\frac{1}{2}} \tag{3.2}$$

TABLE 3.2: M_{sat} and K_{eff} of $Ni_{55}Mn_{21-x}Ga_{24+x}$ (where x = 0, 1, 2 and 3) alloys estimated at room temperature.

Alloy ID	M_{sat} **(Am^2kg^{-1})**	K_{eff} **($\times 10^5\ Jm^{-3}$)**
x = 0	35.77	1.58
x = 1	51.10	1.89
x = 2	51.86	1.96

K_{eff} values of $Ni_{55}Mn_{21-x}Ga_{24+x}$ alloys calculated from the *M-H* data depicted in Figure 3.3 are summarized in Table 3.2. The variation of K_{eff} exhibits a similar tendency as that of M_{sat} for $Ni_{55}Mn_{21-x}Ga_{24+x}$ alloys with $x \leq 2$. Further increase in x in this series of alloys, results in paramagnetic austenite phase instead of the ferromagnetic martensite phase at room temperature. The alloy with x = 2 exhibited the highest K_{eff} value of 1.96×10^5 Jm^{-3} which is comparable with the the highest room temperature K_{eff} (1.95×10^5 Jm^{-3}) of polycrystalline $Ni_{50}Mn_{25+x}Ga_{25-x}$ alloys [JIAN04a].

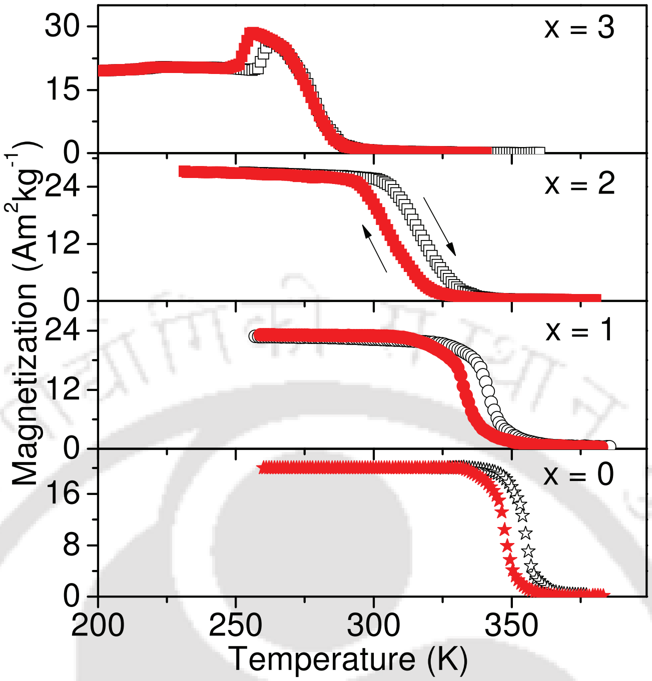

Figure 3.4: *M–T* curves recorded during cooling and heating of $Ni_{55}Mn_{21-x}Ga_{24+x}$ alloys under an applied magnetic field of 0.1 T.

In order to understand the temperature dependent magnetic behaviour of $Ni_{55}Mn_{21-x}Ga_{24+x}$ alloys, *M–T* curves were recorder between 200-385 K. Figure 3.4 shows the *M–T* curves of these alloys recorded under field-cooled (FC) and field heated (FH) conditions with an applied field of 0.1 T. T_C values determined from the inflection point in the *M–T* curves are listed in Table 3.3. With increased Ga substitution, Mn-Mn interactions weaken, leading a decrease in T_C. It is also evident from the *M–T* curves that in the samples with x ≤ 2, the magnetic phase transition at T_C is accompanied by thermal hysteresis, which is a characteristic of first-order phase transition. Figure 3.4 portrays that though the alloys with x ≤ 2 show this behaviour, the magnetic transition with the hysteresis behaviour shifts to lower temperatures with an increase in x. The hysteresis around T_C in these alloys indicates that the second-order magnetic transition is accompanied by a first-order structural transition, i.e., a ferromagnetic martensite phase transforms to paramagnetic austenite phase (or the occurrence of a combined magneto-structural transition). However, the alloy with x = 3 exhibits an altogether different behaviour. When this alloy is heated from low temperature, the ferromagnetic martensite transforms into ferromagnetic austenite. On further heating, the ferromagnetic austenite transforms into paramagnetic austenitic. On cooling this alloy, the magnetization curve re-traces it path through the magnetic transition but shows a hysteresis across the first-order structural transition. Thus, both the structural and magnetic transitions are well separated in this alloy. T_{Ms} (defined as the temperatures at which the maximum magnetization is achieved in the FC $M - T$ data) and T_C of this alloy composition are 255 K and 276 K, respectively, i.e., they are 21 K apart from each other.

3.2.3. Thermal properties

The magneto-structural transition in $Ni_{55}Mn_{21-x}Ga_{24+x}$ alloys has been confirmed by differential scanning calorimeter (DSC) measurements performed at constant heating and cooling rates of 15 K/min. The DSC curves are presented in Figure 3.5, which show only one exothermic and one endothermic peak in the cooling and heating cycles, respectively. The exothermic peak in the cooling cycle is a signature of the forward martensitic transition from the high symmetry austenite to the low symmetry martensite. The endotherm on the heating cycle signifies the reverse martensitic transition. In the DSC curves, T_{Ms}, T_{Mf}, T_{As} and T_{Af} refer to the martensite start, martensite finish, austenite start and the austenite finish temperatures observed in the cooling and heating cycles, respectively. All the temperatures extracted from DSC data are summarized in Table 3.3. It can be seen from Table 3.3 that all the characteristic temperatures of martensitic transition decrease with increasing Ga at.%. For alloys with $x \leq 2$, the characteristic temperatures shift towards room temperature with increasing x.

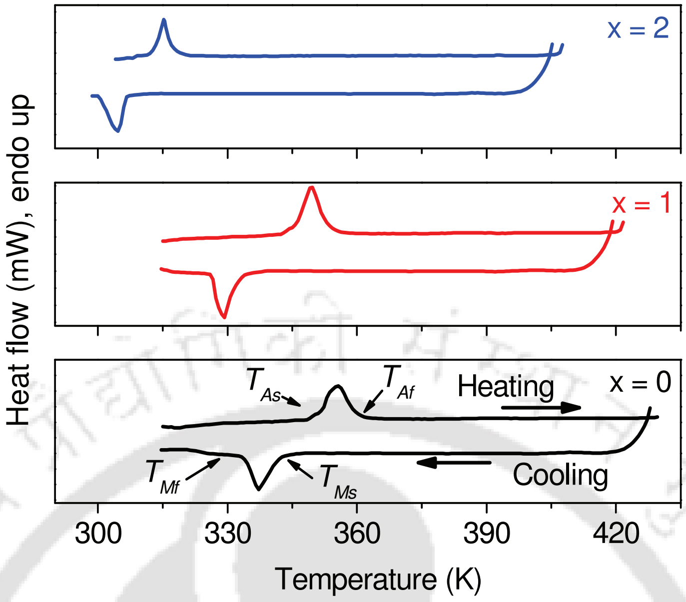

Figure 3.5: DSC curves of $Ni_{55}Mn_{21-x}Ga_{24+x}$ alloys with x = 0, 1 and 2.

TABLE 3.3: Martensite start temperature (T_{Ms}), martensite finish temperatures, austenite start temperatures (T_{As}), austenite finish temperature (T_{Af}), Curie temperature (T_C), thermal hysteresis (ΔT_{hys}), change in total enthalpy (ΔE), change in total entropy (ΔS) and change in free energy (ΔG) of $Ni_{55}Mn_{21-x}Ga_{24+x}$ (x = 0, 1 and 2) alloys.

Alloy ID	T_{Ms} (K)	T_{Mf} (K)	T_{As} (K)	T_{Af} (K)	T_C (K)	ΔT_{hys} (K)	ΔE (kJkg^{-1})	ΔS (Jkg^{-1}K^{-1})	ΔG (Jkg^{-1})
x = 0	348	326	350	364	356	20.0	8.5	23.9	454
x = 1	335	325	342	357	343	19.5	7.1	20.5	410
x = 2	307	299	309	321	315	12.0	5.7	18.2	196

By comparing the DSC results with those obtained from XRD, one can conclude that during cooling, the forward martensite transition occurs from cubic austenite ($L2_1$) to non-modulated tetragonal martensite phase in all the alloys. The martensite transition region can be defined in terms of the equilibrium temperature T_0 [= (T_{Ms} + T_{Af})/2] at which the Gibbs free energies of the austenite and martensite phases are equal.

i.e.,
$$\Delta G = \Delta E - T_0 \Delta S = 0 \tag{3.3}$$

where ΔG, ΔE and ΔS are changes in free energy, enthalpy and entropy, respectively. At the peak martensitic transition temperature T_{Mp},

$$\Delta G = \Delta E - T_{Mp} \Delta S < 0 \tag{3.4}$$

Using equations (3.3) and (3.4), ΔG can be rewritten as

$$\Delta G = \frac{\Delta E\left(T_0 - T_{Mp}\right)}{T_0} \approx \frac{\Delta E\left(T_{Ap} - T_{Mp}\right)}{2T_0} \tag{3.5}$$

where ΔE is estimated from the baseline corrected DSC data using the relation [KREN05b],

$$\Delta E = \int_{T_1}^{T_2} \left(\frac{dQ}{dt}\right)\left(\frac{dT}{dt}\right)^{-1} dT \tag{3.6}$$

The average values of ΔE corresponding to forward and reverse martensitic transitions are listed in Table 3.3. With increasing Ga at.%, the magnitude of ΔE decreases resulting in a corresponding decrease in ΔG from 454 Jkg^{-1} for the alloy with x = 0 to 196 Jkg^{-1} for the alloy with x = 2. Less ΔG at the martensitic phase transition means smaller energy requirement for the martensite - austenite transition, and results in smaller thermal hysteresis, ΔT_{hys}. This is consistent with the calorimetric results in which ΔT_{hys} [= (T_{As} + T_{Af})/2 - (T_{Ms} + T_{Mf})/2] for the alloy with x = 2 was found to be 12 K, which is lower than the value of 20 K obtained for the alloy with x = 0.

When the Gibbs free energies of martensite and austenite are equal, ΔS can be simplified using equation (3.3) as [KHOV03b, KREN05b],

$$\Delta S = \frac{\Delta E}{T_0} \tag{3.7}$$

ΔS estimated for $Ni_{55}Mn_{21-x}Ga_{24+x}$ (x = 0, 1 and 2) alloys using equation (3.7) is listed in Table 3.3. It is evident from this table that the highest ΔS of 23.9 $Jkg^{-1}K^{-1}$ was obtained for x = 0 alloy at 356 K. For the alloy with x = 2, the estimated ΔS was 18.2 $Jkg^{-1}K^{-1}$ near room temperature (314 K). Comparison of this high ΔS estimated for polycrystalline $Ni_{55}Mn_{21}Ga_{24}$ alloy (23.9 $Jkg^{-1}K^{-1}$) with that reported (24 $Jkg^{-1}K^{-1}$) for single crystal $Ni_{55}N_{20}Ga_{25}$ alloy [PASQ05a] highlights the promising results obtained in the present work and the advantage of atomic substitution in polycrystalline alloys.

ΔS around T_0 has three main contributions [KHOV03b], viz.,

$$\Delta S = \Delta S_V + \Delta S_E + \Delta S_M \tag{3.8}$$

where ΔS_E, ΔS_V and ΔS_M are the electronic, vibrational and magnetic contributions. It has been shown that the electronic contribution to ΔS in Ni-Mn-Ga alloys is considerably very small [FRAG91a]. The vibrational contribution ΔS_V depends on the elastic anisotropy at T_0 and the elastic anisotropy constant for a particular crystal structure of martensitic phase is independent of the alloy composition [PLAN92a, KHOV03b]. Hence, the decrease in ΔS upon substitution of Ga for Mn is mainly attributed to the magnetic contribution ΔS_M which clarifies the origin of MCE in FSMAs.

3.2.4. Magneto-caloric properties

It is already mentioned that ΔS_M is a measure of the MCE in a material. ΔS_M has been determined from isothermal initial magnetization curves using the Maxwell relation [TISH03a],

$$\Delta S_M(T,H) = \int_0^H \left(\frac{\partial M}{\partial T}\right)_H dH \tag{3.9}$$

In order to estimate ΔS_M from experimental data, isothermal initial magnetization, $(M - H)_T$, were recorded as a function of increasing magnetic field at different temperatures near the transformation temperature regime while heating and cooling the sample. In measurement process, the sample was held at each temperature for sufficient time to stabilize temperature before recording the isothermal magnetization curves.

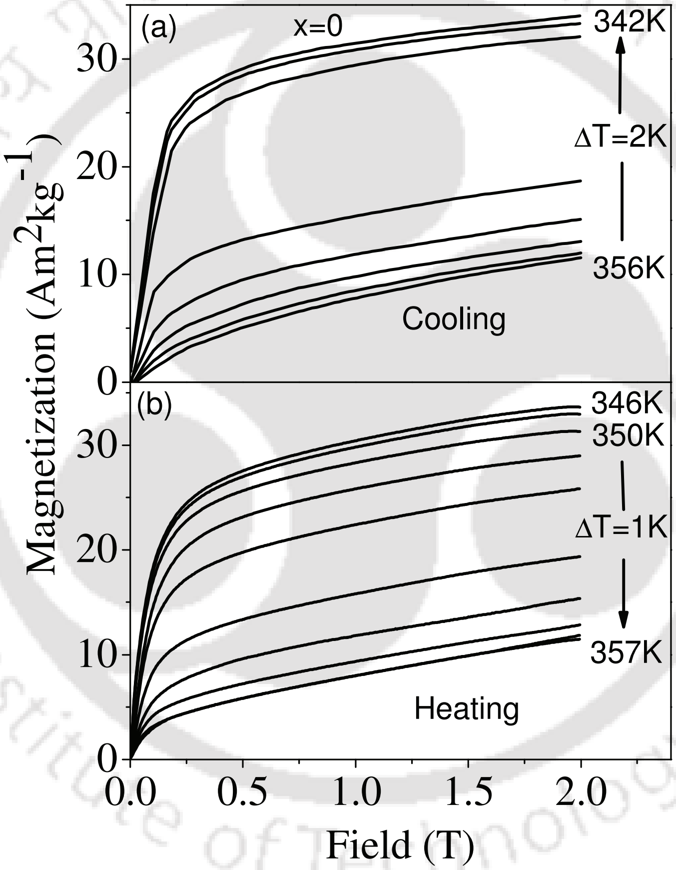

Figure 3.6: Isothermal magnetization curves recorded at various temperatures near T_{Ms} for $Ni_{55}Mn_{21}Ga_{24}$ alloy during (a) cooling and (b) heating cycles.

Figure 3.6 depicts the typical isothermal initial magnetization curves recorded for the alloy with x = 0 near T_{Ms} and T_C on the (a) cooling and (b) heating cycles. Magnetic field was varied from 0 to 2 T. During heating process, the magnitude of magnetization decreased with increasing temperature and a large drop in magnetization was observed between two consecutive isotherms at 352 K and 353 K around the reverse martensitic phase transition temperature. However, during the cooling process, the magnitude of magnetization increased with decreasing the temperature and a sudden increase in magnetization occurs between 348 K and 346 K, around the forward martensitic phase transition temperature. It was also seen in both the cases that the nature of nonlinearity reduced with increasing temperature and magnetization did not saturate up to an applied field of 2 T.

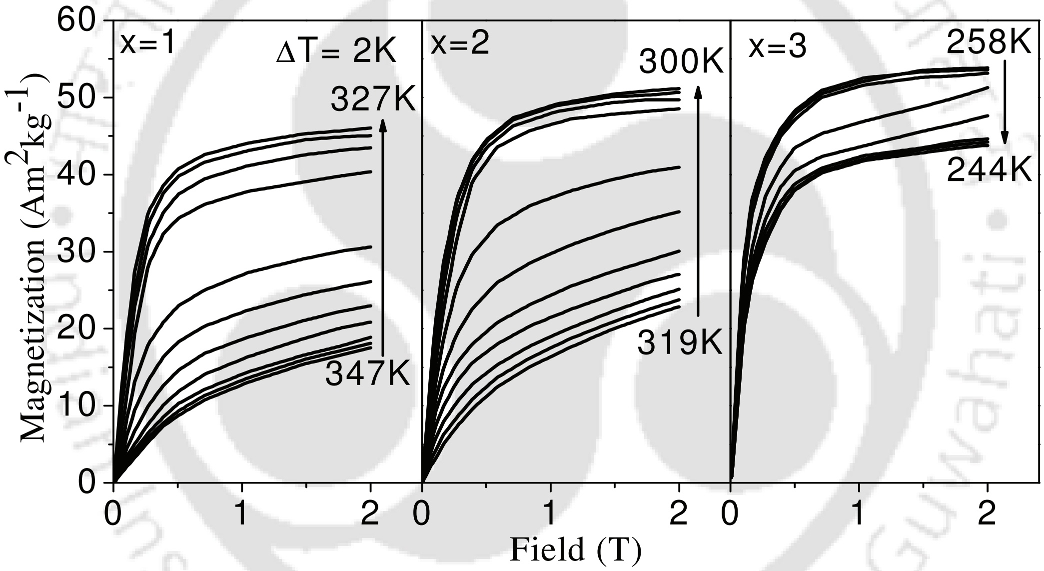

Figure 3.7: Isothermal magnetization curves recorded at various temperatures on the cooling process around T_{Ms} of $Ni_{55}Mn_{21-x}Ga_{24+x}$ alloys with x = 1, 2 and 3.

Figure 3.7 shows the isothermal initial magnetization curves around T_{Ms} for the alloys with x = 1, 2 and 3 measured in the cooling cycle. It was seen that isothermal magnetization characteristics of the alloys x = 1 and 2 are very much similar to that of the alloy with x = 0. But due to the large separation of T_{Ms} from T_C in the alloy with x = 3, the variation of magnetization with the temperature and field is different from that of the other alloys. In this alloy during the cooling process, the $(M-H)_T$ data around T_{Ms} exhibit a trend of decreasing magnetization with decreasing temperature, which is opposite to the response of the other alloys. Due to the pure structural transition exhibited by this alloy at the measured temperature, the $(M-H)_T$ data bear the signature of metamagnetism (S-like curvature at high fields).

Variation of ΔS_M as a function of temperature for $Ni_{55}Mn_{21-x}Ga_{24+x}$ alloys is displayed in Figure 3.8. The peak values of $|\Delta S_M|$ in cooling (heating) process are 12.9 $Jkg^{-1}K^{-1}$ (12.3 $Jkg^{-1}K^{-1}$), 9.7 $Jkg^{-1}K^{-1}$ (8.8 $Jkg^{-1}K^{-1}$), 8.1 $Jkg^{-1}K^{-1}$ (7.1 $Jkg^{-1}K^{-1}$) and 3.7 $Jkg^{-1}K^{-1}$ (1.9 $Jkg^{-1}K^{-1}$) for the alloys with x = 0, 1, 2 and 3, respectively, for a ΔH of 2 T. Despite precise measurement with 1 K interval, the heating process exhibits a smaller peak value of $|\Delta S_M|$ as shown in Figure 3.9. This disparity can be explained by considering a double well energy potential governing the magnetostructural phase transition. If two minima of the double well represent the low temperature ferromagnetic martensite phase and the high temperature paramagnetic austenite phase, respectively, the transformation from one phase to the other will be hindered by an energy barrier. The potential well can be distorted and phase transformation can be induced by the application of temperature as well as the magnetic field. Due to the application of magnetic field in the cooling process, both the temperature and field favour the transformation to the low temperature ferromagnetic martensite phase i.e., the magneto-structural phase transformation can easily occur with sharp change in magnetization accompanied by large $\partial M/\partial T$ value which results in higher peak ΔS_M in the cooling process. On the other hand, if the magnetic field is applied during the heating process, the field always tends to favour the ferromagnetic martensite phase, while the temperature supports the high temperature paramagnetic austenite phase with smaller value of $\partial M/\partial T$, which ultimately results in smaller peak ΔS_M in the heating process.

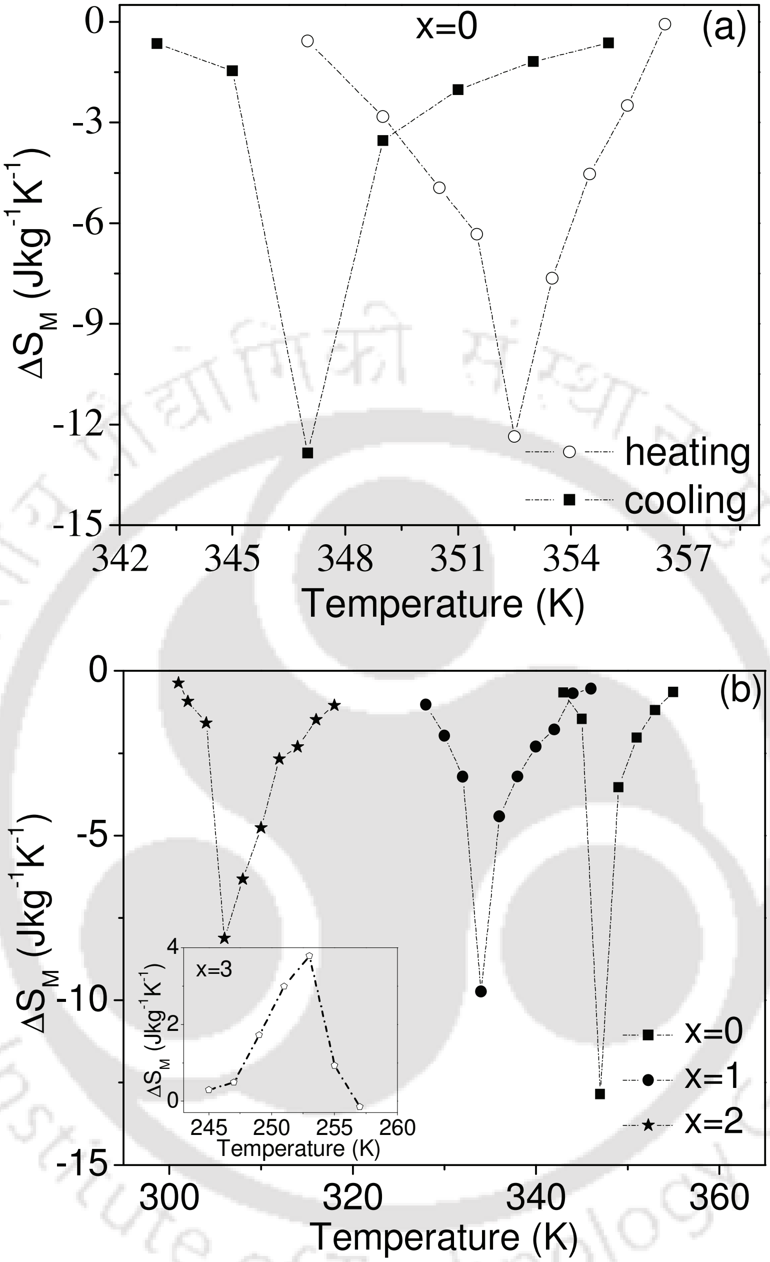

Figure 3.8: ΔS_M as a function of temperature of $Ni_{55}Mn_{21-x}Ga_{24+x}$ alloys for ΔH of 2 T. (a) ΔS_M estimated during the heating and cooling processes of the alloy with x = 0. (b) ΔS_M estimated during the cooling process for all the alloys. Inset in figure (b) presents the positive ΔS_M around the structural phase transition which is well separated from the ferromagnetic transition in the alloy with x = 3.

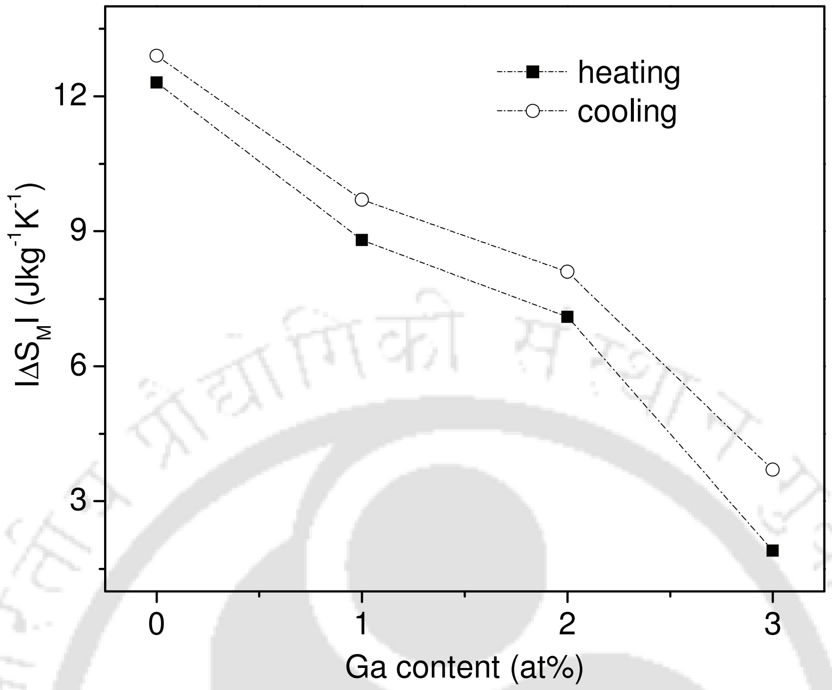

Figure 3.9: Variations of magnitude of ΔS_M on the heating and cooling process as a function of Ga content for a ΔH of 2 T.

However with increasing Ga content, ΔS_M decreases due to the lesser contribution of the term $(\partial M/\partial T)_H$ in the integrated Maxwell's equation (3.9). Since $\partial M/\partial T$ is positive around the structural phase transition which is well separated from ferromagnetic transition in the alloy with x = 3, $\Delta S_M > 0$. ΔS_M is related to ΔT_{ad} by the relation [TISH03a],

$$\Delta T_{ad} = -\frac{T}{C_H}\Delta S_M \tag{3.10}$$

where C_H is the specific heat at constant field. A positive ΔS_M implies that the samples cool down when the external magnetic field is applied adiabatically, i.e., inverse MCE [TISH03a, TEGU02b, ZHAN04a, KREN05a, RANK09a]. On the other hand, due to the negative value of $\partial M/\partial T$ around the magnetotructural phase transition, ΔS_M becomes negative for the alloys with x ≤ 2. In these cases, the sample heats up upon application of magnetic field (commonly known as conventional MCE) [TISH03a, RANK09a].

TABLE 3.4: ΔS_M, full width at half maximum (FWHM), refrigerant capacity (*RC*) and change in applied magnetic field (ΔH) of $Ni_{55}Mn_{21-x}Ga_{24+x}$ (x = 0, 1, 2 and 3) alloys.

Alloy ID	ΔS_M ($Jkg^{-1}K^{-1}$)	FWHM (K)	*RC* (Jkg^{-1})	ΔH (T)
x = 0	-12.9	2.5	24.1	2
x = 1	-9.7	3.3	24.3	2
x = 2	-8.1	6.0	36.3	2
x = 3	+3.7	5.0	14.7	2

It has been already pointed out that refrigerant capacity (*RC*) is an important MCE parameter. *RC* estimated from the following relation [PECH01b, SHAR07a, BING09a],

$$RC = \int_{T_1}^{T_2} \Delta S_M \left(T, H\right) dT \tag{3.11}$$

Experimentally, *RC* values were obtained by integrating the area under the ΔS_M (*T*) curves over their full width at half maximum (FWHM). T_1 and T_2 are the lower and upper limits of the FWHM in ΔS_M (*T*) curves and represent the cold and hot temperatures and making them the analogues of the sink and source temperatures in the conventional refrigeration cycle. So the peak value of ΔS_M and FWHM of ΔS_M (*T*) are important characteristics of magnetic refrigerant materials. The competition between ΔS_M and FWHM gives the optimized value of *RC* which is summarized in the Table 3.4 for different alloy compositions. *RC* increases with increase in x in case of alloys exhibiting magnetostructural phase transition. It is also observed that *RC* value for pure structural transition from ferromagnetic martensite phase to ferromagnetic austenite phase is lower than the value for the single magnetostructural phase transition from a ferromagnetic martensite to a paramagnetic austenite phase.

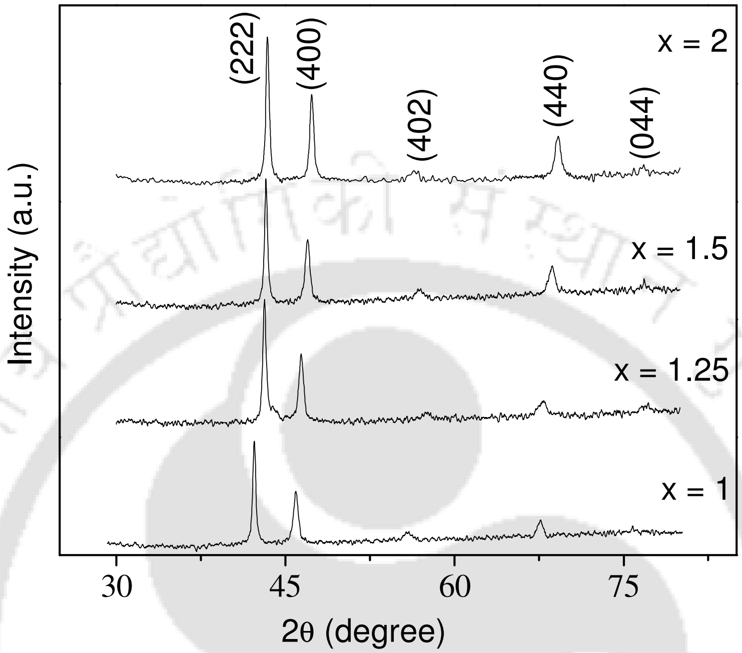

Figure 3.10: Room temperature XRD patterns of $Ni_{53.75}Mn_{21.25-x}Co_xGa_{25}$ alloys.

3.3. Bulk $Ni_{53.75}Mn_{21.25-x}Co_xGa_{25}$ (x = 1, 1.25, 1.5 and 2) alloys

3.3.1. Crystal Structures

The crystal structures of $Ni_{53.75}Mn_{21.25-x}Co_xGa_{25}$ (x = 1, 1.25, 1.5 and 2) alloys are analysed using XRD patterns (shown in Figure 3.10) recorded at room temperature. The crystallographic information obtained from these patterns is summarized in Table 3.5. The XRD patterns of all the alloys could be indexed to a non-modulated tetragonal structure without ambiguity. Lattice parameters of the alloys with x = 1, 1.25, 1.5 and 2 are $a = b =$ 0.7895 ± 0.0008 nm; c = 0.6652 ± 0.0006 nm, $a = b$ = 0.7822 ± 0.0004 nm; c = 0.6773 ±

0.0003 nm, $a = b = 0.7733 \pm 0.0002$ nm; $c = 0.6471 \pm 0.0001$ nm, and $a = b = 0.7673 \pm 0.0004$ nm; $c = 0.6505 \pm 0.0005$ nm, respectively. The slight reduction in unit cell volume with Co addition indicates that Co substitutes for Mn.

TABLE 3.5: Measured composition, *e/a* ratio crystal phase, lattice parameters and unit-cell volume of $Ni_{53.75}Mn_{21.25-x}Co_xGa_{25}$ (x = 1, 1.25, 1.5 and 2) alloys.

Alloy ID	Composition from EDS	e/a	Crystal phase	a (nm)	b (nm)	c (nm)	Unit-cell volume (nm^3)
x = 1.00	$Ni_{53.71}Mn_{20.33}Co_{0.82}Ga_{25.14}$	7.62	Martensite	0.7895	0.7895	0.6652	0.4146
x = 1.25	$Ni_{53.79}Mn_{19.96}Co_{1.14}Ga_{25.11}$	7.63	Martensite	0.7822	0.7822	0.6773	0.4144
x = 1.50	$Ni_{53.73}Mn_{19.83}Co_{1.52}Ga_{24.86}$	7.64	Martensite	0.7733	0.7733	0.6471	0.3870
x = 2.00	$Ni_{53.76}Mn_{19.31}Co_{1.83}Ga_{25.10}$	7.65	Martensite	0.7673	0.7673	0.6505	0.3830

3.3.2. Magnetic properties

Figure 3.11 shows the $M - T$ curves of $Ni_{53.75}Mn_{21.25-x}Co_xGa_{25}$ alloys recorded under an applied magnetic field of 0.1 T. For the alloys with for x = 1.25, 1.5 and 2, T_{Ms} and T_C are very close, thereby resulting in a combined magneto-structural phase transition from a ferromagnetic martensite to a paramagnetic austenite phase. But the alloy with x = 1 presents a different behaviour as seen from the figure. In this case, the ferromagnetic martensite phase first transforms to ferromagnetic austenite phase and then to paramagnetic austenite phase. These two transitions (i.e., magnetic and structural) can be clearly seen in Figure 3.11. It can also be observed that for the x = 1 alloy, T_{Ms} (= 322 K) and T_C (= 340 K) determined from the $M - T$ data obtained under an applied field of 0.1 T are 18 K apart from each other. Moreover, with increase in x (Co content), the ferromagnetic to paramagnetic phase transition at T_C shifts to higher temperatures.

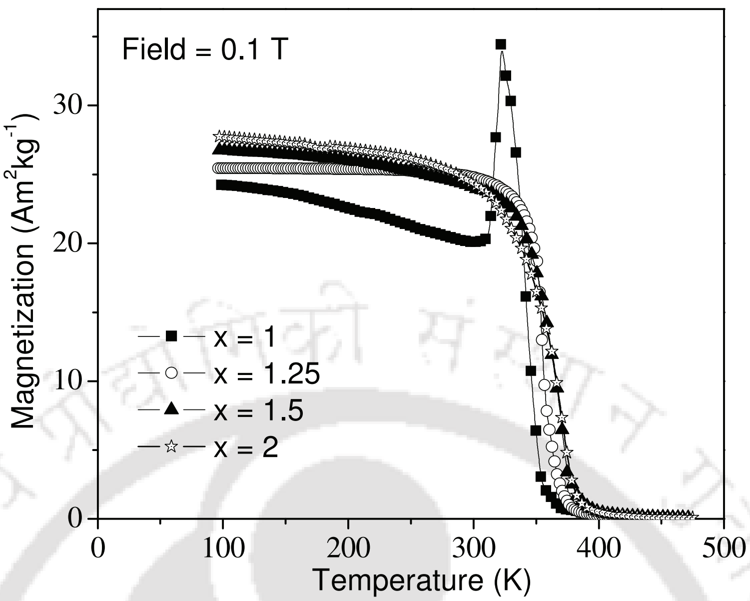

Figure 3.11: *M* – *T* curves of $Ni_{53.75}Mn_{21.25-x}Co_xGa_{25}$ alloys recorded at a magnetic field of 0.1 T.

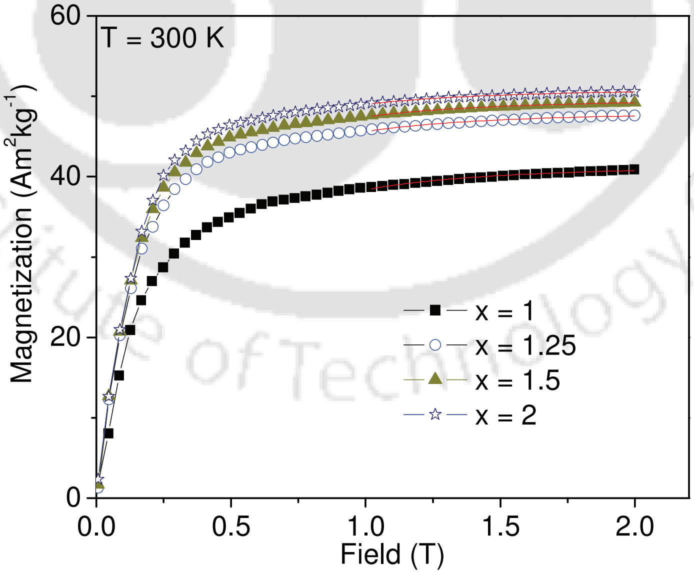

Figure 3.12: Room temperature initial magnetization curves of $Ni_{53.75}Mn_{21.25-x}Co_xGa_{25}$ alloys alloys.

In order to explore the room temperature magnetic properties of $Ni_{53.75}Mn_{21.25-x}Co_xGa_{25}$ alloys, $M - H$ curves shown in the Figure 3.12 were recorded. Initial magnetization curves at room temperature of all the alloys showed a tendency to saturate at an applied field of 2 T clearly indicating that this field strength is higher than the anisotropy field of the system. The values of M_{sat} and K_{eff} estimated from the $M - H$ data using the law of approach to saturation are summarized in Table 3.6. M_{sat} increased and K_{eff} decreased with an increase in Co content. Similar trends have been observed in M_{sat} and K_{eff} in polycrystalline Ni-Mn-Ga by Jiang *el al.* [JIAN04a].

TABLE 3.6: Saturation magnetization (M_{sat}) and magnetocrystalline anisotropy constant (K_{eff}) at room temperature and Curie temperature (T_C) of $Ni_{53.75}Mn_{21.25-x}Co_xGa_{25}$ (x = 1, 1.25, 1.5, 2) alloys.

Alloy ID	**M_{sat} (Am^2kg^{-1})**	**K_{eff} ($X\ 10^5 Jm^{-3}$)**	**T_C (K)**
x = 1.00	41.56	1.78	340
x = 1.25	48.21	1.73	355
x = 1.50	49.79	1.67	370
x = 2.00	51.07	1.59	371

3.3.3. Thermal properties

In order to understand the thermal properties of $Ni_{53.75}Mn_{21.25-x}Co_xGa_{25}$ alloys, DSC curves (shown in Figure 3.13) were recorded over a wide temperature range. It can be seen from Figure 3.13 that except for the alloy with x = 2, all others exhibit a single exothermic or endothermic peak in the cooling or heating curves, respectively. Single peak indicates a one-step martensitic phase transformation in this alloy. In the case of x = 2 alloy, the endothermic peak on heating is made up to two overlapping peak; while on cooling, only one peak is observed. This signature is reproducible during thermal cycling and is similar to other reported results on Ni-Mn-Ga system [CHER98a, DUAN07a, INGA07a, WANG07a]. Based on the reported results, it can be deduced that in forward martensitic transition, the alloy with x = 2 transforms from austenitic to non-modulated martensitic structure in one-step. But in reverse martensitic transition, the alloy undergoes an intermartensitic transition from non-modulated martensitic to modulated martensitic structure first, and then it transforms from modulated martensitic to austenitic structure. The values of the martensitic transition temperatures obtained for the different alloys from the DSC data are listed in Table 3.7.

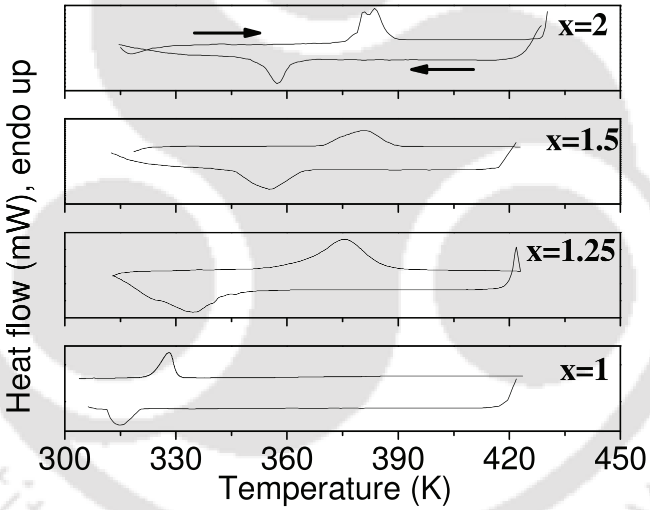

Figure 3.13: DSC curves of $Ni_{53.75}Mn_{21.25-x}Co_xGa_{25}$ alloys. Arrows indicate the forward (on cooling) and reverse (on heating) cycles.

It can be seen that all the characteristic temperatures of martensitic transitions increase with the addition of Co. The decrease in the unit cell volume and the increase of the *e*/*a* ratio with increasing Co are responsible for the increase of the martensitic characteristic temperatures with increasing Co at.% in this alloy system. The enthalpy (entropy) change, i.e., ΔE (ΔS) estimated for x = 1, 1.25, 1.5 and 2 alloys using the procedure described in the previous section are 2.9 $kJkg^{-1}$ (8.9 $Jkg^{-1}K^{-1}$), 8.9 $kJkg^{-1}$ (24.1 $Jkg^{-1}K^{-1}$), 8.1 $kJkg^{-1}$ (21.4 $Jkg^{-1}K^{-1}$) and 7.2 $kJkg^{-1}$ (18.9 $Jkg^{-1}K^{-1}$), respectively. We conclude that the value of ΔE and ΔS for the martensitic transition from ferromagnetic martensite to ferromagnetic austenite is smaller than that for the magnetostructural transition from ferromagnetic martensite to paramagnetic austenite. These arguments are also supported by other reports in the literature [INGA07a]. The same trend was also found in case of change in free energy, ΔG. ΔE, ΔS and ΔG values estimated for these alloys are also listed in Table 3.7. It can be noticed that lower ΔG at the martensitic phase transition can lead to smaller thermal hysteresis, $\Delta T_{hys} = (T_{As} + T_{Af})/2 - (T_{Ms} + T_{Mf})/2$, which means that the martensite - austenite transition can occur easily.

TABLE 3.7: Martensite start and finish temperature (T_{Ms} and T_{Mf}), martensite peak temperatures (T_{Mp}), austenite start and temperatures (T_{As} and T_{Af}), austenite peak temperature (T_{Ap}), thermal hysteresis (ΔT_{hys}), change in total enthalpy (ΔE), change in total entropy (ΔS) and change in free energy (ΔG) of of $Ni_{53.75}Mn_{21.25-x}Co_xGa_{25}$ (x = 1, 1.25, 1.5, and 2) alloys.

Alloy ID	T_{Ms} (K)	T_{Mf} (K)	T_{Mp} (K)	T_{As} (K)	T_{Af} (K)	T_{Ap} (K)	ΔT_{hys} (K)	ΔE ($kJkg^{-1}$)	ΔS ($Jkg^{-1}K^{-1}$)	ΔG (Jkg^{-1})
x = 1.00	320	310	315	322	333	328	12.5	2.9	8.9	57.9
x = 1.25	352	324	335	354	389	375	33.5	8.9	24.1	482.0
x = 1.50	366	343	355	369	391	381	25.5	8.1	21.4	278.2
x = 2.00	369	349	357	373	393	383	24.0	7.2	18.9	245.7

3.3.4. Magneto-caloric properties

In order to measure the MCE in the alloys, ΔS_M was estimated from the isothermal magnetization curves. Figure 3.14 displays the $(M - H)_T$ curves around T_{Ms} and T_C for the alloy with x = 1.25 recorded as a function of increasing magnetic field from 0 to 2 T and decreasing temperature. It is obvious from the data presented in the figure that the magnitude of magnetization and its non-linearity increase with a decrease in temperature. It may also be noted that at a certain temperature, the magnetization increases suddenly. At this temperature, ΔS_M can exhibit the maximum (peak) value.

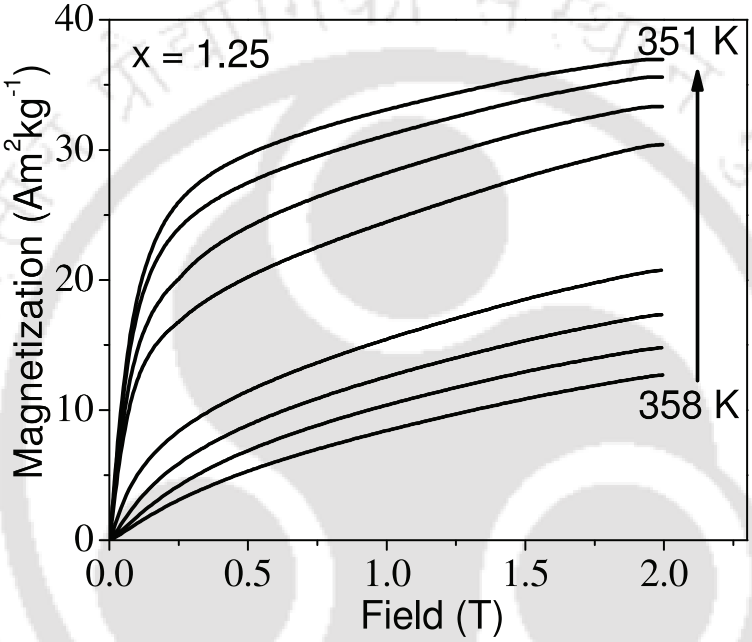

Figure 3.14: Isothermal magnetization curves obtained for $Ni_{53.75}Mn_{20}Co_{1.25}Ga_{25}$ alloy.

The temperature dependence of ΔS_M of the alloys is shown in Figure 3.15. ΔS_M is negative, due to the temperature derivative of the magnetization being negative around the magnetostructural transition. For a ΔH of 2 T, the maximum ΔS_M value for the alloy with x =1.25 is −17.7 Jkg^{-1}K^{-1} at 354.5 K. With increasing Co content, ΔS_M decreases despite the proximity of T_{Ms} to T_C. This decrease in ΔS_M is evidently related to the comparatively smaller contribution from the $(\partial M/\partial T)_H$ term in the Maxwell relation [equation (1.23)]. The alloy with x = 1.25 appears to be the optimized composition for attaining maximum ΔS_M in this series of alloys. The competition between ΔS_M and FWHM gives the optimized value of *RC*. *RC* values of the alloys are summarized in Table 3.8. Highest *RC* (27.94 Jkg^{-1}) value has been obtained in the alloy with x = 1.5.

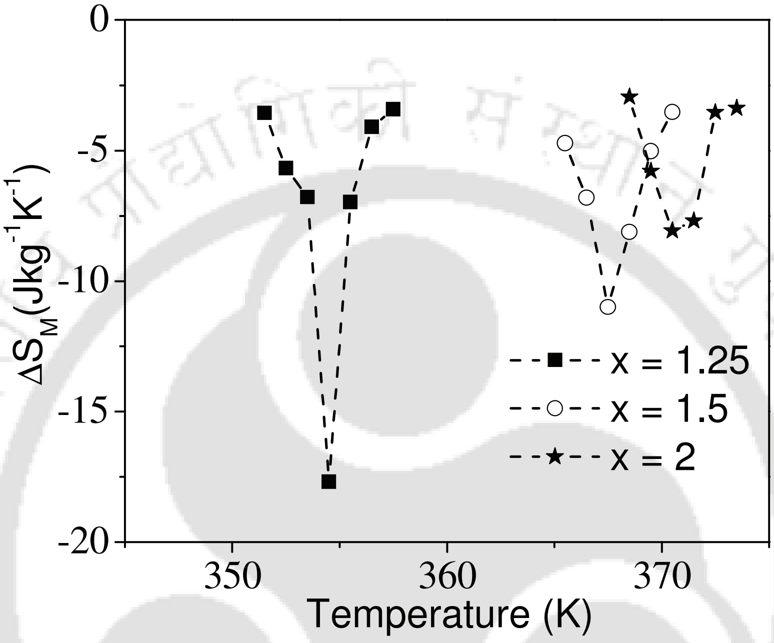

Figure 3.15: Temperature dependence of ΔS_M for a ΔH of 2 T for $Ni_{53.75}Mn_{21.25-x}Co_xGa_{25}$ alloys.

TABLE 3.8: Magnetic entropy chang (ΔS_M), full width at half maximum (FWHM) of ΔS_M (*T*) curve, refrigerant capacity (*RC*) and change in applied magnetic field (ΔH) of $Ni_{53.75}Mn_{21.25-x}Co_xGa_{25}$ alloys.

Alloy ID	ΔS_M ($Jkg^{-1}K^{-1}$)	FWHM (K)	*RC* (Jkg^{-1})	ΔH (T)
x = 1.25	-17.7	1.63	21.7	2
x = 1.50	-11.0	3.46	27.9	2
x = 2.00	-8.1	3.51	23.0	2

3.4. Summary

In this chapter, structural and magnetic properties of arc melted bulk $Ni_{55}Mn_{21-x}Ga_{24+x}$ and $Ni_{53.75}Mn_{21.25-x}Co_xGa_{25}$ alloys have been investigated. The basic interest in these specially chosen compositions is to realize the combined magneto-structural transition and thereby obtain enhanced magnetic properties, so that larger MCE could be obtained. The salient features of the present studies are as follows:

1. In $Ni_{55}Mn_{21-x}Ga_{24+x}$ alloys, samples with $x \leq 2$ exhibited non modulated tetragonal structure in martensitic phase and samples with x = 3 exhibited the typical $L2_1$ structure of the austenite phase at room temperature.
2. Increasing Ga substitution for Mn in $Ni_{55}Mn_{21-x}Ga_{24+x}$ alloys increased the unit-cell volume slightly in same (martensite) phase and finally transformed it into a new (austenite) phase.
3. XRD patterns of all the alloys in Co substituted series could be indexed to a non-modulated tetragonal structure. The slight reduction in unit cell volume with Co addition indicates that Co replaces Mn.
4. In $Ni_{55}Mn_{21-x}Ga_{24+x}$ alloys, the structural and magnetic phase transitions occur simultaneously when e/a ratio has the value of 7.6 - 7.66. On the other hand, $Ni_{53.75}Mn_{21.25-x}Co_xGa_{25}$ alloys show magneto-structural transition for lower e/a ratio range of 7.63 - 7.65.
5. Characteristic temperatures of martensitic transition decrease and increase with an increase in Ga and Co content in $Ni_{55}Mn_{21-x}Ga_{24+x}$ and $Ni_{53.75}Mn_{21.25-x}Co_xGa_{25}$ alloys, respectively.
6. Room temperature value of K_{eff} and M_{sat} for alloys with $x \leq 2$ in $Ni_{55}Mn_{21-x}Ga_{24+x}$ alloy series increased with increase in x. For further increase in x, the alloy transformed to

paramagnetic austenite phase at room temperature. M_{sat} increased and K_{eff} decreased with an increase in Co content in Co substituted Ni-Mn-Ga alloys.

7. $Ni_{53.75}Mn_{20}Co_{1.25}Ga_{25}$ alloy exhibits the highest ΔS (ΔE and ΔG) of 24.1 $Jkg^{-1}K^{-1}$ (8.9 $kJkg^{-1}$ and 482 Jkg^{-1}) accompanied by the highest ΔS_M of -17.7 $Jkg^{-1}K^{-1}$ at 354.5 K for a ΔH of 2T. At higher ΔH, ΔS_M is most dominant contributor to ΔS.
8. This work highlights the use of atomic substitution in polycrystalline alloys for achieving results comparable to those obtained from single crystal alloys.

Chapter 4

INVESTIGATIONS ON Ni-Mn-Sn ALLOYS

For a technical breakthrough in magnetic refrigeration, large MCE near room temperature for viable magnetic fields (< 2 T) is desirable in magnetic refrigerant materials which are cheaper than Gd and more ductile than Ni-Mn-Ga. In the last decade, a new class of Gd as well as Ga free FSMAs has been developed with large change of magnetization at the martensitic transition associated with inverse MCE. Inverse MCE causes the sample to cool under an adiabatically applied magnetic field for which an increase in entropy can be induced when a magnetic field is applied under isothermal condition. Ni-Mn-Sn alloys belong to this new class of FSMAs. These alloys are being intensively studied in recent years since they can exhibit room temperature martensitic transition from cubic austenite phase to orthorhombic martensite phase. Sutou *et al.* [SUTO04a] reported the phase diagram of $Ni_{50}Mn_{50-x}Sn_x$ alloys shown in Figure 4.1. In this alloy system, $Ni_{50}Mn_{37}Sn_{13}$ composition is particularly interesting since in this alloy both the magnetic transition at austenite phase as well as the martensitic structural transition occur around room temperature. The phase transition temperatures and some important physical properties including MCE of the Ni–Mn–Sn alloys can be tailored by atomic substitution of elements such as Cr, Fe, Co, Cu for Ni or Mn [FUKU09a, PASS09a, KREN07b].

Ni–Mn–Sn and its substituted alloys can undergo three phase transitions: one first-order martensitic structural transition and two second order magnetic transitions. Krenke *et al.* [KREN05b], reported that at the high temperature austenitic phase, the alloy is paramagnetic above Curie temperature, $T_{C,A}$ and ferromagnetic below $T_{C,A}$. With decreasing temperature, the martensitic structural transition takes place at T_{Ms} accompanied by a drop in magnetization due to the increase in the proportion of the martensitic phase and the weakening (and ultimate disappearance) of the ferromagnetic exchange in the austenite phase. In the martensitic phase, if the temperature is further decreased, another second order magnetic transition occurs at $T_{C,M}$, the temperature at which the martensitic phase becomes ferromagnetic. In Ni–Mn–Sn based alloys, the magnetization of martensitic phase is lower than that of the austenitic phase. So, these alloys exhibit an inverse MCE. In this chapter, a detailed study of the structural and magnetic transitions as well as the low field inverse MCE in Ni–Mn–Sn alloy influenced by the partial substitution of Fe, Co and Cu atoms for Mn or Ni is presented.

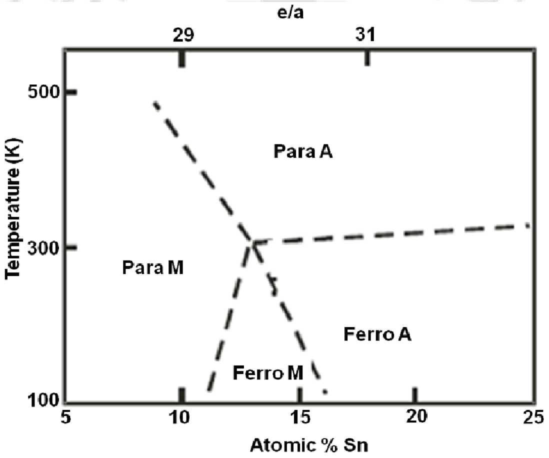

Figure 4.1: Phase diagram of $Ni_{50}Mn_{50-x}Sn_x$ alloys, where Para, Ferro, A and M denote paramagnetic state, ferromagnetic state, austenite phase and martensite phase, respectively [SUTO04a, BROW06a].

4.1. Preparation

Polycrystalline $Ni_{50}Mn_{37-x}Fe_xSn_{13}$ (x = 0, 1, and 1.25) and $Ni_{44}(Co/Cu)_2Mn_{43}Sn_{11}$ alloy ingots were prepared by arc melting method followed by homogenization at 1273 K for 24 h and quenching in ice water. The overall composition of the master alloys was measured by EDS analysis. In this case, the EDS results are the mean value of at least three independent observations. The final alloy composition was nearly the same as the nominal (starting) composition of the respective alloys (Table 4.1).

TABLE 4.1: The overall measured composition of $Ni_{50}Mn_{37-x}Fe_xSn_{13}$ (x= 0, 1, and 1.25) and $Ni_{44}(Co/Cu)_2Mn_{43}Sn_{11}$ alloys.

Nominal Composition	Measured Composition
$Ni_{50}Mn_{37}Sn_{13}$	$Ni_{49.96}Mn_{37.05}Sn_{12.99}$
$Ni_{50}Mn_{36}Fe_1Sn_{13}$	$Ni_{49.89}Mn_{36.13}Fe_{0.96}Sn_{13.02}$
$Ni_{50}Mn_{35.75}Fe_{1.25}Sn_{13}$	$Ni_{50.24}Mn_{35.87}Fe_{1.22}Sn_{12.67}$
$Ni_{46}Mn_{43}Sn_{11}$	$Ni_{45.95}Mn_{43.12}Sn_{10.93}$
$Ni_{44}Mn_{43}Co_2Sn_{11}$	$Ni_{43.50}Mn_{43.33}Co_{2.21}Sn_{10.96}$
$Ni_{44}Mn_{43}Cu_2Sn_{11}$	$Ni_{43.88}Mn_{42.95}Cu_{2.14}Sn_{11.03}$

4.2. Bulk $Ni_{50}Mn_{37-x}Fe_xSn_{13}$ (x= 0, 1, and 1.25) alloys

4.2.1. Crystal structures

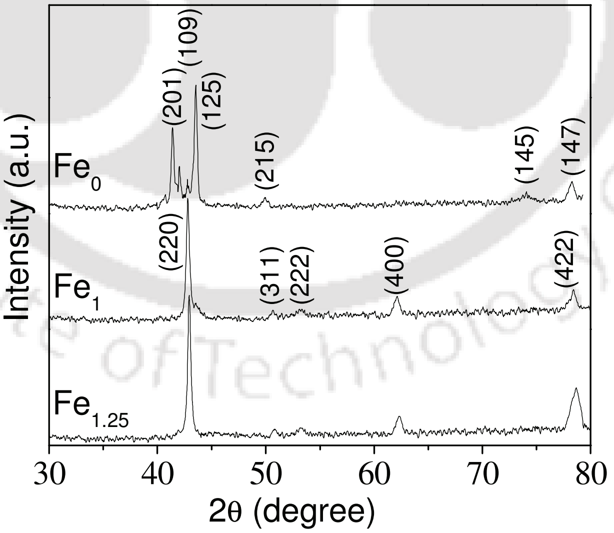

Figure 4.2: X-ray diffraction patterns of $Ni_{50}Mn_{37-x}Fe_xSn_{13}$ (x= 0, 1, and 1.25) alloys recorded at room temperature.

Room temperature powder XRD patterns of $Ni_{50}Mn_{37-x}Fe_xSn_{13}$ alloys are shown in Figure 4.2. The alloys are designated as Fe_x where x refers to the nominal Fe at.% in the alloy. The parent alloy designated as Fe_0 exhibited orthorhombic structure corresponding to the martensite phase, but, alloys with Fe_1 and $Fe_{1.25}$ exhibited cubic $L2_1$ structure corresponding to the austenite phase. Room temperature martensite phase with orthorhombic structure for $Ni_{50}Mn_{37}Sn_{13}$ alloy is already established as seen from reports available in the literature [KREN05b, KHAN08a]. The lattice parameters of Fe_0 were determined to be $a = 0.4332 \pm 0.0004$ nm, $b = 0.5603 \pm 0.0005$ nm, and $c = 2.1813 \pm 0.0004$ nm, whereas those of Fe_1 and $Fe_{1.25}$ are $a = 0.5971 \pm 0.0002$ and $a = 0.5954 \pm 0.0001$ nm, respectively. By replacing Mn with Fe, which has a smaller atomic radius than Mn, the lattice parameter and hence the unit cell volume of the cubic $L2_1$ structure becomes smaller, and the Bragg peak positions shift to larger angles. Such shift in peak position to higher angels with Fe addition has also been observed in $Ni_{45}Mn_{44}Sn_{11}$ alloy by Yan *et al* [YANJ10a].

TABLE 4.2: Crystal phase, lattice parameters and unit-cell volume of $Ni_{50}Mn_{37-x}Fe_xSn_{13}$ (x= 0, 1, and 1.25) alloys.

Alloy ID	**Crystal phase**	***a* (nm)**	***b* (nm)**	***c* (nm)**	**Unit-cell volume (nm^3)**
Fe_0	Martensite	0.4332	0.5603	2.1813	0.5294
Fe_1	Austenite	0.5971	0.5971	0.5971	0.2129
$Fe_{1.25}$	Austenite	0.5954	0.5954	0.5954	0.2111

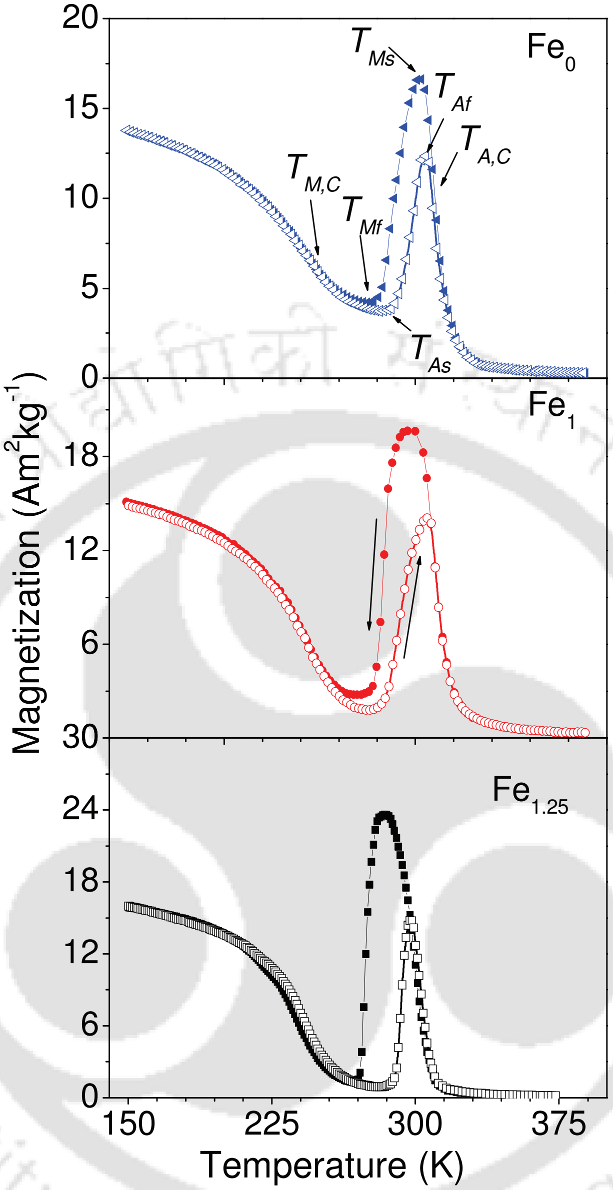

Figure 4.3: $M - T$ curves of $Ni_{50}Mn_{37-x}Fe_xSn_{13}$ alloys measured at an applied field of 0.1 T. Filled and open symbols represent data recorded during field cooling and field heating cycles, respectively.

4.2.2. Magnetic properties

$M - T$ curves obtained for $Ni_{50}Mn_{37-x}Fe_xSn_{13}$ (x= 0, 1, and 1.25) alloys during field cooling (FC) and field heating (FH) processes in a magnetic field of 0.1 T are presented in Figure 4.3.

Curie temperature of martensite phase ($T_{C,M}$), martensite start temperature (T_{Ms}), martensite finish temperature (T_{Mf}), austenite start temperature (T_{As}), austenite finish temperature (T_{Af}) and the Curie temperature of the austenite phase ($T_{C,A}$) are marked on the cooling and heating curves. It can be observed that upon cooling, all the alloys which were at first in the paramagnetic austenite state, undergo a magnetic transition from paramagnetic to ferromagnetic state around $T_{C,A}$ and gain a large magnetization. Ferromagnetism persists until they are cooled down to T_{Ms} after which the magnetization decreases sharply at the martensitic transition. Subsequently, the paramagnetic martensitic phase transforms to ferromagnetic phase at $T_{C,M}$ as the temperature is further decreased.

While heating from the ferromagnetic martensite phase, magnetization decreases through $T_{C,M}$ until it begins to transform into austenite phase at T_{As} and then increases to a maximum value at T_{Af}. On further increasing the temperature, magnetization again decreases to zero through $T_{C,A}$. The data reveal that all the alloys exhibit martensitic transition between these two Curie temperatures (T_C). In these alloys, the magnetization of ferromagnetic austenite phase is higher than that of the ferromagnetic martensite phase. A careful observation of the data in the temperature range $T_{Mf} \leq T \leq T_{Af}$ confirms that the field cooled (FC) and field heated (FH) data do not follow the same path. Thus, a thermal hysteresis, which is the signature of the structural (martensite $\leftrightarrow$ austenite) first-order phase transition, is observed between the FC and FH curves for all the alloys in the temperature range of $T_{Mf} \leq T \leq T_{Af}$. The area under the hysteresis (ΔA) in the $M-T$ curves increases with increasing Fe content. The information extracted from the $M-T$ data are listed in Table 4.3. T_{Ms} ($T_{C,A}$) of Fe_0, Fe_1, and $Fe_{1.25}$ alloys are 302 K (309 K), 291 K (310 K), and 279 K (304 K), respectively. Fe substitution for Mn in these alloys results in a decrease in T_{Ms}. But it can be seen that T_C increases in Fe_1 alloy, but decreases for $Fe_{1.25}$ alloy. However, T_C has been reported to increase with Fe substitution for Mn in $Ni_2Mn_{1.48-x}Fe_xSn_{0.52}$ [FUKU09a] and $Ni_{45}Mn_{44-x}Fe_xSn_{11}$ [YANJ10a]. The transition temperatures of $Ni_{50}Mn_{50-y}Sn_y$ alloy have been found to be sensitive to Sn content with $T_{Ms} > T_{C,A}$ or $T_{Ms} < T_{C,A}$ depending on Sn being less than or more than 13 at.%, respectively [SUTO04a]. In the present studies, EDS analysis show that the measured composition of the $Fe_{1.25}$ alloy is actually $Ni_{50.24}Mn_{35.87}Fe_{1.22}Sn_{12.67}$, which helps us in understanding the reason for its low T_C. It can be also noted from Figure 4.3 that the magnitude of the change in magnetization (ΔM) or $\partial M/\partial T$ at the austenite ↔ martensite transition and the magnetization values at the ferromagnetic state increase with increasing Fe content. This may be attributed to the increased ferromagnetic interaction as the amount of the ferromagnetic element (Fe) is increased. The large $\partial M/\partial T$ is expected to induce large value of MCE as suggested by equation (1.23).

TABLE 4.3: Martensite start temperature (T_{Ms}), Curie temperature of austenite phase ($T_{C,A}$), area under the thermal hysteresis (ΔA), temperature derivative of magnetization ($\partial M/\partial T$) around martensitic transition temperature T_M obtained at 0.1 T field for $Ni_{50}Mn_{37-x}Fe_xSn_{13}$ alloys.

Alloy ID	**T_{Ms} (K)**	**$T_{C,A}$ (K)**	**ΔA ($Am^2kg^{-1}K$)**	**$\partial M/\partial T$ around T_M ($Am^2kg^{-1}K^{-1}$)**
Fe_0	302	309	163.7	0.8
Fe_1	291	310	256.4	2.1
$Fe_{1.25}$	279	304	370.7	4.1

4.2.3. Thermal properties

Calorimetric measurements performed on $Ni_{50}Mn_{37-x}Fe_xSn_{13}$ alloys are graphically presented in Figure 4.4. As can be observed from the DSC curves, all the alloys exhibit a single exothermic and single endothermic peak, which indicate a one-step martensitic phase transformation in these alloys. For the Fe_0 and Fe_1 alloys both the exothermic and endothermic martensitic transition peaks are not sharp but occurs over a broad temperature range. The broad nature of the martensitic peak can be attributed to the incomplete phase transition which can also be noticed from Figure 4.3 where evidence for the presence of some residual ferromagnetic austenite phase in the intermediate temperature range of $T_{C,M} < T < T_{Mf}$. It can be noted that due to less residual austenite phase present in $Fe_{1.25}$ alloy in the temperature range of $T_{C,M} < T < T_{Mf}$ a sharper transition peak is observed. The increase of Fe at.% not only narrows down the peak temperature range but also decreases the transition temperature. All the martensitic characteristic temperatures estimated from DSC data are listed in Table 4.4. Comparison of DSC and $M - T$ data (Figure 4.3) reveals that application of magnetic field induces a shift in the structural transition to lower temperatures. Such field induced martensitic transformation has been observed in other FSMAs [SHAR10a].

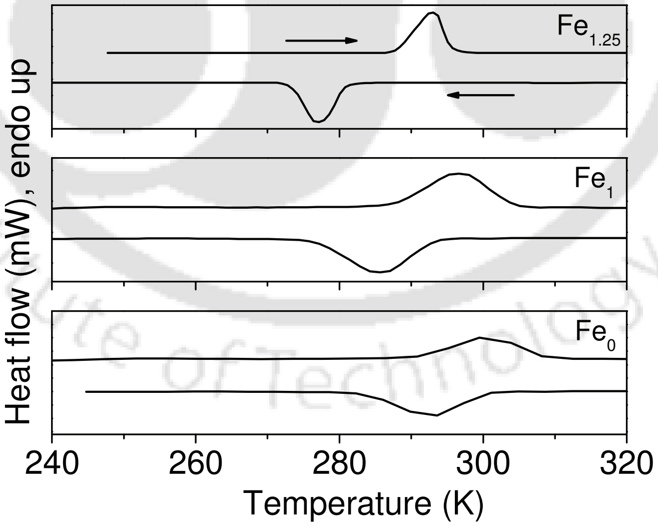

Figure 4.4: DSC curves of $Ni_{50}Mn_{37-x}Fe_xSn_{13}$ alloys.

Since martensitic transition is a first-order phase transition, a thermal hysteresis, ΔT_{hys} is observed during this phase transition. ΔT_{hys} is calculated from characteristic temperatures of martensitic phase transition (T_{Ms}, T_{Mf}, T_{As}, T_{Af}) which are determined from the DSC data. The values of ΔT_{hys} of Fe_0, Fe_1, and $Fe_{1.25}$ alloys are 7.5 K, 12.0 K and 15.0 K respectively. The change in Gibbs free energy (ΔG), enthalpy (ΔE) and entropy (ΔS) associated with the martensitic transition were also estimated using the equation (3.5), (3.6) and (3.7). The values of ΔG (ΔE and ΔS) are 48 Jkg^{-1} (4.9 $kJkg^{-1}$ and 16.0 $Jkg^{-1}K^{-1}$), 91.9 Jkg^{-1} (5.0 $kJkg^{-1}$ and 16.7 $Jkg^{-1}K^{-1}$) and 143.2 Jkg^{-1} (5.2 $kJkg^{-1}$and 17.9 $Jkg^{-1}K^{-1}$) for Fe_0, Fe_1, and $Fe_{1.25}$ alloys respectively. It can be found that the values of ΔG, ΔE and ΔS increase with increase of Fe at.%. The increase in ΔS upon Fe substitution is mainly attributed to the magnetic contribution ΔS_M, which is the source of MCE.

TABLE 4.4: Martensite start temperature (T_{Ms}), martensite finish temperatures (T_{Mf}), austenite start temperatures (T_{As}), austenite finish temperature (T_{Af}), thermal hysteresis (ΔT_{hys}), change in total enthalpy (ΔE), change in total entropy (ΔS) and change in free energy (ΔG) of $Ni_{50}Mn_{37-x}Fe_xSn_{13}$ alloys estimated from DSC data.

Alloy	T_{Ms} **(K)**	T_{Mf} **(K)**	T_{As} **(K)**	T_{Af} **(K)**	ΔT_{hys} **(K)**	ΔE **($kJkg^{-1}$)**	ΔS **($Jkg^{-1}K^{-1}$)**	ΔG **(Jkg^{-1})**
Fe_0	303	280	290	308	7.5	4.9	16.0	48.0
Fe_1	294	276	288	306	12.0	5.0	16.7	91.9
$Fe_{1.25}$	283	272	287	298	15.0	5.2	17.9	143.2

4.2.4. Magneto-caloric Effect

In order to evaluate the MCE parameters, isothermal magnetization [$(M - H)_T$] curves were obtained close to T_{Ms} in a sequence of decreasing temperature and increasing magnetic field from 0 to 1.8 T. Figure 4.5 presents the $(M - H)_T$ curves of $Ni_{50}Mn_{37-x}Fe_xSn_{13}$ alloys. It is obvious from the figure that all the alloys are in ferromagnetic state at T_{Ms}. However, the magnitude of magnetization decreases with decrease in temperature.

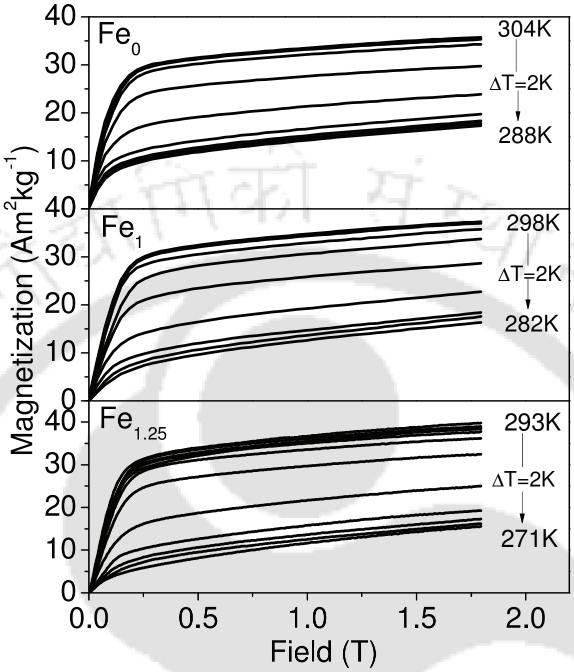

Figure 4.5: Isothermal magnetization curves obtained for $Ni_{50}Mn_{37-x}Fe_xSn_{13}$ alloys for a magnetic field range of 0 to 1.8 T.

It can also be seen from Figure 4.5 that a large jump in magnetization occurs between two consecutive isotherms in the temperature range $T_{Ms} \geq T \geq T_{Mf}$, e.g., between 279 and 281 K for $Fe_{1.25}$. The temperature dependence of ΔS_M calculated from $(M-H)_T$ curves for a ΔH of 1.8 T is presented in Figure 4.6. The maximum values of ΔS_M and *RC* for ΔH of 1.8 T are listed in Table 4.5. The peak ΔS_M (*RC*) value corresponding to the $Ni_{50}Mn_{37-x}Fe_xSn_{13}$ alloys designated as Fe_0, Fe_1, and $Fe_{1.25}$ are 5.4 $Jkg^{-1}K^{-1}$ (25.4 Jkg^{-1}), 5.6 $Jkg^{-1}K^{-1}$ (25.5 Jkg^{-1}), and 6.9 $Jkg^{-1}K^{-1}$ (25.7 Jkg^{-1}), respectively for a ΔH of 1.8 T. Both peak ΔS_M and *RC* increase with an increase in Fe substitution. It is found from Figure 4.3 that a large MCE can be expected from the abrupt drop in magnetization since $\partial M/\partial T$ would be large between T_{Ms} and T_{Mf}. The increase in MCE an increase in Fe content may also be related to Δ*A* of the hysteresis in the $M - T$ curves around T_M. The $\partial M/\partial T$ values are 0.8, 2.1 and 4.1 $Am^2kg^{-1}K^{-1}$ and Δ*A* are 163.7, 256.4 and 370.7 $Am^2kg^{-1}K$ for the alloys with Fe_0, Fe_1, and $Fe_{1.25}$, respectively. These results could be compared with reported ΔS_M values obtained for a Δ*H* of 2 T field change in $Ni_{49}Mn_{37}Fe_1Sn_{13}$ (6 $Jkg^{-1}K^{-1}$ at 241 K), $Ni_{47}Mn_{37}Fe_3Sn_{13}$ (10.2 $Jkg^{-1}K^{-1}$ at 177 K) [KREN07b] and $Ni_{50}Mn_{29}Fe_7Sn_{14}$ (4.8 $Jkg^{-1}K^{-1}$ at 158 K) [PASS09a] alloys.

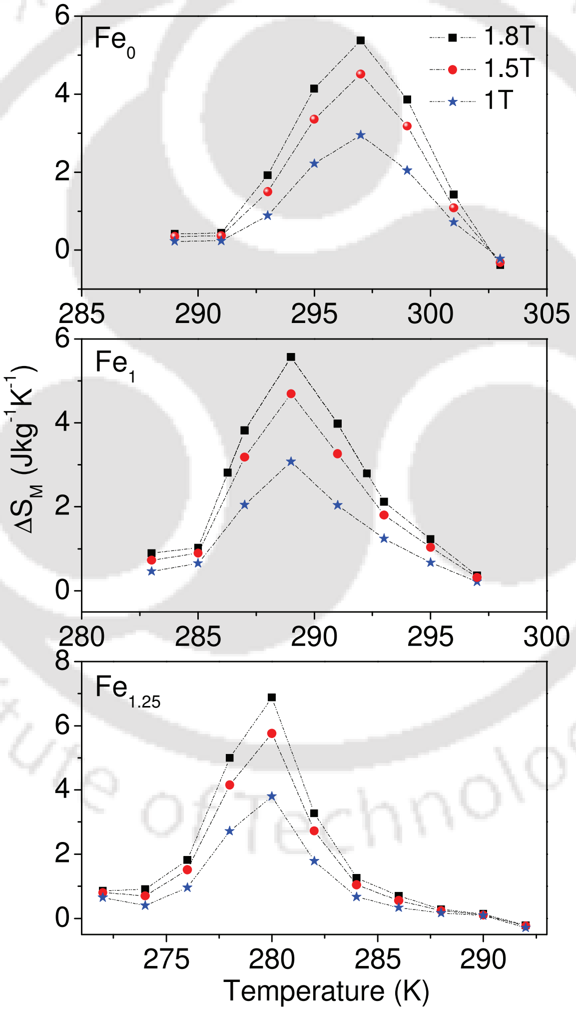

Figure 4.6: Temperature dependence of ΔS_M calculated from $(M - H)_T$ curves for different Δ*H* values of $Ni_{50}Mn_{37-x}Fe_xSn_{13}$ alloys.

TABLE 4.5: Change in magnetic entropy (ΔS_M), temperature (T_{max}) at which ΔS_M is maximum, refrigerant capacity (*RC*), and change in applied magnetic field (ΔH).

Alloy ID	**ΔS_M (Jkg^{-1}K^{-1})**	**T_{max} (K)**	***RC* (Jkg^{-1})**	**ΔH (T)**
Fe_0	5.4	297	25.4	1.8
Fe_1	5.6	289	25.5	1.8
$Fe_{1.25}$	6.9	280	25.7	1.8

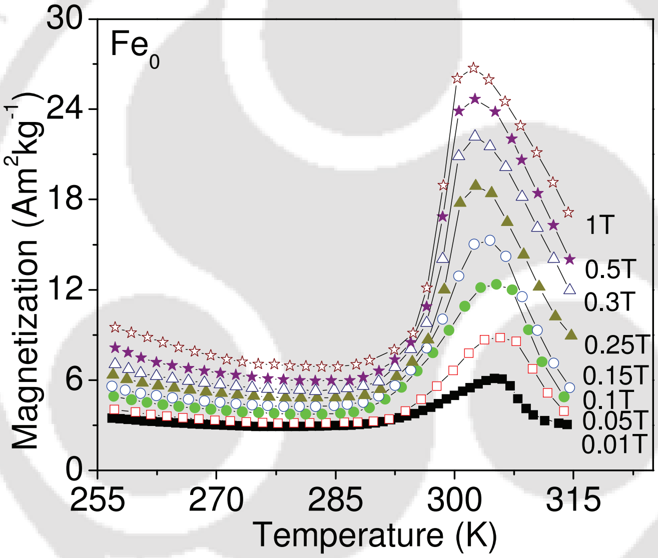

Figure 4.7: Temperature dependence of magnetization of Fe_0 alloy at various fields values.

The value of ΔS_M in Fe_0 alloy has been cross checked by re-estimating ΔS_M from $M - T$ data. For this, isothermal $\partial M/\partial T$ verses field curves were extracted from different isofield $M - T$ data. Numerical integration of isothermal $\partial M/\partial T$ verses field curve from zero to H field enables the estimate of isothermal ΔS_M. $M - T$ data in various applied fields up to 1 T close to the martensitic transition are shown in Figure 4.7. These $M - T$ plots were obtained under FH condition starting each time from a temperature well inside the martensite phase.

With the increase in field, the martensite transition temperature clearly shifts towards lower temperatures. Such behavior, attributed to the field induced martensite transition, has also been observed in other FSMAs [SHAR10a]. Using these $M - T$ plots, the estimated peak value of ΔS_M for 1 T field change is 2.7 Jkg^{-1}K^{-1} as depicted in Figure 4.8. This value of ΔS_M is close to that (2.9 Jkg^{-1}K^{-1}) estimated from the isothermal $M - H$ curves with the same applied field, which shows that both procedures yield the same ΔS_M value.

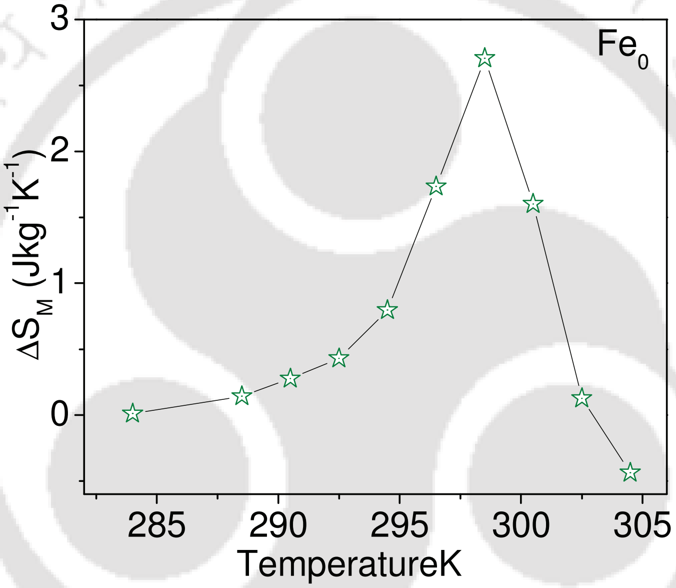

Figure 4.8: Temperature dependence of ΔS_M of Fe_0 alloy estimated from $M - T$ curves for ΔH = 1 T.

4.3. Bulk $Ni_{44}(Co/Cu)_2Mn_{43}Sn_{11}$ alloys

4.3.1. Crystal structures

XRD patterns of $Ni_{44}(Co/Cu)_2Mn_{43}Sn_{11}$ alloys recorded at room temperature are displayed in Figure 4.9. The structural data extracted from these XRD patterns are summarized in Table 4.6. All the diffraction peaks in the XRD patterns of all the alloys could be indexed to cubic

*L*2$_1$ structure corresponding to the austenite phase. Lattice parameters of $Ni_{46}Mn_{43}Sn_{11}$, $Ni_{44}Mn_{43}Co_2Sn_{11}$ and $Ni_{44}Mn_{43}Cu_2Sn_{11}$ alloys are 0.5929 ± 0002 nm, 0.5978 ± 0003 nm, and 0.5922 ± 0001 nm, respectively. The slight increase (decrease) in lattice parameter and unit cell volume with Co (Cu) addition may be attributed to small differences in the atomic radii of Co and Cu with respect to that of Ni.

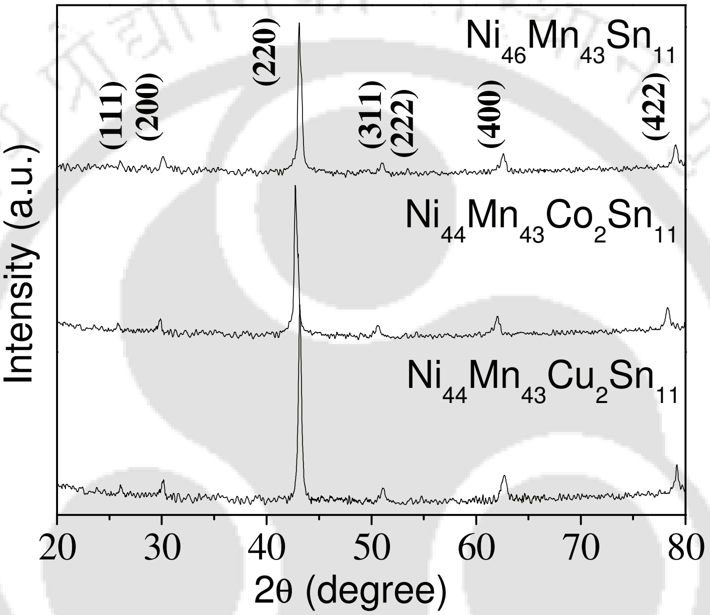

Figure 4.9: Room temperature XRD patterns for $Ni_{46}Mn_{43}Sn_{11}$, $Ni_{44}Mn_{43}Co_2Sn_{11}$ and $Ni_{44}Mn_{43}Cu_2Sn_{11}$ alloys.

TABLE 4.6: Crystal phase, lattice parameters and unit-cell volume of $Ni_{44}(Co/Cu)_2Mn_{43}Sn_{11}$ alloys.

Alloy	Crystal phase	*a* (nm)	*b* (nm)	*c* (nm)	Unit-cell volume (nm^3)
$Ni_{46}Mn_{43}Sn_{11}$	Austenite	0.5929	0.5929	0.5929	0.2084
$Ni_{44}Mn_{43}Co_2Sn_{11}$	Austenite	0.5978	0.5978	0.5978	0.2136
$Ni_{44}Mn_{43}Cu_2Sn_{11}$	Austenite	0.5922	0.5922	0.5922	0.2077

4.3.2. Magnetic properties

Figure 4.10 shows the temperature dependence of magnetization of $Ni_{46}Mn_{43}Sn_{11}$, $Ni_{44}Mn_{43}Co_2Sn_{11}$and $Ni_{44}Mn_{43}Cu_2Sn_{11}$ alloys measured during cooling and heating cycles in a magnetic field of 0.1 T. When the temperature is lowered, the sample orders ferromagnetically in the austenitic state below the $T_{C,A}$ until it begins to undergo martensitic transformation at T_{Ms}. T_{Ms} ($T_{C,A}$) of $Ni_{46}Mn_{43}Sn_{11}$, $Ni_{44}Mn_{43}Co_2Sn_{11}$and $Ni_{44}Mn_{43}Cu_2Sn_{11}$ alloys are 291 K (314 K), 191 K (327 K), and 270 K (298 K), respectively. With the substitution of Co for Ni in $Ni_{46}Mn_{43}Sn_{11}$ alloy, T_{Ms} decreases and $T_{C,A}$ shifts to higher temperatures. On the other hand, Cu substitution for Ni in $Ni_{46}Mn_{43}Sn_{11}$ decreases both T_{Ms} and $T_{C,A}$. A hysteresis (ΔT_{hys}), which is attributed to a first-order structural transition, is present between the FC and FH curves for all the alloys. The hysteresis area becomes progressively wider upon Co and Cu substitution. The magnetization difference (ΔM) across the structural transition is enhanced because the magnetization in austenitic and martensitic phase is significantly different. Upon Co substitution, $T_{C,A}$ shifts from 314 K to 327 K while ΔM (under 0.1 T) increases from 4.6 Am^2kg^{-1} to 7.4 Am^2kg^{-1}. T_{Ms} and ΔT_{hys} change for Co substituted sample from 291 K to 191 K and from 13 K to 22 K, respectively. But, for the Cu substituted alloy, $T_{C,A}$, ΔM, T_{Ms} and ΔT_{hys} are 298 K, 8.6 Am^2kg^{-1}, 270 K and 15 K, respectively. Introduction of Cu in the parent alloy can affect the antiferromagnetic exchange, flip the spin and lead to an enhanced magnetization and a larger ΔM. A larger ΔM produces a larger Zeeman energy $\mu_0 \Delta M.H$ and hence a field-induced structural transformation in a wider temperature range can be expected. Based on this consideration, a detailed study of MCE or magnetic refrigeration properties of $Ni_{46}Mn_{43}Sn_{11}$, $Ni_{44}Mn_{43}Co_2Sn_{11}$and $Ni_{44}Mn_{43}Cu_2Sn_{11}$ alloys was carried out.

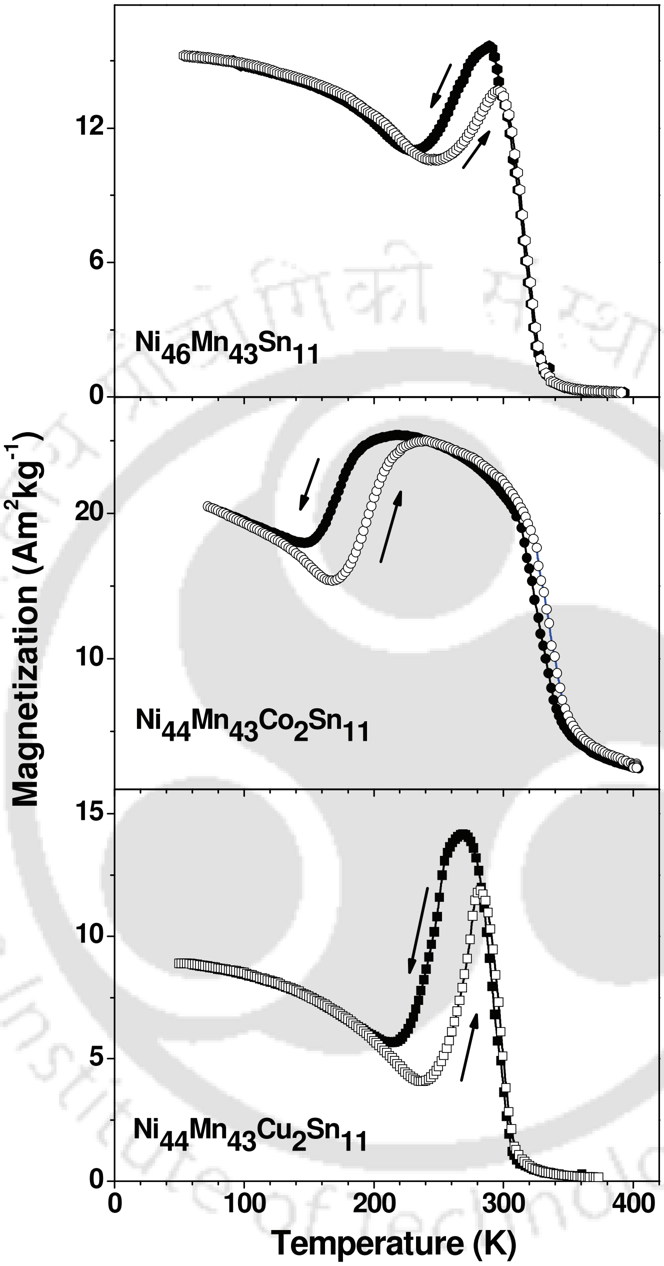

Figure 4.10: *M – T* curves recorded during cooling and heating cycles at a magnetic field of 0.1 T for $Ni_{46}Mn_{43}Sn_{11}$, $Ni_{44}Mn_{43}Co_2Sn_{11}$ and $Ni_{44}Mn_{43}Cu_2Sn_{11}$ alloys.

4.3.3. Thermal properties

DSC curves corresponding to $Ni_{46}Mn_{43}Sn_{11}$, $Ni_{44}Mn_{43}Co_2Sn_{11}$ and $Ni_{44}Mn_{43}Cu_2Sn_{11}$ alloys are shown in Figure 4.11. The direct and reverse martensitic transitions are accompanied by well-defined exothermic and endothermic peaks. From these DSC data, it is easy to determine characteristic temperatures of the direct (T_{Ms} and T_{Mf}) and the reverse (T_{As} and T_{Af}) martensitic transition. The values of the martensitic characteristic temperatures obtained for different alloy compositions from the DSC data are listed in Table 4.7. Comparison of DSC and $M-T$ data (Figure 4.10) reveals that application of magnetic field induces a shift in the structural transition to lower temperatures. Such field induced martensitic transformation has been observed in case of $Ni_{50}Mn_{37-x}Fe_xSn_{13}$ alloys.

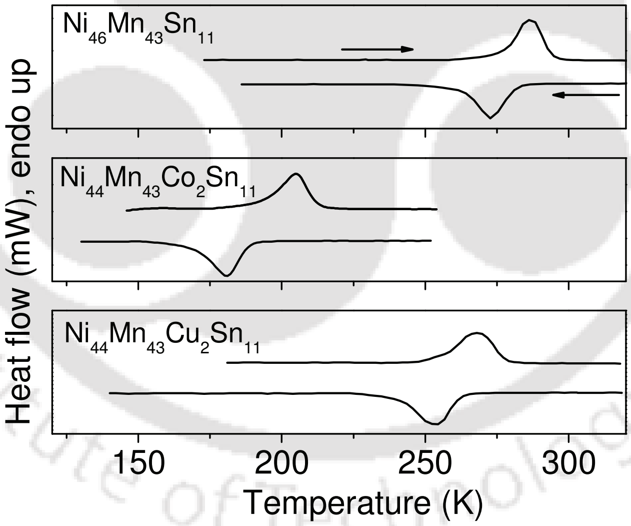

Figure 4.11: DSC curves of $Ni_{44}(Co/Cu)_2Mn_{43}Sn_{11}$ alloys.

Using the DSC data, the change in Gibbs free energy (ΔG), enthalpy (ΔE) and entropy (ΔS) have been estimated for these alloys. The values of ΔG (ΔE and ΔS) are 163.8 Jkg^{-1} (6.9 $kJkg^{-1}$ and 23.4 $Jkg^{-1}K^{-1}$), 308.2 Jkg^{-1} (5.5 $kJkg^{-1}$ and 26.8 $Jkg^{-1}K^{-1}$) and 166.2 Jkg^{-1} (7.7 $kJkg^{-}$

^{1}and 27.7 Jkg^{-1}K^{-1}) for $Ni_{46}Mn_{43}Sn_{11}$, $Ni_{44}Mn_{43}Co_{2}Sn_{11}$ and $Ni_{44}Mn_{43}Cu_{2}Sn_{11}$ alloys, respectively. It can be seen that introducing either Co or Cu in the parent alloy leads to an increase in the ΔS and ΔG around the martensitic transition. It can also be noticed that lower ΔG at the martensitic phase transition result in smaller thermal hysteresis, ΔT_{hys} which are 13 K, 22 K and 15 K for $Ni_{46}Mn_{43}Sn_{11}$, $Ni_{44}Mn_{43}Co_{2}Sn_{11}$ and $Ni_{44}Mn_{43}Cu_{2}Sn_{11}$ alloys, respectively.

TABLE 4.7: Martensite start temperature (T_{Ms}), martensite finish temperatures (T_{Mf}), austenite start temperatures (T_{As}), austenite finish temperature (T_{Af}), thermal hysteresis (ΔT_{hys}), change in total enthalpy (ΔE), change in total entropy (ΔS) and change in free energy (ΔG) of $Ni_{44}(Co/Cu)_{2}Mn_{43}Sn_{11}$ alloys estimated from DSC data.

Alloy	T_{Ms} (K)	T_{Mf} (K)	T_{As} (K)	T_{Af} (K)	ΔT_{hys} (K)	ΔE (kJkg^{-1})	ΔS (Jkg^{-1}K^{-1})	ΔG (Jkg^{-1})
$Ni_{46}Mn_{43}Sn_{11}$	292	240	259	299	13.0	6.9	23.4	163.8
$Ni_{44}Mn_{43}Co_{2}Sn_{11}$	194	157	178	217	22.0	5.5	26.8	308.2
$Ni_{44}Mn_{43}Cu_{2}Sn_{11}$	273	225	245	283	15.0	7.7	27.7	166.2

4.3.4. Magneto-caloric properties

MCE has been estimated numerically from $M - H$ isotherms using the Maxwell's relation [equation (1.23)]. Figure 4.12 shows the isothermal initial magnetization curves obtained around T_{Ms} for these alloys. The magnetization curves were recorded as functions of increasing magnetic field from 0 to 1.8 T and decreasing temperature. It can be inferred from the figure that all the alloys are in ferromagnetic state at T_{Ms} and the magnitude of magnetization decreases with decrease in temperature. It is also seen from the $M - H$ isotherms that at a certain temperature a large jump in magnetization occurs at which point a correspondingly large ΔS_M can be expected. The temperature dependence of ΔS_M in the three samples is depicted in Figure 4.13. ΔS_M is positive in all the cases, due to the temperature derivative of the magnetization being positive around $T_{Ms.}$ As mentioned earlier, positive ΔS_M implies that the sample cools down when the external magnetic field is applied adiabatically. The maximum value of ΔS_M and the width of the ΔS_M are the characteristic features of the MCE. The enhancement in ΔS_M upon Co/Cu substitution is evident from Table 4.8. Peak ΔS_M value obtained for the parent, Co substituted and Cu substituted alloys are 7.9, 11.3 and 18.8 $Jkg^{-1}K^{-1}$, respectively. Figure 4.14 shows a linear variation of the peak ΔS_M value in the field range of 0.5 T to 1.8 T for the three alloys. It can also be noticed from the slopes of the three linear fits, the substituted alloys exhibit larger variation in ΔS_M per unit ΔH change. The change in peak ΔS_M for unit change in field has been estimated to be 4.6, 6.9 and 11.4 $Jkg^{-1}K^{-1}T^{-1}$ for $Ni_{46}Mn_{43}Sn_{11}$, $Ni_{44}Mn_{43}Co_2Sn_{11}$ and $Ni_{44}Mn_{43}Cu_2Sn_{11}$, respectively. The temperature (T_{max}) at which the peak ΔS_M is observed for $Ni_{46}Mn_{43}Sn_{11}$, $Ni_{44}Mn_{43}Co_2Sn_{11}$ and $Ni_{44}Mn_{43}Cu_2Sn_{11}$ alloys are 288 K, 190 K and 270.5 K, respectively. These results indicate that high ΔS_M can be achieved in Ni-Mn-Sn alloys near room temperature by appropriate substitution of Cu for Ni for relatively low ΔH. *RC* values corresponding to $\Delta S_M(T)$ curves of $Ni_{46}Mn_{43}Sn_{11}$, $Ni_{44}Mn_{43}Co_2Sn_{11}$ and $Ni_{44}Mn_{43}Cu_2Sn_{11}$ alloys are 30.2 Jkg^{-1}, 30.3 Jkg^{-1} and 24.1 Jkg^{-1}, respectively. The highest *RC* (30.3 Jkg^{-1}) was obtained for $Ni_{44}Mn_{43}Co_2Sn_{11}$ alloy which shows this alloy would give the best performance as a magnetic refrigerant amongs the three alloys.

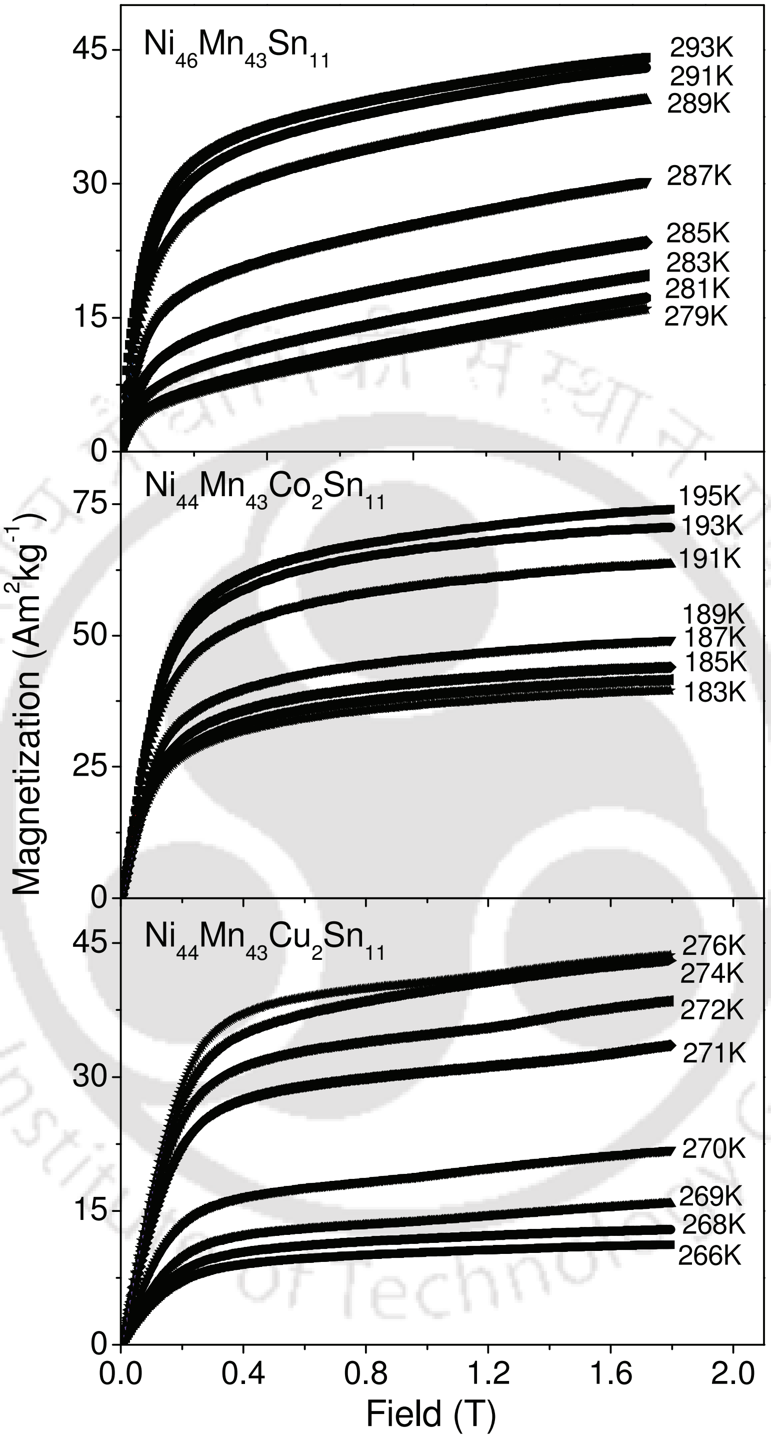

Figure 4.12: Isothermal initial magnetization curves obtained for $Ni_{46}Mn_{43}Sn_{11}$, $Ni_{44}Mn_{43}Co_2Sn_{11}$ and $Ni_{44}Mn_{43}Cu_2Sn_{11}$ alloys.

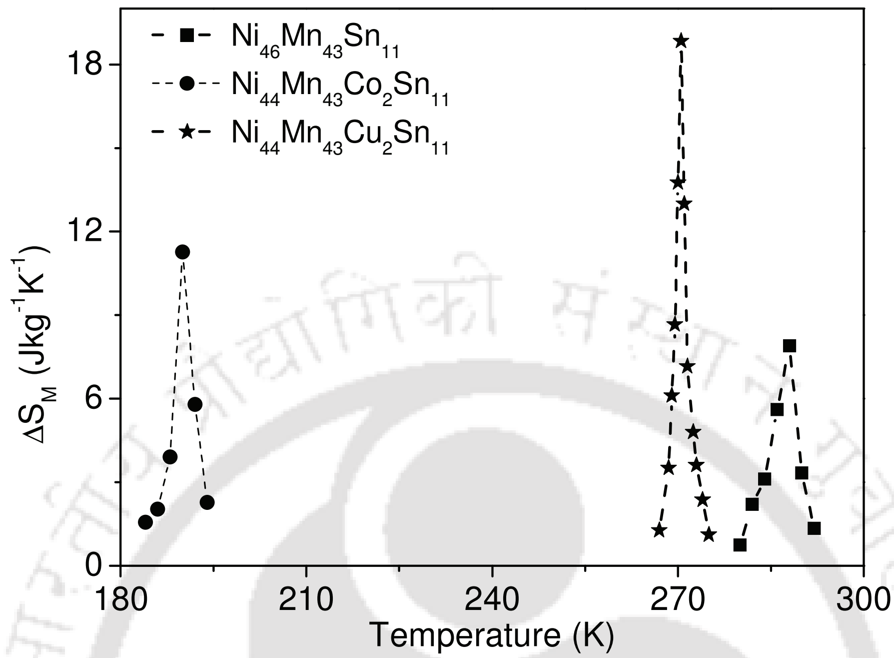

Figure 4.13: Temperature dependent magnetic entropy change (ΔS_M) for $Ni_{46}Mn_{43}Sn_{11}$, $Ni_{44}Mn_{43}Co_2Sn_{11}$ and $Ni_{44}Mn_{43}Cu_2Sn_{11}$ alloys.

TABLE 4.8: Martensite start temperature (T_{Ms}), Curie temperature ($T_{C,A}$), change in magnetic entropy (ΔS_M), temperature at which ΔS_M is maximum (T_{max}), refrigerant capacity (*RC*), and change in applied magnetic field (ΔH) for the three alloys.

Alloy Composition	T_{MS} **(K)**	$T_{C,A}$ **(K)**	ΔS_M **(Jkg^{-1}K^{-1})**	T_{max} **(K)**	***RC*** **(Jkg^{-1})**	ΔH **(Tesla)**
$Ni_{46}Mn_{43}Sn_{11}$	291	314	7.9	288	30.2	1.8
$Ni_{44}Mn_{43}Co_2Sn_{11}$	191	327	11.3	190	30.3	1.8
$Ni_{44}Mn_{43}Cu_2Sn_{11}$	270	298	18.8	270.5	24.1	1.8

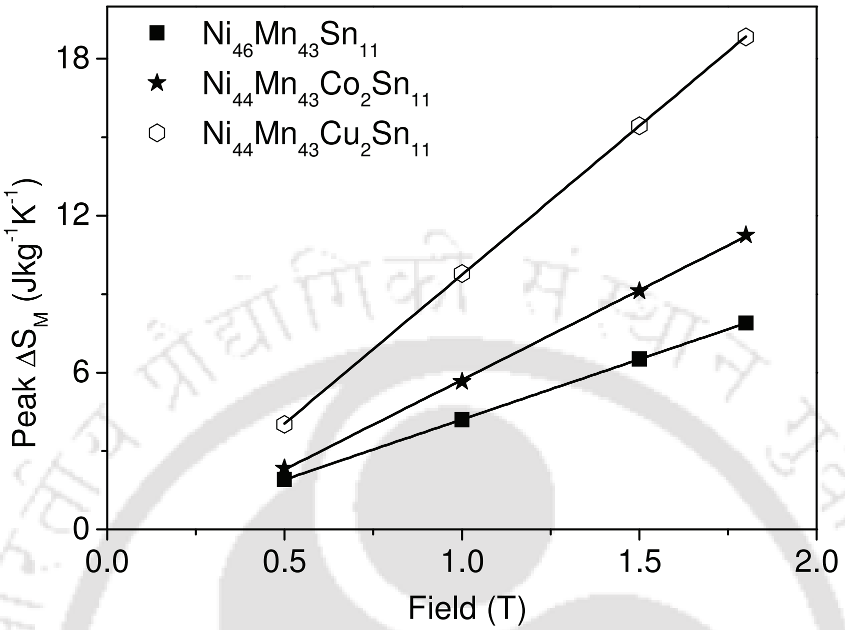

Figure 4.14: Variation of peak magnetic entropy change with applied field for $Ni_{46}Mn_{43}Sn_{11}$, $Ni_{44}Mn_{43}Co_2Sn_{11}$ and $Ni_{44}Mn_{43}Cu_2Sn_{11}$ alloys.

4.4. Summary

In this chapter, structural, magnetic and magneto-caloric properties of arc melted polycrystalline $Ni_{50}Mn_{37-x}Fe_xSn_{13}$ (x= 0, 1, and 1.25) and $Ni_{44}(Co/Cu)_2Mn_{43}Sn_{11}$ alloy ingots have been investigated. The highlights of the present investigations on these alloy ingots are

1. In $Ni_{50}Mn_{37-x}Fe_xSn_{13}$ alloys, though Fe_0 exhibited an orthorhombic structure corresponding to the martensite phase at room temperature, further addition of Fe led to stabilization of cubic $L2_1$ structure corresponding to the austenite phase.
2. $Ni_{44}(Co/Cu)_2Mn_{43}Sn_{11}$ alloys exhibited cubic $L2_1$ structure corresponding to the austenite phase at room temperature.

3. On replacing Mn with Fe, the lattice parameter and unit cell volume of the cubic $L2_1$ structure decrease and the Bragg peak positions shift to larger angles. On the other hand, the slight increase (decrease) in lattice parameter and unit cell volume was observed when Co (Cu) was substituted for Ni.
4. Substitution of Fe for Mn leads to a decrease in T_{MS} and an increase in the magnetization change and area under hysteresis around the martensitic transition which are responsible for the increase in observed ΔS_M and *RC* in $Ni_{50}Mn_{37-x}Fe_xSn_{13}$ alloys.
5. The martensitic start temperature decreases and Curie temperature increases due to Co substitution in $Ni_{46}Mn_{43}Sn_{11}$. But upon Cu substitution, both these temperatures decrease. Introducing either of these elements leads to an increase in the area under thermal hysteresis and magnetization change around the structural transition.
6. These studies establishes a procedure for tailoring both the MCE and the temperature at which maximum MCE occurs in Ni-Mn-Sn alloys by Fe, Co and Cu substitution.

Chapter 5

INVESTIGATIONS ON Ni-Mn-In-Si ALLOYS

One of the recently developed FSMAs is Ni-Mn-In which has features very similar to Ni-Mn-Sn alloys discussed in the previous chapter. It is now known that the characteristic temperatures and the MCE parameters such as ΔS_M, ΔT_{ad} and *RC* of FSMAs can be tailored markedly by small variations in composition or by partial substitution of an additional element in the ternary FSMA [PATH07a, PATH08a, CHAT10a, KAZA11a, SHAR10a, SHAR11a]. Moreover, rapid solidification by melt spinning or reducing particle size by ball milling have been found to influence the structural, magnetic and magneto-caloric properties of FMSAs [FENG07a, SANT08a, TIAN08a, GUAN11a, ROSA12a]. The melt spinning method can yield long lengths of ribbon shaped homogeneous samples with desired microstructure and degree of crystalline order suited for industrial applications [ROSA12a]. On the other hand, ball milled powdered alloy samples have the inherent advantage of being capable of compaction into any desired macroscopic net shape. In this chapter, the effect of atomic substitution on the structural and magneto-caloric parameters of Ni-Mn-In based bulk samples as well as the roles of solidification rate on melt spun ribbons and particle size on ball milled powders of the best alloy composition are presented.

5.1. Preparation

Bulk (B) $Ni_{50+x}Mn_{35-x}In_{15-y}Si_y$ alloy ingots were prepared from high purity elements by arc melting followed by annealing at 1173 K for 20 h and quenching in ice water as described in the second chapter. In these alloy systems, the best results in terms of room temperature crystalline and magnetic ordering was obtained for $Ni_{50}Mn_{35}In_{15}$, $Ni_{51}Mn_{34}In_{15}$, $Ni_{50}Mn_{35}In_{14}Si_1$ and $Ni_{51}Mn_{34}In_{14}Si_1$ alloys. Hence, further investigations were performed on these compositions only. The annealed $Ni_{51}Mn_{34}In_{14}Si_1$ ingot was melt spun on a rotating copper wheel set at different constant linear speeds of 12 m/s, 16 m/s and 32 m/s under argon atmosphere while maintaining other process parameters invariant. As-spun ribbon samples obtained under different wheel speeds were designated as R_1 (spun with linear wheel speed of 12 m/s), R_2 (spun with linear wheel speed of 16 m/s), and R_3 (spun with linear wheel speed of 32 m/s), respectively. Parts of as-spun ribbons were sealed in fused silica ampoules under a pressure of 10^{-3} Pa and annealed at two different temperatures of 823 K and 1073 K for ½ h each. To prepare the $Ni_{51}Mn_{34}In_{14}Si_1$ alloy powders, the annealed ingot was crushed into particles of size < 3 mm and milled for 7 h in a planetary ball mill (Insmart make). Hardened steel vial and hardened steel balls were used and a ball-to-powder weight ratio of 10:1 was maintained during the milling process. The mill was operated at a constant speed of 500 rpm. To avoid overheating of the vial, milling was carried out in cycles of 15 min followed by 10 min of idling. As-milled powders were subjected to the same heat treatment as the original ingot to minimize the strains accumulated during the milling process. Subsequently, the annealed powder was sieved using different pore sized metallic sieves conforming to American Society for Testing and Materials (ASTM) standards and classified into different particle size ranges. The alloy powders studied are classified into thirteen sets depending on their size as B (bulk), P_1 (850 – 1180 μm), P_2 (710 – 850 μm), P_3 (600 – 710 μm), P_4 (500 – 600 μm), P_5 (425 – 500 μm), P_6 (300 – 425 μm), P_7 (125 – 300 μm), P_8 (106 – 125 μm), P_9 (90 – 106 μm), P_{10} (38 – 45 μm), P_{11} (20 – 38 μm), and P_{12} (< 20 μm).

5.2. Bulk $Ni_{50+x}Mn_{35-x}In_{15-y}Si_y$ alloys

5.2.1. Crystal structures

XRD patterns (shown in Figure 5.1a) indicate that at room temperature, $Ni_{50}Mn_{35}In_{15}$ and $Ni_{51}Mn_{34}In_{15}$ alloys are in martensitic phase (with orthorhombic unit cell) and $Ni_{50}Mn_{35}In_{14}Si_1$ and $Ni_{51}Mn_{34}In_{14}Si_1$ alloys are in austenitic phase (with cubic $L2_1$ structure), respectively, as depicted in Figure 5.1b. The slight reduction in unit cell volume with Ni addition indicates that the large Mn atoms have been substituted by Ni. The overall composition of the alloys obtained from EDS analysis is summarised in Table 5.1. It can be seen that the final alloy composition is very close to the nominal (starting) composition of the respective alloys.

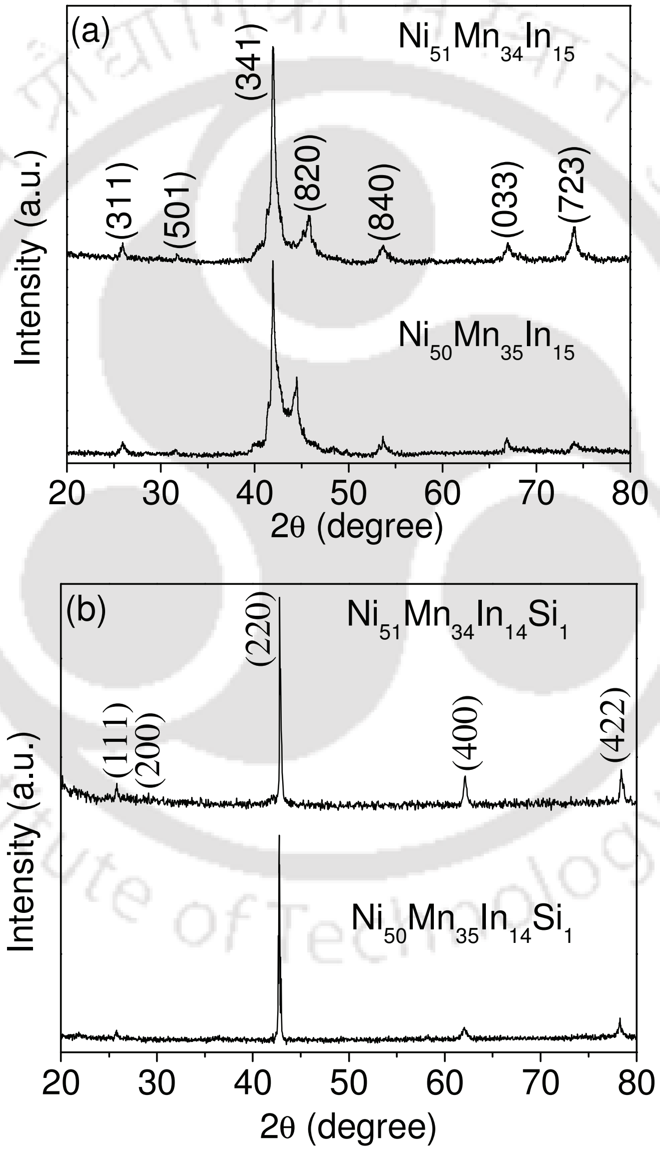

Figure 5.1: Room temperature XRD patterns of (a) $Ni_{50}Mn_{35}In_{15}$ and $Ni_{51}Mn_{34}In_{15}$, and (b) $Ni_{50}Mn_{35}In_{14}Si_1$ and $Ni_{51}Mn_{34}In_{14}Si_1$ alloys.

TABLE 5.1: Nominal composition, measured composition, electron concentration (*e/a* ratio), room temperature crystal phase, lattice parameters (*a*, *b* and *c*) and unit-cell volume (*V*) of $Ni_{50}Mn_{35}In_{15}$, $Ni_{51}Mn_{34}In_{15}$, $Ni_{50}Mn_{35}In_{14}Si_1$ and $Ni_{51}Mn_{34}In_{14}Si_1$ alloys.

Nominal Composition	Composition from EDS	*e/a*	Crystal phase	*a* (nm)	*b* (nm)	*c* (nm)	*V* (nm^3)
$Ni_{50}Mn_{35}In_{15}$	$Ni_{50.21}Mn_{34.95}In_{14.84}$	7.91	Martensite	1.7578	1.1661	0.4583	0.9394
$Ni_{51}Mn_{34}In_{15}$	$Ni_{50.97}Mn_{33.45}In_{15.58}$	7.91	Martensite	1.7062	1.0701	0.4689	0.8561
$Ni_{50}Mn_{35}In_{14}Si_1$	$Ni_{49.81}Mn_{34.99}In_{13.84}Si_{1.36}$	7.90	Austenite	0.5982	0.5982	0.5982	0.2141
$Ni_{51}Mn_{34}In_{14}Si_1$	$Ni_{50.69}Mn_{33.83}In_{14.07}Si_{1.41}$	7.92	Austenite	0.5969	0.5969	0.5969	0.2127

5.2.2. Magnetic properties

Figure 5.2 depicts the thermomagnetization (*M-T*) curves of the alloys recorded under an applied field of 0.1 T in zero-field-cooled (ZFC) and field-cooled (FC) conditions. For ZFC measurements, the samples were first cooled down to 50 K in the absence of magnetic field, whereas for the FC measurements, the samples were cooled down to 50 K in the presence of an external magnetic field of 0.1 T. Figure 5.2 shows that as the temperature is reduced from 375 K, magnetization first increases sharply due to the second-order paramagnetic to ferromagnetic transition and then abruptly decreases due to the structural (austenite to martensite) transformation. On further decreasing the temperature below 235 K, the samples exhibit a large increase in magnetization. This signifies the paramagnetic to ferromagnetic transition occurring in the martensite phase of the sample. Thus, all the alloys exhibit three phase transitions, viz., one structural transition at the martensite start temperature (T_{Ms}) and two magnetic transitions, one in the austenite phase (marked as $T_{C,A}$) and another in martensite phase (marked as $T_{C,M}$).

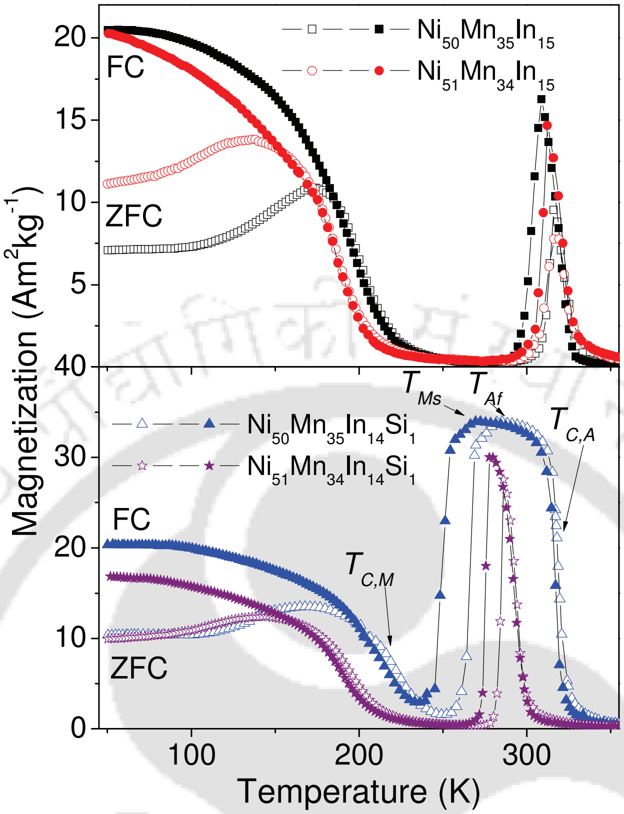

Figure 5.2: *M-T* curves of four bulk alloys obtained at an applied field of 0.1 T. Filled and open symbols represent FC and ZFC data, respectively. Curie temperature of martensitic phase ($T_{C,M}$), martensite start temperature (T_{Ms}), austenite finish temperature (T_{Af}), and the Curie temperature of the austenite phase ($T_{C,A}$) are shown.

Below $T_{C,M}$ and in the temperature interval $T_{Ms} < T < T_{C,A}$, ferromagnetic ordering is observed in the samples. Paramagnetic behavior is observed in the temperature intervals $T_{C,M} < T < T_{Mf}$ and $T > T_{C,A}$. At lower temperatures (below 197 K), ZFC and FC curves deviate from each other showing a bifurcation. It can be noticed that the bifurcation temperature (T_{bifur}) shifts to lower temperatures with increase in Ni/Mn ratio in both Ni-Mn-In and Ni-Mn-In-Si alloys as shown in Table 5.2.

TABLE 5.2: Martensite start temperature (T_{Ms}), martensite finish temperature (T_{Mf}), austenite start temperature (T_{As}), austenite finish temperature (T_{Af}), thermal hysteresis (ΔT_{hys}), martensite Curie temperature ($T_{C,M}$), austenite Curie temperature ($T_{C,A}$), bifurcation temperature (T_{bifur}) obtained at 0.1 T field for $Ni_{50}Mn_{35}In_{15}$, $Ni_{51}Mn_{34}In_{15}$, $Ni_{50}Mn_{35}In_{14}Si_1$ and $Ni_{51}Mn_{34}In_{14}Si_1$ alloys.

Alloy	T_{Ms} (K)	T_{Mf} (K)	T_{As} (K)	T_{Af} (K)	ΔT_{hys} (K)	$T_{C,M}$ (K)	$T_{C,A}$ (K)	T_{bifur} (K)
$Ni_{50}Mn_{35}In_{15}$	309	295	305	316	8.5	205	321	185
$Ni_{51}Mn_{34}In_{15}$	311	302	307	318	6.0	186	320	153
$Ni_{50}Mn_{35}In_{14}Si_1$	269	239	255	282	14.5	217	317	197
$Ni_{51}Mn_{34}In_{14}Si_1$	278	270	279	287	9.0	191	294	157

A hysteresis behavior, attributed to structural transition is also observed in the *M-T* curves when the samples are thermally cycled. This thermal hysteresis (ΔT_{hys}) can be estimated from the characteristic temperature obtained from the *M–T* curves and is given by the relation,

$$\Delta T_{hys} = \frac{\left(T_{As} + T_{Af}\right)}{2} - \frac{\left(T_{Ms} + T_{Mf}\right)}{2} \tag{5.1}$$

where the suffixes *s* and *f* refer to the 'start' and 'finish' temperatures of the austenite and martensite phases, respectively. The lowest (highest) ΔT_{hys} of 6 K (14.5 K) is observed in $Ni_{51}Mn_{34}In_{15}$ ($Ni_{50}Mn_{35}In_{14}Si_1$) alloy. T_{Ms} ($T_{C,M}$, $T_{C,A}$) of $Ni_{50}Mn_{35}In_{15}$, $Ni_{51}Mn_{34}In_{15}$, $Ni_{50}Mn_{35}In_{14}Si_1$ and $Ni_{51}Mn_{34}In_{14}Si_1$ alloys are 309 K (205 K, 321 K), 311 K (186 K, 320 K), 269 K (217 K, 317 K) and 278 K (191 K, 294 K), respectively. With the substitution of Ni for Mn in $Ni_{50}Mn_{35}In_{15}$ and $Ni_{50}Mn_{35}In_{14}Si_1$, T_{Ms} shifts to higher temperatures, whereas, $T_{C,M}$ and $T_{C,A}$ shift to lower temperatures. An earlier work [KREN06a, GAOB09c] on $Ni_{50-x}Mn_{35+x}In_{15}$

alloys showed that T_{Ms} increases with increase in *e/a* ratio. In this work, the measured compositions of $Ni_{50}Mn_{35}In_{15}$ and $Ni_{51}Mn_{34}In_{15}$ show nearly the same *e/a* ratio due to the inevitable elemental loss during arc melting. Hence, T_{Ms} of these alloys differ by merely 2 K. Such small variations in T_{Ms} of alloys with same *e/a* has also been observed in some earlier work [ITOW07a]. In the case of Ni-Mn-In-Si alloys, T_{Ms} increases with an increase in *e/a* ratio. Figure 5.2 shows an interesting feature, viz., the magnitude of magnetization change (ΔM) at the structural transition decreases with increasing Ni/Mn ratio. This behaviour closely follows the observed variation in unit cell volume, which is in turn related to the Mn-Mn interatomic distance. Thus, the magnetic properties of Ni–Mn–X alloys are primarily determined by the Mn atoms and are described in terms of exchange interaction via conduction electrons as pointed out in the literature [BROW99a, LIUG06a].

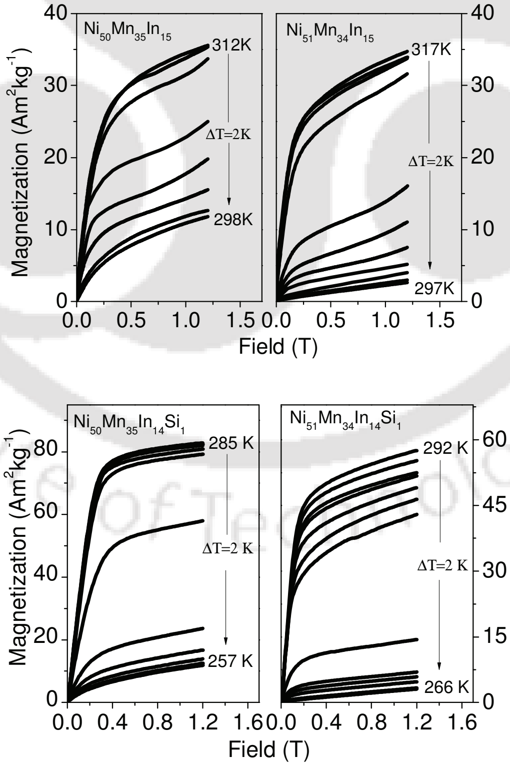

Figure 5.3: *M* - *H* curves of $Ni_{50}Mn_{35}In_{15}$, $Ni_{51}Mn_{34}In_{15}$, $Ni_{50}Mn_{35}In_{14}Si_1$ and $Ni_{51}Mn_{34}In_{14}Si_1$ alloys recorded at 2 K interval (ΔT) around martensite start temperature (T_{Ms}).

In order to confirm the occurrence of first-order structural transition at T_{Ms} in these alloys, isothermal magnetization $(M\text{-}H)_T$ curves (shown in Figure 5.3) were recorded close to the structural transition and Arrott (M^2 vs. H/M) plots were constructed from these data. Arrott plots have been used to investigate the order of martensitic transition in NiMnGa [ZHOU06a] and NiCoMnSb based alloys [SAHO11a]. When the Arrott plots are linear across the transition, they describe a second order phase transition. In the case of martensitic transition, Arrott plots are non-linear with an S-type behavior, which can be ascribed to a first-order phase transition. It can be seen that the Arrott plots (Figure 5.4) are nonlinear (S-shaped), which confirms the occurrence of a first-order phase transition at this temperature [DUCN02a].

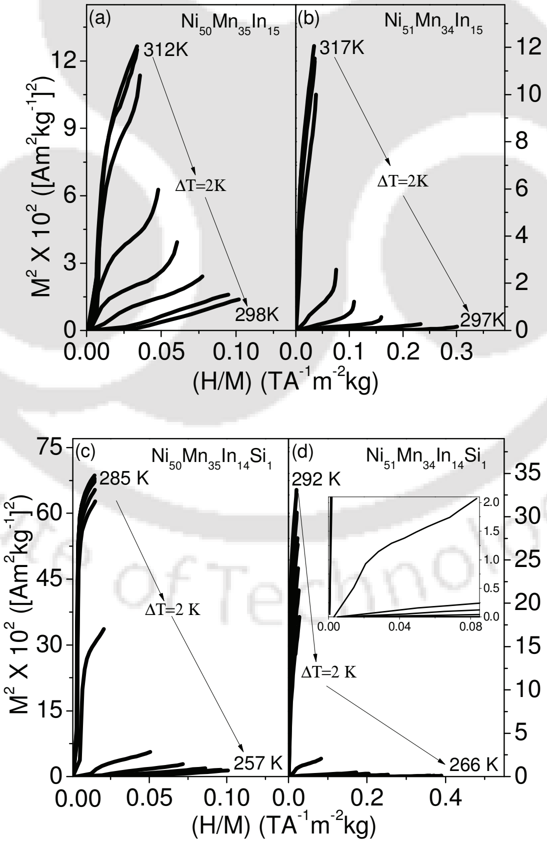

Figure 5.4: Arrott plots for (a) $Ni_{50}Mn_{35}In_{15}$, (b) $Ni_{51}Mn_{34}In_{15}$, (c) $Ni_{50}Mn_{35}In_{14}Si_1$ and (d) $Ni_{51}Mn_{34}In_{14}Si_1$ alloys. Inset in Figure 5.4(d) shows an enlarged view of data near the origin.

5.2.3. Thermal properties

Thermal properties of $Ni_{50+x}Mn_{35-x}In_{15-y}Si_y$ alloys are investigated from DSC curves (shown in Figure 5.5) which were recorded over a wide temperature range during heating and cooling cycles at a constant rate of 0.17 Ks^{-1}. As can be observed from the DSC curves, all the alloys exhibit a single exothermic and single endothermic peak in the cooling and heating curves, confirming a one-step martensitic phase transformation in these alloys. The values of the martensitic transition temperatures obtained for different alloy compositions from the DSC data are listed in Table 5.3.

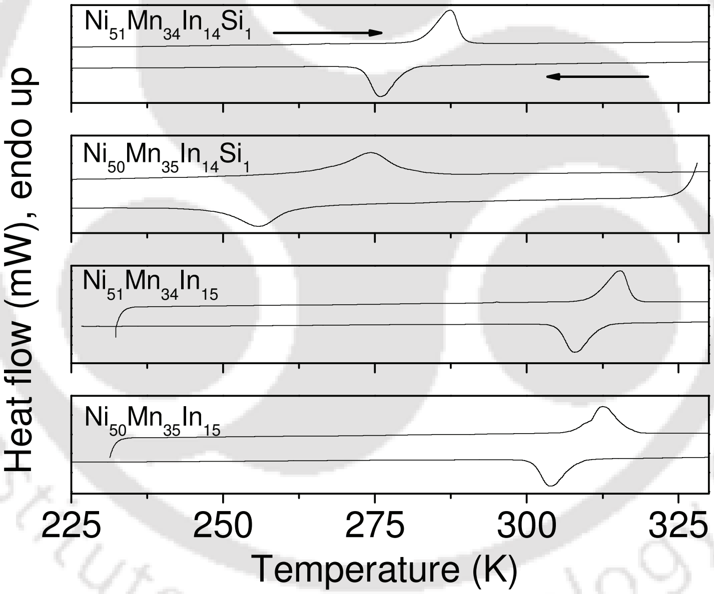

Figure 5.5: DSC curves of $Ni_{50+x}Mn_{35-x}In_{15-y}Si_y$ alloys. Arrows indicate the forward (on cooling) and reverse (on heating) martensitic transformations.

It can be inferred from the DSC curves that the start (peak, finish) temperature of the forward martensitic transition, T_{Ms} (T_{Mp}, T_{Mf}) are 311 K (304 K, 299 K), 314 K (308 K, 303 K), 271 K (256 K, 243 K), and 283 K (276 K, 270 K), and the start (peak, finish) temperature of the reverse martensitic transition, T_{As} (T_{Ap}, T_{Af}) are 307 K (312 K, 319 K), 310 K (316 K, 320 K), 261 K (274 K, 286 K), and 281 K (288 K, 291 K), of $Ni_{50}Mn_{35}In_{15}$, $Ni_{51}Mn_{34}In_{15}$, $Ni_{50}Mn_{35}In_{14}Si_1$ and $Ni_{51}Mn_{34}In_{14}Si_1$ alloys respectively. Comparison of DSC and $M-T$ data (Figure 5.2) reveals that application of magnetic field induces a shift in the structural transition to lower temperatures. Such field induced martensitic transformation has been observed in Ni-Mn-Sn alloys in the present studies as well as in other FSMAs [SHAR10a]. The thermal hysteresis, ΔT_{hys} determined from the DSC data is 8.0 K, 6.5 K, 16.5 K and 9.5 K for $Ni_{50}Mn_{35}In_{15}$, $Ni_{51}Mn_{34}In_{15}$, $Ni_{50}Mn_{35}In_{14}Si_1$ and $Ni_{51}Mn_{34}In_{14}Si_1$ alloys respectively.

TABLE 5.3: Martensite start temperature (T_{Ms}), martensite finish temperatures (T_{Mf}), austenite start temperatures (T_{As}), austenite finish temperature (T_{Af}), thermal hysteresis (ΔT_{hys}), change in total enthalpy (ΔE), change in total entropy (ΔS) and change in free energy (ΔG) of $Ni_{50+x}Mn_{35-x}In_{15-y}Si_y$ bulk samples estimated from DSC data.

Alloy	T_{Ms} **(K)**	T_{Mf} **(K)**	T_{As} **(K)**	T_{Af} **(K)**	ΔT_{hys} **(K)**	ΔE **(kJkg^{-1})**	ΔS **(Jkg^{-1}K^{-1})**	ΔG **(Jkg^{-1})**
$Ni_{50}Mn_{35}In_{15}$	311	299	307	319	8.0	8.6	27.3	109.2
$Ni_{51}Mn_{34}In_{15}$	314	303	310	320	6.5	8.9	28.1	105.4
$Ni_{50}Mn_{35}In_{14}Si_1$	271	243	261	286	16.5	7.5	26.9	242.1
$Ni_{51}Mn_{34}In_{14}Si_1$	283	270	281	291	9.5	8.7	30.3	175.7

The enthalpy change (ΔE) and entropy change, (ΔS) associated with the martensitic transition were also estimated using the equation (3.6) and (3.7). The values of ΔE (ΔS) are 8.6 kJkg^{-1} (27.3 Jkg^{-1}K^{-1}), 8.9 kJkg^{-1} (28.1 Jkg^{-1}K^{-1}), 7.5 kJkg^{-1} (26.9 Jkg^{-1}K^{-1}) and 8.7 kJkg^{-1} (30.3 Jkg^{-1}K^{-1}), for $Ni_{50}Mn_{35}In_{15}$, $Ni_{51}Mn_{34}In_{15}$, $Ni_{50}Mn_{35}In_{14}Si_1$ and $Ni_{51}Mn_{34}In_{14}Si_1$ alloys respectively. ΔE and ΔS increase with the substitution of Ni for Mn atom in both the parent as well as Si substituted samples. But a reverse trend was observed in case of change in free energy, ΔG which decreases with the substitution of Ni for Mn atom in both the cases. ΔE, ΔS and ΔG values estimated for these alloys are also listed in Table 5.3. The value of ΔG for $Ni_{50}Mn_{35}In_{15}$, $Ni_{51}Mn_{34}In_{15}$, $Ni_{50}Mn_{35}In_{14}Si_1$ and $Ni_{51}Mn_{34}In_{14}Si_1$ alloys are 109.2 Jkg^{-1}, 105.4 Jkg^{-1}, 242.1 Jkg^{-1} and 175.7 Jkg^{-1}, respectively. As discussed in the previous chapters, a lower ΔG at the martensitic phase transition result in smaller $\Delta T_{hys,}$ which means that the martensite - austenite transition can occur easily in parent alloys. This behavior is similar to the case of Ni-Mn-Ga alloys reported in chapter 3.

5.2.4. Magneto-caloric properties

Since entropy is discontinuous at the first-order phase transition, ΔS_M will be large near T_{Ms}. ΔS_M was calculated from $(M\text{-}H)_T$ data using the integrated Maxwell equation (1.23). $(M\text{-}H)_T$ curves were recorded as a function of increasing magnetic field from 0 to 1.2 T at different temperatures near T_{Ms} for the alloys (*cf.* figure 5.3). Figure 5.6 depicts the variation of ΔS_M as a function of temperature for all the alloys. *RC*, was obtained by integrating the area under the $\Delta S_M(T)$ curves over the full width at half maximum. ΔS_M and *RC* value obtained for $Ni_{50}Mn_{35}In_{15}$, $Ni_{51}Mn_{34}In_{15}$, $Ni_{50}Mn_{35}In_{14}Si_1$ and $Ni_{51}Mn_{34}In_{14}Si_1$ alloys are listed in Table 5.4. The peak ΔS_M (*RC*) value corresponding to $Ni_{50}Mn_{35}In_{15}$, $Ni_{51}Mn_{34}In_{15}$, $Ni_{50}Mn_{35}In_{14}Si_1$ and $Ni_{51}Mn_{34}In_{14}Si_1$ alloys are 4.3 $Jkg^{-1}K^{-1}$ (14.9 Jkg^{-1}), 8.5 $Jkg^{-1}K^{-1}$ (17.4 Jkg^{-1}), 17.5 $Jkg^{-1}K^{-1}$ (52.9 Jkg^{-1}) and 19.9 $Jkg^{-1}K^{-1}$ (35.9 Jkg^{-1}), respectively. The highest ΔS_M was exhibited by $Ni_{51}Mn_{34}In_{14}Si_1$ alloy at 279 K. ΔS_M is clearly related to the sharpness of the structural transition or the $(\partial M/\partial T)_H$ term in the integrated Maxwell relation [equation 1.23]. It can be noticed that a relatively sharper structural transition is observed in Si substituted alloys. For an applied magnetic field of 0.1 T, $Ni_{51}Mn_{34}In_{14}Si_1$ alloy exhibits the highest $(\partial M/\partial T)_H$ value of 6.6 $Am^2kg^{-1}K^{-1}$, among the four alloy compositions.

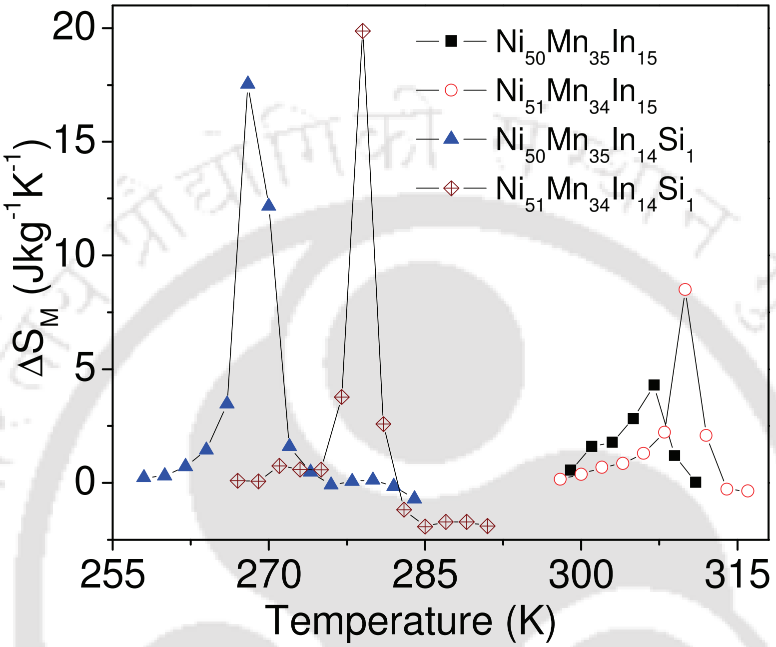

Figure 5.6: Temperature dependence of ΔS_M obtained for a ΔH of 1.2 T in $Ni_{50}Mn_{35}In_{15}$, $Ni_{51}Mn_{34}In_{15}$, $Ni_{50}Mn_{35}In_{14}Si_1$ and $Ni_{51}Mn_{34}In_{14}Si_1$ alloys.

On the other hand, ΔS_M for ΔH of 1.2 T calculated from $(M - H)_T$ curves is the difference of zero field entropy ($S_{H=0}$) and the entropy for an applied field of 1.2 T ($S_{H=1.2T}$). The entropy at 1.2 T is given by

$$S(T)_{H=1.2T} = S(T)_{H=0} + \Delta S_M(T)_{\Delta H=1.2T} \tag{5.2}$$

$S_{H=0}$ as a function of temperature can be evaluated from the heat capacity data at zero field, $C_{H=0}$ shown as inset in Figure 5.7 using the relation [SHAR07a, PECH01b],

$$S(T)_{H=0} = \int_0^T \frac{C(T)_{H=0}}{T} dT + S(T=0) \tag{5.3}$$

TABLE 5.4: Peak magnetic entropy change (peak ΔS_M), temperature at which peak or maximum ΔS_M is observed (T_{max}), refrigerant capacity (RC), and exchange bias (H_E) obtained for 1.2 T field change for $Ni_{50}Mn_{35}In_{15}$, $Ni_{51}Mn_{34}In_{15}$, $Ni_{50}Mn_{35}In_{14}Si_1$ and $Ni_{51}Mn_{34}In_{14}Si_1$ alloys.

Alloy	**Peak ΔS_M ($Jkg^{-1}K^{-1}$)**	**T_{max} (K)**	**RC (Jkg^{-1})**	**H_E (mT) at 50 K**
$Ni_{50}Mn_{35}In_{15}$	4.3	307	14.9	9.3
$Ni_{51}Mn_{34}In_{15}$	8.5	310	17.4	7.7
$Ni_{50}Mn_{35}In_{14}Si_1$	17.5	268	52.9	8.6
$Ni_{51}Mn_{34}In_{14}Si_1$	19.9	279	35.9	5.4

For solids, S (T = 0) is independent of H and can be assumed to be a constant or zero. Following isentropic paths from $S(T)_{H=0}$ to $S(T)_{H>0}$ curves, the adiabatic temperature change (ΔT_{ad}) as a function of temperature can be expressed as

$$\Delta T_{ad}(T)_H = [T_H - T_{H=0}]_S \tag{5.4}$$

Figure 5.7 depicts the temperature dependence of ΔT_{ad} for $Ni_{51}Mn_{34}In_{14}Si_1$ alloy. A moderate ΔT_{ad} of −3.9 K corresponding to the highest ΔS_M (19.9 $Jkg^{-1}K^{-1}$) is exhibited by this alloy at 279 K for ΔH = 1.2 T. This value may be compared with ΔT_{ad} = −1.5 K and −1.99 K reported for Ge and Al substituted Ni-Mn-In alloy for ΔH = 1.8 T, respectively [KAZA11a]. The moderately high ΔT_{ad} obtained at relatively lower ΔH can be attributed to the higher ΔS_M exhibited by this alloy at lower ΔH. This comparison serves to highlight the strong potential of the current samples for magnetic refrigerant application.

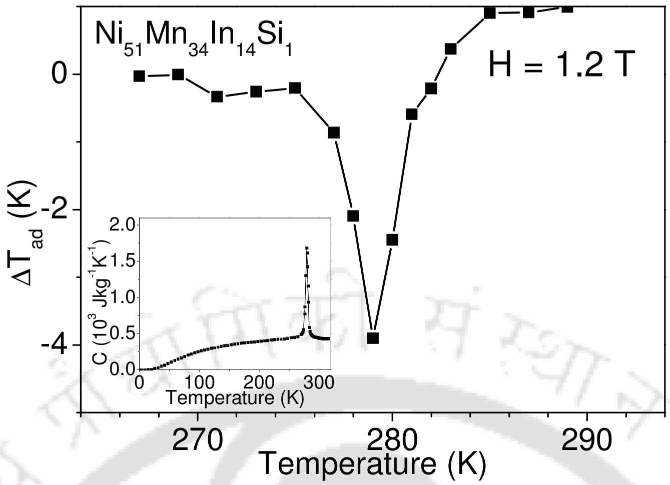

Figure 5.7: Temperature dependence of adiabatic temperature change (ΔT_{ad}) obtained for 1.2 T field change. Inset shows temperature dependent heat capacity of $Ni_{51}Mn_{34}In_{14}Si_1$ alloy at zero-field.

5.2.5. Exchange bias

The bifurcation observed below T_{bifur} between the FC and ZFC curves in the *M-T* curves shown in Figure 5.2 can be attributed to the co-existence of ferromagnetic and antiferromagnetic interactions in the alloys. When such a system is cooled below T_{bifur} under a magnetic field, one can expect a shift in the *M-H* loop towards the negative field axis can be observed which is a manifestation of exchange bias, H_E [VALL08a]. H_E can be estimated from the relation [WANG08a],

$$H_E = -\left(\frac{H_{c1} + H_{c2}}{2}\right) \tag{5.5}$$

where, H_{c1} and H_{c2} are the negative and positive coercive fields at which the magnetization is zero.

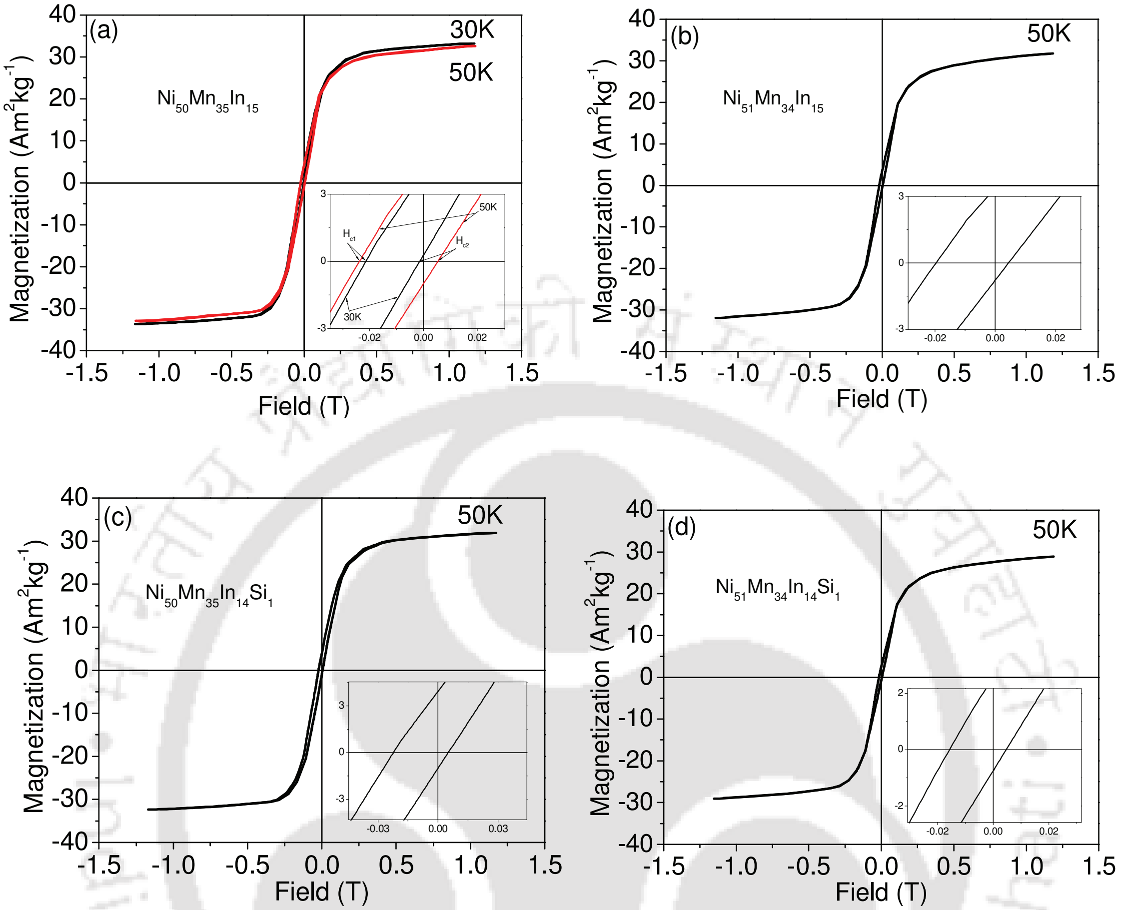

Figure 5.8. Typical *M-H* loops under 1.2 T field obtained for (a) $Ni_{50}Mn_{35}In_{15}$ at 30 K and 50 K, (b) $Ni_{51}Mn_{34}In_{15}$ at 50 K, (c) $Ni_{50}Mn_{35}In_{14}Si_1$ at 50 K, and (d) $Ni_{51}Mn_{34}In_{14}Si_1$ at 50 K. Inset shows an expanded view of the data near the origin.

Figure 5.8 (a) shows the *M-H* loops for $Ni_{50}Mn_{35}In_{15}$ alloy recorded at two temperatures well below T_{bifur}. It is evident from the figure that the *M-H* loop shifts more towards the negative field axis as the temperature is decreased. H_E measured at 50 K and 30 K are 9.3 and 11 mT, respectively. Similar behaviour is also shown by Ni and Si substituted $Ni_{50}Mn_{35}In_{15}$ alloy as illustrated by the corresponding H_E in figure 5.8 (b-d) and the data listed in Table 5.4. With an increase in Ni/Mn ratio, H_E decreases. Observation of exchange bias verifies the coexistence of ferromagnetic and antiferromagnetic interactions in these alloys. Existence of antiferromagnetic coupling in Ni-Mn-X alloys has been proposed by many researchers [PATH09a, BROW06a, WANG08a, JING09a, ESAK11a]. However, experimentally the same has been established in $Ni_2Mn_{1.44}Sn_{0.56}$ alloys by neutron diffraction studies [BROW06a]. In FSMAs, Mn occupying Mn sites results in ferromagnetic interaction. On the other hand, Mn occupying Ni or In anti-sites induces antiferromagnetic interactions. When Ni/Mn ratio is decreased in Ni-Mn-In (and Ni-Mn-In-Si) alloys, the excess Mn atoms occupying Ni (or In) anti-sites can result in antiferromagnetic coupling [ZHAO10a]. This leads to an increase in H_E in Ni-Mn-In and Ni-Mn-In-Si alloys as indicated in Table 5.4. H_E values observed in this work may be compared with those reported for $Ni_{50}Mn_{35}In_{15}$ (~9.6 mT) [JING09a], $Ni_{49.5}Mn_{34.5}In_{16}$ (~8.4 mT) [WANG08a] and $Ni_{50}Mn_{35}In_{14}Si_1$ (~6.7 mT) [PATH09b] alloys at 50 K. Exchange bias properties are generally observed in inhomogeneous materials or thin films [NOGU99a, KOOL96a]. Observation of this phenomenon in bulk samples may indicate certain amount of inhomogenety in the present alloys. These results may lead to some interesting applications.

5.2.6. Critical behavior

A set of critical exponents, β, γ and δ corresponding to the temperature dependence of spontaneous magnetization, initial susceptibility and isothermal magnetization respectively, can be used to characterised the second-order FM–PM phase transition occurring at the critical temperature T_C. Since $Ni_{50}Mn_{35}In_{14}Si_1$ FSMA exhibits both austenite and martensite ferromagnetic phases with the corresponding T_C in the M–T data (inset of Figure 5.9), the critical behaviour of polycrystalline $Ni_{50}Mn_{35}In_{14}Si_1$ alloy near the second-order ferromagnetic phase transitions at austenite $T_{C,A}$ and at martensite $T_{C,M}$ have been studied by determining the critical exponents β, γ, and δ.

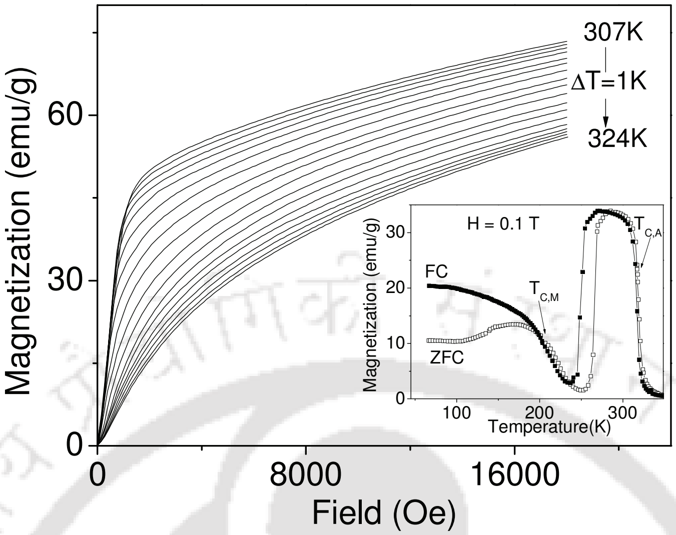

Figure 5.9: Isothermal magnetization $(M - H)_T$ at different temperatures close to $T_{C,A}$ of $Ni_{50}Mn_{35}In_{14}Si_1$ alloy. Inset shows the plot of magnetization versus temperature $(M - T)$ data.

The power law behavior of spontaneous magnetization, $M_s(T)$, inverse susceptibility, $\chi_0^{-1}(T)$ and isothermal magnetization at T_C, $M(H, T = T_C)$ with respect to the critical exponents β, γ and δ are defined as [STAN71a],

$$\begin{aligned} &M_s(T) \propto |t|^{\beta} \qquad t<0 \\ &\chi_0^{-1}(T) \propto |t|^{\gamma} \qquad t>0 \\ &M(H, T=T_C) \propto H^{\frac{1}{\delta}} \qquad t=0 \end{aligned} \tag{5.6}$$

where $t = (T - T_C)/T_C$ is the reduced temperature. Different procedures such as modified Arrott plots (MAPs) technique, Kouvel–Fisher (KF) method, and Widom scaling relation are available to determine these critical exponents and the T_C [WANG09a]. According to the Landau theory, the Gibbs potential of a magnetic system, $G(T, M)$ about the critical point or in the vicinity of the magnetic phase transition can be written as [LEVY00a, AMAR05a, AMAR10a]

$$G(T,M) = G_0 - MH + pM^2 + qM^4 + ... \qquad (5.7)$$

where the coefficients p and q are temperature dependent parameters. Applying the minimization condition ($\partial G/\partial M = 0$), the simplest form of equation (5.7) is

$$\frac{H}{M} = 2p + 4qM^2 \qquad (5.8)$$

Equation (5.8) represents a straight line equation which has a positive slope [ARRO57a, BANE64a]. Arrott and Noakes [ARRO67a] proposed the general expression for the equation (5.8) as,

$$\left(\frac{H}{M}\right)^{\frac{1}{\gamma}} = \frac{(T - T_C)}{T'} + \left(\frac{M}{M'}\right)^{\frac{1}{\beta}} \qquad (5.9)$$

where T' and M' are material dependent constants. Using the values of the mean field theory ($\beta = 0.5$ and $\gamma = 1$), equation (5.9) can be reduced to equation (5.8).

In order to evaluate the critical behavior of the present sample in the vicinity of both the T_C, initial isothermal M–H data (Figure 5.9) were recorded as functions of increasing magnetic field and temperature at close (1 K) temperature intervals. These data show that the magnitude of magnetization decreased with increasing temperature. The M – H data were then converted into the form of MAPs by appropriately choosing the initial β and γ values such that the plots are linear at the high field region. On the other hand, due to mutual misalignment of magnetic domains at low field region, the MAPs deviate from linearity. To get the correct β and γ values, the temperature dependences of M_s and χ_0^{-1} are obtained from the extrapolation of the initial MAPs data for temperatures below and above T_C, respectively.

By fitting the ln(Ms) versus ln(t) plot for $t < 0$ and the ln(χ_0^{-1}) versus ln(t) plot for $t > 0$ to a straight line, new values of β and γ, were determined from the slopes and intercepts. The values of M_s and χ_0^{-1} were then improved using the new β and γ. After iterative fitting, stable values of the exponents were obtained. Using the stable values of exponents the final MAPs were plotted as shown in Figure 5.10.

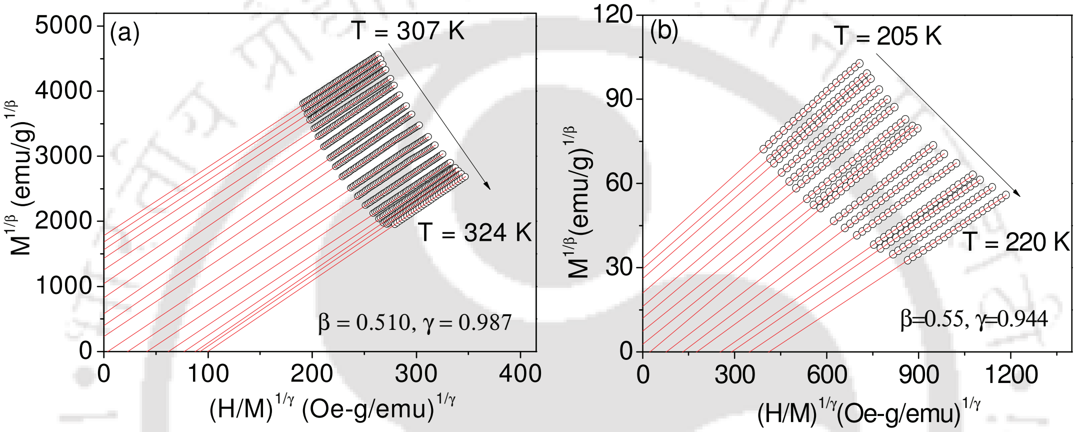

Figure 5.10: Modified Arrott plot isotherms close to (a) $T_{C,A}$ and (b) $T_{C,M}$ for $Ni_{50}Mn_{35}In_{14}Si_1$ alloy.

The quality of the MAPs is defined by a set of parallel lines. The line passing through the origin was used to obtain the accurate value of T_C which are $T_{C,A}$ = 316.5±0.5 K and $T_{C,M}$ = 213 ± 0.5 K, respectively corresponding to the austenite and martensite phases. These T_C values are lower than the values measured from $M - T$ data due to the basic different in methodology used to determine T_C in both the cases. T_C obtained from the MAPs is certainly more accurate than the T_C obtained from $M - T$ data. Figure 5.11 shows the temperature dependence of final M_s and χ_0^{-1} obtained using data in Figure 5.10. The final values of β and γ estimated from the ln-ln plots (Figure 5.12) are β = 0.510 and 0.550 and γ = 0.987 and 0.944 around $T_{C,A}$ and $T_{C,M}$, respectively.

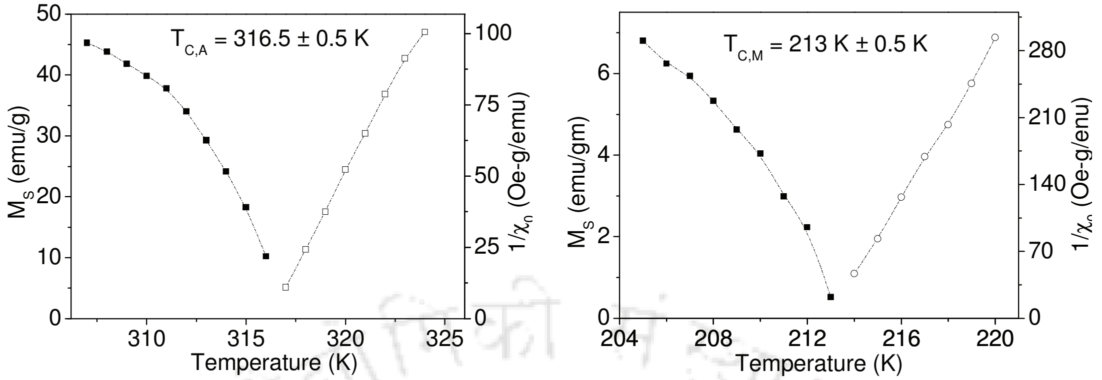

Figure 5.11: Temperature dependence of the spontaneous magnetization $M_s(T)$ and the inverse initial susceptibility $\chi_0^{-1}(T)$ in the vicinity of (a) $T_{C,A}$ and (b) $T_{C,M}$ for $Ni_{50}Mn_{35}In_{14}Si_1$ alloy.

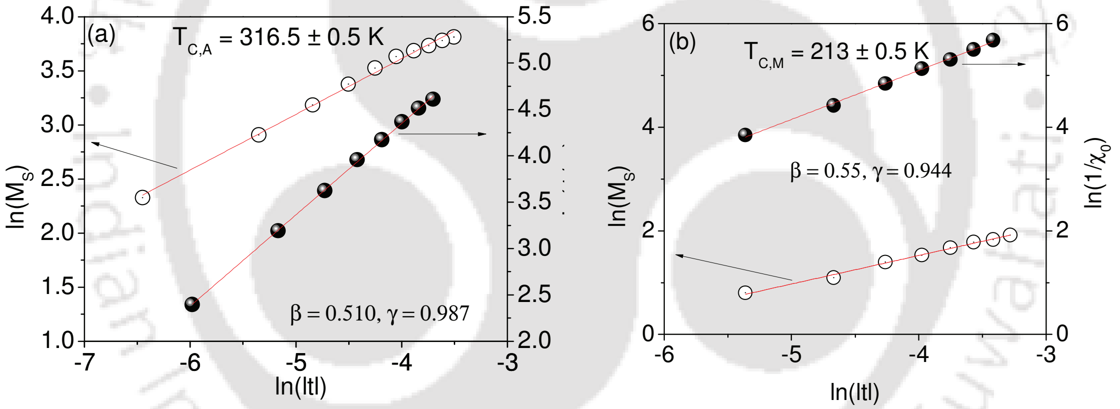

Figure 5.12: ln(Ms) versus ln(t) and ln(χ_0^{-1}) versus ln(t) along with the fitting around (a) $T_{C,A}$ and (b) $T_{C,M}$ for $Ni_{50}Mn_{35}In_{14}Si_1$ alloy.

In addition, the scaling analysis can also be used as a further verification of the correctness of critical exponent values and T_C. According to the scaling hypothesis $M(H, t)$ is a universal function of H and t, which is given as

$$M(H,t)|t|^{-\beta} = f_{\pm}\left(H|t|^{-(\beta+\gamma)}\right) \tag{5.10}$$

where f_+ and f_- are regular analytical functions for $T > T_C$ and $T < T_C$, respectively. Using the values of the critical temperature T_C and critical exponent β and γ obtained from Figure 5.10 and Figure 5.12 the scaled data are plotted as shown in Figure 5.13. It may be noted that all the points collapsed into two sets curves one for $T > T_C$ and the other for $T < T_C$. This means that the obtained values of β and γ and T_C are reasonably accurate.

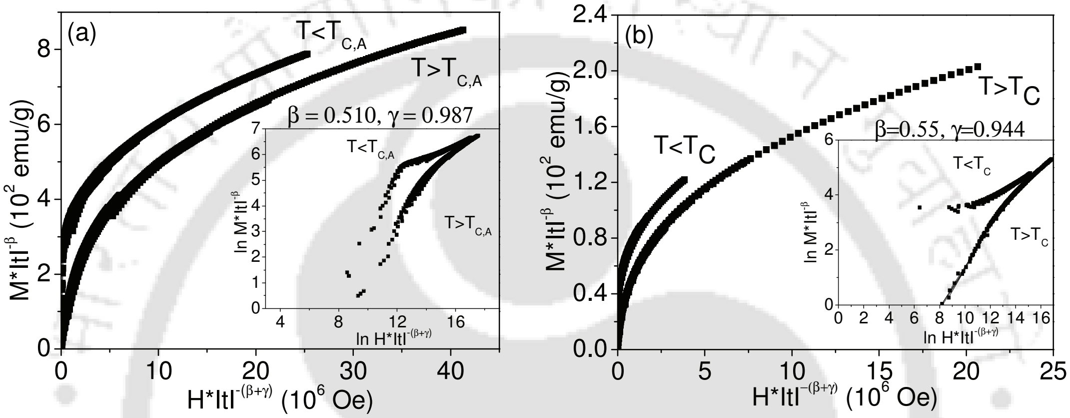

Figure 5.13: Scaling plots of $Ni_{50}Mn_{35}In_{14}Si_1$ below and above (a) $T_{C,A}$ and (b) $T_{C,M}$. Inset: Scaling plots on the logarithmic scale.

The values of another critical exponents δ associated with $M(H, T = T_C)$ are 2.935 and 2.716 for $T_{C,A}$ and $T_{C,M}$ respectively, which have been calculated using the Widom scaling relation [WIDO64a],

$$\delta = 1 + \frac{\gamma}{\beta} \tag{5.11}$$

Again, the linear fit to of lnM-lnH data (Figure 5.14) at $T_{C,A}$ and $T_{C,M}$ yield δ values of 2.950 and 2.670, respectively. The values of δ obtained from different methods are close to each other, which validate the results obtained.

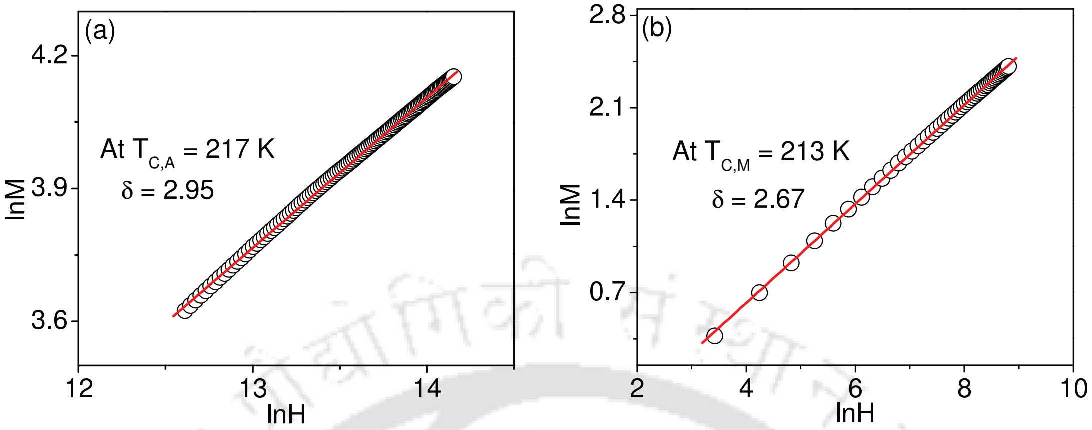

Figure 5.14: The high fields critical isotherm on a logarithmic scale at (a) $T_{C,A}$ and (b) $T_{C,M}$ along with the fitting curve (straight line) based on equation (5.6).

Isothermal ΔS_M as a function of applied magnetic field was evaluated from $(M - H)_T$ curves using the integrated Maxwell's relation [equation (1.23)]. Figure 5.15 shows the ΔS_M (H) data at $T_{C,A} \approx 316.5$ K and $T_{C,M} \approx 212.5$ K for the bulk $Ni_{50}Mn_{35}In_{14}Si_1$ alloy. An exponent n corresponding to ΔS_M at T_C of the magnetic material can be obtained using the relation [OEST84a, FRAN06a, FRAN08a].

$$\left(\Delta S_M\right)_{\max} \propto H^n \tag{5.12}$$

The nonlinear power law fit to the experimental $\Delta S_M (H)$ data provides $n = 0.671$ and 0.693 at $T_{C,A}$ and $T_{C,M}$ respectively. The correlation between n and the critical exponents (β and δ) near T_C of magnetic material can be expressed as [FRAN06a, FRAN08a].

$$n = 1 + \frac{1}{\delta}\left(1 - \frac{1}{\beta}\right) \tag{5.13}$$

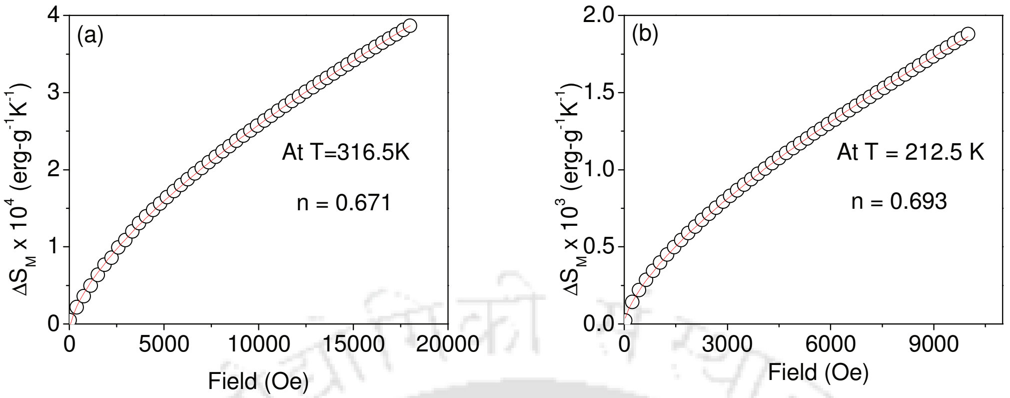

Figure 5.15: Field dependence of $(\Delta S_M)_{\max}$ at (a) $T_{C,A}$ and (b) $T_{C,M}$ for $Ni_{50}Mn_{35}In_{14}Si_1$ alloy (solid line is the fit to data shown as open circles).

n was estimated at T_C to be 0.753 in $Fe_{77}Co_{5.5}Ni_{5.5}Zr_7B_4Cu_1$ alloy [FRAN11a]. Considering that n = 0.667 as per mean-field theory (β = 0.5 and γ = 1), n = 0.638 as per 3D Heisenberg model (β = 0.365 and γ = 1.386) and n = 0.569 as per 3D Ising model (β = 0.325 and γ = 1.24) model [OLEG04a], the result obtained for $Fe_{77}Co_{5.5}Ni_{5.5}Zr_7B_4Cu_1$ alloy was not conclusively supporting any of the above models. Using the estimated values of β, γ and δ, for $Ni_{50}Mn_{35}In_{14}Si_1$ alloy, we have n =0.674 and 0.694 for $T_{C,A}$ and $T_{C,M}$ respectively which shows that the ΔS_M due to second-order phase transition is proportional to $H^{0.674}$ and $H^{0.694}$ for austenite and martensite phase respectively. These results agree well with the values obtained using the Maxwell's relation as well as mean field theory considerations which indicates long range magnetic interactions in both the phases.

According to Kim *et al.* [KIMD02a], due to small average crystallite size of polycrystalline sample as compared single-crystal sample, the reduced-temperature range is smaller than the fluctuation effects. These fluctuation effects may be responsible for the mean-field behaviour observed in the present case. Paskin [PASK60a] has shown that long-range interactions in ferromagnetic materials arising from the exchange interaction via conduction electrons and unfilled inner-shell electrons, do not disappear explicitly. Further, nuclear magnetic resonance studies on Cu-Mn alloys show the same magnitude of long range and the short-range interactions in these alloys [PASK60a]. In $Ni_{50}Mn_{35}In_{14}Si_1$ alloy due to high particle concentration or Mn rich concentration, the inter-particle magnetic interactions via Mn-Mn interaction can result in the formation of a collective or mean field state as indicated by the observed values of the critical exponents.

5.3. As-melt spun and annealed $Ni_{51}Mn_{34}In_{14}Si_1$ ribbons

The excellent MCE properties demonstrated by Si substituted Ni-Mn-In alloys motivated us to explore the potential of melt spinning method for enhancing the magnetic refrigerant properties of $Ni_{51}Mn_{34}In_{14}Si_1$ alloy. Therefore, a systematic study of the influence of solidification rate and heat treatment on the structural, magnetic and magneto-caloric properties of $Ni_{51}Mn_{34}In_{14}Si_1$ melt spun ribbons was carried out.

5.3.1. Crystal structures

Room temperature XRD patterns of as-spun $Ni_{51}Mn_{34}In_{14}Si_1$ alloy ribbons are shown in Figure 5.16(a). Cubic $L2_1$ structure corresponding to the austenite phase was observed in R_1 (melt spun with linear wheel speed of 12 m/s) and R_2 (melt spun with linear wheel speed of 16 m/s) ribbons, whereas R_3 (melt spun with linear wheel speed of 32 m/s) displayed a partially ordered cubic $B2$ structure. Thus, higher solidification rate induced by higher wheel speed of the melt spinner led to the introduction of partial ($B2$) crystalline order in this alloy ribbons. However, a brief heat treatment above 823 K was sufficient to convert the disordered alloy into the stable, ordered $L2_1$ structure as shown in Figure 5.16(b). $L2_1$ structure can be identified by the characteristic reflections from (111) and (311) planes. An XRD pattern of Heusler alloy devoid of these characteristic $L2_1$ peaks but exhibiting the (200) reflection indicates the presence of *B*2 structure in the alloy. Szytula *et al.* [SZYT89a] showed that when all the Miller indices are either even or odd, the cubic $L2_1$ structure with Heusler X_2YZ composition gives Bragg reflections with non-zero structure factors. For the first three reflections, the structure factors are $F(111) = 4(f_y - f_z)$, $F(200) = 4[2f_x - (f_y + f_z)]$, and $F(220) = 4[2f_x + f_y + f_z]$, where f_x, f_y and f_z are average scattering amplitudes for respective sub-lattices X, Y and Z. Since Y and Z atoms get intermixed in the *B*2 unit cell, $F(111)$ becomes zero, i.e., absence of peaks with all odd indices in the XRD patterns indicates a transition from the fully ordered $L2_1$ to partially ordered *B*2 structure.

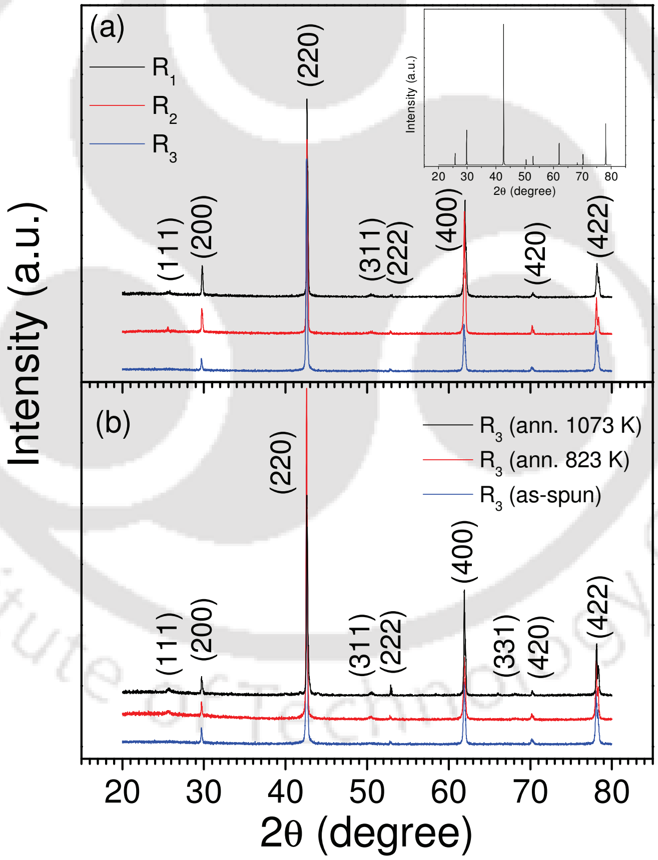

Figure 5.16. Room temperature XRD patterns of (a) as-spun R_1, R_2 and R_3 ribbons, and (b) R_3 ribbons annealed at different temperatures. Inset of (a) shows the theoretically simulated XRD pattern for the alloys using powder cell.

Degree of $L2_1$ order was estimated from the XRD patterns using the relation,

$$Degree\ \ of\ \ L_{21}\ \ order = (I_{111}/I_{220})_{\exp}/(I_{111}/I_{220})_{th} \tag{5.14}$$

where I_{hkl} represent the intensity of the reflection from the plane with Miller indices (*hkl*), and the suffices '*exp*' and '*th*' correspond to experimentally obtained and theoretically simulated data, respectively. Inset of Figure 5.16 (a) shows the theoretical XRD patterns which were simulated using powder cell software [KRAU96a, GORB11a].

Table 5.5: Lattice parameter, degree of order of $L2_1$ phase and average grain size for $Ni_{51}Mn_{34}In_{14}Si_1$ alloy ribbons prepared at different linear wheel speeds and annealed at different temperatures.

Sample (Anneal Temp.)	Lattice parameter (nm)	Degree of $L2_1$ order (%)	Average grain size (μm)
R_1 (as-spun)	0.5991 ± 0.0003	28	16.3
R_1 (823 K)	0.5983 ± 0.0002	29	18.1
R_1 (1073 K)	0.5975 ± 0.0003	31	19.3
R_2 (as-spun)	0.6000 ± 0.0003	22	2.9
R_2 (823 K)	0.5992 ± 0.0004	23	4.4
R_2 (1073 K)	0.5998 ± 0.0003	25	6.7
R_3 (as-spun)	0.6010 ± 0.0004	0	0.7
R_3 (823 K)	0.6000 ± 0.0002	17	0.8
R_3 (1073 K)	0.5998 ± 0.0002	27	2.3

Degree of $L2_1$ phase ordering in as-spun and heat treated ribbons estimated using relation 5.14 is listed in Table 5.5. Alloys melt spun at higher wheel speeds, showed a decrease (increase) in the degree of $L2_1$ order (lattice constant). It would be shown later that the solidification rate increases with an increase in linear wheel speed. On the other hand, with increasing heat treatment temperature, degree of $L2_1$ order (lattice parameter) increases (decreases). Higher solidification rates at faster wheel speeds introduce more disorder in the crystalline material, resulting in a decrease in the $L2_1$ order as well as a slight increase in the unit cell volume. Absence of $L2_1$ order in as-spun R_3 ribbons shows that such high solidification rates result in the disordered $B2$ structure. On the other hand, heat treatment provides thermal energy for the atoms to rearrange themselves into equilibrium ($L2_1$) configuration thereby relieving internal stresses accumulated during the rapid solidification process [SANC10a, XUAN08a]. This explains the increase in $L2_1$ order and slight reduction in the unit cell volume with increase in annealing temperature.

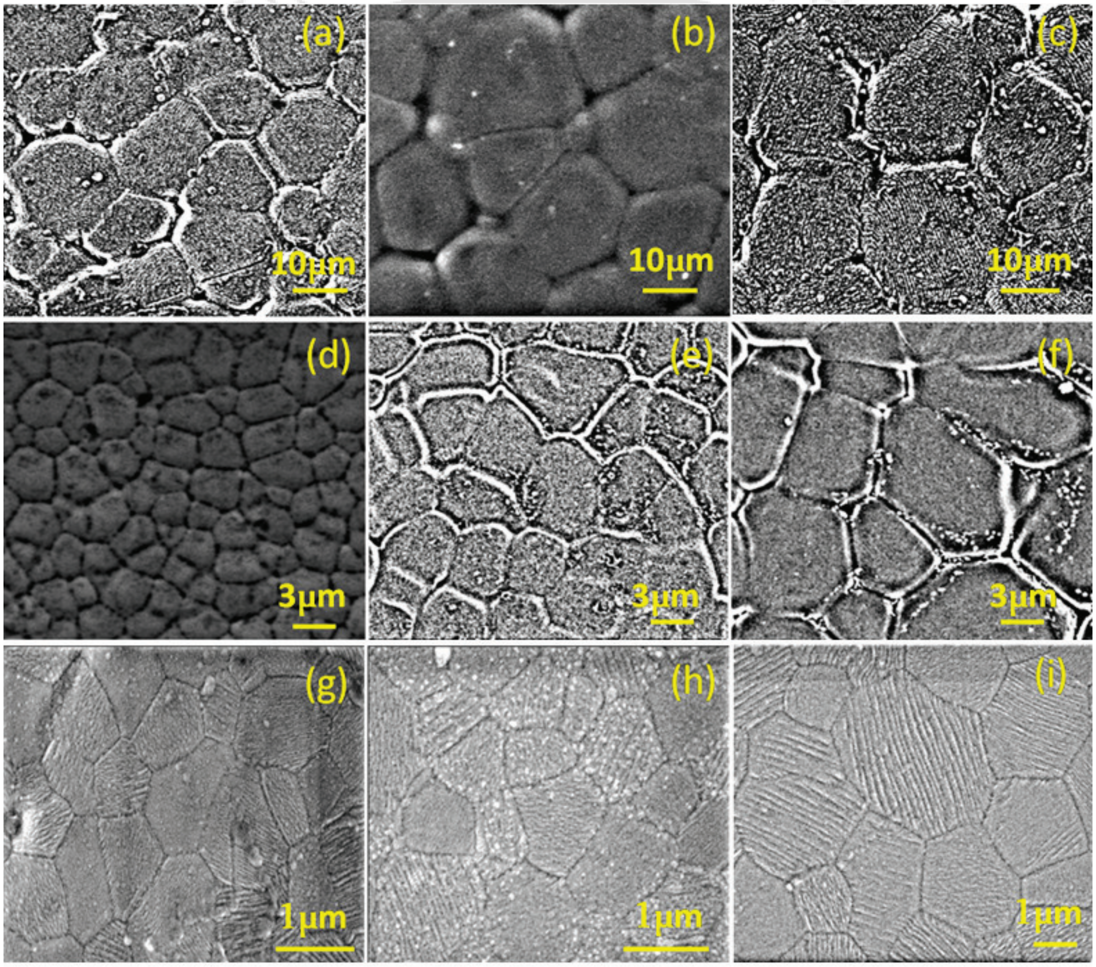

Figure 5.17: FESEM images of (a) as-spun R_1, (b) 823 K annealed R_1, (c) 1073 K annealed R_1, (d) as-spun R_2, (e) 823 K annealed R_2, (f) 1073 K annealed R_2, (g) as-spun R_3, (h) 823 K annealed R_3, and (i) 1073 K annealed R_3 ribbons.

5.3.2. Microstructure and thickness analysis

The FESEM micrographs of as-spun and heat treated (at 823 K and 1073 K) ribbons are shown in Figure 5.17. The micrographs illustrate that heat treatment not only relieves the accumulated stresses in the as-spun ribbons but also increases the average grain size as the annealing temperature is increased. The average grain sizes of as-spun and heat treated alloy ribbons are summarized in Table 5.5.

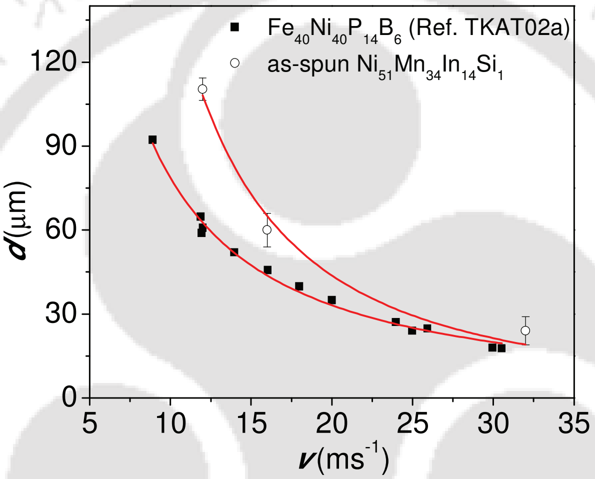

Figure 5.18: Dependence of ribbon thickness (d) on wheel speed (v) of as-spun ribbons. Data taken from ref. [TKAT02a] are shown for comparison.

Figure 5.18 presents the variation of ribbon thickness (d) with the linear wheel speed (v). In a typical cold block melt spinning process with orifice dimension, angle of melt injection and orifice-to-wheel distance kept constant, the solidification or quenching rate (dT/dt) is related to the linear wheel speed (v) as $dT/dt \propto v^n$ [LIEB81a, TKAT02a]. A power law fit for as-spun $Ni_{51}Mn_{34}In_{14}Si_1$ ribbons reveals a functional dependence of d on v as given by, $d \propto v^{-1.7}$. This empirical relation may be compared with a detailed study carried out by Tkatch *et al.* [TKAT02a] on $Fe_{40}Ni_{40}P_{14}B_6$ alloy ribbons which yielded the relations, $d \propto v^{-1.3}$ and $dT/dt \propto d^{-m}$ (where, $m = 3.1$). Greer [GREE82a] estimated the exponent m to be between

2 and 4 in the case of amorphous $Fe_{80}B_{20}$ melt-spun ribbons. Thus, higher wheel speed decreases (increases) d (cooling rate, dT/dt) [HUAN81a, GILL85a, BEWL86a]. Using a reasonable estimate for m (= 3), dT/dt was estimated for the present samples, which showed that solidification rate increases by nearly two orders of magnitude when the wheel speed is varied between 12 and 32 m/s.

5.3.3. Phase transitions

The characteristic temperatures related to phase transitions were obtained from the $M – T$ data. Figure 5.19 displays the $M – T$ curves of as-spun and heat treated R_2 ribbons recorded during cooling (solid symbols) and heating (open symbols) cycles in a magnetic field of 0.1 T. Inset of Figure 5.19 shows $M – T$ curves corresponding to the as-spun ribbons R_1, R_2 and R_3, which portrays the influence of solidification rate on the temperature dependent magnetization of the as-spun ribbons. It can be observed from the $M – T$ curves that magnetization values of the ribbons vary with temperature in the following manner: (i) As the temperature is increased from 100 K, magnetization decreased to almost zero around 240 K and then increased to a maximum value near 285 K. (ii) On further increasing the temperature, magnetization again decreased to zero. (iii) On the other hand, while decreasing the temperature from 300 K, magnetization first increased to a maximum value near 277 K. (iv) After reaching the maximum value, magnetization decreased to almost zero and then continuously increased on further decrease in temperature. (v) A careful inspection of the data around the range 235 K – 288 K confirms that the field cooled (FC) and field heated (FH) data do not follow the same path. A thermal hysteresis (ΔT_{hys}), due to the structural (martensite ↔ austenite) first-order phase transition is observed between the FC and FH curves for all the samples in the temperature range of 235 K – 288 K. The data reveal that all the samples exhibit one structural (martensite ↔ austenite) first-order phase transition and two magnetic transitions: one is in austenite phase (at $T_{C,A}$) and another in martensite phase (at $T_{C,M}$). Since MCE near $T_{C,M}$ is considerably smaller and is not of interest to this work, only $T_{C,A}$ would be referred in the remaining part of this chapter. It can also be observed that the samples are ferromagnetically ordered in austenite phase below $T_{C,A}$, until they begin to transform into martensite phase at T_{Ms}.

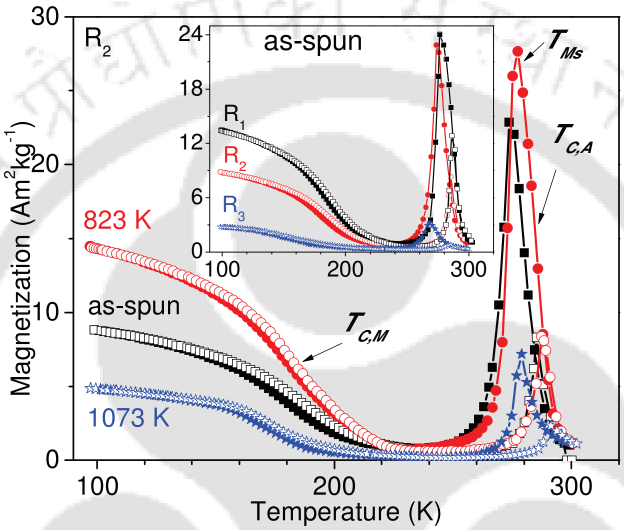

Figure 5.19: $M-T$ curves of as-spun and annealed R_2 ribbons recorded under an applied field of 0.1 T. Inset shows the $M-T$ curves of as-spun ribbons.

Characteristic temperatures of the alloy ribbons, viz., T_{Ms}, T_{As}, T_{Mf} and T_{Af} extracted from the $M-T$ data are summarized in Table 5.6. Characteristic temperatures of the ribbons decreased (increased) with increasing solidification rate (annealing temperature). ΔT_{hys} increased with increasing solidification rate. It can be noticed that ΔT_{hys} does not change upon annealing R_1 ribbon, whereas it decreases with increasing annealing temperature for R_2 and R_3 ribbons. Thermal hysteresis in FSMA is known to be a complicated process. From the microscopic view point, it is generally related to the nucleation of the new phase and the interaction of interfaces with defects. But from the mesoscopic view, it originates from the formation, annihilation, and rearrangement of elastically interacting domains [HUFX09a]. In addition, the friction from domain rearrangement and phase boundary motions also contribute to the hysteresis. Thus, ΔT_{hys} characterizes the strength of the friction during the transformation. In the present case, the effects of solidification rate and heat treatment on ΔT_{hys} confirm that the higher solidification rate can induce large internal stresses as well as defects in the alloy ribbons. As the annealing temperature is increased, internal stresses get relieved and defects get reduced resulting in an increase in the grain size. This results in a reduction in ΔT_{hys} in annealed samples as indicated in Table 5.6. On the other hand, the friction (caused by domain rearrangement and phase boundary motion during first-order phase transition) results in an incomplete transformation between martensite and austenite phases.

Table 5.6: Structural and magnetic parameters of (as-spun and heat treated $Ni_{51}Mn_{34}In_{14}Si_1$ alloy ribbons) obtained from $M - T$ data recorded at 0.1 T.

Sample	T_{Ms} **(K)**	T_{Mf} **(K)**	T_{As} **(K)**	T_{Af} **(K)**	$T_{C,A}$ **(K)**	ΔT_{hys} **(K)**
R_1 (as-spun)	276	254	271	286	290	13.5
R_1 (823 K)	278	256	274	287	294	13.5
R_1 (1073 K)	279	265	280	291	294	13.5
R_2 (as-spun)	274	245	269	285	288	17.5
R_2 (823 K)	277	252	273	287	290	16.5
R_2 (1073 K)	279	265	284	291	294	15.5
R_3 (as-spun)	269	243	268	284	287	20.0
R_3 (823 K)	275	246	271	286	289	18.0
R_3 (1073 K)	278	254	278	289	293	17.5

The nature of magnetism in the intermediate temperature range $T_{C,M} < T < T_{Mf}$ has evoked considerable interest among researchers in recent years. For an FSMA exhibiting complete transformation between the martensite and austenite phases, one would expect ideal paramagnetic state in this regime [RAMA10a]. Mossbauer studies on Ni-Mn-Sn alloy with ^{57}Fe has shown paramagnetic phase in this regime [UMET08a]. However, neutron polarization analysis of Ni-Mn-Sn alloy indicates the presence of antiferromagnetism in this regime [AKSO09a]. In order to understand the magnetic behavior in the present data in this temperature regime, we recorded isothermal magnetization curve at $T = 235$ K, where $T_{C,M} < T < T_{Mf}$ for our samples. Figure 5.20 shows the $M - H$ curves obtained for both as-spun and heat treated R_2 ribbons. Inset in Figure 5.20 portrays the data corresponding to the three as-spun ribbons. The nonlinear behaviour of the data at low field region indicates the presence of a small fraction of spontaneous magnetization (or ferromagnetism) in the intermediate temperature regime. Straight lines in the figure denote linear fits to the data in the high field region. Linear fits extrapolated to zero field yield the spontaneous magnetization of the impurity ferromagnetic phase present in the samples. The fraction of ferromagnetic phase present in the intermediate temperature ($T_{C,M} < T < T_{Mf}$) regime decreased as solidification rate and annealing temperature are increased. The impurity ferromagnetic phase is the residual (untransformed) austenite phase present in the samples.

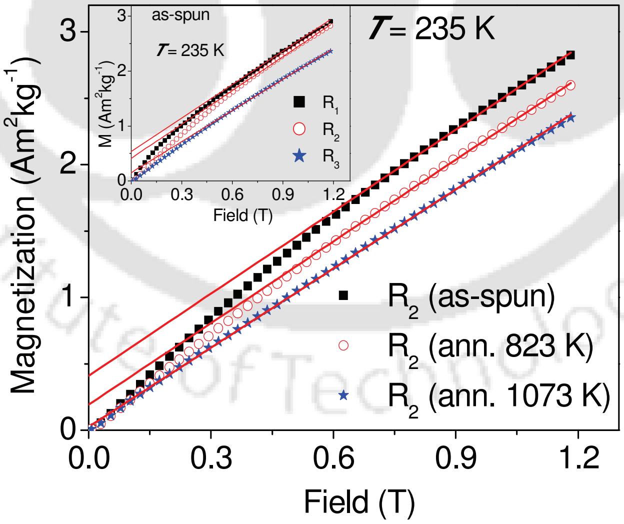

Figure 5.20: Initial magnetization curves recorded at $T = 235$ K for R_2 ribbons annealed at different temperatures. The inset presents the data corresponding to as-spun ribbons.

It is worthy to point out here that Aksoy *et al*. [AKSO09a] have also pointed out the existence of austenite fraction in this temperature regime in Ni-Mn-Sn alloy. Considering the evidence given by them for antiferromagnetism in this regime, presence of antiferromagnetic interaction cannot be ignored in the present case. However, given the convex nature of the nonlinearity near the origin in the *M-H* data shown in Figure 5.20, only observe the signature of weak ferromagnetism due to the untransformed austenite phase could be observed in the present samples in this temperature regime.

It can be also noted from Figure 5.19 that the magnitude of ΔM at the austenite to martensite transition and the magnetization values at the ferromagnetic state of the martensite phase decrease with increasing solidification rate. Annealing at lower temperature (823 K) improves magnetization at structural phase transition. On the other hand, higher annealing temperature (1073 K) decreases the magnetization drastically and shifts the phase transition temperatures to higher temperature as reported earlier [ROSA12a]. These dramatic magnetic and structural behaviours upon heat treatment could be attributed to increase in grain size, reduction of internal stresses accumulated during the rapid solidification process and reduction in Mn-Mn distance. In full Heusler (X_2YZ) alloys such as $Ni_{50}Mn_{25}In_{25}$, Mn atoms occupy the (½ ½ ½) position in the $L2_1$ unit cell. In off-stoichiometric Heusler compositions such as $Ni_{51}Mn_{34}In_{14}Si_1$, the excess Mn atoms occupy other positions such as (0 0 0) which is usually occupied by In atoms. Mn-Mn exchange interaction is very sensitive to interatomic distance. Annealing tends to modify the Mn atomic position, leading to reduction in interatomic distance [ROSA12a].

5.3.4. Magneto-caloric properties

In order to evaluate the MCE parameters such as ΔS_M and *RC*, initial isothermal magnetization curves ($M - H$) were recorded at close temperature intervals for all the ribbons around T_{Ms}. $M - H$ data were recorded as functions of increasing magnetic field from 0 to 1.2 T and decreasing temperature. Figure 5.21 shows the $M - H$ data for ribbons annealed at 823 K. These data show that the magnitude of magnetization decreased not only with increasing solidification rate but also with decrease in temperature. This behavior can be attributed either to the reduction in the grain size or to difficulty encountered in magnetization due to the presence of considerable amount of stresses accumulated during rapid solidification [XUAN08a]. ΔS_M was calculated as a function of temperature for ΔH of 1.2 T from $M - H$ curves using the integrated Maxwell's relation [equation (1.23)].

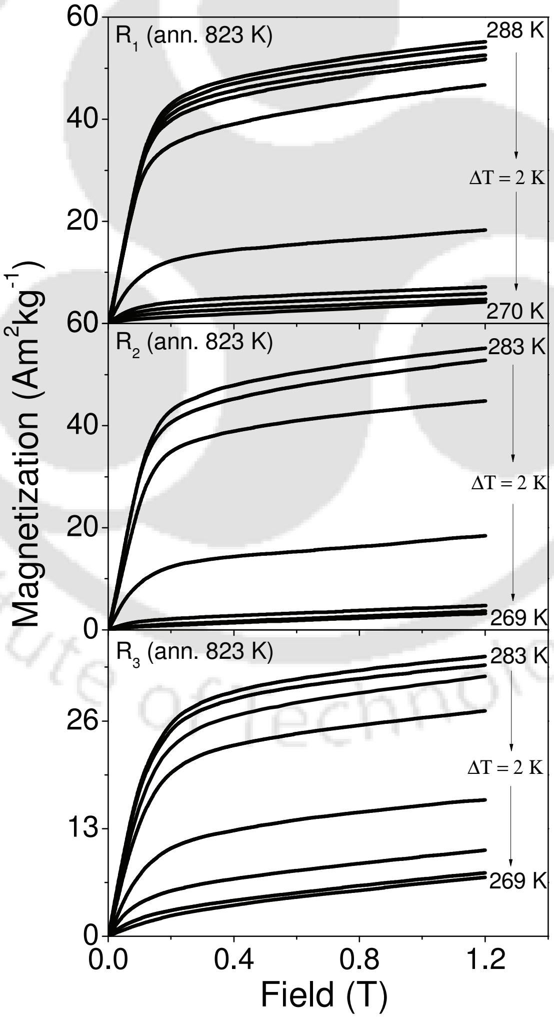

Figure 5.21: M-H curves of $Ni_{51}Mn_{34}In_{14}Si_1$ ribbons annealed at 823 K.

Temperature dependence of ΔS_M of the three ribbons annealed at 823 K is depicted in Figure 5.22 (a). Since *dM/dT* is positive around first-order structural phase transition, $\Delta S_M > 0$ in all the cases i.e. the samples cool down when the external magnetic field is applied adiabatically [TISH03a]. ΔS_M [FWHM of ΔS_M (T)] decreases [increases] with increase in solidification rate and annealing temperature. Annealing at lower temperature improves ΔS_M as shown in the Table 5.7. It can be observed that all the ribbons are in ferromagnetic state at T_{Ms} and due to the sudden jump in magnetization at a certain temperature, they exhibit a peak in ΔS_M [GAOB09a]. The highest peak ΔS_M (= 14.6 Jkg^{-1}K^{-1}) is obtained for the 823 K annealed R_1 ribbon. Almost the same ΔS_M (= 14.1 Jkg^{-1}K^{-1}) value with moderately large FWHM (= 3.5 K) is exhibited by 823 K heat treated R_2 ribbon. This peak ΔS_M of the ribbons can be correlated with the corresponding *dM*/*dT* value.

Table 5.7: Temperature derivative (*dM/dT*) at T_{Ms} obtained at 0.1 T field, magnetic entropy change (ΔS_M), full width at half maximum (FWHM) of $\Delta S_M(T)$, and refrigerant capacity (*RC*) for ΔH = 1.2 T and exchange bias (H_E) in $Ni_{51}Mn_{34}In_{14}Si_1$ alloy ribbons prepared at different wheel speeds and annealed at different temperatures.

Sample	d*M*/d*T* (Am^{2}kg^{-1}K^{-1})	ΔS_M (Jkg^{-1}K^{-1}) for ΔH = 1.2T	FWHM (K)	*RC* (Jkg^{-1})	H_E (mT) at 50 K
R_1 (as-spun)	3.8	11.2	3.1	29.0	4.5
R_1 (823 K)	4.4	14.6	2.9	31.8	5.1
R_1 (1073 K)	2.6	9.8	3.8	20.4	3.6
R_2 (as-spun)	2.9	10.5	3.6	23.0	4.2
R_2 (823 K)	4.2	14.1	3.5	37.3	4.8
R_2 (1073 K)	1.0	0.8	8.0	5.3	2.0
R_3 (as-spun)	0.3	0.7	7.3	4.0	1.9
R_3 (823 K)	2.2	5.7	4.0	17.3	3.3
R_3 (1073 K)	0.2	0.3	11.1	2.5	1.1

Comparison of these ΔS_M values with those reported in the literatures for ΔH of 1.2 T such as ~ 1.7 $Jkg^{-1}K^{-1}$ at 230 K for $Mn_{50}Ni_{40}In_{10}$ as-quenched ribbon [HUFX09a], ~5.5 $Jkg^{-1}K^{-1}$ at 284 K for $Ni_{45.5}Mn_{43}In_{11.5}$ ribbon annealed at 873 K [ROSA12a] and ~12.5 $Jkg^{-1}K^{-1}$ at ~198 K for $Ni_{48}Mn_{39}In_{12}Si_1$ ribbon annealed at 1173 K [ZHAO11a] reveals that the current results are very promising. *RC* of the magnetic refrigerant materials was obtained from ΔS_M (*T*) curves using equation (1.30). The highest *RC* (37.3 Jkg^{-1}) was obtained for 823 K annealed R_2 ribbon. The combined values of ΔS_M and *RC* values achieved in this work may also be compared with the values obtained for higher ΔH (0 – 3 T) in $Mn_{50}Ni_{40}In_{10}$ as-spun ribbon (3.6 $Jkg^{-1}K^{-1}$ and 71 Jkg^{-1} at 230 K) [HERN09a].

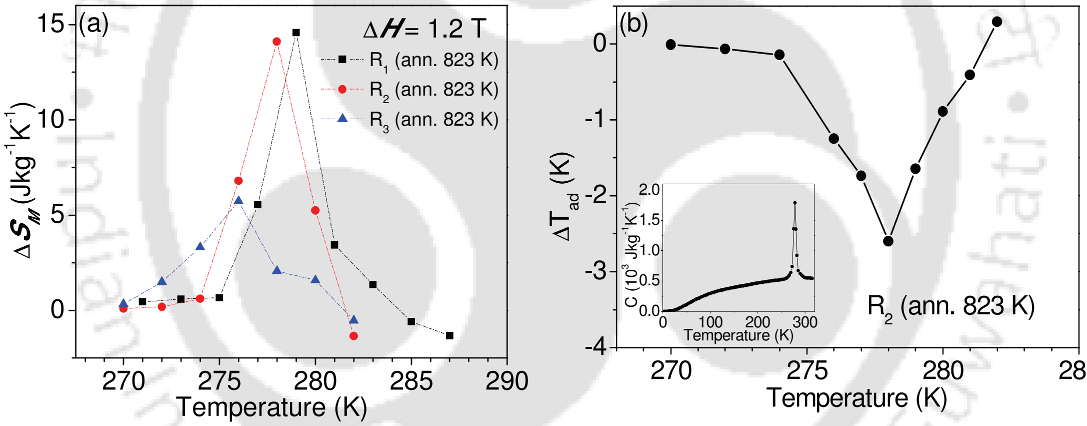

Figure 5.22: (a) Temperature dependence of ΔS_M for ΔH of 1.2 T obtained for ribbons annealed at 823K, (b) Temperature dependence of ΔT_{ad} obtained for ΔH of 1.2 T for R_2 ribbon annealed at 823 K. Inset show temperature dependent heat capacity at zero field.

ΔS_M for ΔH of 1.2 T calculated from $(M - H)_T$ curves is the difference of entropy for field of 1.2 T ($S_{H=1.2T}$) and the zero field entropy ($S_{H=0}$). $S_{H=0}$ can be evaluated from the heat capacity data at zero fields shown as inset in Figure 5.22 (b). $S_{H=1.2T}$ as a function of temperature has been estimated using the procedure outlined in chapter 2. Isentropic paths from $S(T)_{H=0}$ curve to $S(T)_{H=1.2T}$ curve at different temperatures result in $\Delta T_{ad}(T)$ shown in

Figure 5.22 (b). A moderate ΔT_{ad} of −2.6 K corresponding to ΔS_M of 14.1 Jkg^{-1}K^{-1} for ΔH of 1.2 T was exhibited by the R$_2$ ribbon annealed at 823 K. Since, higher *RC* signifies a larger heat transport, very high *RC* with reasonably high FWHM, ΔS_M and ΔT_{ad} values exhibited at temperatures close to the ambient temperature by 823 K annealed R$_2$ ribbon shows its potential for magnetic refrigerant application.

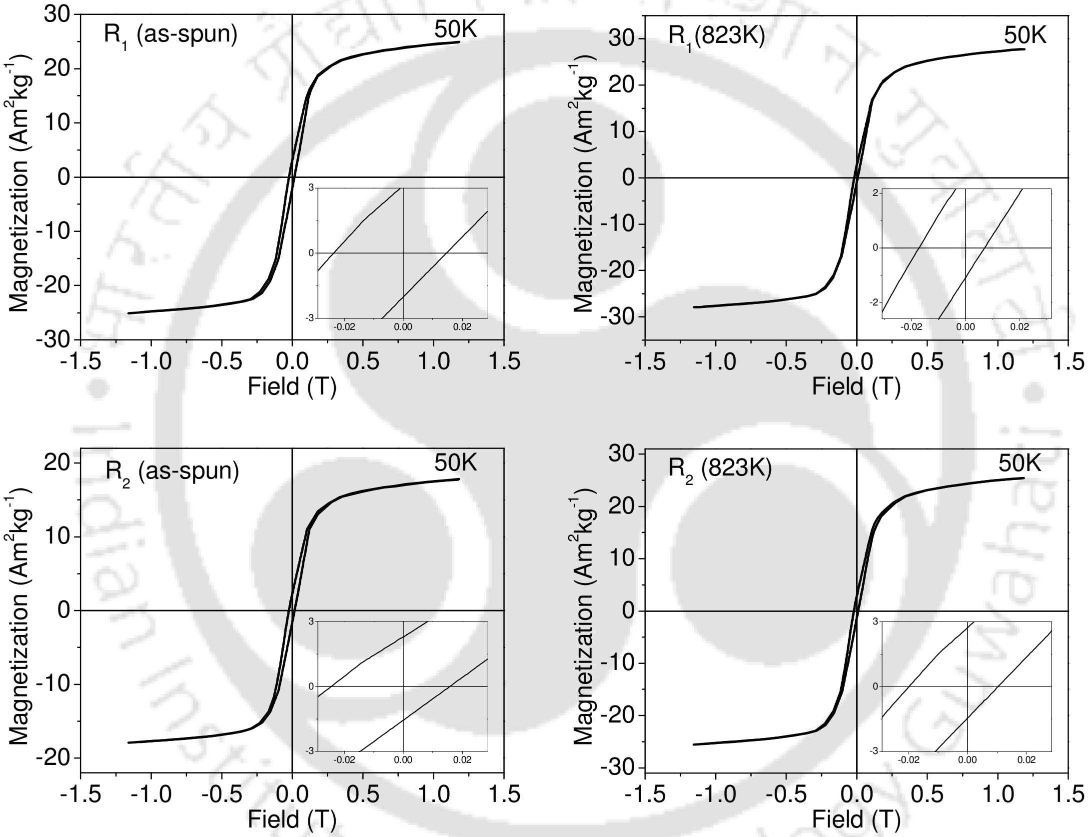

Figure 5.23. Magnetic hysteresis loops recorded under 1.2 T field at 50 K for $Ni_{51}Mn_{34}In_{14}Si_1$ as-spun and annealed ribbons. Inset shows an expanded view of the data near the origin.

5.3.5. Exchange bias

In order to investigate exchange bias effect in $Ni_{51}Mn_{34}In_{14}S_1$ ribbons, magnetic hysteresis loops were obtained from -1.2 T to +1.2 T at 50 K. M-H loops of as-spun and annealed R_1 and R_2 ribbons recorded at 50 K are depicted in Figure 5.23. H_E value of the ribbons was found to be less compared to the bulk. H_E was also found to decrease with increase in solidification rate. Annealing at lower temperature improves H_E as shown in Table 5.7. The highest H_E (= 5.1 mT) is obtained for the 823 K annealed R_1 ribbon. Observation of H_E suggests the presence of antiferromagnetic interactions in $Ni_{51}Mn_{34}In_{14}S_1$ ribbons. This can be correlated to the ferromagnetic exchange coupling between Mn atoms in the Mn sites and the antiferromagnetic interaction between Mn atoms in Ni or In anti-sites in the martensite state. After annealing, the as-spun ribbons undergo a structural relaxation and growth in grain size. These result in a slight modification of the atom site as well as the Mn–Mn distance which may disturb the ferromagnetic/antiferromagnetic exchange interaction in the system, leading to a change in H_E. The above results indicate that the exchange bias behavior in Ni–Mn based alloys can be tailored by changing the solidification rate and annealing temperature which affect the grain size and the degree of atomic ordering in the alloys.

5.4. Ball milled $Ni_{51}Mn_{34}In_{14}Si_1$ powders

Since particle size refinement can enhance *RC* despite reducing ΔS_M, it is expected that particle size refinement of an FSMA composition exhibiting very high ΔS_M can provide a means to tailor its ΔS_M and *RC* to required values suitable for magnetic refrigerant application for reasonably low magnetic field change. However, no systematic studies on the effect of Heusler alloy particle size over a wide range of sizes on MCE are available in the literature. In addition, it is important to note that for commercial exploitation of these magnetic refrigerants, large *RC* and ΔS_M near room temperature for viable magnetic fields (< 2 T) are required. This motivated a systematic investigation of the structural phase transition, magnetic phase transition and magneto-caloric properties of $Ni_{51}Mn_{34}In_{14}Si_1$ alloy with different particle sizes reported below.

5.4.1. Crystal structure

Figure 5.24 depicts the room temperature XRD patterns of heat treated bulk and three sets of sorted $Ni_{51}Mn_{34}In_{14}Si_1$ alloy powders. The particle preparation from bulk alloy by ball milling and the procedure adopted for size wise sorting of the heat treated powders are already discussed in detail at the beginning of this chapter. All the sets of powder samples exhibited the cubic $L2_1$ structure corresponding to $Fm\overline{3}m$ space group of austenite phase. No additional (martensite or impurity) phases were found in the XRD patterns. The $L2_1$ structure is identified by the characteristic (111) and (311) peaks as mentioned earlier. Rietveld analysis of the XRD patterns shown in Figure 5.25 reveal that alloy particles with sizes larger than 106 μm have the same unit cell dimension with lattice constant $a = 0.5974 \pm 0.0002$ nm. The lattice constant a increases to 0.5981 ± 0.0004 nm and 0.5992 ± 0.0002 nm for the finer samples P_{11} and P_{12}, respectively.

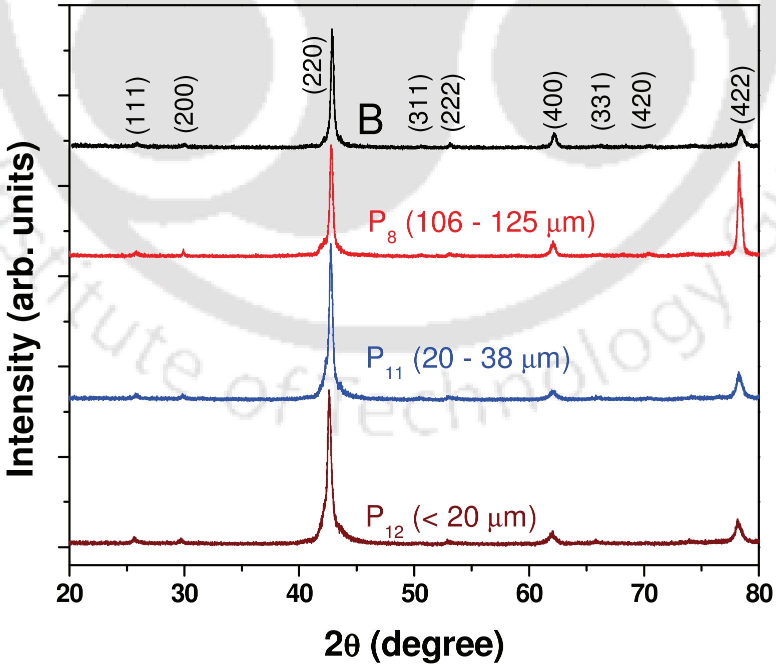

Figure 5.24: Room temperature XRD patterns of bulk and milled $Ni_{51}Mn_{34}In_{14}Si_1$ alloy powders with different average particle size (d_{av}).

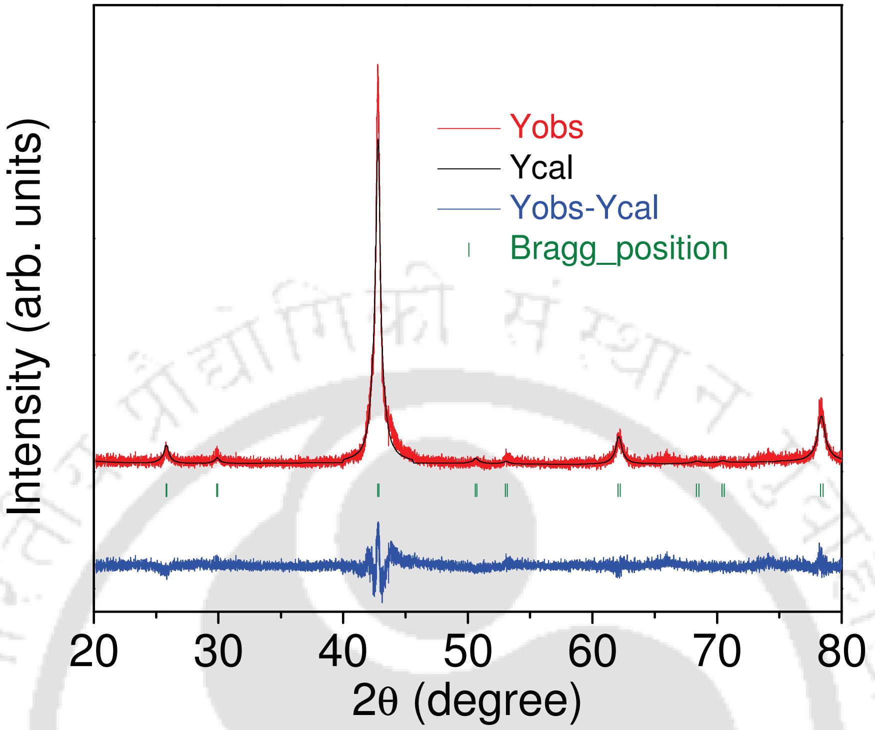

Figure 5.25: Typical Rietveld fit to room temperature XRD pattern of $Ni_{51}Mn_{34}In_{14}Si_1$ alloy powder $P_{11}$with particle size between 20 and 38 μm.

This slight variation in lattice constant could be attributed to the presence of residual stresses in the finer particles even after the annealing treatment. Features in the XRD pattern such as the pronounced asymmetrical tail of (220) reflection in P_{11} and P_{12} samples indicate inhomogenities in the alloy powder in the course of the milling process. This shows the presence of residual strain in the powder samples even after the annealing treatment. Microstrain estimated using Rietveld analysis of the XRD data was found to increase considerably in powders with particle size d_{av}< 125 µm. The crystallographic data obtained from the analysis are summarized in Table 5.8.

TABLE 5.8: Space group, Wyckoff positions, particle size, measured alloy composition, lattice parameter (*a*), unit cell volume (*V*), and microstrain obtained for bulk and milled alloy.

Space Group	**Wyckoff positions**
$Fm\bar{3}m$	In (0, 0, 0); Si (0, 0, 0); Mn (0, 0, 0) and (1/2, 1/2, 1/2); Ni (1/2, 1/2, 1/2) and (1/4, 1/4, 1/4).

Alloy ID	**Particle size, d_{av} (μm)**	**Composition from EDS**	***a*** (nm)	***V*** (nm)^3	**Microstrain $\times 10^{-2}$ (%)**
B	Bulk	$Ni_{50.69}Mn_{33.83}In_{14.07}Si_{1.41}$	0.5974	0.2132	25.9
P_1	850 – 1180	$Ni_{50.72}Mn_{33.89}In_{14.00}Si_{1.39}$	0.5974	0.2132	26.1
P_2	710 – 850	$Ni_{50.65}Mn_{33.85}In_{14.10}Si_{1.40}$	0.5974	0.2132	26.1
P_3	600 – 710	$Ni_{50.68}Mn_{33.90}In_{14.06}Si_{1.36}$	0.5974	0.2132	26.2
P_4	500 – 600	$Ni_{50.74}Mn_{33.91}In_{14.03}Si_{1.32}$	0.5974	0.2132	26.3
P_5	425 – 500	$Ni_{50.66}Mn_{33.80}In_{14.12}Si_{1.42}$	0.5974	0.2132	26.5
P_6	300 – 425	$Ni_{50.69}Mn_{33.89}In_{14.00}Si_{1.42}$	0.5974	0.2132	27.0
P_7	125 – 300	$Ni_{50.67}Mn_{33.85}In_{14.07}Si_{1.41}$	0.5974	0.2132	27.3
P_8	106 – 125	$Ni_{50.70}Mn_{33.87}In_{14.09}Si_{1.34}$	0.5974	0.2132	28.9
P_9	90 – 106	$Ni_{50.72}Mn_{33.88}In_{14.00}Si_{1.40}$	0.5975	0.2132	32.5
P_{10}	38 – 45	$Ni_{50.67}Mn_{33.83}In_{14.09}Si_{1.41}$	0.5977	0.2133	41.8
P_{11}	20 – 38	$Ni_{50.68}Mn_{33.84}In_{14.08}Si_{1.40}$	0.5981	0.2140	52.4
P_{12}	< 20	$Ni_{50.71}Mn_{33.85}In_{14.02}Si_{1.42}$	0.5992	0.2151	68.9

5.4.2. Microstructure and composition analysis

Figure 5.26 shows the SEM micrographs of four sets of $Ni_{51}Mn_{34}In_{14}Si_1$ alloy powders sorted by systematic sieving. All the dry milled powders show a typical flake-like morphology as they are subjected to cold welding and fracture inside the vial. The average size (d_{av}) of the particles was measured along the longest side of the flakes. It can be noticed that as the average particle size decreased, the particle shape becomes more spherical. Composition analysis of the samples by EDS reveal that the final composition of all the samples after milling and annealing is close to the starting composition. The results of the EDS analysis are summarized in Table 5.8.

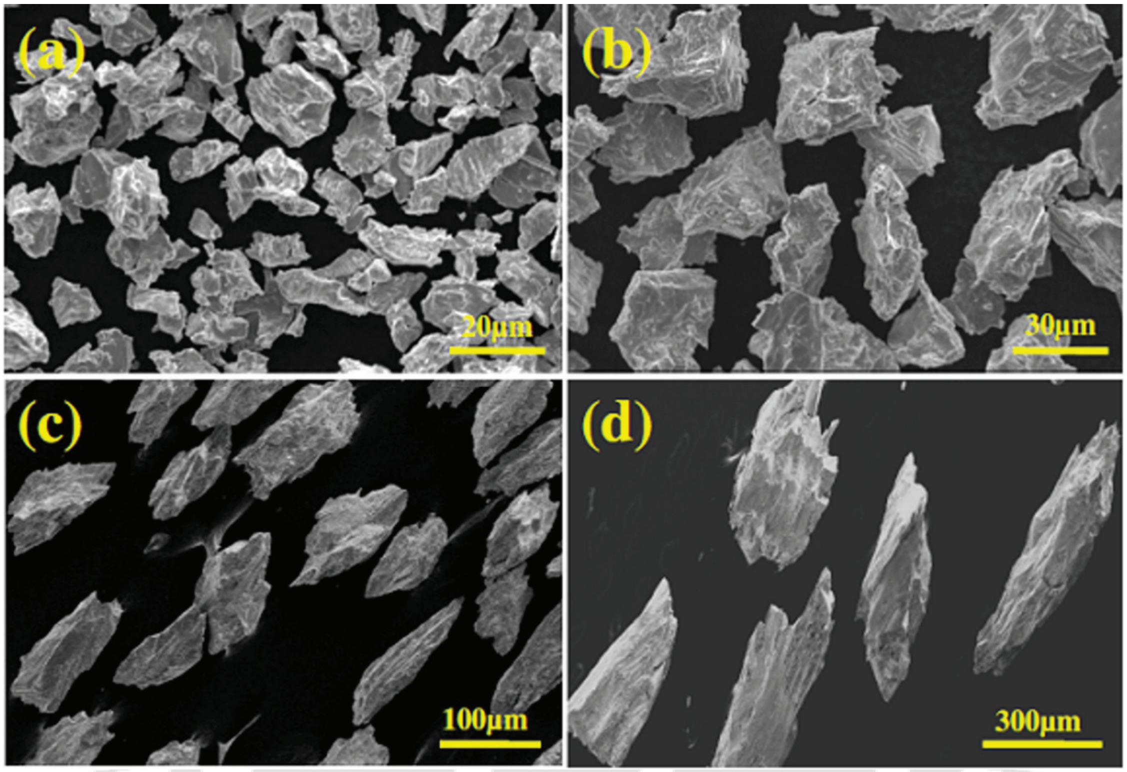

Figure 5.26**:** SEM images of sieved $Ni_{51}Mn_{34}In_{14}Si_1$ alloy powders sorted in different size ranges: (a) P_{12} (< 20 μm), (b) P_{11} (20 – 38 μm), (c) P_8 (106 – 125 μm) and (d) P_3 (600 – 710 μm).

5.4.3. Phase transitions

In order to understand the effect of particle size variation on the phase transition temperatures of the powder samples, temperature dependent magnetic properties were evaluated. Figure 5.27 shows the $M - T$ curves of the samples measured during field cooling (FC) and field heating (FH) cycles in a magnetic field of 0.1 T.

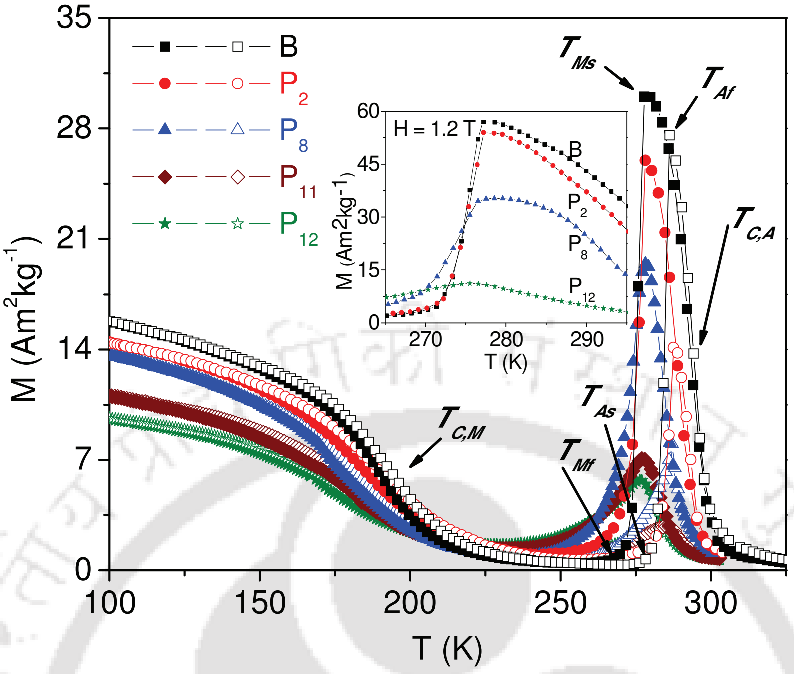

Figure 5.27: Plots of $M - T$ curves of bulk and sorted $Ni_{51}Mn_{34}In_{14}Si_{1}$ powders recorded under an applied field of 0.1 T. Filled and open symbols represent data recorded during field cooling and field heating, respectively. The inset presents the FC $M - T$ curves recorded at an applied field of 1.2 T.

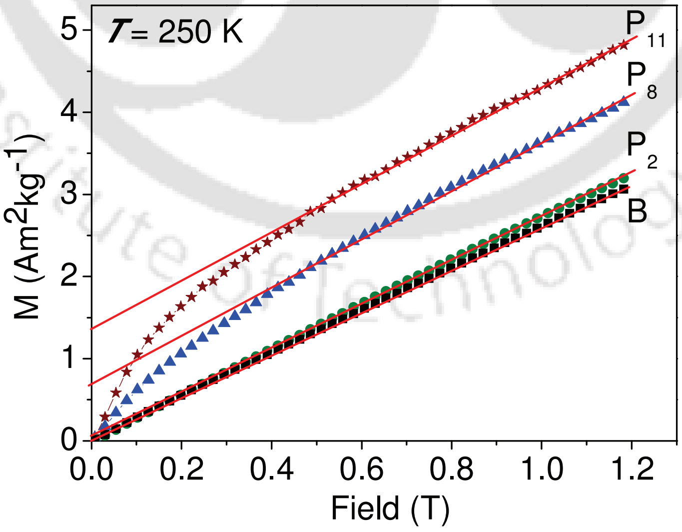

Figure 5.28: Initial magnetization curves recorded at $T = 250$ K for bulk and sorted three sets of $Ni_{51}Mn_{34}In_{14}Si_{1}$ alloy powders. Lines denote linear fit to the data at the high field.

The observed results reveal that all the samples are in austenite phase above room temperature and with decreasing temperature, the samples exhibit a magnetic phase transition from the paramagnetic state to ferromagnetic state in austenite phase (at $T_{C,A}$). Below $T_{C,A}$, the samples order ferromagnetically in the austenite phase until they begin to transform into the martensite phase at the martensite start temperature T_{Ms}. On further cooling the samples, they display another magnetic phase transition from the paramagnetic state to ferromagnetic state in the martensite phase (at $T_{C,M}$). All samples exhibit these two magnetic transitions. The characteristic temperatures (T_{Ms}, T_{As}, T_{Mf} and T_{Af}) are indicated in Figure 5.27. T_{Ms}, T_{As}, T_{Mf} and T_{Af} of all the samples extracted from the $M-T$ data are listed in Table 5.9. $M-T$ data recorded under FC condition at a higher magnetic field of 1.2 T is shown as an inset in Figure 5.27. Comparison of this data with the corresponding one in Figure 5.27 reveals a slight shift in the martensitic transition temperature towards lower temperatures at higher applied magnetic field. Such behaviour also observed in other FSMAs has been attributed to the magnetic field induced martensitic transition [SHAR10a]. $T_{C,A}$ and T_{Ms} for the bulk sample are 294 K and 278 K, respectively. In the case of the milled samples, $T_{C,A}$ and T_{Ms} do not deviate from the bulk value up to a particle size of 710 μm and 90 μm, respectively. For particles below this size, both $T_{C,A}$ and T_{Ms} decrease with a decrease in particle size (*cf.* Table 5.9). Figure 5.27 shows that the magnitude of ΔM at the martensitic phase transition decreases with decreasing particle size. This may be due to the change in the fraction of the martensite phase in the alloy and/or the change in the magnetic properties of the sample with a reduction in particle size. A thermal hysteresis (ΔT_{hys}) observed between the FC and FH curves for all the samples in the temperature range of 230 K to 290 K is attributed to the first-order martensitic transition. ΔT_{hys} was close to 9 K for particles with d_{av} down to 500 μm, after which a larger increase is seen with further decrease in particle size. As discussed in the case of the ribbon samples, ΔT_{hys} is generally related to the nucleation of the new phase and the interaction of interfaces with defects from the microscopic point of view. But from the mesoscopic point of view, the same originates from the formation, annihilation, and rearrangement of elastically interacting domains [HUFX09a]. In addition, the friction from domain rearrangement and phase boundary motions also contribute to the hysteresis. In other words, ΔT_{hys} characterizes the strength of the friction during the transformation. In the present case, the variation of ΔT_{hys} with particle size confirms that the friction encountered during the transformation increases with decreasing particle size. The reduction in the number of domains with reduction in particle size is understandable. However, when one considers the change in the shape of the hysteresis, contributions from the other factors listed above cannot be overruled. One such contribution is the incomplete transformation between the martensite and austenite phases which manifests as the non-zero magnetization observed in $M - T$ curves of the powder samples (Figure 5.27) in the temperature range $T_{C,M} < T < T_{Mf}$. $M - H$ data of $Ni_{50-x}Mn_{37+x}In_{13}$ alloys [RAMA10a] show typical paramagnetic behaviour in this intermediate temperature range. In order to explore this feature, isothermal magnetization curve was recorded at $T = 250$ K, where $T_{C,M} < T < T_{Mf}$ for our samples. Figure 5.28 depicts the $M - H$ curves obtained for samples designated as B, P_2, P_8 and P_{11}. While the bulk (B) sample shows linear field dependence which is characteristic of a paramagnet, the powder samples exhibit a nonlinear behaviour at low fields indicating the presence of a small fraction of spontaneous magnetization (or ferromagnetism). Straight lines, passing through the data points are linear fits to the data in the high field region, extrapolated to zero field yield the spontaneous magnetization of the impurity ferromagnetic phase present in the samples. Fraction of ferromagnetic phase present in the $T_{C,M} < T < T_{Mf}$ regime increases with a decrease in particle size. The impurity ferromagnetic phase is the residual (untransformed) austenite phase present in the samples. Also, the ratio between the maximum magnetization of FC curve in the austenite phase and the magnetization at the ferromagnetic martensite phase decreases significantly with decreasing particle size. This is mainly due to the increased number of particle surfaces in a given volume of the sample which tend to reduce the average magnetization of the sample as the particle size is decreased.

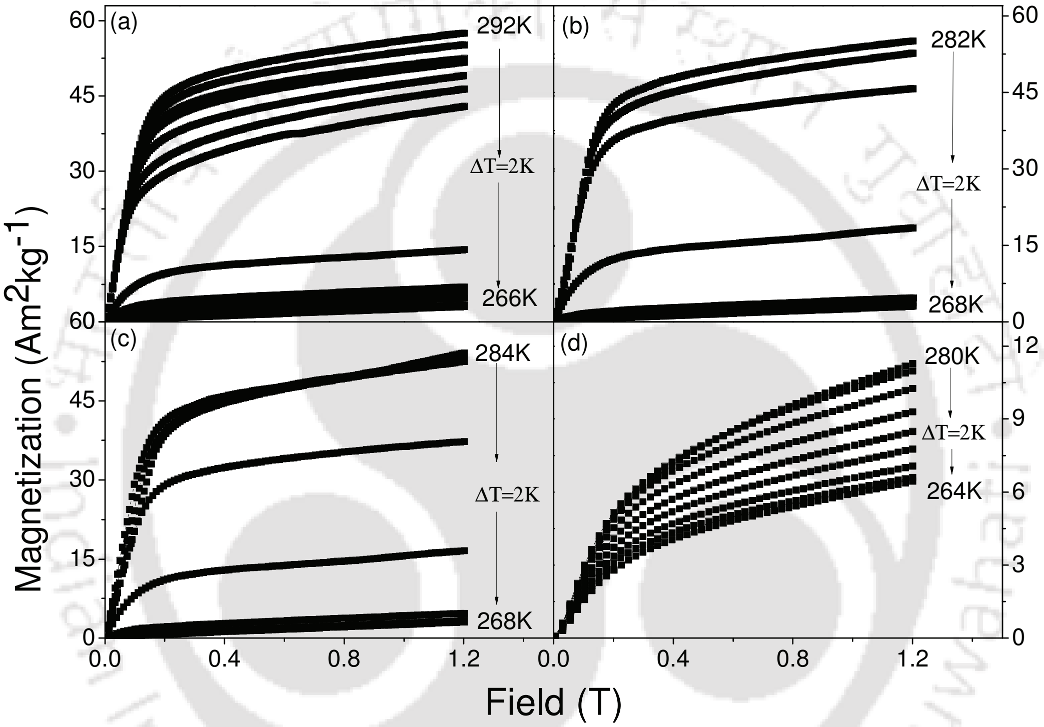

Figure 5.29: $M - H$ curves obtained for (a) B (bulk), (b) P_2 (710 – 850 μm), (c) P_3 (600 – 710 μm) and (d) P_{12} (< 20 μm) samples.

5.4.4. Magneto-caloric properties

Figure 5.29 displays the $M - H$ curves of $Ni_{51}Mn_{34}In_{14}Si_1$ samples with four different particle size ranges recorded close to T_{Ms}. It is obvious that all the samples are in ferromagnetic state at T_{Ms}. However, the magnitude of magnetization decreased with decreasing particle size as well as with decrease in temperature. The nature of the magnetization curves changes with decreasing particle size and magnetization did not saturate up to an applied field of 1.2 T.

This can be attributed either to the reduction in the particle size, which increases the number of particle surfaces and hence each particle would act like a single domain particle, or to the difficulty encountered in magnetization reversal due to the presence of considerable amount of strain in the smaller particles induced by the milling process. Nevertheless, it may be noted in each of the graphs that at a certain temperature the magnetization decreased suddenly [GAOB09a].

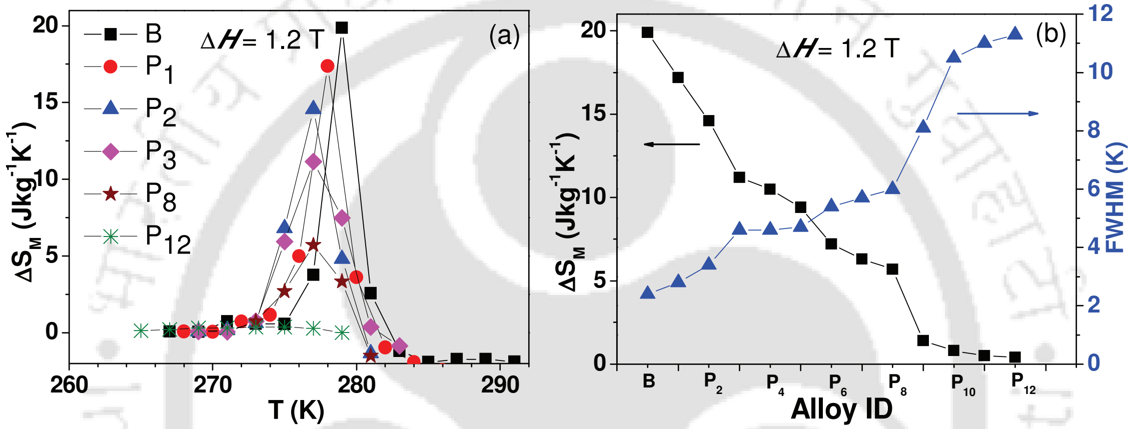

Figure 5.30: (a) Temperature dependence of ΔS_M obtained for ΔH of 1.2 T in bulk and milled $Ni_{51}Mn_{34}In_{14}Si_1$ alloy. (b) Peak ΔS_M(■) and FWHM of $\Delta S_M(T)$ curve (▲) of $Ni_{51}Mn_{34}In_{14}Si_1$ alloy powders of different particle sizes.

Using the integrated Maxwell's relation (equation 1.23), the temperature dependence of ΔS_M was evaluated from isothermal $M - H$ curves for a ΔH of 1.2 T. Figure 5.30a depicts ΔS_M as a function of temperature for the powders with different particle size ranges. ΔS_M is positive in all the cases because $\partial M/\partial T$ is positive at the martensitic phase transition. Positive ΔS_M implies that the sample cools down upon application of external magnetic field [RANK09a]. The characteristic features of MCE, viz., ΔS_M and FWHM of $\Delta S_M(T)$ decreased and increased, respectively, with a decrease in particle size as shown in the Table 5.9. The temperature at which peak ΔS_M is observed for each set of samples shows a shift towards lower values with a decrease in particle size (*cf.* Figure 5.30a). This feature can be correlated with the corresponding variation of $\partial M/\partial T$ with particle size depicted in Figure 5.27.

TABLE 5.9: Curie temperature ($T_{C,A}$), austenite start temperature (T_{As}), austenite finish temperature (T_{Af}), martensite start temperature (T_{Ms}), martensite finish temperature (T_{Mf}), thermal hysteresis (ΔT_{hys}) obtained at 0.1 T field, magneto-caloric parameters [magnetic entropy change (ΔS_M), full width at half maxima (FWHM) of $\Delta S_M(T)$ data, and refrigerant capacity (*RC*) obtained for 1.2 T field change] and exchange bias (H_E) of bulk and milled $Ni_{51}Mn_{34}In_{14}Si_1$ alloy.

Alloy ID	$T_{C,A}$ (K)	T_{As} (K)	T_{Af} (K)	T_{Ms} (K)	T_{Mf} (K)	ΔT_{hys} (K)	ΔS_M ($Jkg^{-1}K^{-1}$)	FWHM (K)	*RC* (Jkg^{-1})	H_E (mT) at 50 K
B	294	279	287	278	270	9.0	19.9	2.4	35.9	5.4
P_1	294	279	287	278	270	9.0	17.2	2.8	36.1	5.3
P_2	294	279	287	278	270	9.0	14.6	3.4	36.7	5.1
P_3	293	279	287	278	270	9.0	11.2	4.6	40.4	4.7
P_4	293	279	287	278	270	9.0	10.5	4.6	36.0	4.4
P_5	292	278	287	278	265	11.0	9.4	4.7	33.4	4.1
P_6	292	275	287	278	259	12.5	7.2	5.4	31.5	3.8
P_7	290	272	286	278	254	13.0	6.3	5.7	26.9	3.7
P_8	288	268	286	278	250	13.0	5.7	6.0	21.7	3.5
P_9	287	265	285	278	245	13.5	1.4	8.1	12.2	3.2
P_{10}	285	261	284	277	241	13.5	0.8	10.5	4.5	2.5
P_{11}	283	260	283	277	238	14.0	0.5	11.0	4.0	2.0
P_{12}	282.6	259	282	276	237	14.0	0.4	11.3	3.5	1.6

Though the highest peak ΔS_M (= 19.9 $Jkg^{-1}K^{-1}$) has been obtained for the bulk alloy, this sample has the disadvantage of having the narrowest operating temperature range (FWHM = 2.4 K). As can be seen from Figure 5.30b and Table 5.9, this disadvantage can be overcome by optimizing the particle size. An estimate of ΔT_{ad} of these samples would be useful for the potential of this material for magnetic refrigerant application. For this, $S(T)_H$

curves for H = 1.2 T were obtained using the ΔS_M for ΔH of 1.2 T and the zero field entropy ($S_{H=0}$), which can be evaluated from the heat capacity data obtained at zero field (*cf.* inset in Figure 5.31),

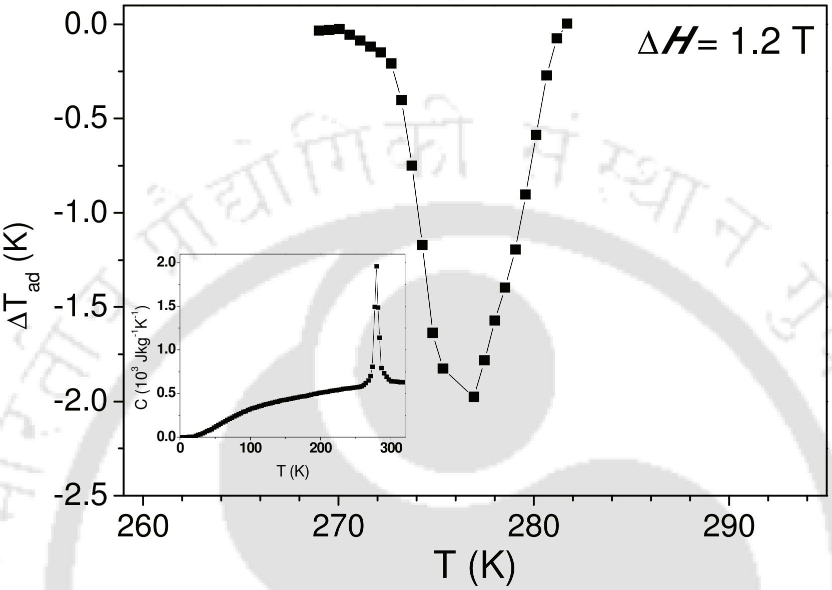

Figure 5.31: Temperature dependence of ΔT_{ad} for ΔH of 1.2 T corresponding to $Ni_{51}Mn_{34}In_{14}Si_1$ alloy particles with size in 600 – 710 µm range. Inset shows temperature dependent heat capacity at zero fields for the same particles.

Isentropic paths from $S(T)_{H=0}$ curve to $S(T)_{H=1.2T}$ curve at different temperatures yield $\Delta T_{ad}(T)$ shown in Figure 5.31. A moderate ΔT_{ad} of −1.99 K corresponding to ΔS_M (11.2 Jkg^{-1}K^{-1}) is exhibited by the P_3 powder sample (particles size between 600 – 710 μm) at 277 K for ΔH = 1.2 T. This value may be compared with ΔT_{ad} = −1.5 K and −1.99 K reported for Ge and Al substituted NiMnIn alloy for ΔH = 1.8 T, respectively [KAZA11a]. This comparison serves to highlight the potential of $Ni_{51}Mn_{34}In_{14}Si_1$ alloy powder for magnetic refrigerant application. *RC* values corresponding to the $\Delta S_M(T)$ curves first increased to the highest value and then decreased with particle size (depicted in Figure 5.32). Highest *RC* (40.4 Jkg^{-1}) value has been obtained for particles in the size range of 600 - 710 μm. Particles in this size range also exhibit moderately high values of FWHM (4.6 K), ΔS_M (11.2 $\mathrm{Jkg^{-1}K^{-1}}$) (*cf.* Figure 5.30b) and ΔT_{ad} (−1.99 K). The enhancement observed in *RC* values by decreasing the particle size range up to 600 – 710 μm is mainly influenced by the microstructural characteristics of the processed samples, which in turn impose significant control on the magneto-structural coupling [SANT08a, MARC03a], thereby leading to an overall increase in MCE.

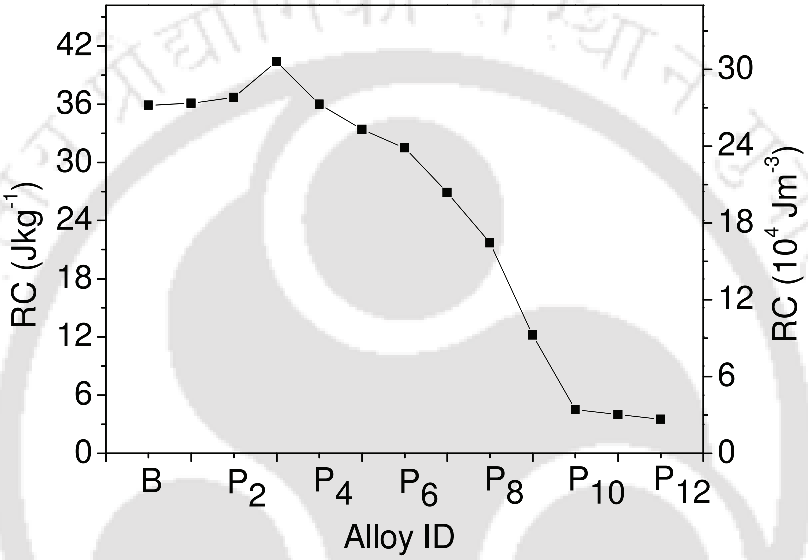

Figure 5.32: Temperature dependence of refrigerant capacity of bulk and milled $Ni_{51}Mn_{34}In_{14}Si_1$ alloy.

In addition, a survey of the literature and comparison with earlier reports [SANT08a, TANG05a] show that these combined values of MCE parameters appear to be highest ever reported for any FSMA powder. Since higher *RC* signifies a larger heat transport, $Ni_{51}Mn_{34}In_{14}Si_1$ alloy with particle size between 600 μm and 710 μm along with their high ΔS_M for a reasonably small ΔH of 1.2 T at temperatures close to the ambient show a lot of promise for magnetic refrigeration application. It would also be worthy to investigate the effect of particle shape and its influence on ΔS_M and *RC* of the powder particles. Particles with appropriate shape may yield higher ΔS_M and *RC* values. Powder particles have the inherent advantage of being capable of compaction into any desired macroscopic net shape, which may also be an advantage in their application as refrigerant as compared to the inflexible bulk samples.

5.4.5. Exchange bias

The exchange bias effect at 50 K in $Ni_{51}Mn_{34}In_{14}Si_1$ alloy powders is characterized by a shift of the $M - H$ loop (Figure 5.33) towards the negative field direction. H_E values of the powder samples were found to be smaller than that of the bulk. H_E decreases with decreasing particle size as shown in the Table 5.9. This observation suggests that with decreasing particle size, the antiferromagnetic contribution reduces and/or ferromagnetic fraction in the matrix increases, as a consequence of misplacement of Mn atoms in the Mn excess alloy favouring the local magnetic order to be either ferromagnetic or antiferromagnetic. This could lead to an antiferromagnetic phase segregation being dispersed in a ferromagnetic matrix. This antiferromagnetic contribution may be suppressed due to stray field which is strongly dependent on the particle size. Thus, the stray field destabilizes the antiferromagnetic alignment and reduces H_E.

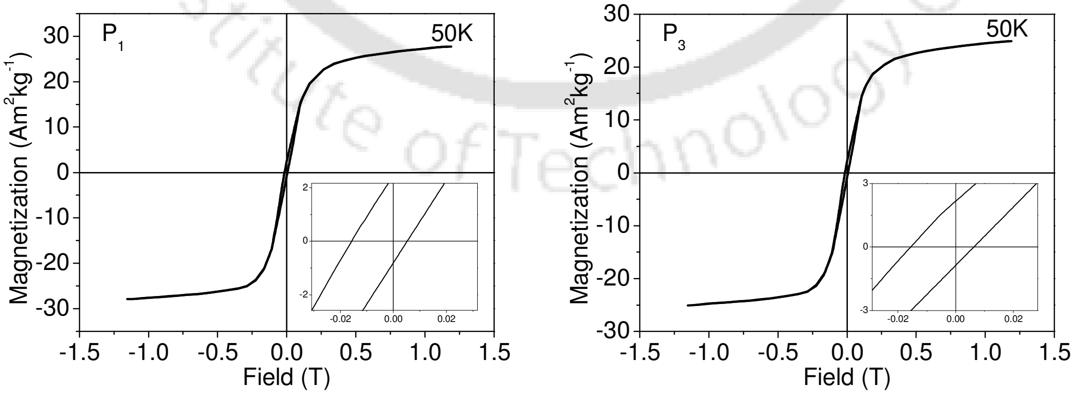

Figure 5.33. Magnetic hysteresis loops under 1.2 T field obtained at 50 K of two $Ni_{51}Mn_{34}In_{14}Si_1$ powder alloys. Inset shows an expanded view of the data near the origin.

5.5. Summary

Variations in magnetic and magneto-caloric properties by small change in Ni/Mn ratio in $Ni_{50}Mn_{35}In_{15}$ and $Ni_{50}Mn_{35}In_{14}Si_1$ bulk alloys have been studied. ΔS_M is positive in all the investigated alloys because $\partial M/\partial T$ is positive at the first order structural phase transition. Positive ΔS_M (or inverse MCE) implies that the sample cools down upon application of external magnetic field. Maximum ΔS_M of 19.9 $Jkg^{-1}K^{-1}$ was obtained for $Ni_{51}Mn_{34}In_{14}Si_1$ alloy at 279 K, just below the ambient temperature for a magnetic field change of 0 to 1.2 T in this study.

Effects of solidification rate and heat treatment temperature on the structural and magnetic refrigerant properties of $Ni_{51}Mn_{34}In_{14}Si_1$ ribbons have also been investigated. The study reveals that the grain size, inter-atomic distance and degree of atomic ordering in the melt spun ribbons can be controlled by process parameters such as wheel speed and annealing temperature. As-spun R_3 ribbon which crystallized in partially ordered $B2$ phase transformed to the equilibrium $L2_1$ structure after a short time (1/2 h) heat treatment above 823 K. T_{Ms} and $T_{C,A}$ shifted to higher temperatures upon heat treatment of the as-spun ribbons. Melt spinning at linear wheel speed of 16 m/s followed by annealing at 823 K proved to be the best choice of processing condition to achieve moderate ΔS_M (14.1 $Jkg^{-1}K^{-1}$) and highest RC (37.3 Jkg^{-1}) for a ΔH of 1.2 T. The highest ΔS_M (14.6 $Jkg^{-1}K^{-1}$) for ΔH of 1.2 T was found in heat treated R_1 (12 m/s) ribbons mainly due to its large dM/dT (4.4 $Am^2kg^{-1}K^{-1}$).

Magnetic and magneto-caloric properties of $Ni_{51}Mn_{34}In_{14}Si_1$ alloys with different particle sizes have been studied. The largest value of ΔS_M (19.9 $Jkg^{-1}K^{-1}$) was obtained for bulk $Ni_{51}Mn_{34}In_{14}Si_1$ alloy at 279 K for $\Delta H = 1.2$ T, owing mainly due to the large $\partial M/\partial T$ and ΔM realized at the martensitic phase transition. But, due to the smallest FWHM, the bulk sample may not be suitable for magnetic refrigerant application. Compared with the bulk, powdered particles show better magnetic refrigeration ability due to their larger *RC* as well as FWHM. The present studies on $Ni_{51}Mn_{34}In_{14}Si_{1}$ alloy show that optimization of the particle size of this alloy can yield powders with the desired combination of large ΔS_M, FWHM and *RC* near T_{Ms}. Particles in the size range of 600 – 710 μm exhibit moderately high values of FWHM (4.6 K), ΔS_M (11.2 $Jkg^{-1}K^{-1}$), and *RC* (40.4 Jkg^{-1}). $\Delta S_M(T)$ curves broaden with a decrease in particle size. The largest value of FWHM obtained was 11.3 K for particles with size < 20 μm, although they exhibit the lowest ΔS_M (0.4 $Jkg^{-1}K^{-1}$) and *RC* (3.5 Jkg^{-1}).

However, the best result of this study with maximum *RC* = 40.4 Jkg^{-1} corresponding to FWHM of 4.6 K and peak ΔS_M (ΔT_{ad}) of 11.2 $Jkg^{-1}K^{-1}$ (-1.99K) was obtained for the P_2 powder (particles within the size range of 600 μm to 710 μm). The present work indicates a methodology for tailoring the structural, magnetic and magneto-caloric properties of a promising magnetic refrigerant alloy by adopting different processing routes.

Exchange bias phenomenon has been observed in all the forms (bulk, ribbon and powder) of Ni-Mn-In-Si alloys studied. Bulk samples exhibited the highest H_E. Influence of shape and size as well as Ni/Mn ratio on H_E has been reported for the first time in these alloys. These results are expected to aid technological exploitation of these alloys in futuristic magnetic devices such as read heads for ultra-high density magnetic recording and spintronics devices.

Chapter 6

CONCLUSION AND SCOPE FOR FUTURE WORK

6.1. Conclusion

In any FSMA, the magneto-caloric properties are intimately linked with its phase transitions. In this thesis, the phase transitions (structural and magnetic) and MCE in selected Ni–Mn–X (Ga, Sn, In) based FSMAs such as $Ni_{55}Mn_{21-x}Ga_{24+x}$, $Ni_{53.75}Mn_{21.25-x}Co_xGa_{25}$, $Ni_{50}Mn_{37-x}Fe_xSn_{13}$, $Ni_{44}(Co/Cu)_2Mn_{43}Sn_{11}$ and $Ni_{50+x}Mn_{35-x}In_{15-y}Si_y$ alloys have been investigated. The compositions in each series of alloys were chosen such that the alloy has a room temperature martensite phase. The results presented in the previous three chapters would be of interest not only for the view point of investigation of phase transitions and the properties at these transitions but also from the application aspect related to novel magnetic refrigerant materials operating at low fields and at temperatures close to the ambient. The latter aspect is especially important in the tryst to develop cost effective environment friendly refrigeration systems. Some of the salient results obtained in the current thesis work are summarized below:

In $Ni_{55}Mn_{21-x}Ga_{24+x}$ series of alloys, samples with $x \leq 2$ exhibited tetragonal structure in martensitic phase and samples with x = 3 exhibited the typical $L2_1$ structure of the austenite phase at room temperature. With increasing Ga substitution for Mn, the unit-cell volume increased slightly in same (martensite) phase and finally transformed it into a new (austenite) phase. With increased Ga substitution in these alloys, Mn-Mn interactions weaken, leading a decrease in T_C. In samples with $x \leq 2$, the magnetic phase transition at T_C is accompanied by thermal hysteresis. The hysteresis around T_C in these alloys indicates that the second-order magnetic transition is accompanied by a first-order structural transition, i.e., a ferromagnetic martensite phase transforms to paramagnetic austenite phase (or the occurrence of a magneto-structural transition). The structural and magnetic phase transitions occur simultaneously when *e*/*a* ratio has the value of 7.6 – 7.66. Characteristic temperatures of magneto-structural transitions decrease with an increase in Ga content. The increase in M_{sat} at 2 T from 35.77 Am^2kg^{-1} for x = 0 to 51.86 Am^2kg^{-1} for the alloy with x = 2 at room temperature in the martensite state of $Ni_{55}Mn_{21-x}Ga_{24+x}$ alloys is mainly associated with magnetic moments of Mn atoms. K_{eff} exhibits a similar tendency as that of M_{sat} in this series of alloys. At room temperature, the alloy with x = 2 exhibited the highest K_{eff} value of 1.96×10^5 Jm^{-3}. With increasing Ga at.%, the magnitude of ΔE decreases resulting in a corresponding decrease in ΔG from 454 Jkg^{-1} for the alloy with x = 0 to 196 Jkg^{-1} for the alloy with x = 2. Lower energy change at the martensitic phase transition means smaller energy requirement for the martensite to austenite transition, which in turn results in smaller thermal hysteresis, ΔT_{hys}. $Ni_{55}Mn_{21}Ga_{24}$ alloy having same T_C and equilibrium temperature (T_0) exhibits the highest ΔE (ΔS and ΔG) of 8.5 $kJkg^{-1}$ (23.9 $Jkg^{-1}K^{-1}$ and 454 Jkg^{-1}) at 356 K, accompanied by the highest ΔS_M of -12.9 $Jkg^{-1}K^{-1}$ for ΔH of 2 T.

In $Ni_{53.75}Mn_{21.25-x}Co_xGa_{25}$ series of alloys, the XRD patterns could be indexed to a non-modulated tetragonal structure. The slight reduction in unit cell volume with Co addition indicates that Co replaces Mn. The magnetostructural transition occurs for *e*/*a* ratio range of 7.63 – 7.65. The characteristic temperatures of phase transitions and M_{sat} increased but K_{eff} decreased with increasing Co content. In the series, $Ni_{53.75}Mn_{20}Co_{1.25}Ga_{25}$ alloy exhibits the highest ΔS (ΔE and ΔG) of 24.1 $Jkg^{-1}K^{-1}$ (8.9 $kJkg^{-1}$ and 482 Jkg^{-1}), accompanied by highest ΔS_M of -17.7 $Jkg^{-1}K^{-1}$ at 354.5 K for a ΔH

of 2 T. Since the sign of ΔS_M is negative a direct or conventional MCE is present, i.e., the sample heats up when a magnetic field is applied adiabatically in the sample.

In $Ni_{50}Mn_{37-x}Fe_xSn_{13}$ alloys, though the parent sample devoid of Fe (designated as Fe_0) exhibited an orthorhombic structure corresponding to the martensite phase at room temperature, Fe addition led to the stabilization of cubic $L2_1$ structure corresponding to the austenite phase. The substitution of Fe leads to a decrease in the martensite start temperature (T_{Ms}) and an increase in the magnetization change (ΔM or $\partial M/\partial T$) as well as the area (ΔA) under the thermal hysteresis around the martensitic transition which are responsible for the increase in observed ΔS_M and RC in these alloys. $\partial M/\partial T$ values are 0.8, 2.1 and 4.1 A m^2 $kg^{-1}K^{-1}$ and ΔA are 163.7, 256.4 and 370.7 $Am^2kg^{-1}K$ for the alloys with x = 0, 1 and 1.25, respectively. The peak ΔS_M (RC) corresponding to the alloy composition with x = 0, 1, and 1.25 are 5.4 $Jkg^{-1}K^{-1}$ (25.4 Jkg^{-1}), 5.6 $Jkg^{-1}K^{-1}$ (25.5 Jkg^{-1}) and 6.9 $Jkg^{-1}K^{-1}$ (25.7 Jkg^{-1}), respectively for a ΔH of 1.8 T. Both peak ΔS_M and RC increase with an increase in Fe substitution.

In the case of $Ni_{44}Mn_{43}(Co/Cu)_2Sn_{11}$ alloys, Curie temperature ($T_{C,A}$) shifts from 314 K to 327 K while ΔM measured under 0.1 T increases from 4.6 Am^2kg^{-1} to 7.4 Am^2kg^{-1} upon Co substitution. T_{Ms} (thermal hysteresis) changes for the Co substituted sample from 291 K to 191 K (from 13 K to 22 K). However, for the Cu substituted alloy, T_C, ΔM, T_{Ms} and the thermal hysteresis are 298 K, 8.6 Am^2kg^{-1}, 270 K and 15 K, respectively. The martensitic transition of the parent ternary alloy ($Ni_{46}Mn_{43}Sn_{11}$) shifts to lower temperatures upon Co and Cu substitution. Peak ΔS_M obtained for the parent, Co substituted and Cu substituted alloys are 7.9, 11.3 and 18.8 $Jkg^{-1}K^{-1}$, respectively. It is evident from the studies that ΔS_M increased upon Co/Cu substitution. RC values corresponding to $\Delta S_M(T)$ curves obtained for $Ni_{46}Mn_{43}Sn_{11}$, $Ni_{44}Mn_{43}Co_2Sn_{11}$ and $Ni_{44}Mn_{43}Cu_2Sn_{11}$ alloys are 30.2 Jkg^{-1}, 30.3 Jkg^{-1} and 24.1 Jkg^{-1}, respectively. These results demonstrate a means of tailoring MCE (ΔS_M and RC) and the transition temperatures in Ni-Mn-Sn alloys by Fe, Co and Cu substitution. $Ni_{44}Mn_{43}Cu_2Sn_{11}$ alloys exhibited the highest positive ΔS_M of 18.8 $Jkg^{-1}K^{-1}$ for ΔH of 1.8 T at 270.5 K.

In Ni-Mn-In alloy system, the effect of variation of Ni/Mn ratio on the structural (martensitic) and magnetic phase transitions including associated properties of $Ni_{50}Mn_{35}In_{15}$ and $Ni_{50}Mn_{35}In_{14}Si_1$ bulk alloys was investigated. Exchange bias (H_E) phenomenon originating from the competition between antiferromagnetism and ferromagnetism in this FSMA has also been studied in all the bulk alloy compositions. Influence of Ni/Mn ratio on H_E has been reported for the first time in these alloys. These results are expected to aid technological exploitation of these alloys in futuristic magnetic devices such as read heads for ultra-high density magnetic recording and spintronics devices. Apart from these, the nature of magnetic interaction in the martensite and austenite phases in $Ni_{50}Mn_{35}In_{14}Si_1$ bulk alloy has been studied by examining the critical behaviour near the magnetic phase transitions. Comparison of the critical behaviour of magnetic phase transition in martensite and austenite phases of $Ni_{50}Mn_{35}In_{14}Si_1$ alloy provides new insights on the nature of magnetism in this alloy.

In order to understand the influence of shape and particle size on the structural, magnetic and magneto-caloric properties of $Ni_{51}Mn_{34}In_{14}Si_1$ alloy was prepared in ribbon and powder forms by melting spinning and ball milling routes. The highest ΔS_M (= 19.9 $Jkg^{-1}K^{-1}$) was observed for ΔH of 1.2 T field in bulk $Ni_{51}Mn_{34}In_{14}Si_1$ alloy. But this sample has a narrow operating temperature range [FWHM of $\Delta S_M(T)$ = 2.4 K] as well as relatively small *RC* (= 35.9 $\mathrm{Jkg^{-1}}$). Melt spinning at different wheel speeds and reduction of particle size by ball milling provided a way to vary the MCE parameters. The maximum *RC* of 40.4 $\mathrm{Jkg^{-1}}$, maximum FWHM of ΔS_M(T) of 4.6 K and high ΔS_M of 11.2 $\mathrm{Jkg^{-1}K^{-1}}$ were realized in annealed $\mathrm{Ni_{51}Mn_{34}In_{14}Si_1}$ alloy powder with particle size ranging between 600 μm and 710 μm. This is the best combination of MCE parameters ever reported for any FSMA in powder form. On the other hand, the best combination of MCE parameters (*RC* = 37.3 $\mathrm{Jkg^{-1}}$, FWHM = 3.5 K and ΔS_M = 14.1 $\mathrm{Jkg^{-1}K^{-1}}$) was obtained for melt spun (and annealed) ribbons prepared at a wheel speed of 16 $\mathrm{ms^{-1}}$. Solidification rate of melt spun ribbons and particle size of ball milled powders of Ni-Mn-In-Si FSMA provided two distinct mechanisms for tailoring the magnetic and magneto-caloric properties of the alloys as well as highlighting the role of size and shape variations of these alloys for possible applications.

Apart from these, the sign of ΔS_M is positive for all Ni-Mn-Sn and Ni-Mn-In based alloys due to the positive value of $\partial M/\partial T$ around the structural phase transition. This positive ΔS_M indicates inverse MCE, i.e., the sample cools when a magnetic field is applied adiabatically to these alloys.

6.2. Scope for future work

The present investigations on ternary and quaternary Ni-Mn-X FSMAs show how the structural, magnetic and magnetic refrigerant properties of these alloys could be tailored for operation at different temperatures by atomic substitution and particle size/shape variations. Since the martensitic transition of Ni-Mn-X alloys can be tuned by varying the electronic concentration (*e/a* ratio), selective additives can improve the multifunctional properties of these alloys. There is still a lot of scope for exploring the effect of different magnetic and non-magnetic additives with the view to further enhance the MCE properties of Ni-Mn-X alloys.

These FSMAs exhibit multifunctional (electrical, magnetic, thermal and mechanical) properties which have not yet been fully explored. Due to the martensitic transition, these materials can display varied phenomena such as large MFIS and magnetic super-elasticity. These properties have the potential for next generation actuator/sensor applications.

In the present work, the main focus was on tailoring the phase transition temperatures of Ni-Mn-X FSMAs and enhancing the associated magneto-caloric properties displayed by these systems. There is ample scope to study various other interesting physical properties of these FSMAs such as thermal conductivity, thermopower, Hall effect, kinetic arrest of magnetostructural transition, etc. Apart from these, investigating the effect of shape and size variations on their various physical properties may also provide interesting insights on these alloys.

Last but not the least, it would be pertinent to build a $Ni_{51}Mn_{34}In_{14}Si_1$ alloy based magnetic refrigeration system to validate the encouraging results obtained in this work and to showcase a Heusler alloy based magnetic refrigeration system with a better performance.

REFERENCES

[ABDU91a] Abdul-Razzaq W, Wu M, J. Appl. Phys. 69 (1991) 5078.

[AIKE93a] Aiken I D, Nims D K, Whittaker A S and Kelly J M, Earthquake Spectra 9 (1993) 3.

[AKSO09a] Aksoy S, Acet M, Deen P P, Mañosa L and Planes A, Phys. Rev. B 79 (2009) 212401.

[ALAM08a] Alam M S, Youssef M A and Nehdi M, Eng. Struct. 30 (2008) 3399.

[AMAR05a] Amaral J S, Reis M S, Amaral V S, Mendonca T M, Araujo J P, Sa M A, Tavares P B and Vieira J M, J. Magn. Magn. Mater. 290 (2005) 686.

[AMAR10a] Amaral J S and Amaral V S, J. Magn. Magn. Mater. 322 (2010) 1552.

[ANAN84a] Anantharaman T R, Metallic Glasses: Production, Properties and Applications, Trans Tech Publications, USA (1984).

[ANDR97a] Andreev S V, Bartashevich M I, Pushkarsky V I, Maltsev V N, Pamyatnykh A, Tarasov E N, Kudravatykh N V and Goto T, J. Alloys Compd. 260 (1997) 196.

[ANIN01a] An introduction to the program fullprof 2000 (Version July 2001).

[ARAK02a] Araki S, Sato K, Kagami T, Saruki S, Uesugi T, Kasahara N, Kuwashima T, Ohta N, Sun J, Nagai K, Li S, Hachisuka N, Hatate H, Kagotani T, Takahashi N, Ueda K and Matsuzaki M, IEEE Trans. Magn. 38 (2002) 72.

[ARRO57a] Arrott A, Phys. Rev 108 (1957) 1394.

[ARRO67a] Arrott A and Noakes J E, Phys. Rev. Lett. 19 (1967) 786.

[AVAD08a] Avadhanulu M N and Kshirsagar P G, A textbook of engineering physics for B.E., B.Sc. (Engg.), S. Chand and Company LTD. (2008).

[BANE64a] Banerjee S K, Phys. Lett 12 (1964) 16.

[BAOB08a] Bao B, Long Y, Duan J F, Shi P J, Wu G H, Ye R C, Chang Y Q, Zhang J and Rong C B, J. Appl. Phys. 103 (2008) 07B335.

[BARI11a] Barik S K, Krishnamoorthi C and Mahendiran R, J. Magn. Magn. Mater. 323 (2011) 1015.

[BAZA64a] Bazarov I P, Thermodynamics, Oxford, New York, Pergamon Press (1964).

[BEAN60a] Bean C P, Neugebauer C A, Newkirk J B and Vermilyea D A, Structure and Properties of Thin Films, Wiley, New York (1960).

[BEWL86a] Bewlay B P and Cantor B, Int. J. Rapid Solidification 2 (1986) 107.

[BHAN12a] Bhandari B, Sonsik Journal 4 (2012) 46.

[BHAT03a] Bhattacharya K, Microstructure of Martensite; Why it forms and How it Gives Rise to Shape Memory Effect, Oxford University Press, Oxford (2003).

[BHOB07a] Bhobe P A, Priolkar K R and Nigam A K, Appl. Phys. Lett. 91 (2007) 242503.

[BING09a] Bingham N S, Phan M H, Srikanth H, Torija M A and Leighton C, J. Appl Phys. 106 (2009) 023909.

[BOYD96a] Boyd J G and Lagoudas D C, Int. J. of plasticity 12 (1996) 805.

[BROW99a] Brown P J, Bargawi A Y, Crangle J, Neumann K U and Ziebeck K R A, J. Phys.: Condens. Matter 11 (1999) 4715.

[BROW05a] Brown P J, Kanomata T, Matzumoto M, Neumann K U and Ziebeck K R A, The structure and Transformation Mechanism in the Ferromagnetic Shape Memory Alloy Ni2MnGa" , in A. Planes, L. Mañosa, A. Saxena, Magnetism and Structure in Functional Materials, Springer-Verlag, berlin Heidelberg (2005).

[BROW06a] Brown P J, Gandy A P, Ishida K, Kainuma R, Kanomata T, Neumann K U, Oikawa K, Ouladdiaf B and Ziebeck K R A, J. Phys.: Condens. Matter 18 (2006) 2249.

[BRUC05a] Bruck E, J. Phys. D: Appl. Phys. 38 (2005) R381.

[BRUC08a] Br¨uck E, Magnetocaloric refrigeration at ambient temperature Handbook of Magnetic Materials, Amsterdam: Elsevier Science (2008).

[BRUC08b] Brück E, Tegus O, Cam Thanh D T, Trung N T, Buschow K H J, Int. J. Refrig. 31 (2008) 763.

[BUEH63a] Buehler W J, Gilfrich J V and Wiley R C, J. Appl. Phys. 34 (1963) 1475.

[CAHN83a] Cahn R W, Physical Metallurgy, Elsevier Science Publishers B V (1983).

[CAMP86a] Campbell I A, Hurdequint H and Hippert F, Phys. Rev. B 33 (1986) 3540.

[CHAI98a] Chaikin P M and Lubensky T C, Principles of condensed matter physics, Cambridge University Press, Cambridge (1998).

[CHAT10a] Chattopadhyay M K, Manekar M A, Sharma V K, Arora P, Tiwari P, Tiwari M K and Roy S B, J. Appl. Phys. 108 (2010) 073909.

[CHER98a] Chernenko V A, Segui C, Cesari E, Pons J and Kokorin V V, Phys. Rev. B. 57 (1998) 2659.

[CHER01a] Cherechukin A A, Dikshtein I E, Ermakov D I, Glebov A V, Koledov V V, Kosolapov D A, Shavrov V G, Tulaikova A A, Krasnoperov E P and Takagi T, Phys. Lett. A 291 (2001) 175.

[CHER03a] Cherechukin A A, Khovailo V V, Koposiv R V, Krasnoperov E P, Takagi T and Tani J, J. Magn. Magn. Mater. 258/259 (2003) 523.

[CHER04a] Cherechukin A A, Takagi T, Miki H, Matsumoto M, and Ohtsuka M, J. Appl Phys. 95 (2004) 1740.

[CHMI09a] Chmielus M, Zhang X X, Witherspoon C, Dunand D C and MÄullner P, Nat. Mater. 8 (2009) 863.

[COMS96a] Comstock R J, Buchheit T F, Somerday M and Wert J A, Acta Mater. 44 (1996) 3505.

[CULL01a] Cullity B D and Stock S R, Elements of X-ray diffraction, 3rd Edition, Pearson Education, Boston (2001).

[CULS96a] Culshaw B, Smart Structures and Materials, Artech House Publisher, San Diego, CA, (1996).

[DARN61a] Darnell F J, J Appl. Phys. 32 (Suppl.) (1961) 186S.

[DAUG93a] Daughton J M and Chen Y J, IEEE Trans. Magn. 29 (1993) 2705.

[DEBY26a] Debye P, Ann. Phys. 81 (1926) 1154.

[DEZF13a] Dezfuli F H, and Alam M S, Smart Mater. Struct. 22 (2013) 045013.

[DIEN91a] Dieny B, Speriosu V S, Parkin S S P, Gurney B A, Wilhoit D R and Mauri D, Phys. Rev. B 43 (1991) 1297.

[DIEN94a] Dieny B, J. Magn. Magn. Mater. 136 (1994) 335.

[DOER01a] Doerner M, Bian X, Madison M, Tang K, Peng Q, Polcyn A, Arnoldussen T, Toney M F, Mirzamaani M, Takano K, Fullerton E, Margulies D, Schabes M, Rubin K, Pinarbasi M, Yuan S, Parker M and Weller D, IEEE Trans. Magn. 37 (2001) 1052.

[DONK70a] Donkersloota H C and Van Vucht J H N, J. Less-Common Met. 20 (1970) 83.

[DUAN07a] Duan J F, Huang P, Zhang H, Long Y, Wu G H, Ye R C, Chang Y Q and Wan F R, J. Alloys and Comp. 441 (2007) 29.

[DUCN02a] Duc N H, Kim Anh D T and Brommer P E, Physica B. 319 (2002) 1.

[DUJZ07a] Du J, Zheng Q, Ren W J, Feng W J, Liu X G and Zhang Z D, J. Phys. D: Appl. Phys. 40 (2007) 5523.

[ESAK11a] Esakki Muthu S, Rama Rao N V, Sridhara Rao D V, Manivel Raja M, Devarajan U and Arumugam S, J. Appl. Phys. 110 (2011) 023904.

[FAHN78a] Fähnle M and Kronmüller H, J. Magn. Magn. Mater. 8 (1978) 149.
[FAJA10a] Fajar A, Gunawan, Kartini E, Mugirahardjo H and Ihsan M, Atom Indonesia 36 (2010) 111.
[FARA11a] Farahbakhsh I, Zakeri A, Manikandan P, Tanaka S and Hokamoto K, Jpn. J. Appl. Phys. 50 (2011) 01BE06.
[FENG07a] Feng C, Bing T, Li L and Yu-feng Z, Trans. Nonferrous Met. Soc. 17 (2007) s614.
[FEUC03a] Feuchtwanger J, Michael S, Juang J, Bono D, O'Handley R C, Allen S M, Jenkins C, Goldie J and Berkowitz A, J. Appl. Phys. 93 (2003) 8528
[FRAG91a] Fraga G L F, Branda˜o D E and Sereni J G, J. Magn. Magn. Mater. 102 (1991) 199.
[FRAN06a] Franco V, Bl´azquez J S and Conde A, Appl. Phys. Lett.89 (2006) 222512.
[FRAN08a] Franco V, Conde A, Romero-Enrique J M and Blazquez J S, J. Phys. Condens. Matter 20 (2008) 285207.
[FRAN11a] Franco V, Caballero-Flores R, Conde A, Knipling K E and Willard M A, J. Appl. Phys. 109 (2011) 07A905.
[FRAN12a] Franco V, Bl´azquez J S, Ingale B and Conde A, Annu. Rev. Mater. Res., 42 (2012) 305.
[FUJI02a] Fujieda S, Fujita A and Fukamichi K, Appl. Phys. Lett. 81 (2002) 1276.
[FUKU09a] Fukushima K, Sano K, Kanomata T, Nishihara H, Furutani Y, Shishido T, Ito W, Umetsu R Y, Kainuma R, Oikawa K and Ishida K, Scr. Mater. **61** (2009) 813.
[GAIT09a] Gaitzsch U, PÄotschke M, Roth S, Rellinghaus B and Schultz L, Acta Mater. 57 (2009) 365.
[GANG92a] Gangopadhyay S, Hadjipanayis G C, Sorensen C M and Klabunde K J, IEEE Trans. Magn. 28 (1992) 3174.
[GANG00a] Gangopadhyay S, Subramanian K, Ryan P, Mack A, Murdock E, Covault M L, Yan E, Champion E, Tampolsky G J, Feng Y C, Zhang Z, Chen D Q, Harkness S D, Ranjan R Y, Rauch G C and Richter H J, J. Appl. Phys. 87 (2000) 5407.
[GAOB09a] Gao B, Hu F X, Shen J, Wang J, Sun J R and Shen B G, J. Magn. Magn. Mater. 321 (2009) 2571.
[GAOB09b] Gao B, Shen J, Hu F X, Wang J, Sun J R and Shen B G, Appl. Phys. A 97 (2009) 443.
[GAOB09c] Gao B, Hu F X, Shen J, Wang J, Sun J R and Shen B G, J. Appl. Phys. 105 (2009) 083902.
[GAOL06a] Gao L, Cai W, Liu A L and Zhao L C, J. Alloys Compd. 425 (2006) 314.
[GAOL08a] Gao L, Sui J H and Cai W, J. Magn. Magn. Mater. 320 (2008) 63.
[GARV75a] Garvie R C, Hannink R H and Pascoe R T, Nature 258 (1975) 703.
[GEJI99a] Gejima F, Sutou Y, Kainuma R and Ishida K, Matell. Mater. Trans. 30 (1999) 2721.
[GEOG95a] Geoghegan D S, McCormick P G, Street R, Mater. Sci. Forum 179-181 (1995) 629.
[GHOS98a] Ghosh K, Lobb C J, Greene R L, Karabashev S G, Shulyatev D A, Arsenov A A and Mukovskii Y, Phys. Rev. Lett. 81 (1998) 4740.
[GIAU27a] Giauque W F, J. Am. Chem. Soc. 49 (1927) 1864.
[GIAU33a] Giauque W F and MacDougall D P, Phys. Rev. 43 (1933) 768.
[GILL85a] Gillen A G and Cantor B, Acta Metall. 33 (1985) 1813

[GLAV72a] Glazer A A, Potapov A P and Tagirov R I, Sov. Phys. JETP. Lett. 15 (1972) 259.

[GLAV06a] Glavatskyy I, Glavatska N, S¨oderberg O, Hannula S P and Hoffmann J U, Scripta Mater. 54 (2006) 1891.

[GOLU04a] Golub V O, Vovk A Y, Malkinski L, O'Connor C J, Wang Z and Tang J, J. Appl. Phys. 96 (2004) 3865.

[GOME06a] Gomes A M, Khan M, Stadler S, Ali N, Dubenko I, Takeuchi A Y and Guimarães A P, J. Appl. Phys. 99 (2006) 08Q106.

[GORB11a] Gorbachuk N P, Powd. Metall. Met. Ceram. 50 (2011) 239.

[GORD68a] Gordon P, Principles of phase diagrams in materials systems McGraw-Hill book company (1968).

[GRAH93a] Graham C D and Gibbs M R J, IEEE Trans. Magnet. 29 (1993) 3457.

[GREE82a] Greer A L, Acta Metall. 30 (1982) 171

[GRIFF95a] Griffith D J, Introduction to Electrodynamics, 2nd ed., Prentice hall, NewDelhi (1995).

[GSCH94a] Gschneidner Jr. K A, Takeya H., Moorman J O and Pecharsky V K, Appl. Phys. Lett. 64 (1994) 253.

[GSCH96a] Gschneidner Jr. K A, Pecharsky V K and Malik S K, Adv. Cryog. Eng. 42A (1996) 475.

[GSCH00b] Gschneidner Jr. K A and V K Pecharsky, Annu. Rev. Mater. Sci. 30 (2000) 387.

[GSCH08a] Gschneidner Jr. K A and Pecharsky V K, Int. J. Refrig. 31 (2008) 945.

[GUAN11a] Guan W, Liu Q R, Gao B, Yang S, Wang Y, Xu M W, Sun Z B and Song X P, J. Appl. Phys. 109 (2011) 07A903.

[GUPT78a] Gupta T K, Lange F F and Bechtold J H, J. Mater. Sci. 13 (1978) 1464.

[GURN97a] Gurney B A, Speriosu V S, Wilhoit D R, Lefakis H, Fontana Jr. R E, Heim D E and Dovek M, J. Appl. Phys. 81 (1997) 3998.

[HANZ06a] Han Z D, Wang D H, Zhang C L, Tang S L, Gu B X and Du Y W, Appl. Phys. Lett. 89 (2006) 182507.

[HARG81a] Hargitai C, Bakonyi I and Kemeny T, Metallic Glasses: Science and Technology proceedings, Central Research Institute for Physics, Hungary (1981).

[HATA98a] Hatakeyama T and Liu Z, Hand Book of Thermal Analysis, John Wiley & Sons, Chichister (1998).

[HEAT04a] Heat Capacity Option User's Manual 11th edition, Physical Property Measurement System (PPMS, Quantum Design) (2004).

[HEIM94a] Heim D E, Fontana Jr. R E, Tsang C, Speriosu V S, Gurney B A and Williams M L, IEEE Trans. Magn. 30 (1994) 216.

[HERN09a] Hernando B, Sa´nchez Llamazares J L, Prida V M, Baldomir D, Serantes D, llyn M and Gonzalez J, J Appl. Phys. Lett. 94 (2009) 222502.

[HEUS03a] Heusler F, Verh. dt. phys. Ges 5 (1903) 219.

[HOHN03a] Höhne G W H, Hemminger W F and Flammersheim H J, Differential Scanning Caloriemeter, Springer Verlag, Germany (2003).

[HORS06a] Horst C, Saito T and Smith L, Springer Handbook of materials measurement methods, Springer, Germany (2006).

[HSUC94a] Hsu C M, Lin H M and Tsai K R, J Appl Phys. 76 (1994) 4793.

[HUAN63a] Huang K, Statistical mechanics, John Willey & Sons, New York (1963).

[HUAN81a] Huang S and Fiedler H, Mater. Sci. Eng. 51 (1981) 39.

[HUFS00a] Hu F, Shen B and Sun J, Appl. Phys. Lett. 76 (2000) 3460.

[HUFS01a] Hu F, Shen B, Sun J and Wu G, Phys. Rev. B 64 (2001)132412.

[HUFX09a] Hu F X, Wang J, Shen J, Gao B, Sun J R and Shen B G, J. Appl. Phys. 105 (2009) 07A940.

[HUJS07a] Hu, J. Shape memory polymers and textiles, Woodhead Publishing Limited, Cambridge (2007).

[IMAN06a] Imano Y, Omori T, Oikawa K, Sutou Y, Kainuma R and Ishida K, Mater. Sci. Eng. A 438–440 (2006) 970.

[INGA07a] Ingale B, Gopalan R, Manivel Raja M, Chandrasekaran V and Ram S, J. Appl. Phys. 102 (2007) 013906.

[ITOW07a] Ito W, Imano Y, Kainuma R, Suto Y, Oikawa K and Ishida K, Metall Mater Trans A, 38A (2007) 759.

[IWAT70a] Iwata T, Kai K, Nakamichi T and Yamamoto M, J. Phys. Soc. Japan 28 (1970) 582.

[JACO63a] Jacobs I S and Bean C P, Magnetism, Academic Press, New York (1963).

[JAME96a] James R D and Wuttig M, Proc. SPIE 2715 (1996) 420.

[JIAN04a] Jiang C, Muhammad Y, Deng L, Wu W and Xu H, Acta Mater. 52 (2004) 2779.

[JING09a] Jing C, Chen J, Li Z, Qiao Y, Kang B, Cao S and Zhang J, J. Alloys Compd. 475 (2009) 1.

[JINZ98a] Jin Z Q, Tang W, Zhang J R, Qin H X and Du Y W, Eur. Phys J.B 3 (1998) 41.

[KAIN96a] Kainuma R, Ise M , Jia C C, Ohtani H and Ishida K, Intermetallics 4 (1996) S151.

[KARA09a] Karaca H E, Karaman I, Basaran B, Ren Y, Chumlyakov Y I and Maier H J, Adv. Funct. Mater. 19, (2009) 983.

[KAUL85a] Kaul S N, J. Magn. Magn. Mater 53 (1985) 5.

[KAZA11a] Kazakov A P, Prudnikov V N, Granovsky A B, Zhukov A P, Gonzalez J, Dubenko I, Pathak A K, Stadler S, and Ali N, Appl. Phys. Lett. 98 (2011) 131911.

[KHAN05a] Khan M , Dubenko I, Stadler S and Ali N, J. Appl. Phys. 97 (2005) 10M304.

[KHAN07a] Khan M, Ali N and Stadler S, J. Appl. Phys. 101 (2007) 053919.

[KHAN07b] Khan M, Stadler S and Ali N, J. Appl. Phys. 101 (2007) 09C515.

[KHAN07c] Khan M, Dubenko I, Stadler S and Ali N, Appl. Phys. Lett. 91(2007)072510.

[KHAN07d] Khan M, Dubenko I, Stadler S and Ali N, J. Appl. Phys. 102 (2007) 113914.

[KHAN08a] Khan M, Pathak A K, Paudel, M R, Dubenko I, Stadler S and Ali N, J. Magn. Magn. Mater. 320 (2008) L21.

[KHOV03a] Khovailo V V, Abe T, Koledov V V, Matsumoto M, Makamura H, Note R, Ohtsuka M, Shavrov V G and Takagi T, Mater. Trans. 44 (2003) 2509.

[KHOV03b] Khovailo V V, Oikawa K, Abe T, and Takagi T, J. Appl. Phys. 93 (2003) 8483.

[KIMD02a] Kim D, Zink B L, Hellman F and Coey J M D, Phys. Rev. B 65 (2002) 214424.

[KOGA82a] Koga S and Narita K, J. Appl. Phys. 53 (1982) 1655.

[KOHL99a] Kohl M, Liu Y, Krevet B, DÄurr S and Ohtsuka M, J. Phys. IV (France) 115 (2004) 333.

[KOHO04a] Koho K, S¨oderberg O, Lanska N, Ge Y, Liu X, Straka L, Vimpari J, Heczko O and Lindroos V K, Mater Sci. Eng. A 378 (2004) 384.

[KOOK93a] Kook L J and Hwan K, J. Mater. Sci. Lett. 12 (1993) 976.
[KOOL96a] Kools J C S, IEEE Trans. Magn. 32 (1996) 3165.
[KOUV59a] Kouvel J S and Graham C D Jr, J. Phys. Chem. Sol. 11 (1959) 220.
[KOUV61a] Kouvel J S, J. Phys. Chem. Sol. 21 (1961) 57.
[KOUV63a] Kouvel, J S J. Phys. Chem. Sol. 24 (1963) 795.
[KRAU96a] Kraus W and G. Nolze G, J. Appl. Cryst. 29 (1996) 301.
[KRAU05a] Krauss G, ASM International (2005).
[KREN05a] Krenke T, Duman E, Acet M, Wassermann E F, Moya X, Ma˜nosa L and Planes A, Nat. Mater. 4 (2005) 450.
[KREN05b] Krenke T, Acet M, Wassermann E F, Moya X, Mañosa L and Planes A. Phys. Rev. B 72 (2005) 014412.
[KREN06a] Krenke T, Acet M, Wassermann E F, Moya X, Mañosa L and Planes A, Phys. Rev. B 73 (2006) 174413.
[KREN07a] Krenke T, Duman E, Acet M, Wassermann E F, Moya X, Mañosa L, Planes A, Suard E and Ouladdiaf B, Phys. Rev. B 75 (2007) 104414.
[KREN07b] Krenke T, Duman E, Acet M, Moya X, Mañosa L and Planes A, J. Appl. Phys. 102 (2007) 033903.
[LANG05a] Langevin P, Ann. Chim. Phys. 5 (1905) 70.
[LEND02a] Lendlein A, and Kelch S, Angew. Chem. Int. Ed. 41 (2002) 2034.
[LENG08a] Leng Y, JohnWiley & Sons (Asia) Pte Ltd, Singapore (2008).
[LENS97a] Lenssen K M H, van Kestern H W, Rijks T G S M, Kools J C S, de Nooijer M C, Coehoorn R and Folkerts W, Sensors and Actuators A 60 (1997) 90.
[LEVY00a] Le´vy L P, Magnetism and Superconductivity, Springer, Berlin (2000).
[LIAN90a] Liang C, The Constitutive Modelling of Shape Memory Alloys, PhD Dissertation, Department of Mechanical Engineering, Virginia Polytechnic Institute and State University (1990).
[LIEB81a] Liebermann H H, J. Mater. Sci. 15 (1981) 2771.
[LINT00a] Lin T, Mauri D and Luo Y, IEEE Trans. Magn. 36(2000) 2563.
[LIUF00a] Liu F H, Stoev K, Shi X, Tong H C, Chien C, Dong Z W, Yan X, Gibbons M, Funada S, Liu Y, Prabhu P, Dey S, Schultz M, Malhotra S, Lal B, Kimmal J, Russak M and Kern P, IEEE Trans. Magn. 36(2000) 2140.
[LIUG06a] Liu G D, Dai X F, S. Yu S Y, Zhu Z Y, Chen J L, Wu G H, Zhu H and Xiao J Q, Phys. Rev. B 74 (2006) 054435.
[LIUY03a] Liu Y, Mater. Sci. Eng. A 354 (2003) 286.
[LIUZ02a] Liu Z H, Zhang M, Wang W Q, Wang W H, Chen J L, Wu G H, Meng F B, Liu H Y, Liu B D, Qu J P and Li Y X, J. Appl. Phys. 92 (2002) 5006.
[LIZJ07a] Li Z, Jing C, Chen J, Yuan S, Cao S and Zhang, J Appl. Phys. Lett. 91(2007) 112505.
[LOBO11a] Lobodyuk V A, Koval Y N and Pushin V G, Physics of Metals and Metallography 111 (2011) 165.
[LOFF97a] Loffler J, Wagner W, Swygenhoven H van, Meier J, Doudin B, Ansermet J P, Mater. Sci. Forum 235-238 (1997) 699.
[LOFF97b] Loffler J, Swygenhoven H van, Wagner W, Meier J, Doudin B, Ansermet J P, NanoStruct. Mater. 9 (1997) 523.
[LOUE98a] Louer D, Acta Cryst. A 54 (1998) 922.
[LUBO62a] Luborsky FS, Electro-Technology (1962).
[LUBO83a] Luborsky F E, Amorphous Metallic Alloys, Butterworth-Heinemann, UK (1983).

[LUOH13a] Luo H, Meng F, Liu G, Liu H, Jia P, Liu E, Wang W, Wu G, Intermetallics 38 (2013) 139.

[MACH03a] Machado L G and Savi M A, Braz. J. Med. Biol. Res. 36 (2003) 683.

[MACK01a] Mack A M, Subramanian K, Pust L R, Rea C J, Amin N, Seigler M A, Mao S, Xue S and Gangopadhyay S, IEEE Trans. Magn. 37(2001) 1727.

[MAGN13a] Magnetic Materials: Hard Magnets, University of Birmingham (2013).

[MARC84a] March N H, Lambin P and Herman F, J. Magn. Magn. Mater. 44 (1984) 1.

[MARC03a] Marcos J, Planes A, Manosa L, Casanova F, Batlle X and Labarta A, Phys. Rev. B 68 (2003) 094401.

[MARC04a] Marcos J, Ph.D. Thesis, Universitat de Barcelona, Barcelona (2004).

[MATS02a] Matsuzono A, Terada S, Ono H, Furukawa A, Sone T, Sasaki S, Kakihara Y, Takeda Y, Chiyokubo N and Matsuki H, J. Appl. Phys. 91(2002) 7267.

[MEIK56a] Meiklejohn W H and Bean C P, Phys. Rev. 102(1956) 1413.

[MEIK57a] Meiklejohn W H and Bean C P, Phys. Rev. 105 (1957) 904.

[MEIK58a] Meiklejohn W H, J. Appl. Phys. 29 (1958) 454.

[MEIK62a] Meiklejohn W H, J. Appl. Phys. 33 (1962) 1328.

[MOHA98a] Mohan Ch V, Seeger M, Kronmuller H, Murugaraj P and Maier J, J. Magn. Magn. Mater. 183 (1998) 348.

[MORI86a] Morita H, Hiroyoshi H, Fukamichi K, J. Phys. F 16 (1986) 507.

[MORI07a] Morito H, Fujita A, Oikawa K, Ishida K, Fukamichi K and Kainuma R, Appl. Phys. Lett. 90 (2007) 062505.

[MORI09a] Morito H, Oikawa K, Fujita A, Fukamichi K, Kainuma R and Ishida K, J. Phys.: Condens. Matter 21 (2009) 256002.

[MOYA06a] Moya X, Man˜ osa L, Planes A, Krenke T, Acet M and Wassermann E F, Mater. Sci. Eng. A 438–440 (2006) 911.

[NARA79a] Narasimhan M C, US Patent No. 4 (1979) 142 571.

[NIRM11a] Nirmala B, Vallal Peruman K, Amuthan R, Mahendran M, Nanosci. Nanotechno.1 (2011) 8.

[NOGU99a] Nogues J and Schuller I K, J. Magn. Magn. Mater. 192 (1999) 203.

[NOGU06a] Nogu´es J, Skumryev V, Sort J, Stoyanov S and Givord D, Phys. Rev. Lett. 97(2006) 157203.

[OEST84a] Oesterreicher H and Parker F T, J. Appl. Phys. 55 (1984) 4336.

[OIKA01a] Oikawa K , Wulff L, Iijima T, Gejima F, Ohmori T, Fujita A, Fukamichi K, Kainuma R and Ishida K, Appl. Phys. Lett. 79 (2001) 3290.

[OIKA01b] Oikawa K, Ota T, Gejima F, Ohmori T, Kainuma R and Ishida K, Mater. Trans. 42 (2001) 2472.

[OIKA02a] Oikawa K, Ota T, Sutou Y, Ohmori T, Kainuma R and Ishida K, Mater. Trans. 43 (2002) 2360.

[OIKA02b] Oikawa K, Ota T, Ohmori T, Tanaka Y, Morito H, Fujita A, Kainuma R, Fukamichi K and Ishida K, Appl. Phys. Lett. 81 (2002) 5201.

[OIKA06a] Oikawa K, Ito W, Imano Y, Sutou Y, Kainuma R, Ishida K, Okamoto S, Kitakami O, and Kanomata T, Appl. Phys. Lett. 88 (2006) 122507.

[OLEG04a] Olega A, Salazar A, Prabhakaran D and Boothroyd A T, Phys. Rev. B 70 (2004) 184402.

[OMOR11a] Omori T, Ando K, Okano M, Xu X, Tanaka Y, Ohnuma I, Kainuma R and Ishida K, Science 333 (2011) 68.

[OTSU98a] Otsuka K and Wayman C M, Shape Memory Materials, Cambridge University Press, UK (1998).

[OTSU99a] Otsuka K and Ren X, Intermetallics 7 (1999) 511.

[OTSU02a] Ostuka K and Kakeshita T, MRS Bulletin 27(2002) 91.

[PAPA90a] Papaefthymiou V, Kostikas A, Simopulos A, Niarchos D, Gangopadhyay S, Hadjipanayis G C, Sorensen C M and Klabunde K J, J. Appl. Phys. 67 (1990) 4487.

[PARE03a] Pareti L, Solzi M, Albertini F and Paoluzi A, Eur. Phys. J. B 32 (2003) 303.

[PASK60a] Paskin A, J. Appl. Phys. 31 (1960) S318.

[PASQ05a] Pasquale M, Sasso C P, Lewis L H, Giudici L, Lograsso T and Schlagel D, Phys. Rev. B 72 (2005) 094435.

[PASS09a] Passamani E C, Xavier F, Favre-Nicolin E, Larica C, Takeuchi A Y, Castro I L and Proveti J R, J. Appl. Phys. 105 (2009) 033919.

[PATH07a] Pathak A K, Khan M, Dubenko I, Stadler S and Ali N, Appl. Phys. Lett.. 90(2007) 262504.

[PATH08a] Pathak A K, Khan M, Dubenko I, Stadler S and Ali N, J. Phys. D: Appl. Phys. 41(2008) 202004.

[PATH09a] Pathak A K, Khan M, Gautam B R, Stadler S, Dubenko I and Ali N, J. Magn. Magn. Mater. 321(2009) 963

[PATH09b] Pathak A K, Dubenko I, Stadler S and Ali N, IEEE Trans. Magn. 45(2009) 3855.

[PECH97a] Pecharsky V K and Gschneider K A, Phys. Rev. Lett. 78 (1997) 4494.

[PECH99b] Pecharsky V K and Gschneidner K A Jr, J. Magn. Magn. Mater. 200 (1999) 44.

[PECH01a] Pecharsky V K, Gschneider K A Jr, Pecharsky A O and Tishin A M, Phys. Rev. B 64 (2001) 144406.

[PECH01b] Pecharsky V K and Gschneidner K A Jr, J. Appl. Phys. 90 (2001) 4614.

[PECH05a] Gschneidner K A Jr, Pecharsky V K and Tsokol A O, Rep. Prog. Phys. 68 (2005) 1479.

[PECH06a] Pecharskya V K, Gschneidner K A Jr, Int. J. Refrig. 29 (2006) 1239.

[PERK99a] Perkins J and Hodgson D, The Two-Way Shape Memory Effect, in: Engineering Aspects of Shape Memory Alloys, 1st ed. T. W. Duerig et al., eds., Stoneham, Massachusetts: Butterworth-Heinemann, (1999).

[PHAN05a] Phan M H, Yu S C, Hur N H, Appl. Phys. Lett. 86 (2005) 072504.

[PHAN07a] Phan M H, Yu S C, J. Magn. Magn. Mater. 308 (2007) 325.

[PICO08a] Picornell C, Pons J, Cesari E and Dutkiewicz J, Intermetallics 16 (2008) 751.

[PLAN92a] Planes A, Man˜osa L, Rı´os-Jara D, and Ortı´n J, Phys. Rev. B 45 (1992) 7633.

[PLAN09a] Planes A, Ma˜nosa L, Moya X, Marcos J, Acet M, Krenke T, Aksoy S and Wassermann E F, Adv. Mater. Res. 52(2008) 221.

[PLAN09b] Planes A, Mañosa L, and Acet M, Phys. Condens. Matter 21 (2009) 233201.

[PONS08a] Pons J, Cesari E, Segu´I C, Masdeu F, Santamarta R, Mater. Sci. Eng. A 481–482 (2008) 57.

[PORT92a] Porter D A and Easterling K E, Phase Transformations in Metals and Alloys, Chapman and Hall (1992).

[QINQ06a] Qin Q D, Zhao Y G, Cong P J, Liang Y H, Zhou W, J. Alloys Compd. 420 (2006) 121.

[RAMA10a] Rama Rao N V, Chandrasekaran V and Suresh K G, J. Appl. Phys. 108 (2010) 043913.

[RAME12a] Ramezani M, Neitzert T, Journal of Achievements in Materials and Manufacturing Engineering 55 (2012) 790.

[RANK09a] Ranke P J von, Oliveira N A de, Alho B P, Plaza E J R, Sousa V S R de, Caron L and Reis M S, J. Phys.: Condens. Matter 21 (2009) 056004.

[REIC80a] Reichl L E, A modern course in statistical mechanics, University of Texas press, Austin (1980).

[RIET67a] Rietveld H M, Acta Cryst. 22 (1967) 151.

[RIET69a] Rietveld H M, Acta Cryst. 2 (1969) 65.

[ROME13a] RomeroGo´mez J, FerreiroGarcia R, De MiguelCatoira A and RomeroGo´mez M, Renew. Sust. Energ. Rev. 17 (2013) 74.

[ROSA12a] Rosa W O, Gonzalez L, Garcıa J, Sanchez T, Vega V, Escoda Ll, Su˜nol J J, Santos J D, Alves M J P, Sommer R L, Prida V M and Hernando B, Phys. Res. Inter. 2012 (2011) 794171.

[SAHO11a] Sahoo R, Nayak A K, Suresh K G and Nigam A K, J. Appl. Phys. 109 (2011) 07A921.

[SANC10a] Sánchez T, Sánchez Llamazares J L, Hernando B, Santos J D, Sánchez M L, Perez M J , Suñol J J, Sato Turtelli R and Grössinger R, Mater. Sci. Forum 635 (2010) 81.

[SANT08a] Santanna Y V B de, Melo M A C de, Santos I A, Coelho A A, Gama S, and Cótica L F, Solid State Commun. 148 (2008) 289.

[SARM09a] Sarma S, Ph. D thesis, Indian Institute of Technology Guwahati (2009).

[SCAN12a] Scanning Electron Microscope, Copyright © 2012 Stress Engineering Services, Inc. [http://www.stress.com/servicetier3.php?sid=8&pid=385]

[SCHE07a] Scheerbaum N, Hinz D, Gutfleisch O, MÄuller K H and Schultz L, Acta Mater. 55 (2007) 2707.

[SCHE08a] Scheerbaum N, Heczko O, Liu J, Hinz D, Schultz L and Gutfleisch O, New J. Phys. 10 (2008) 073002.

[SCHM60a] Schmid H, Cobalt 6 (1960) 8.

[SHAR07a] Sharma V K, Chattopadhyay M K, Kumar R, Ganguli T, Tiwari P and Roy S B, J. Phys.: Condens. Matter 19 (2007) 496207.

[SHAR07b] Sharma V K, Chattopadhyay M K and Roy S B, J. Phys. D: Appl. Phys. 40 (2007) 1869.

[SHAR10a] Sharma V K, Chattopadhyay M K, Khandelwal A, and Roy S B, Phys. Rev. B 82 (2010) 172411.

[SHAR10b] Sharma V K, Chattopadhyay M K, Nath S K, Sokhey K J S, Kumar R, Tiwari P and Roy S B, J. Phys. Condens. Matter. 22 (2010) 486007.

[SHAR11a] Sharma V K, Ph. D thesis, Raja Ramanna Centre for Advanced Technology, Indore (2011).

[SKUM03a] Skumryev V, Stoyanov S, Zhang Y, Hadjipanayis G, Givord D and Nogu´es J Nature 423 (2003) 850

[SONG00a] Song D, Nowak J, Larson R, Kolbo P and Chellew R, IEEE Trans. Magn. 36 (2000) 2545.

[SORT99a] Sort J, Nogu´es J, Amils X, Suri˜nach S, Mu˜noz J S and Baro M D Appl. Phys. Lett. 75 (1999) 3177.

[SORT00a] Sort J, Nogu´es J, Amils X, Suri˜nach S, Mu˜noz J S and Baro M D, J. Magn. Magn. Mater. 219(2000) 53.

[SORT01a] Sort J, Nogu´es J, Suri˜nach S, Mu˜noz J S, Baro M D, Chappel E, Dupont F and Chouteau G, Appl. Phys. Lett. 79(2001) 1142.

[SORT02a] Sort J, Suri˜nach S, Mu˜noz J S, Bar´o M D, Nogu´es J, Chouteau G, Skumryev V and Hadjipanayis G C, Phys. Rev. B 65(2002) 174420.

[SOZI02a] Sozinov A, Likhachev A A, Lanska N and Ullakko K, Appl. Phys. Lett. 80 (2002) 1746.

[SOZI13a] Sozinov A, Lanska N, Soroka A and Zou W, Appl. Phys. Lett. 102(2013) 021902.

[SPIC05a] Spichkin Y I and Tishin A M, J. Alloys Comp. 403 (2005) 38.

[STAN71a] Stanley H E, ntroduction to Phase Transitions and Critical Phenomena, Oxford University Press, New York (1971).

[STRN95a] Strnadel B, Ohashi S, Ohtsuka H, Ishihara T and Miyazaki S, Mater. Sci. Eng. A 202 (1995) 148.

[SURE11a] Suresh Kumar V and Mahendiran R, J Appl. Phys. 109 (2011) 023903.

[SURY01a] Suryanarayana C, Prog. Mater. Sci. 46 (2001) 1.

[SUTO04a] Sutou Y , Imano Y, Koeda N, Omori T, Kainuma R, Ishida K and Oikawa K Appl. Phys. Lett. 85 (2004) 4358.

[SVOB04a] Svoboda J, Magnetic Techniques for the treatment of materials, Kluwer Academic Publishers, The Netherlands (2004).

[SWAL62a] Swalin R A, Thermodynamics of Solids, John Wiley & Sons, New York (1962).

[SZYT89a] Szytula A, Ptasiewicz-Bak H and Leciejewicz J, J. Magn. Magn. Mater. 80 (1989) 195.

[TANA02a] Tanaka A, Shimizu Y, Seyama Y, Nagasaka K, Kondo R, Oshima H, Eguchi S and Kanai H, IEEE Trans. Magn. 38(2002) 84

[TANA10a] Tanaka Y, Himuro Y, Kainuma R, Sutou Y, Omori T and Ishida K Science 327 (2010) 1488.

[TANG84a] Tang C, J. Appl. Phys. 55 (1984) 2226.

[TANG05a] Tang Y J, Solomon V C, Smith D J, Harper H and Berkowitz A E, J. Appl. Phys. 97 (2005) 10M309.

[TANH08a] Tan H and Elahinia M H, Commun. Nonlinear Sci. Numer. Simul. 13 (2008) 1917.

[TEGU02a] Tegus O, Bruck E, Buschow K H and de Boer F R, Nature 415 (2002) 150.

[TEGU02b] Tegus O, Brück E, Zhang L, Dagula, Buschow K. H. J. and de Boer F R, Physica B 319 (2002) 174.

[THOM00a] Thompson D A and Best J S, IBM J. Res. Dev. 44 (2000) 311.

[TIAN08a] B. Tian B Chen F, Liu Y and Zheng Y F, Intermetallics, 16(2008) 1279.

[TISH99b] Tishin A M, Handbook of Magnetic Materials, North Holland, Amsterdam, (1999).

[TISH03a] Tishin A M and Spichkin Y I, The Magnetocaloric Effect and its Applications, IOP, Bristol (2003).

[TKAT02a] Tkatch V I, Limanovskii A I, Denisenko S N and Rassolov S G, Mater. Sci. Eng. A 323 (2002) 91.

[TONG99a] Tong H C, Shi X, Liu F, Qian C, Dong Z W, Yan X, Barr R, Miloslavsky L, Zhou S, Perlas J, Prabhu P, Mao M, Funada S, Leng Q, Zhu J G and Dey S, IEEE Trans. Magn. 35(1999) 2574.

[TSAN97a] Tsang C, Lin T, MacDonald S, Pinarbasi M, Robertson N, Santini H, Doerner M, Reith T, Vo L, Diola T and Arnett P, IEEE Trans. Magn. 33(1997) 2866.

[TSAN99a] Tsang C, Pinarbasi M, Santini H, Marinero E, Arnett P, Olson R, Hsiao R, Williams M, Payne R, Wang R, Moore J, Gurney B, Lin T and Fontana R, IEEE Trans. Magn. 35(1999) 689.

[ULLA96a] Ullakko K, Huang J K, Kantner C, O'Handley R C and Kokorin V V, Appl. Phys. Lett. 69 (1996) 1966.

[ULLA97a] Ullakko K, Huang J K, Kokorin V V and O'Handley R C, Scripta Mater. 36 (1997)1133.

[ULLA01a] Ullakko K, Ezer Y, Sozinov A, Kimmel G, Yakovenko P and Lindroos V K, Scripta Mater. 44 (2001) 475.

[UMET08a] Umetsu R Y, Kainuma R, Amako Y, Taniguchi Y, Kanomata T, Fukushima K, Fujita A, Oikawa K and Ishida K, Appl. Phys. Lett. 93 (2008) 042509.

[VALL08a] Vallejo-Fernandez G, Fernandez-Outon L E and O'Grady K, J. Appl. Phys. 103 (2008) 07C101.

[VASI99a] Vasil'ev A N, Bozhko A D, Khovailo V V, Dikshtein I E, Shavrov V G, Buchelnikov D, Matzumoto M, Suzuki S, Takagi T, Tani J, Phys. Rev. B 59 (1999) 1113.

[VONO74a] Vonsovskii S V, Magnetism, Israel Program Sci. Translations, Jerusalem (1974).

[WADA01a] Wada H and Tanabe Y, Appl. Phys. Lett. 79 (2001) 3302.

[WANG91a] Wang F E, Recent Advances in Nitinol Technology, ADPA/AIAA /ASME/SPIE Conference on Active Materials and Adaptive Structures-Session 10 (1991) 177.

[WANG95a] Wang J P, Han D H, Luo H L, Lu Q X and Sun Y W, Appl. Phys. A 61 (1995) 407.

[WANG01a] Wang Z M, Ni G, Xu Q Y, Sang H and Du Y W, J. Magn. Magn.Mater. 234 (2001) 371.

[WANG06a] Wang W H, Ren X and Wu G H, Phys. Rev. B 73 (2006) 092101.

[WANG07a] Wang Y D, Ren Y, Nie Z H, Liu D M, Zuo L, Choo H, Li H, Liaw P K, Yan J Q, McQueeney R J, Richardson J W and Huq A, J. Appl. Phys. 101 (2007) 063530.

[WANG08a] Wang B M, Liu Y, Wang L, Huang S L, Zhao Y, Yang Y and Zhang H, J. Appl. Phys. 104 (2008) 043916.

[WANG09a] Wang B M, Wang L, Liu Y and Zhao B C, J. Appl. Phys. 105 (2009) 023913.

[WANG12a] Wang Q, and Wu N, Smart Mater. Struct. 21 (2012) 013001.

[WARB81a] Warburg E, Ann. Phys. 13 (1881) 141.

[WAYM99a] Wayman C M and Duerig T W, An Introduction to Martensite and Shape Memory, in: Engineering Aspects of Shape Memory Alloys, Stoneham, Massachusetts: Butterworth-Heinemann, (1999).

[WEBS73a] Webster P J and Ziebeck K R A, J. Phys. Chem. Solids 34 (1973) 1647.

[WEBS84a] Webster P J, Ziebeck K R A, Town S L and Peak M S, Philos. Mag. B 49 (1984) 295.

[WELL99a] Weller D and Moser A, IEEE Trans. Magn. 35 (1999) 4423.

[WHIT97a] Whitcher F D, Computers and Structures 64 (1997) 1005.

[WIDO64a] Widom B, J. Chem. Phys. 41 (1964) 1633.

[WIRT97a] Wirth S, Leithe-Jasper A, Vasil'ev A N, Coey J M D, J. Magn. Magn. Mater. 167 (1997) L7.

[WOHL59a] Wohlfarth E P, Adv. Phys. 8 (1959) 87.

[WUGH02a] Wu G H, Wang W H, Chen J L, Ao L, Liu Z H, Zhan W S, Liang T and Xu H B, Appl. Phys. Lett. 80 (2002) 634.

[WUMI00a] Wu M H and Schetky L M, Proceedings, SMST-2000, Pacific Grove, California (2000) 171.

[WUTT01a] Wuttig M, Li J and Craciunescu C A Scripta Mater. 44 (2001) 2393–2397.

[XUAN08a] Xuan H C, Xie K X, Wang D H, Han Z D, Zhang C L, Gu B X and Du Y W, Appl. Phys. Lett.92 (2008) 242506.

[YANJ10a] Yan J L, Li Z Z, Chen X, Zhou K W, Shen S X and Zhou H B, J, Alloys Comp. 506 (2010) 516.

[YAOY95a] Yao Y D, Chen Y Y, Hsu C M, Lin H M, Tung C Y, Tai M F, Wang D H, Wu K T and Suo C T, NanoStruct. Mater. 6 (1995) 933.

[YAOY96a] Yao Y D, Chen Y Y, Tai M F, Wang D H and Lin H M, Mater. Sci. Eng. A 217-218 (1996) 281.

[YELO71a] Yelon A, Physics of Thin Films, Academic Press, NewYork (1971).

[ZASI90a] Zasimchuk I K, Kokorin V V, Martynov V V, Tkachenko A V and Chernenko V A, Fiz. Met. Metalloved. 6 (1990) 110.

[ZHAN02a] Zhang J, Huai Y and Lederman M, J. Appl. Phys. 91(2002) 7285; Jang E, Wang G, Cho K Y and Lee H, J. Appl. Phys. 91 (2002) 8769.

[ZHAN02b] Zhang Z, Feng Y C, Clinton T, Badran G, Yeh N H, Tarnopolsky G, Girt E, Munteanu M, Harkness S, Richter H, Nolan T, Ranjan R, Hwang S, Rauch G, Ghaly M, Larson D, Singleton E, Vas′ko V, Ho J, Stageberg F, Kong V, Duxstad K and Slade S, IEEE Trans. Magn. 38(2002) 1861.

[ZHAN04a] Zhang Y Q and Zhang Z D, J. Alloys Comp. 365 (2004) 35.

[ZHAN08a] Zhang G, Schlarb A K, Tria S and Elkedim O, Compos Sci Technol 68 (2008) 3073.

[ZHAN09a] Zhang Y, Hu H and Zhu S, Struct. Control Health Monit. 16 (2009) 668.

[ZHAO04a] Zhao Z Q, Xiong W, Wu S X and Wang X L, J. Iron Steel Res. 111 (2004) 55.

[ZHAO04b] Zhao Z Q, Wu S X, Wang F S, Wang Q, Jiang L P and Wang X L, Rare Met. 23 (2004) 241.

[ZHAO10a] Zhao X G, Hsieh C C, Lai J H, Cheng X J, Chang W C, Cui W B, Liu W and Zhang Z D, Scr. Mater. 63 (2010) 250.

[ZHAO11a] Zhao X, Yang J, Wang X, Hsieh C C, Chang W C, Liu W and Zhangg Z, IEEE Trans. Magn. 47 (2011) 2455.

[ZHEN03a] Zheng Y K, Wu Y H, Li K B, Qiu J J, Shen Y T, An L H, Guo Z B, Han G C, Luo P, You D and Liu Z Y, J. Appl. Phys. 93 (2003) 7307.

[ZHEN04a] Zheng Y K, Li K B, Qiu J J, Han G C, Guo Z B, Zong B Y, An L H, Luo P, Liu Z Y and Wu Y H, IEEE Trans. Magn. 40 (2004) 2248.

[ZHOU05a] Zhou X, Li W, Kunkel H P and Williams G, J. Appl. Phys. 97 (2005)10M515.

[ZHOU06a] Zhou X, Li W, Kunkel H P and Williams G, Phys. Rev. B 73 (2006) 012412.

[ZIDE88a] Zider R B, Krumme J F and Yeglass E, US patent number 4,772, 112 (1988).

[ZIEB01a] Ziebeck K A and Neumann K U, Magnetic Properties of Metals, Berlin, Springer-Verlag (2001).

PUBLICATIONS

IN JOURNALS:

1) Effect of Co and Cu substitution on the magnetic entropy change in $Ni_{46}Mn_{43}Sn_{11}$ alloy,
Rahul Das, S. Sarma, A. Perumal and A. Srinivasan,
J. Appl. Phys. **109** (2011) 07A901.

2) Evaluation of Ni-Mn-In-Si alloys for magnetic refrigerant application,
Rahul Das, A. Perumal and A. Srinivasan,
IEEE Trans. Magn. **47** (2011) 2463.

3) Tailoring the magnetocaloric properties of $Ni_{51}Mn_{34}In_{15}$ alloy by Ge and Si substitution for In,
Rahul Das, A. Perumal and A. Srinivasan,
Phys. Express **3** (2013) 13.

4) Effect of particle size on the magneto-caloric properties of $Ni_{51}Mn_{34}In_{14}Si_1$ alloy,
Rahul Das, A. Perumal and A. Srinivasan,
J. Alloys. Compd. **572** (2013) 192**.**

5) Influence of solidification rate and heat treatment on magnetic refrigerant properties of melt spun $Ni_{51}Mn_{34}In_{14}Si_1$ ribbons,
Rahul Das, P. Saravanan, D. Arvindha Babu, A. Perumal, A. Srinivasan,
J. Magn. Magn. Mater. **344** (2013) 152.

6) Variations in structural and magnetic phase transitions of Ni-Mn-In-Si alloy with change in Ni/Mn ratio,
Rahul Das, S. Sarma, B. Deka, A. Perumal and A. Srinivasan,
Phys. Express **4** (2014) 7.

7) Estimation of entropy change at the first order martensitic transition in Ni-Mn-X based ferromagnetic shape memory alloys,
Rahul Das, A. Perumal and A. Srinivasan,
Physica B: Condens Matter (Under Review).

8) Critical behaviour and magnetocaloric effect near Curie temperature of $Ni_{50}Mn_{35}In_{14}Si_1$ alloy
Rahul Das, P. Saravanan, A. Perumal and A. Srinivasan,
(To be communicated).

IN CONFERENCE PROCEEDINGS:

1) Room temperature magnetocaloric effect in Co substituted Ni-Mn-Sn alloy,
R. Das, A. Perumal and A. Srinivasan,
Proc. NABSET-2010 (Don Bosco College of Engg. & Tech. Guwahati, 12-13 March, 2010).

2) Magnetic properties and magnetocaloric effect in $Ni_{55}Mn_{21-x}Ga_{24+x}$ alloys,
R. Das, A. Perumal and A. Srinivasan,
Proc. CMDays-2011 (Gauhati Univ., Guwahati, 24-26 August, 2011).

3) Enhanced magnetocaloric effect in cobalt substituted Ni-Mn-Ga alloys,
Rahul Das, S. Sarma, A. Perumal and A. Srinivasan,
AIP Conf. Proc. **1347** (2011) 107.

4) Magnetic refrigerant properties of $Ni_{50}Mn_{37-x}Fe_xSn_{13}$ alloy at low magnetic fields,
Rahul Das, A. Perumal and A. Srinivasan,
AIP Conf. Proc. **1447** (2012) 1173.

5) Estimation of latent heat and entropy changes at the first order structural transition in $Ni_{55}Mn_{21-x}Ga_{24+x}$ alloys,
Rahul Das, A. Perumal and A. Srinivasan,
Proc. Intl. Symp. Proc. Fab. Adv. Mater. (PFAM-21) (IIT Guwahati, Guwahati, 10-13 December, 2012).

****